ISSN 1997-1397 (Print)
ISSN 2313-6022 (Online)

Журнал Сибирского федерального университета

Математика и физика

Journal of Siberian Federal University

Mathematics & Physics

2026 19 (1)

ISSN 1997-1397
(Print)

ISSN 2313-6022
(Online)

2026 19 (1)

ЖУРНАЛ СИБИРСКОГО ФЕДЕРАЛЬНОГО УНИВЕРСИТЕТА
Математика и Физика

JOURNAL OF SIBERIAN FEDERAL UNIVERSITY
Mathematics & Physics

Издание индексируется Scopus (Elsevier), Emerging Sources Citation Index (WoS, Clarivate Analytics), Российским индексом научного цитирования (НЭБ), представлено в международных и российских информационных базах: Ulrich's periodicals directiory, ProQuest, EBSCO (США), Google Scholar, MathNet.ru, КиберЛенинке.

Включено в список Высшей аттестационной комиссии «Рецензируемые научные издания, входящие в международные реферативные базы данных и системы цитирования».

Все статьи представлены в открытом доступе http://journal.sfu-kras.ru/en/series/mathematics_physics.

Журнал Сибирского федерального университета.
Математика и физика.
Journal of Siberian Federal University. Mathematics & Physics.

Учредитель: Федеральное государственное автономное образовательное учреждение высшего образования "Сибирский федеральный университет"(СФУ)
Главный редактор: А.М. Кытманов. Редакторы: В.Е. Зализняк, А.В. Щуплев.
Компьютерная верстка: Г.В. Хрусталева
№ 1. 26.02.2026. Индекс: 42327. Тираж: 1000 экз. Свободная цена
Адрес редакции и издателя: 660041 г. Красноярск, пр. Свободный, 79, оф. 32-03.
Отпечатано в типографии Издательства БИК СФУ
660041 г. Красноярск, пр. Свободный, 82а.
Свидетельство о регистрации СМИ ПИ № ФС 77-28724 от 29.06.2007 г., выданное Федеральной службой по надзору в сфере массовых коммуникаций, связи и охраны культурного наследия
http://journal.sfu-kras.ru
Подписано в печать 15.02.26. Формат 84×108/16. Усл.печ. л. 12,0.
Уч.-изд. л. 11,8. Бумага тип. Печать офсетная.
Тираж 1000 экз. Заказ 25228
Возрастная маркировка в соответствии с Федеральным законом № 436-ФЗ:16+

Editorial Board:

Consulting Editors Mathematics & Physics:

CONTENTS

СОДЕРЖАНИЕ

EDN: BHSYRS
УДК 537.84

Comparative Analysis of Experimental and Numerical Data on Turbulent Pipe Flow of Liquid Metal Affected by Transverse Magnetic Field and Heating From Below

Daniil A. Berdyugin*
Joint Institute for High Temperatures of the Russian Academy of Sciences
Moscow, Russian Federation
Yaroslav I. Listratov†
National Research University «Moscow Power Engineering Institute»
Moscow, Russian Federation
Ivan A. Belyaev‡
Joint Institute for High Temperatures of the Russian Academy of Sciences
Moscow, Russian Federation

Received 10.08.2025, received in revised form 17.09.2025, accepted 27.10.2025

Abstract. The article presents the results of direct numerical simulation of mercury flow in a horizontal pipe under non-uniform bottom heating in the presence of a transverse magnetic field. The study focuses on the analysis of hydrodynamics and heat transfer under conditions of thermogravitational convection induced by localized heating and magnetohydrodynamic effects. It is shown that the transverse magnetic field significantly suppresses transverse velocity components, stabilizes the flow, and alters the structure of convective vortices, leading to anisotropy in turbulent transport and the formation of characteristic Hartmann and boundary layers. Analysis of velocity and temperature fields reveals regimes of instability suppression and restructuring of large-scale circulation. A comparison of statistical characteristics of temperature fluctuation intensities, as well as dimensionless quantities, with experimental data [1] is performed. The comparison and analysis of the obtained results enhance the understanding of processes occurring in liquid metals under the combined influence of gravitational, thermal, and electromagnetic fields, which is of interest for the development of cooling systems in nuclear reactors with liquid metal coolants.

Keywords: liquid metal, DNS, convection, MCF, heat transfer, transverse magnetic field.

Citation: D.A. Berdyugin, Y.I. Listratov, I.A. Belyaev, Comparative Analysis of Experimental and Numerical Data on Turbulent Pipe Flow of Liquid Metal Affected by Transverse Magnetic Field and Heating From Below, J. Sib. Fed. Univ. Math. Phys., 2026, 19(1), 5–20. EDN: BHSYRS.

Introduction

Fusion technologies development involves studying of liquid metals (LM) behavior under the influence of strong magnetic field combined with high thermal loads [2]. In tokamak-type reactors, LM can be used in tritium breeding systems, for thermal protection, and as coolants in the blanket and divertor [3]. The hydrodynamics and heat transfer of LM flowing through channels under

*berdyugindaniel@yandex.ru
†yaroslav.listratov@yandex.ru https://orcid.org/0000-0002-6288-9787
‡bia@ihed.ras.ru https://orcid.org/0000-0002-6397-3251

conditions typical for a fusion reactor blanket are the subject of the present research. One of the interesting phenomena that may negatively affect the performance of designed facilities is the occurrence of abnormally high-amplitude, low-frequency temperature fluctuations in the LM flow. As shown, for example, in the review [4], their appearance is possible in various geometric configurations and is caused by the combined effect of buoyancy forces and magnetic field.

The study of such effects began with the experimental work [5], where abnormally high quasiperiodic temperature fluctuations of mercury were observed under mixed turbulent convection and transverse magnetic field in a horizontally oriented tube heated from below. The experiments were conducted under the following parameter conditions: $\mathrm{Re} = 10^4$, $\mathrm{Gr} = 3.5 \cdot 10^7$, $\mathrm{Ha} = 0 \div 300$. In the absence of a magnetic field, temperature fluctuations within the mercury flow are similar to those in developed turbulent flow, taking into account the peculiarities of mixed convection. Increasing the magnetic induction to $\mathrm{Ha} = 100$ leads to flow laminarization and almost complete suppression of flow fluctuations. Further increase to $\mathrm{Ha} = 300$ alters the flow structure such that the amplitude of fluctuations, generated at a single frequency, sharply increases to high values.

Work [6] presents a detailed investigation at the parameter conditions $\mathrm{Re} = 10^4$, $\mathrm{Gr} = 4.4 \cdot 10^7$, $\mathrm{Ha} = 0 \div 300$, where anomalous fluctuation within mercury under mixed convection in a transverse magnetic field were also detected. Numerical simulation of a similar problem using the DNS (Direct Numerical Simulation) method was carried out in several studies [7, 8], providing a more comprehensive understanding of how temperature fluctuations arise as the flow structure reorganizes. Despite a considerable number of studies, the behavior of flows at very high parameter values (Gr и Ha) remains not fully clear. For instance, under blanket conditions, expected thermal loads correspond to $\mathrm{Gr} \sim 10^{10} - 10^{12}$, and magnetic fields up to $\mathrm{Ha} \sim 10^4$. Preliminary results, particularly obtained from numerical models based on asymptotic two-dimensional approximations at high Ha numbers, indicate that regimes with magneto-convective temperature fluctuations will occur even at high Ha and Gr, and the amplitudes of these fluctuations may reach hundreds of degrees [9]. Some practically important configurations, however, are still insufficiently studied. In particular, this concerns extending the region of magnetic field influence on the flow, which better reflects the real situation in the blanket. Expanding the range of investigated parameters and increasing the magnetic field interaction zone was the primary objective of this work.

1. Research methodology

1.1. Problem statement

The flow and heat transfer of mercury in a horizontal pipe are investigated. The pipe is uniformly heated along its length and non-uniformly around its perimeter (the lower half is heated at a constant heat flux $q_1(z) = const \neq 0$, while the upper half is thermally insulated – $q_2(z) = 0$). The pipe is placed in the gap of an electromagnet with a constant transverse magnetic field B (Fig. 1). This configuration corresponds to an unstable density stratification due to heating. Thermogravitational convection significantly affects heat transfer under forced flow of the liquid metal, giving rise to intense secondary convective flows.

The experimental part of the work, with which the numerical calculations are compared, was carried out on the RK-3 facility. The description of the facility is provided in [10].

The experimental setup employs a test section consisting of a stainless steel pipe with a length

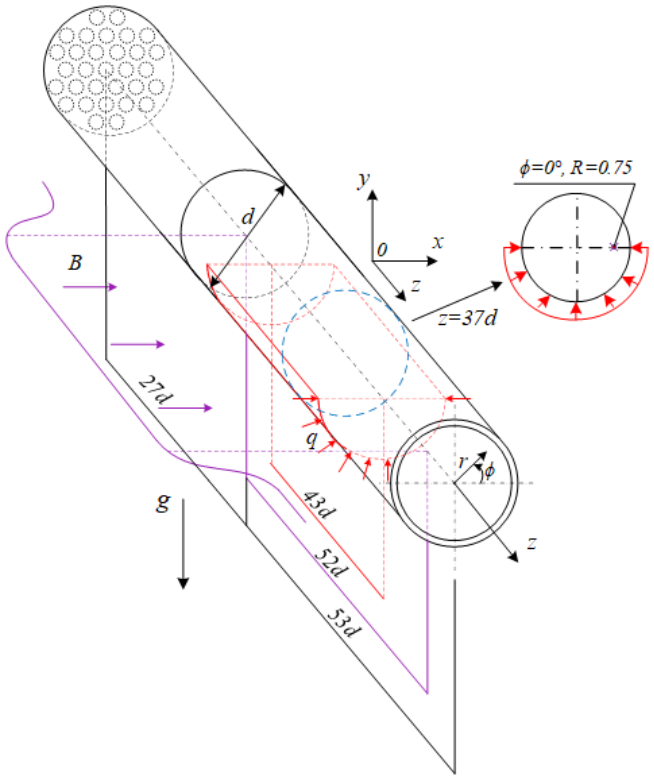

Fig. 1. The test section in the studied configuration: total length of 80 diameters, a special inlet section for generating a turbulent velocity field at the entrance to the magnetic field $z/d \in [-32, -5]$ (length — 27 diameters), the region of homogeneous magnetic field $z/d \in [-5, 47]$ (length — 52 diameters), and the heating zone $z/d \in [0, 43]$ (length – 43 diameters)

of $L = 2$ m, an inner diameter of $d = 19$ mm, and a wall thickness of $\delta_w = 0.5$ mm, terminating in a mixing chamber with an outlet nozzle. The inner surface of the pipe was polished using cast-iron lapping tools. The test section comprises, in turn, a hydrodynamic stabilization region longer than 60 diameters and a subsequent heating area. Along the length of the latter (43 diameters), a ribbon-type two-section indirect heater is installed to provide non-uniform circumferential heat loading. The design of this section is identical to that used in [6]. The origin of the coordinate system ($z = 0$) coincides with the beginning of the heating zone.

Local measurements of the temperature field were performed using invasive immersion probes. The probe possesses sufficient strength and rigidity to withstand buoyancy forces and the dynamic pressure of the incoming mercury flow. An important advantage of the probe technique is the ability to avoid errors in determining heat transfer coefficients introduced by the so-called contact thermal resistance, which arises due to the displacement of liquid metal oxides and other possible impurities from the wall. The probe method was employed to measure temperature fields. Some of the experimental results are partially described in [11].

Flow parameters for the numerical simulations were chosen to closely match those of the experimental studies in [1]. The thermophysical properties of mercury were assumed constant and set to their values at an average mercury temperature of 30°C [12], as listed in Tab. 1.

The main flow regimes under investigation corresponded to an average flow velocity $\overline{u}$ up to

Table 1. Thermophysical properties of mercury

Property	**Value**
Density ρ, kg/m^3	$1.352 \cdot 10^4$
Kinematic viscosity ν, m^2/s	$1.12 \cdot 10^{-7}$
Thermal conductivity λ, W/(m·K)	8.64
Specific heat capacity C_p, J/(kg·K)	139.2
Electrical conductivity σ, (Om·m)$^{-1}$	$1.04 \cdot 10^6$
Thermal expansion coefficient β, 1/K	$1.809 \cdot 10^{-4}$
Prandtl number Pr $= \lambda/(\rho C_p \nu)$	0.0248

0.012 m/s, a magnetic field induction B_0 in the uniform region up to 2.7 T, and an average heat flux on the heated wall section $\overline{q} = (q_1 + q_2)/2 \equiv 27.5$ kW/m^2 (see Tab. 2).

1.2. Physical model

We consider unsteady forced pipe flow of a viscous incompressible fluid with constant properties. The fluid mass flow rate is maintained constant and equal to $G = \rho\overline{u}(\pi d^2/4) = \text{const}$. To account for the influence of the magnetic field, we employ the quasi-static (inductionless) MHD approximation [7], which essentially assumes that under the conditions of small magnetic Reynolds number $\mathrm{Re_m} = \overline{u}d\sigma\mu_0 \ll 1$ and magnetic Prandtl number $\mathrm{Pr_m} = \nu\sigma\mu_0 \ll 1$ (μ_0 being the magnetic permeability of vacuum), the induced magnetic field $\mathbf{b}$ is much smaller than the externally applied magnetic field $\mathbf{B_0}$, and the induced electric currents in Ohm's law $\mathbf{j} = \sigma(\mathbf{E} + \mathbf{u} \times \mathbf{B_0})$ change "instantaneously" with variations in the velocity field. Thus, the interaction between the moving electrically conducting medium and the magnetic field reduces to a one-way influence of the magnetic field on the flow. Neglecting the Coulomb component of the electromagnetic force, this influence is represented in the momentum equation for the continuum by the Ampere force $\mathbf{F}_{em} = \mathbf{j} \times \mathbf{B_0}$. Density variations caused by temperature inhomogeneities due to heating of the lower part of the pipe are taken into account only in the momentum equation (Boussinesq approximation [7]). By neglecting viscous and Joule dissipation in the enthalpy balance equation of the flow, we obtain the system of equations governing the continuum dynamics under an externally applied magnetic field, consisting of the continuity equation (1), the momentum equation (2), and the enthalpy balance equation (3), expressed in terms of temperature:

$$\nabla \cdot \mathbf{u} = 0, \tag{1}$$

$$\frac{\partial \mathbf{u}}{\partial t} + (\mathbf{u} \cdot \nabla)\mathbf{u} = -\nabla p/\rho + \nu\nabla^2\mathbf{u} + \mathbf{F}_{em}/\rho + \mathbf{g}\beta(T - T_0), \tag{2}$$

$$\frac{\partial T}{\partial t} + (\mathbf{u} \cdot \nabla)T = \frac{\lambda}{\rho c_p}\nabla^2 T, \tag{3}$$

where ρ, ν, β, λ, c_p are the density, kinematic viscosity coefficient, thermal coefficient of volume expansion, thermal conductivity, and isobaric heat capacity of the fluid, respectively, T_0 is the flow temperature at the inlet to the heated region, and $\mathbf{g}$ is the gravitational acceleration vector.

To compute the electric current density and the Ampere force in equation (2), Kirchhoff's law $\nabla \cdot \mathbf{j} = 0$ is used. Applying this to Ohm's law, taking into account $\mathbf{E} = -\nabla\varphi$, yields the

Poisson equation for the electric potential:

$$\nabla^2\varphi = \nabla \cdot (\mathbf{u} \times \mathbf{B_0}). \tag{4}$$

By introducing characteristic scales (see Tab. 2) for the quantities appearing in equations (2)–(4), one can obtain the system of equations in dimensionless form:

$$\nabla \cdot \tilde{\mathbf{u}} = 0, \tag{5}$$

$$\frac{\partial \tilde{\mathbf{u}}}{\partial \tilde{t}} + (\tilde{\mathbf{u}} \cdot \nabla)\tilde{\mathbf{u}} = -\nabla\tilde{p} + \mathrm{Re}^{-1}\nabla^2\tilde{\mathbf{u}} + \mathrm{Ha}^2\mathrm{Re}^{-1}\left[-\nabla\tilde{\varphi} + \tilde{\mathbf{u}} \times \mathbf{e}_b\right] \times \mathbf{e}_b + \mathrm{Gr}_q\mathrm{Re}^{-2}\theta\mathbf{e}_g, \tag{6}$$

$$\nabla^2\tilde{\varphi} = \nabla \cdot (\tilde{\mathbf{u}} \times \mathbf{e}_b), \tag{7}$$

$$\frac{\partial \theta}{\partial \tilde{t}} + (\tilde{\mathbf{u}} \cdot \nabla)\theta = (\mathrm{RePr})^{-1}\nabla^2\theta, \tag{8}$$

where the dimensionless Reynolds (Re), Grashof ($\mathrm{Gr_q}$), and Hartmann (Ha) numbers are the governing similarity criteria of the problem (see Tab. 2), and $\mathbf{e}_b = \left\{\tilde{B}_r, \tilde{B}_\phi, \tilde{B}_z\right\}$ and $\mathbf{e}_g = \{\tilde{g}_r, \tilde{g}_\phi, 0\}$ are the dimensionless vectors of the external magnetic field induction and gravity, respectively.

Table 2. Characteristic scale parameters of the problem and the corresponding dimensionless similarity criteria

Name	**Parameter**	**Value**
Length scale	Pipe diameter d, mm	19
Velocity scale	Flow velocity $\overline{u}$, mm/s	$4 \div 12$
Time scale	$t_0 = d/\overline{u}$, s	$1.61 \div 4.61$
Pressure scale	$p_0 = \rho\overline{u}^2$, Pa	$0.22 \div 1.95$
Reynolds number	$\mathrm{Re} = \overline{u}d/\nu$	$7 \cdot 10^3 \div 20 \cdot 10^3$
Magnetic induction scale	B_0, T	$0 \div 2.7$
Electric current density scale	$j_0 = \sigma\overline{u}B_0$, A/m^2	$3.3 \cdot 10^4$
Electric potential scale	$\varphi_0 = \overline{u}dB_0$, V	$0.6 \cdot 10^{-3}$
Hartmann number	$\mathrm{Ha} = B_0 d\sqrt{\sigma/\rho\nu}$	$0 \div 1350$
Temperature scale	$\Delta T = \overline{q}d/\lambda$, K	60.5
Grashof number	$\mathrm{Gr_q} = g\beta\overline{q}d^4/\nu^2\lambda$	$6.05 \cdot 10^7$

1.3. Boundary conditions

Inlet conditions. In the experiment, an isothermal fluid flow enters the magnetic field region under turbulent flow conditions ($\mathrm{Re}_{cr} \sim 2200$ for pipe flow) with a fully developed velocity profile. To replicate these conditions in the numerical model, an additional isothermal section of length 27 diameters is introduced, at the inlet of which a velocity field is prescribed (Fig. 2.a), simulating a "honeycomb" insert with $m = 31$ holes, a number determined through preliminary test simulations. A parabolic distribution of the axial velocity, corresponding to the flow rate per hole, is specified within each honeycomb cell, with additional random velocity fluctuations of

about 1% of the bulk velocity superimposed. The flow downstream of the honeycomb, consisting of interacting and decaying jets, naturally develops into a turbulent flow by the end of this special section, which then enters the magnetic field region (Fig. 2.b).

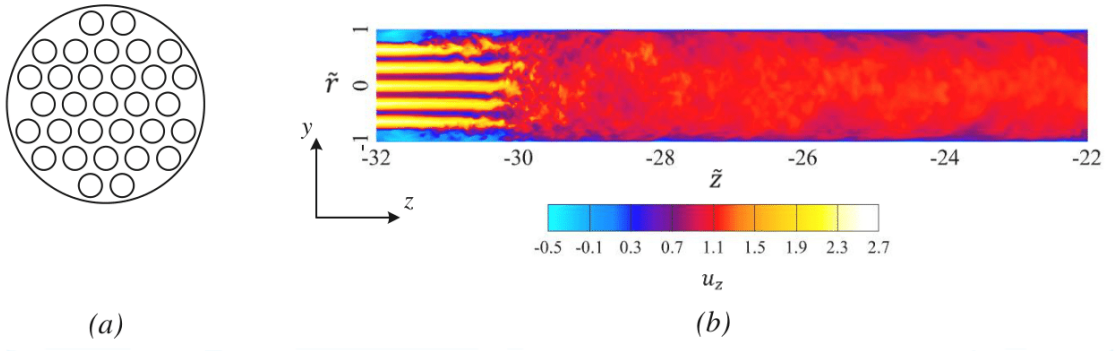

Fig. 2. Special section for forming the boundary condition of the velocity field: a — "honeycomb" insert, b — instantaneous longitudinal velocity field behind the honeycomb (fragment for $z/d \in [-32, -22]$)

Wall conditions. Given the relatively thin pipe wall thickness $\delta_w/d \simeq 0.025$, the walls were not explicitly included in the simulation. We neglect heat conduction within the wall and assume that the relative electrical conductivity of the wall is much smaller than that of the fluid, $C_w \equiv \sigma_w \delta_w/(\sigma d) \ll 1$ (in the experiment $C_w \sim 0.02$), meaning the walls are electrically insulating. The boundary conditions at the "fluid–solid wall" interface are set as follows: for velocity – the no-slip condition $\mathbf{u}|_w = 0$; for temperature – the second-kind boundary condition $\lambda \dfrac{\partial T}{\partial n}\bigg|_w = q(z)$, where $q = q_1(z)$ is a constant positive heat flux in the heating zone on the lower half of the pipe, and $q = q_2 = 0$ on the upper half of the pipe and outside the heating zone; for electric potential – the normal component of the current density is zero, $j_n|_w = \sigma \left(\dfrac{\partial \varphi}{\partial n}\right)\bigg|_w = 0$.

External magnetic field. The non-uniform magnetic field of the electromagnet was modeled using expressions for a two-dimensional dipole approximation [13]. Thus, at the inlet and outlet regions of the magnetic field, the magnetic induction vector has two components: B_x and B_z, whose values were compared with experimental data.

Outlet conditions. At the outlet, a convective (mixed) boundary condition was applied for velocity: $\dfrac{\partial \mathbf{u}}{\partial t} + \overline{u}\dfrac{\partial \mathbf{u}}{\partial z} = 0$; for temperature – the second-kind (Neumann) boundary condition $\dfrac{\partial T}{\partial z} = 0$; and for electric potential at both inlet and outlet – the Neumann boundary condition $\dfrac{\partial \varphi}{\partial z} = 0$, which corresponds to the situation where the induced current does not leave the considered flow domain.

1.4. Numerical procedure

The problem was solved using direct numerical simulation (DNS) with a conservative second-order finite-difference scheme on a structured collocated grid [14] in cylindrical coordinates (r, ϕ, z). Its accuracy and efficiency in simulating flows at high Hartmann numbers have been demonstrated, for example, in [15]. Details and specific features of the method for

cylindrical coordinates are described in [7]. Simulations were performed on a grid consisting of $N = N_r \times N_\phi \times N_z = 128 \times 256 \times 4096$ nodes, uniform in the axial z-direction and azimuthal angle ϕ, and non-uniform in the radial direction according to the transformation $r = d\tanh(A_r\eta)/(2\tanh(A_r))$, with grid clustering near the pipe walls controlled by the parameter A_r, where $\eta \in [0,1]$ is a transformed coordinate corresponding to a uniform computational grid. The number of grid points and the wall clustering parameter were selected based on preliminary simulations assessing grid convergence, ensuring adequate resolution of turbulent scales and thin near-wall Hartmann layers. The time step was set to $\delta t = 10^{-3}$ in dimensionless convective units, which is significantly smaller than the Kolmogorov time scale of turbulence.

1.5. Calculation of parameters

Statistical parameters. The standard root mean square deviation (RMS) is used to calculate the fluctuation intensity. This value can be obtained by averaging over time Δt any measured or simulated parameter $g(t)$ after the quasi-steady state has been reached:

$$\overline{g} = \frac{1}{\Delta t}\int_0^{\Delta t} g(t)dt \simeq \frac{1}{n}\sum_k^n g_k, \tag{9}$$

$$\sigma_g^2 = \frac{1}{\Delta t}\int_0^{\Delta t} \left[g(t)-\overline{g}\right]^2 dt \simeq \frac{1}{n}\sum_k^n (g_k-\overline{g})^2, \tag{10}$$

To estimate the amplitude spectrum of fluctuations for $g(t)$, the discrete Fourier transform $A_j(f_j)$ was used, implemented in the Python programming language:

$$g(t) = \sum_{j=-\infty}^{+\infty} A_j e^{i\omega_j t}; \quad A_j = \frac{1}{\Delta t}\int_0^{\Delta t} g(t)e^{-i\omega_j t}dt \simeq \frac{1}{n}\sum_k^n g_k e^{-i2\pi jk/n}; \quad \omega_j = 2\pi f_j \tag{11}$$

Heat transfer coefficients. In heat transfer problems involving flow through channels, one can introduce the bulk (or mass-averaged) fluid temperature $\overline{T}$, defined based on the thermal balance of the moving fluid over the heated section:

$$\overline{T}(\tilde{z}) = T_0 + \frac{\overline{q}(\pi d^2\tilde{z})}{Gc_p} \equiv T_0 + \frac{4\overline{q}d/\lambda}{\mathrm{RePr}}\tilde{z}, \tag{12}$$

while the corresponding dimensionless temperature is:

$$\overline{\theta}(\tilde{z}) = \frac{T(\tilde{z})-T_0}{\Delta T} \equiv \frac{4\tilde{z}}{\mathrm{RePr}}. \tag{13}$$

The dimensionless local heat transfer coefficient (Nusselt number) is defined using the Newton–Rihmann relation $\alpha = \overline{q}/(T_w - \overline{T})$ as:

$$\mathrm{Nu}_l(\tilde{z}) = \frac{\alpha_l(\tilde{z})d}{\lambda} = \frac{\overline{q}d}{\lambda\left[T_{w,l}(\tilde{z}) - \overline{T}(\tilde{z})\right]} \equiv \frac{1}{\theta_{w.l}(\tilde{z}) - \overline{\theta}(\tilde{z})}, \tag{14}$$

where $T_{w,l}$ is the wall local temperature.

The mean Nusselt number is defined based on the perimeter-averaged wall temperature, $\overline{T}_w = \frac{1}{\pi}\int\limits_{\pi}^{2\pi} T_{w,l}\, d\phi$, in the transverse section $\tilde{z}$:

$$\overline{\mathrm{Nu}}(\tilde{z}) = \frac{1}{\overline{\theta}_w(\tilde{z}) - \overline{\theta}(\tilde{z})}\,. \tag{15}$$

Since it is problematic in experiments to precisely position the sensor at a specific angular coordinate (there is always uncertainty in its placement), we will use the temperature averaged near the lower generatrix of the pipe ($\phi = 270 \pm 15°$) for comparing local Nusselt numbers.

2. Results and discussion

The numerical simulation was performed for three different Reynolds numbers: $7 \cdot 10^3$, 10^4, and $1.5 \cdot 10^4$, with a Grashof number $\mathrm{Gr_q} = 6.05 \cdot 10^7$ and Hartmann numbers varying from 0 to 1350, corresponding to the experimental parameters (see Tab. 2). The time required to reach quasi-steady-state regimes did not exceed ~ 75 dimensionless convective units (c.u.) for all simulations. After achieving the quasi-steady state, the transient velocity and temperature fields obtained from solving the governing equations (5–8) were averaged over a period of ~ 100 c.u. This duration corresponds to twice the flow-through time across the heated section and was therefore considered sufficient to obtain fully developed flow characteristics. The results were analyzed and compared both along the length of the heated section and at a characteristic cross-section $z/d = 37$ from the start of heating (see Fig. 1).

2.1. Flow structure

After entering the working section, the flow is subjected to two body forces: buoyancy force and electromagnetic (ponderomotive) force, which govern the formation of the initial hydrodynamic and thermal entry regions, as well as the transformation of the flow structure (see e.g. [4]). The ponderomotive force, arising from the interaction between induced electric currents in the fluid and the applied magnetic field, decelerates the flow in the central region and accelerates it near the solid walls perpendicular to the direction of the magnetic induction – within the so-called Hartmann boundary layers. A second effect of the magnetic field is turbulence suppression, governed by the mechanism of "Joule dissipation" of kinetic energy in the Hartmann layers, which depends on the Hartmann number. The resulting laminarized flows are generally unstable, particularly with respect to two-dimensional perturbations in the form of vortical structures with axes aligned along the magnetic field. The buoyancy force acts within the heated section of the flow. In a horizontal pipe heated from below, this force induces paired helical (secondary) flows, resulting from the superposition of the axial forced flow and the free convective motion of heated fluid — rising along the heated lower wall and descending in the central region of the pipe.

Both of these effects are confirmed by the simulation results. Fig. 3 shows instantaneous distributions of the axial velocity in the cross-section located $z/d = 37$ units downstream from the start of the heating section. In the absence of a magnetic field (Ha = 0, Fig. 3a), the velocity field exhibits spatial inhomogeneity typical for turbulent flow. The velocity maximum shifts toward the lower half of the pipe, and the velocity iso-contours (isotachs) become distorted due to the influence of buoyancy forces. When a magnetic field is applied (Ha = 100, Fig. 3b), the overall axial symmetry of the flow field is restored. The magnetic field decelerates the central part of the flow, reduces turbulent velocity fluctuations, and stabilizes vortical structures, promoting the formation of counter-rotating vortex pairs with axes aligned in the streamwise direction. With further increase in the magnetic field strength (Ha = 220, Fig. 3c), flow perturbations are almost entirely suppressed. At Ha = 300 (Fig. 3d), the flow transitions to a different type of

secondary motion. In this regime, distinct boundary layer structures emerge near the solid walls: Hartmann layers at $\phi = 0°$ and 180°, and Roberts layers at $\phi = 90°$ and 270° (see e.g [16]).

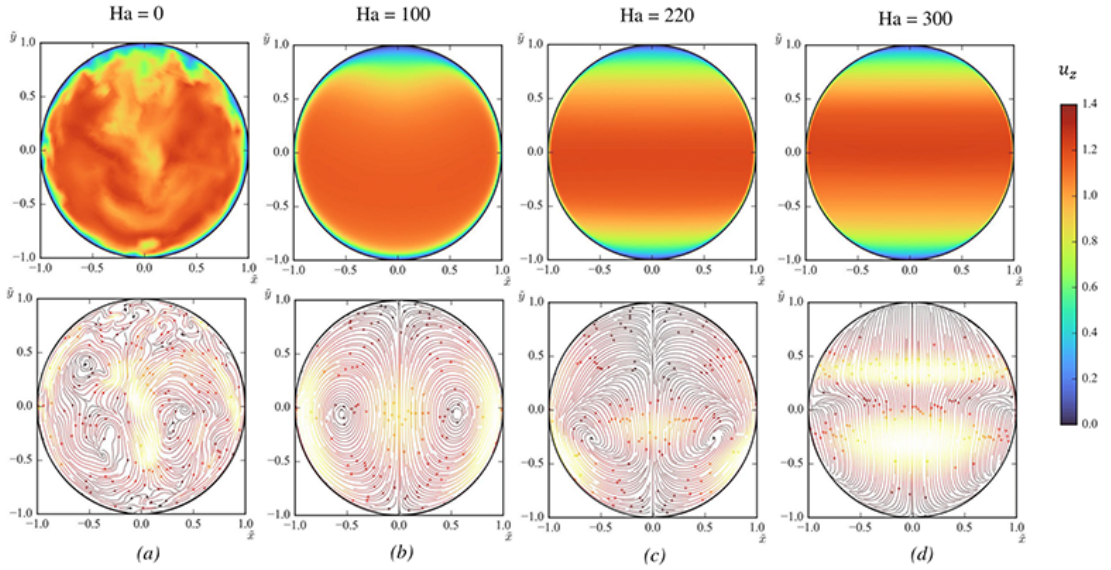

Fig. 3. The fields of instantaneous axial velocity u_z (top) and streamlines constructed from transverse velocity components $[u_x, u_y]$ (bottom) in the cross-section at $z/d = 37$ from the heating start for different Hartmann numbers: $\mathrm{Re} = 10^4$, $\mathrm{Gr_q} = 6.05 \cdot 10^7$

The flow transformation along the length of the heated section is illustrated in Fig. 4, which shows isosurfaces of transverse velocity and temperature. At Ha = 0 and Ha = 100, secondary flows in the form of streamwise (longitudinal) vortex structures are observed (Fig. 4a–b). The intensity of these vortices decreases with increasing Hartmann number. In this regime, the flow remains relatively well macroscopically mixed, as evidenced by the temperature isosurfaces. In the range from Ha = 220 to Ha = 300, a transition occurs to a completely different flow structure, characterized by disturbances (vortex formations) with axes aligned along the magnetic field direction (Fig. 4c–d). The intensity of these structures grows along the heated section and depends on the Hartmann number. These vortices distort the isothermal surfaces; however, the temperature field remains well stratified. With further increase in the Hartmann number, the intensity of these structures and the disturbances they induce gradually diminish. The temperature field becomes more uniform and approaches a distribution characteristic of conductive heat transfer in the fluid volume, particularly in the lower part of the pipe (Fig. 4e–f).

2.2. Temperature fluctuations

Fig. 5 shows the time-dependent temperature fluctuations relative to the mean value and their corresponding power spectra for the flow regime with $\mathrm{Re} = 10^4$, $\mathrm{Gr_q} = 6.05 \cdot 10^7$, and $\mathrm{Ha} = 0; 100; 300; 700$. For comparison with experimental measurements, a point located near the lateral generatrix of the pipe at $r/r_0 = 0.75$ (indicated in Fig. 1) in the cross-section at $z/d = 37$ from the start of the heated section was selected.

The obtained simulation results show good agreement with experimental data and, importantly, confirm the flow structure transformation described in Section 2.1. At Ha = 0 (Fig. 5a),

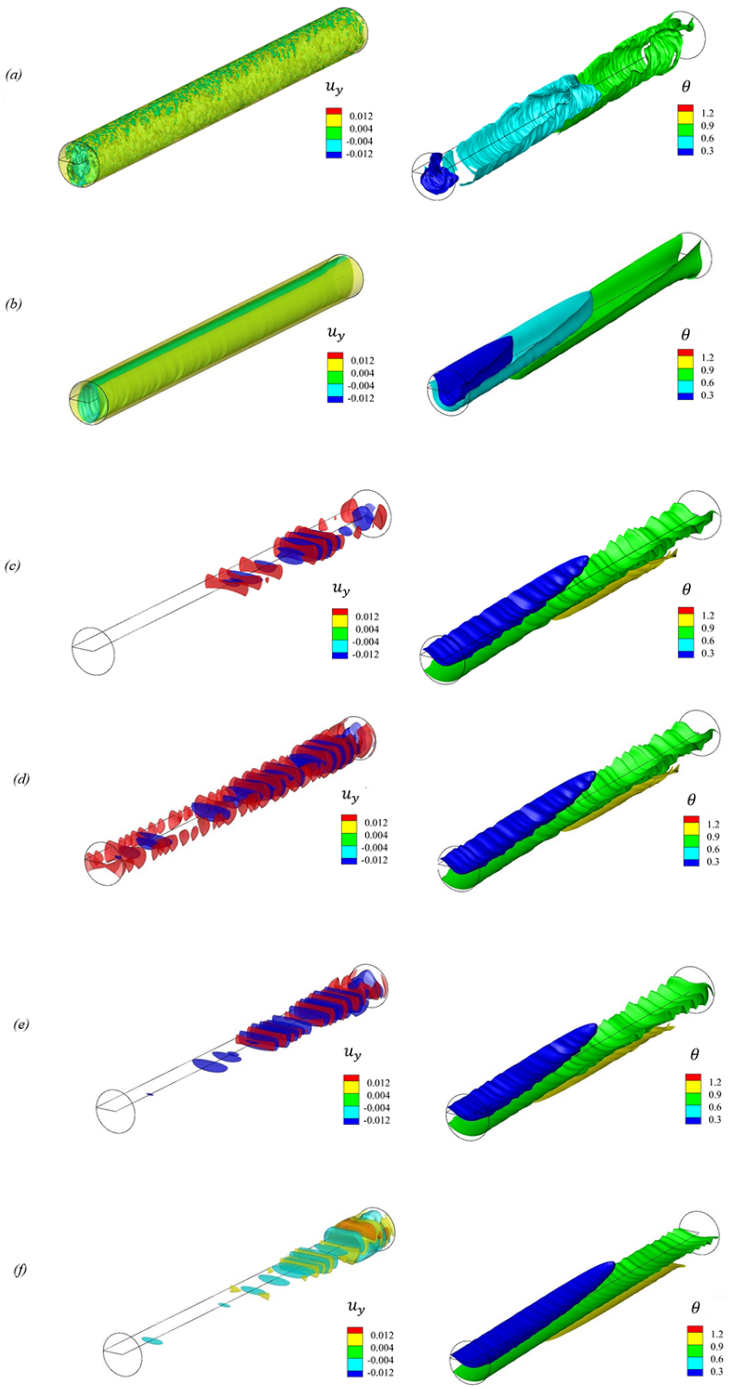

Fig. 4. Isosurfaces of instantaneous vertical velocity u_y and temperature θ within the heated section $z/d \in [0 \div 37]$ are presented for various Hartmann numbers at $\mathrm{Re} = 10^4$ and $\mathrm{Gr_q} = 6.05 \cdot 10^7$. The scales of transverse and streamwise coordinates are related as 1:4 for visualization purposes

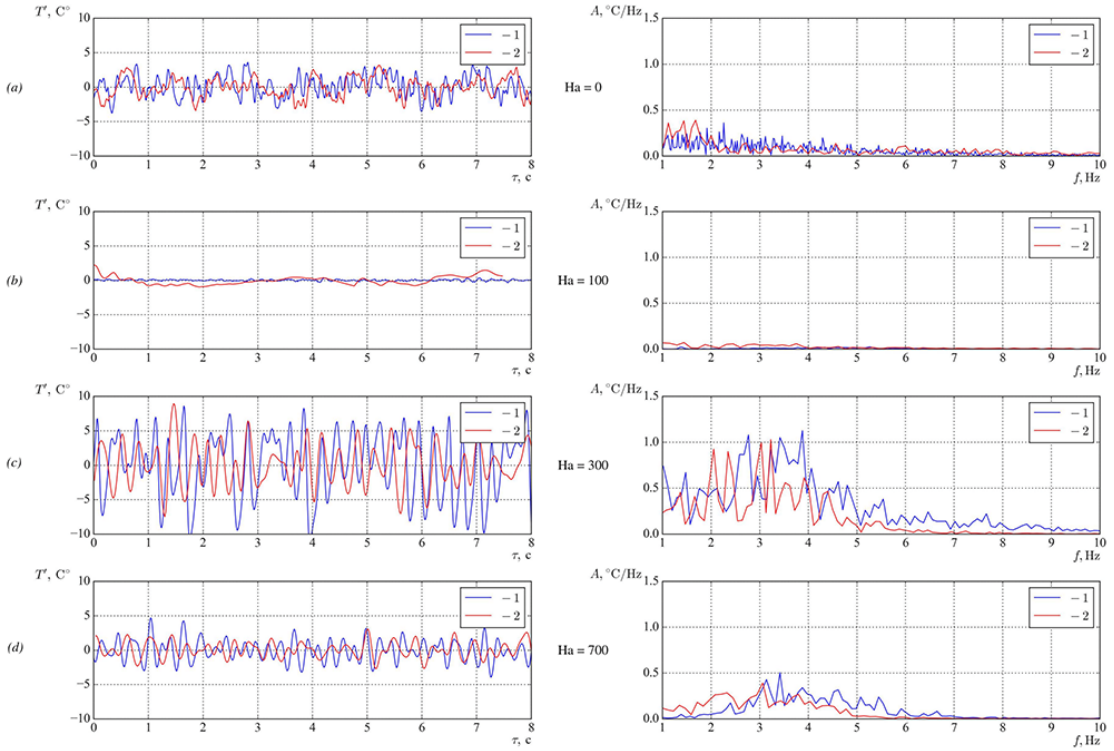

Fig. 5. Comparison of temperature fluctuation measurements in the experiment (1) and numerical simulation (2) near the side generator in the heated region ($z/d = 37$, $\phi = 0$, $r/r_0 = 0.75$): left – oscillograms of temperature fluctuations [1]; right – amplitude spectrum of the signal for various Hartmann numbers: $\mathrm{Re} = 10^4$, $\mathrm{Gr_q} = 6.05 \cdot 10^7$

temperature fluctuations typical of turbulent mixed convection in a pipe are observed. When $\mathrm{Ha} = 100$ (Fig. 5b), temperature fluctuations are almost completely suppressed, indicating flow laminarization, as turbulent temperature fluctuations are inherently linked to velocity fluctuations. As the Hartmann number increases further, at $\mathrm{Ha} = 300$ (Fig. 5c), temperature fluctuations reappear with a quasi-harmonic character and exhibit dominant frequencies in the range of $3 \div 4$ Hz in the spectrum. With even stronger magnetic field ($\mathrm{Ha} = 700$, Fig. 5d), the intensity of temperature fluctuations and their spectral energy decrease significantly, suggesting a return to a more stable, less fluctuating flow regime dominated by diffusive heat transfer.

Tab. 3 presents the intensity of temperature fluctuations, $\sigma_\theta = \sigma_T/\Delta T$, as a function of the Hartmann number for different Reynolds numbers, obtained both experimentally and from numerical simulations. The results show good qualitative agreement, with some minor quantitative discrepancies. For all considered Reynolds numbers, the dependence of temperature fluctuation intensity on the Hartmann number follows the same general trend: initially, the intensity decreases up to $\mathrm{Ha} \sim 200$, then increases again reaching a maximum around $\mathrm{Ha} \sim 400$, and finally decreases sharply at higher Hartmann numbers, approaching nearly zero at $\mathrm{Ha} \gtrsim 700$. This non-monotonic behavior reflects the complex interplay between magnetic stabilization, flow structuring, and the development of magnetohydrodynamic instabilities aligned with the magnetic field. Good qualitative and, in many cases, quantitative agreement is observed between

experimental and computational results at the corresponding data points. It is worth noting that the Reynolds number significantly influences both the amplitude and frequency of temperature fluctuations in the region of peak fluctuation intensity. With increasing Re, the fluctuation intensity decreases noticeably, while the dominant frequency increases. This indicates that stronger forced convection suppresses the development of large-scale flow structures with axes aligned along the magnetic field, enhancing their advection through the heated section and reducing their residence time, thereby limiting their growth. The characteristic frequency f, determined from the peak in the power spectrum, increases with Re, consistent with faster convective transport of disturbances. This trend further supports the conclusion that higher flow rates impede the formation and amplification of magnetically aligned vortices, leading to weaker thermal fluctuations despite the presence of secondary motion.

Table 3. Temperature fluctuation intensity $\sigma_\theta = \sigma_T/\Delta T$ and characteristic frequency f (determined from the peak of spectra) near the lateral generatrix of the pipe ($\phi = 0°$, $r/r_0 = 0.75$) at cross-section $z/d = 37$. Values are given as *experimental / numerical* (where available)

Experiment / Simulation						
Re	$7 \cdot 10^3$		10^4		$1.5 \cdot 10^4$	
Ha	σ_θ	f [Hz]	σ_θ	f [Hz]	σ_θ	f [Hz]
0	0.028 / 0.025	– / –	0.024 / 0.020	– / –	0.021 / 0.017	– / –
200	0.049 / –	1.97 / –	0.047 / 0.045	3.63 / –	0.007 / –	6.32 / –
300	0.063 / –	2.23 / –	0.075 / 0.078	2.84 / 2.71	0.012 / –	6.28 / –
400	0.063 / 0.059	1.82 / 1.61	0.079 / 0.080	3.63 / –	0.008 / 0.014	6.73 / 6.24
550	0.065 / –	1.67 / –	0.056 / 0.065	3.63 / –	0.004 / –	6.013 / –
700	0.076 / 0.070	– / –	0.024 / 0.020	– / –	0.003 / –	– / –
1000	0.042 / –	– / –	0.004 / 0.008	– / –	0.003 / –	– / –

2.3. Heat transfer

The intensity of heat transfer between the moving fluid and the pipe wall can be evaluated using the local Nusselt number (14), the perimeter-averaged Nusselt number (15), as well as directly through the wall temperature distribution in the region of interest. In the considered configuration, the upper part of the pipe is unheated, so the primary focus lies on the wall temperature distribution and heat transfer coefficients in the lower, heated portion of the pipe.

Fig. 6 shows the circumferential distribution of wall temperature at the cross-section $z/d = 37$, located within the thermally developed region. At the upper generatrix ($\phi = 90°$), the wall temperature is minimal due to the absence of heating. Nevertheless, the largest discrepancies between experimental and numerical results are observed in this region under applied magnetic fields (Ha > 0), where convective heat transfer is suppressed and thermal conduction becomes the dominant heat transfer mechanism. This deviation is likely due to the absence of a solid wall in the computational model that would allow for lateral heat conduction from the heated lower part to the unheated upper part of the pipe, as occurs in the physical experiment. For all cases with Ha > 0, the maximum wall temperature occurs at the lower generatrix ($\phi = 270°$), indicating deteriorated heat transfer in this region. Moreover, as the Hartmann number increases, the wall temperature rises, implying a reduction in the local heat transfer coefficient. This trend is

attributed to the magnetic field's suppression of turbulent transport and damping of longitudinal vortex structures driven by free convection. These vortices, which enhance mixing and heat removal under non-magnetic conditions, are progressively inhibited as Ha increases. Despite some quantitative deviations — particularly in the unheated zone — the experimental and numerical results show good qualitative agreement in the heated lower region, especially considering the uncertainties inherent in temperature measurements. The simulations adequately capture the overall trend of heat transfer degradation with increasing magnetic field strength.

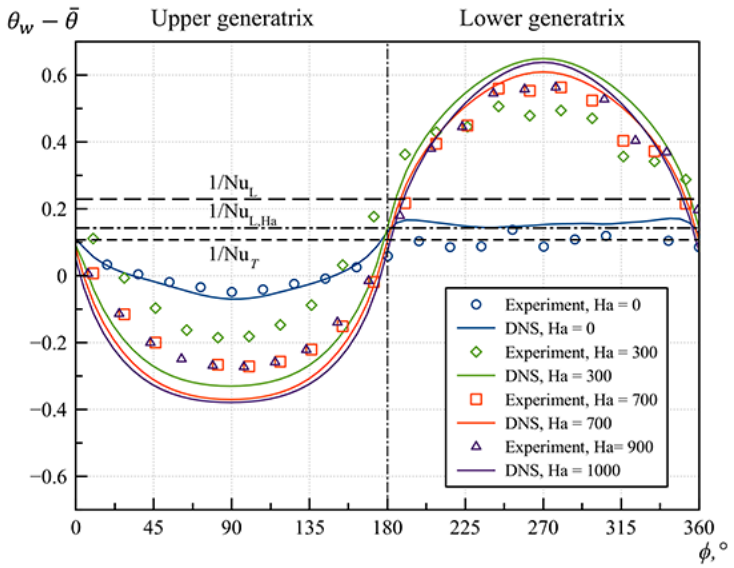

Fig. 6. Distribution of dimensionless wall temperature along the perimeter of the pipe cross-section at $z/d = 37$ for various Hartmann numbers: $\mathrm{Re} = 10^4$, $\mathrm{Gr_q} = 6.05 \cdot 10^7$

Fig. 7 presents the variation of local Nusselt numbers along the heated section, determined at the lower generator region taking into account uncertainty in the probe position ($\phi = 270° \pm 15°$), as well as the perimeter-averaged Nusselt numbers over the heated part of the cross-section. In the absence of a magnetic field ($\mathrm{Ha} = 0$), three characteristic regions are observed in the Nusselt number distribution: $0 \div 5$ diameters – the initial thermal entrance region, corresponding to the development of the temperature field; $5 \div 15$ diameters – the onset of buoyancy forces' influence on the flow and the formation of temperature fields corresponding to the mixed convection regime; and $15 \div 43$ diameters – the thermally stabilized heat transfer regime, where temperature changes nearly linearly along the length, and the Nusselt number reaches a nearly constant value of ~ 10. The averaged Nusselt numbers are slightly lower than the local ones – convective transport is more intense near the lower generator than near the lateral walls of the pipe. At $\mathrm{Ha} = 100$, turbulent transport is suppressed, and the formation of stabilized temperature fields occurs under the action of two body forces and extends over $15 \div 20$ diameters downstream. The Nusselt numbers decrease, and the averaged values remain slightly lower than the local ones — the influence of secondary flows with axes aligned along the pipe on heat transfer persists. A different situation arises with the change in flow structure ($\mathrm{Ha} > 220$). The influence of buoyancy forces is practically negligible under complete suppression of turbulent transport. The Nusselt number values for different Ha almost coincide and reach levels typical of laminar flows. At the

same time, the averaged Nusselt numbers become higher than the local values — the change in flow structure deteriorates fluid motion near the lower generator and increases the role of the lateral generators in heat removal from the wall. The values of local Nusselt numbers for all regimes are in good agreement with the experimental results, taking into account measurement uncertainties.

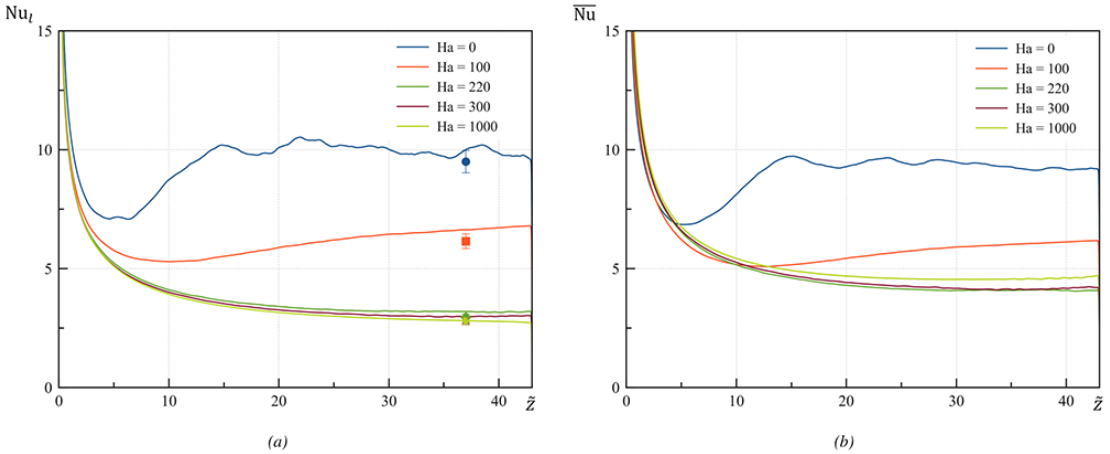

Fig. 7. Distribution of local (a) and average (b) Nusselt numbers along the length of the heating zone for various Hartmann numbers: $\mathrm{Re} = 10^4$, $\mathrm{Gr_q} = 6.05 \cdot 10^7$

Conclusions

The magnetic field and heating significantly alter the flow structure and the dynamics of temperature fluctuations in a liquid metal flow. In the absence of a magnetic field ($\mathrm{Ha} = 0$), a turbulent flow is observed, with streamlines deformed under the action of buoyancy forces. A moderate magnetic field ($\mathrm{Ha} = 100$) suppresses turbulence and velocity/temperature fluctuations, leading to flow laminarization. With further increase in the Hartmann number ($\mathrm{Ha} = 300$), quasi-harmonic temperature fluctuations emerge, associated with vortex structures aligned along the magnetic field direction. An increase in the Reynolds number reduces the amplitude of these fluctuations at high Ha, indicating competition between forced convection and magneto-convective effects.

Comparison of statistical and spectral characteristics between experiment and simulation confirms the reliability of the numerical model. Analysis of temperature fluctuations standard deviation and spectra shows good agreement between experimental and computational data. This is particularly important for model validation, as spectral features — such as dominant frequencies of $\sim 3 \div 4$Hz at $\mathrm{Ha} = 300$ — reflect key physical mechanisms underlying flow reorganization.

The analysis of not only time-averaged parameters (e.g., Nusselt numbers) but also the spectral composition of temperature fluctuations enables a comprehensive assessment of both the accuracy of the numerical simulations (DNS) and the consistency of experimental measurements. This combined approach confirms that the applied physical approximations – such as the quasi-static MHD approximation, neglect of the induced magnetic field, and the Boussinesq approximation – are adequate within the investigated parameter range ($\mathrm{Re} \sim 10^4$, $\mathrm{Ha} \leqslant 1350$), and also helps identify the limits of model applicability under more extreme conditions.

The work was carried out with the support of a grant from the Ministry of Science and Higher Education of the Russian Federation within the framework of State Assignment No. FSWF-2023-0017 (Agreement No. 075-03-2023-383 dated January 18, 2023) in the field of scientific activity for 2023–2025.

References

[1] I.M.Roznin, Temperature pulsations in MHD flow of liquid metal in horizontal non-uniformly heated channels, International Youth Conference on Radio Electronics, Electrical and Power Engineering (REEPE) : Proc., Moscow, 2020, 815 (in Russian).

[2] S.Smolentsev, Physical background, computations and practical issues of the magnetohydrodynamic pressure drop in a fusion liquid metal blanket, *Fluids*, **6**(2021), no. 3, 110. DOI: 10.3390/fluids6030110

[3] P.Lorenzetto, J.Andrade, S.Banetta, et al., EU contribution to the procurement of blanket first wall and divertor components for ITER, *Fusion Engineering and Design*, **136**(2018), 975–982. DOI: 10.1016/j.fusengdes.2018.04.050

[4] O.Zikanov, I.Belyaev, Y.Listratov, P.Frick, N.Razuvanov, V.Sviridov, Mixed convection in pipe and duct flows with strong magnetic fields, *Applied Mechanics Reviews*, **73** (2021), no. 1, 010801–35. DOI: 10.1115/1.4049833

[5] L.G.Genin, V.G.Zhilin, Yu.P.Ivochkin, N.G.Razuvanov, I.A.Belyaev, Ya.I.Listratov, V.G.Sviridov, Temperature fluctuations in a heated horizontal tube affected by transverse magnetic field, Proc. of the 8th International Pamir Conference on Fundamental and Applied MHD, Borgo, Corsica, 2011, 37–41.

[6] I.A.Belyaev, Yu.P.Ivochkin, Ya.I.Listratov, N.G.Razuvanov, V.G.Sviridov, Temperature fluctuations in a liquid metal MHD-flow in a horizontal inhomogeneously heated tube, *High Temperature*, **53**(2015), no. 5, 734–741. DOI: 10.1134/S0018151X15050041

[7] O.Zikanov, Y.I.Listratov, V.G.Sviridov, Natural convection in horizontal pipe flow with a strong transverse magnetic field, *Journal of Fluid Mechanics*, **720**(2013), 486–516. DOI: 10.1017/jfm.2013.45

[8] Ya.Listratov, D.Ognerubov, O.Zikanov, V.Sviridov, Numerical simulations of mixed convection in liquid metal flow within a horizontal pipe with transverse magnetic field, *Fluid Dynamics Research*, **50**(2018), no. 5, 051407. DOI: 10.1088/1873-7005/aab382

[9] R.Akhmedagaev, O.Zikanov, Y.Listratov, Magnetoconvection in a horizontal duct flow at very high Hartmann and Grashof numbers, *Journal of Fluid Mechanics*, **931**(2022), A29. DOI: 10.1017/jfm.2021.987

[10] I.A.Belyaev, V.G.Sviridov, V.M.Batenin, et al., Test facility for investigation of heat transfer of promising coolants for the nuclear power industry, *Thermal Engineering*, **64**(2017), no. 11, 841–848. DOI: 10.1134/S0040601517110027

[11] I.A.Belyaev, V.G.Sviridov, V.M.Batenin, et al., A technique for scanning probe measurement of temperature fields in a liquid flow, *Thermal Engineering*, **66**(2019), no. 6, 377–387. DOI: 10.1134/S0040601519060016

[12] N.B.Vargaftik, Y.K.Vinogradov, V.S.Yargin, Handbook of Physical Properties of Liquids and Gases, Pure Substances and Mixtures, Begel House, 1996, 321.

[13] E.V.Votyakov, S.C.Kassinos, X.Albets-Chico, Analytic models of heterogenous magnetic fields for liquid metal flow simulations, *Theoretical and Computational Fluid Dynamics*, **23**(2009), no. 6, 571–578. DOI: 10.1007/s00162-009-0114-9

[14] Y.Morinishi, T.S.Lund, O.V.Vasilyev, P.Moin, Fully conservative higher order finite difference schemes for incompressible flow, *J. Comput. Phys.*, **143**(1998), 90–124. DOI: 10.1006/jcph.1998.5962

[15] D.Krasnov, O.Zikanov, T.Boeck, Comparative study of finite difference approaches in simulation of magnetohydrodynamic turbulence at low magnetic Reynolds number, *Computers & fluids*, **50**(2011), no. 1, 46–59. DOI: 10.1016/j.compfluid.2011.06.015

[16] J.A.Shercliff, Magnetohydrodynamic pipe flow part2. high hartmann number, *Journal of Fluid Mechanics*, **13**(1962), no. 4, 513–518.

Сравнительный анализ экспериментальных и расчетных данных по турбулентному течению жидкого металла в трубе под действием поперечного магнитного поля и нагрева снизу

Даниил А. Бердюгин
Объединённый институт высоких температур РАН
Москва, Российская Федерация

Ярослав И. Листратов
Национальный исследовательский университет «Московский энергетический институт»
Москва, Российская Федерация

Иван А. Беляев
Объединённый институт высоких температур РАН
Москва, Российская Федерация

Аннотация. В статье представлены результаты прямого численного моделирования течения ртути в круглой горизонтальной трубе при неоднородном нижнем обогреве в присутствии поперечного магнитного поля. Исследование посвящено анализу гидродинамики и теплообмена в условиях термогравитационной конвекции, индуцированной локализованным нагревом, и магнитогидродинамических эффектов. Показано, что поперечное магнитное поле существенно подавляет поперечные компоненты скорости, стабилизирует течение и изменяет структуру конвективных вихрей, приводя к анизотропии турбулентного переноса и формированию характерных гартмановских и пограничных слоёв. Анализ полей скорости и температур позволяет выявить режимы подавления неустойчивости и перестройки крупномасштабной циркуляции. Проведено сравнение статистических характеристик интенсивностей пульсаций температуры, а также безразмерных величин с экспериментальными данными [1]. Сравнение и анализ полученных результатов позволяет расширить понимание о процессах, происходящих в жидких металлах при совместном действии гравитационных, тепловых и электромагнитных полей, что представляет интерес для разработки систем охлаждения в ядерных реакторах с жидкометаллическими теплоносителями.

Ключевые слова: жидкий металл, DNS, конвекция, МКФ, теплообмен, поперечное магнитное поле.

EDN: AYOFWA
УДК 519.67

Verifying a Numerical Technique for Modeling Two-phase Flows of Immiscible Non-Newtonian Liquids in Porous Media

Dmitriy V. Guzei*
Siberian Federal University
Krasnoyarsk, Russian Federation
Andrey A. Gavrilov†
Aleksandr A. Dekterev‡
Siberian Federal University
Krasnoyarsk, Russian Federation
Institute of Thermophysics SB RAS
Novosibirsk, Russian Federation
Andrey V. Minakov§
Siberian Federal University
Krasnoyarsk, Russian Federation

Received 26.07.2025, received in revised form 25.08.2025, accepted 27.09.2025

Abstract. The paper presents the results of the development and verification of a computational technique for modeling two-phase immiscible flows in porous media, taking into account the transfer of polymers that change the rheology of fluids in the process of their flow. The mathematical model is based on the Navier–Stokes equations and the VOF method. The model includes a convective-diffusion concentration transfer equation with a constant effective diffusion coefficient. Within the framework of this model, the rheology of the displacing fluid is described by a nonlinear model of viscoplastic media (Herschel–Bulkley) based on the generalized viscosity approach. The rheological parameters of the model depend on the local polymer concentration. To regularize the effective viscosity and eliminate infinite values, an approach with exponential regularization of the shear rate at small values is used. The developed calculation methodology has been tested and verified to show that the numerical solutions found with this methodology are qualitatively and quantitatively in good agreement with known analytical solutions and with numerical solutions obtained using the Ansys Fluent reference CFD solver.

Keywords: digital models of porous media, immiscible displacement, non-Newtonian flow, polymer solutions, VOF method, testing.

Citation: D.V. Guzei, A.A. Gavrilov, A.A. Dekterev, A.V. Minakov, Verifying a Numerical Technique for Modeling Two-phase Flows of Immiscible Non-Newtonian Liquids in Porous Media, J. Sib. Fed. Univ. Math. Phys., 2026, 19(1), 21–34. EDN: AYOFWA.

Introduction

Modern numerical modeling methods enable the creation of complex hydrodynamic reservoir models based on geological data, which is important for analyzing and optimizing oil production processes. Currently, specialized software systems are widely used to simulate thermal, gas, and physico-chemical methods of influencing oil formations with the view of predicting the effectiveness of various technologies for increasing oil recovery [1–2]. Digital twins of deposits allow simulating various development scenarios in real time, choosing optimal production methods,

*gudimas@yandex.ru https://orcid.org/0000-0003-2226-1837
†gavand@yandex.ru https://orcid.org/0009-0004-8061-0040
‡dekterev@mail.ru
§tov-andrey@yandex.ru https://orcid.org/0000-0003-1956-5506

and predicting reservoir behavior taking into account a variety of factors [3]. Digital twins combining the Internet of Things systems for data collection and predictive analytics systems are becoming a powerful tool for managing oil fields [4–5]. A special place in numerical modeling of oil and gas fields is occupied by the development of mathematical models and software for describing multiphase flows in rocks at the micro- and nano-scales. This is especially true for complex deposits with low-permeability formations. This area of modeling is called "digital core technologies" [6–7]. A digital core is a high-precision 3D model of a rock based on microtomography or other high-resolution scanning methods. Such models are used for numerical modeling of filtration processes and oil recovery at the pore level. In the last decade, a large number of studies aimed at developing and improving numerical methods for modeling multiphase flows at the pore scale have been carried out. A large number of different methods have been developed in this area. These are, first of all, methods of direct numerical modeling of the interface. In this approach, the computational domain is formed directly from the data on the pore structure of the core, obtained using three-dimensional tomography. Next, a multiphase flow is modeled using well-known computational methods or those with a movable interface, adapted to capillary flows. Among the mesh methods, the most common are those based on the VOF method [8], the Level Set method [9], and various options of Phase Field methods [10]. Among the particle methods for modeling digital core problems, various options of the Boltzmann lattice equation (LBM) method have become the most widespread [11]. Another type of mesh-free methods is the smoothed particle method (SPH). It is also used to model flows in porous media, though much more rarely [12]. Mesh methods are more conservative and use fewer approximations. Particle methods are computationally faster. In addition to direct methods for modeling flows in porous media, a large number of approximate ones, based on the use of semi-analytical techniques, are actively used. The latter include the method of inscribed spheres [13] and the capillary tube bundle method [14]. They are very fast and allow making estimates of capillary pressure curves and relative phase permeability, but they are not universal because of a large number of the used assumptions. The more universal of the semi-analytical methods are pore-network methods [15]. In this group, the actual pore space is simplified to two separate elements: the pores, which contain the bulk of the liquids, and the channels that connect the pores and through which the flow is transported. The pore-network models significantly surpass the models with direct resolution of the interface in counting speed and are more accurate than semi-analytical methods. A review of the literature shows that, in general, the digital core field is currently developing intensively. The models are gradually becoming more complex and expanded to take into account a larger number of physical phenomena that occur in a porous medium during oil production: three-phase flows, phase transitions, the formation of asphaltenes and paraffins, the transfer and adsorption of surfactants, etc. [16]. An important property that must be taken into account when developing digital core models is fluid rheology. This is especially important when modeling the process of oil displacement with polymer solutions that have non-Newtonian rheology in order to increase the efficiency of oil recovery by increasing viscosity. Despite the current intense development of numerical modeling for the study of multiphase flows in digital core models, there are still many unresolved issues related to improving the performance and reliability of the developed computational algorithms and software. This paper presents the results of verification of a computational technique for modeling the two-phase immiscible flows in porous media, taking into account the transfer of polymers that change the rheology of fluids in the flow.

1. Mathematical model of two-phase immiscible non-Newtonian flow in digital core models

Previously, based on the software core of the domestic SigmaFlow CFD software package [17–19], a numerical method was developed to describe the unsteady flow of immiscible liquids

in three-dimensional digital core models with interfacial resolution. It was based on the Navier-Stokes model for an incompressible liquid and the Volume of Fluid method (VOF) [20] and took into account the surface tension forces and the effects of surface wetting, as well as the effect of the transfer of modifying additives (surfactant/polymer solutions and nanosuspensions) in the process of oil recovery [21–22]. The problem statement is as follows. At the initial moment, the porous medium is filled with a displaced liquid (index 2), usually oil. Next, a displacing liquid (index 1) is supplied to the porous medium, usually an aqueous solution. The displacing and displaced liquids do not mix with each other. In this case, a polymer additive with a mass concentration ϕ may be present inside the aqueous phase. In this case, within the framework of the VOF method, the two-phase medium is considered as a single-liquid medium consisting of two components, and has a continuous distribution of density and viscosity, depending on the volume fraction of the liquid in the cell α:

$$\rho = \alpha\rho_1(\phi) + (1-\alpha)\rho_2; \quad \mu = \alpha\mu_1(\phi) + (1-\alpha)\mu_2. \tag{1}$$

The motion of a liquid is described by the Navier–Stokes equations for an incompressible medium:

$$\bigtriangledown \cdot \mathbf{u} = 0 \tag{2}$$

$$\rho\left(\frac{\partial \mathbf{u}}{\partial t} + (\mathbf{u}\cdot\bigtriangledown)\mathbf{u}\right) = -\bigtriangledown p + \bigtriangledown\cdot(2\mu\mathbf{S}) + (\rho-\rho_\infty)\mathbf{g} + (\mathbf{f}_c - \bigtriangledown p_c), \tag{3}$$

where $\mathbf{u}$ is the velocity vector, p is the dynamic pressure, $\mathbf{S} = 0.5(\bigtriangledown\mathbf{u} + \bigtriangledown\mathbf{u}^T)$ is the strain rate tensor, ρ_∞ is the characteristic density, $\mathbf{f}_c$ is the bulk surface tension force, and p_c is the capillary pressure.

The equation for the transfer of the volume fraction of liquid in a cell has the form:

$$\frac{\partial \alpha}{\partial t} + \bigtriangledown\cdot(\mathbf{u}\alpha) = 0. \tag{4}$$

The calculation of capillary forces, which are described in this case within the framework of the CSF (continuum surface force) approach [23], plays a key role in modeling the flow in porous media:

$$\mathbf{f}_c = \sigma(\phi)k\mathbf{n}_s\delta_s, \tag{5}$$

where $\sigma(\phi)$ is the coefficient of interfacial tension and the curvature of the interface is determined by the distribution of the volume fraction:

$$k = \bigtriangledown\cdot\mathbf{n}_s, \tag{6}$$

where the normal to the interface is:

$$\mathbf{n}_s = \frac{\bigtriangledown\alpha}{|\bigtriangledown\alpha|}. \tag{7}$$

On solid surfaces, the contact angle $\theta(\phi)$ is used to determine the direction of the normal vector to the interface of liquids at the contact line:

$$\mathbf{n}_s = \mathbf{n}_w\cos(\theta(\phi)) + \mathbf{s}_w\sin(\theta(\phi)), \tag{8}$$

where $\mathbf{n}_w$ is the normal to a solid surface and $\mathbf{s}_w$ is the unit tangential vector to the surface at the contact line of liquids.

The equation for capillary pressure has the form:

$$\bigtriangledown\cdot\bigtriangledown p_c = \bigtriangledown\cdot\mathbf{f}_c. \tag{9}$$

As already mentioned, in order to increase the efficiency of displacing oil from a porous medium, a polymer ϕ is added to water for changing the properties of the displacing liquid,

primarily the viscosity. The transfer equation of the polymer concentration ϕ in the aqueous phase α has the form:

$$\frac{\partial(\alpha\phi)}{\partial t} + \bigtriangledown \cdot (\mathbf{u}\alpha\phi) - \bigtriangledown \cdot (\alpha D_\phi \bigtriangledown \phi) = 0, \tag{10}$$

where D_ϕ is the diffusion coefficient of the polymer in water [m^2/s]. The addition of a polymer leads to a change in the properties of the aqueous solution. The dependence of the interfacial tension coefficient and the wetting edge angle of the displacing liquid on the polymer concentration ϕ is given by the power formula:

$$\sigma(\phi) = \sigma_0 \left(1 + c_1\phi + c_2\phi^2\right), \tag{11}$$

$$\theta(\phi) = \theta_0 \left(1 + c_1\phi + c_2\phi^2\right), \tag{12}$$

where σ_0 and θ_0 are the values of these parameters for water, c_1 and c_2 are the correlation coefficients, determined from experiments for each of the properties under consideration.

The numerical implementation is based on the modified transfer equation [21–22]:

$$\frac{\partial(\phi)}{\partial t} + \bigtriangledown \cdot (\mathbf{u}\phi + (1-\alpha)\mathbf{u}_r\phi) - \bigtriangledown \cdot (\alpha D_\phi \bigtriangledown \phi) = 0. \tag{13}$$

The most important property that must be taken into account when oil is displaced by polymer solutions is fluid rheology. In this regard, this work determines non-Newtonian rheology of a displacing fluid based on the Herschel–Bulkley model. The effective viscosity of the aqueous polymer solution is calculated using the formula:

$$\mu_1(\phi) = \left(\tau_y(\phi) + k_v(\phi)\dot{\gamma}_f^{n(\phi)}\right) / \dot{\gamma}_f, \tag{14}$$

where $\tau_y(\phi)$ is the limiting voltage, $k_v(\phi)$ is the indicator of consistency and $n(\phi)$ is the indicator of the degree of a liquid, which depend on the concentration of the additive ϕ. The presence of an impurity affects the rheological properties. In this version of the model, the dependence of the coefficients of the Herschel–Bulkeley model on the polymer concentration is given as a quadratic polynomial:

$$\tau(\phi) = \tau_0 \left(1 + c_1\phi + c_2\phi^2\right), \tag{15}$$

$$n(\phi) = n_0 \left(1 + c_1\phi + c_2\phi^2\right), \tag{16}$$

$$k_v(\phi) = k_{v,0} \left(1 + c_1\phi + c_2\phi^2\right), \tag{17}$$

where τ_0, n_0 and $k_{v,0}$ are the base values of the parameters and c_1 and c_2 are the coefficients of the model obtained for each of the parameters.

When modeling viscoplastic flows, there is a known problem of the occurrence of singularity in the flow regions with the shear rate equal to zero. For viscoplastic fluids with a nonzero limiting stress τ_0 in the flow region $|\tau| < \tau_0$, the shear rate tends to zero, which is why the effective viscosity of the liquid increases indefinitely. In order to overcome this difficulty, various regularizations of the initial rheological models are used. The simplest option involves artificially limiting the effective viscosity of the liquid in the region $|\tau| < \tau_0$ by a certain maximum value $\mu_{max} : \mu = max\,(\mu, \mu_{max})$. The second approach proposed for Bingham liquids in [24] is to approximate the expression for effective viscosity by an exponential function:

$$\mu\,(\dot{\gamma}) = \frac{k\dot{\gamma} + \tau_0 \left(1 - e^{-m\dot{\gamma}/\dot{\Gamma}}\right)}{\dot{\gamma}}, \tag{18}$$

which, when $\dot{\gamma}$ tends to zero, allows limiting the effective viscosity. The exponential multiplier m must be large enough (in most papers, its value ranges from 100 to 3000).

For the more general case of the Herschel–Bulkley fluid, in our work, an approach with exponential regularization of the shear rate at small values is used to regularize the effective viscosity and eliminate infinite values:

$$\tilde{\dot{\gamma}} = \dot{\gamma} / \left(1 - e^{-m\dot{\gamma}/\dot{\gamma}_{ref}}\right), \tag{19}$$

where $\dot{\gamma}_{ref}$ is the characteristic shear rate for the problem under consideration and m is the regularization parameter.

Thus, the viscosity of a two-component medium depends on the proportion of liquid, polymer concentration, and flow shear rate:

$$\mu = \mu_1 \left(\dot{\gamma}_f, \phi\right) \alpha + \mu_2 \left(1 - \alpha\right). \tag{20}$$

On solid walls, impermeability and no-slip conditions are set for velocity and a zero normal derivative is set for pressure. The velocity, the fraction of the displacing phase, and the polymer concentration ϕ are recorded at the input boundary. At the output boundary, a condition of the flow uniformity is set; it is expressed in the equality of the normal derivatives of all scalar quantities to zero.

The calculations are performed in a non-stationary formulation, and the time step is bounded using the algorithm proposed in [25] and is additionally limited by the value of the convective Courant number (CFL) at the interface, which, by default, does not exceed 0.1. The numerical method is based on the methodology [26] developed specifically for recovery problems. The main details of the algorithm are described in detail in our works [21–22].

2. Test results of a computational algorithm for non-Newtonian fluid flow problems

The developed calculation methodology was tested and verified. The problems of single-phase and multiphase immiscible flow of non-Newtonian fluids in a rectangular, flat and circular channel were considered. The calculated data were compared with analytical dependences and the results of calculations obtained in the Ansys Fluent software product.

2.1. A single-phase flow of polymer solution in a flat channel

First, a single-phase isothermal flow of a power-law liquid in a rectangular flat channel was considered. The channel width in the calculations was 0.01 m and the length was 1 m. An orthogonal grid with a total number of calculation nodes equal to 75,000 was used. The flow of a polyacrylamide polymer (PAA) solution with different concentrations was examined. The concentration of polyacrylamide in solutions ranged from 0.01 to 0.1 wt.%. To obtain data on the rheological characteristics of the polymer solution, its dynamic viscosity coefficient depending on the shear rate was in advance measured using a Brookfield DV2TL rotary viscometer. The viscometer had a specified error of ±2%, depending on the range used. The measurements were carried out for a temperature of 25℃. An analysis of experimentally obtained flow and viscosity curves has shown that the rheology of PAA solutions is well described by a power law model, which is a special case of the Herschel–Bulkley model $\tau = k_v \dot{\gamma}^n$, where k_v is the liquid consistency coefficient and n is the flow index. The dependence of rheological parameters on the concentration of polyacrylamide is shown in Tab. 1. The concentration of 0% in the table corresponds to water. These parameters are set to calculate the flow of the polymer solution in the channels.

At the entrance to the computational domain, a constant velocity value of 0.005 m/s was preset. The Neumann boundary condition was set at its output. The boundary no-slip and impermeability conditions were set on the channel walls. The results of calculations performed

Table 1. Dependence of rheological parameters on PAA concentration

%	n	k_v, Pa×s^n
0	1	0.001
0.01	0.8103	0.005606
0.05	0.45559	0.25862
0.1	0.50166	0.44057

using the developed numerical methodology were compared with those obtained using Ansys Fluent. The calculations were realized on the same grid. To do this, the computational grid from SigmaFlow was transferred to Ansys Fluent. A comparison of the velocity profiles at the outlet of a rectangular flat channel for water and various concentrations of polymer solution obtained during calculations on SigmaFlow and Ansys Fluent is shown in Fig. 1. As can be seen from the presented graphs, there is a good agreement between the calculated velocity profiles obtained with the used software products for solutions with different concentrations of polyacrylamide. The maximum difference does not exceed 0.1%.

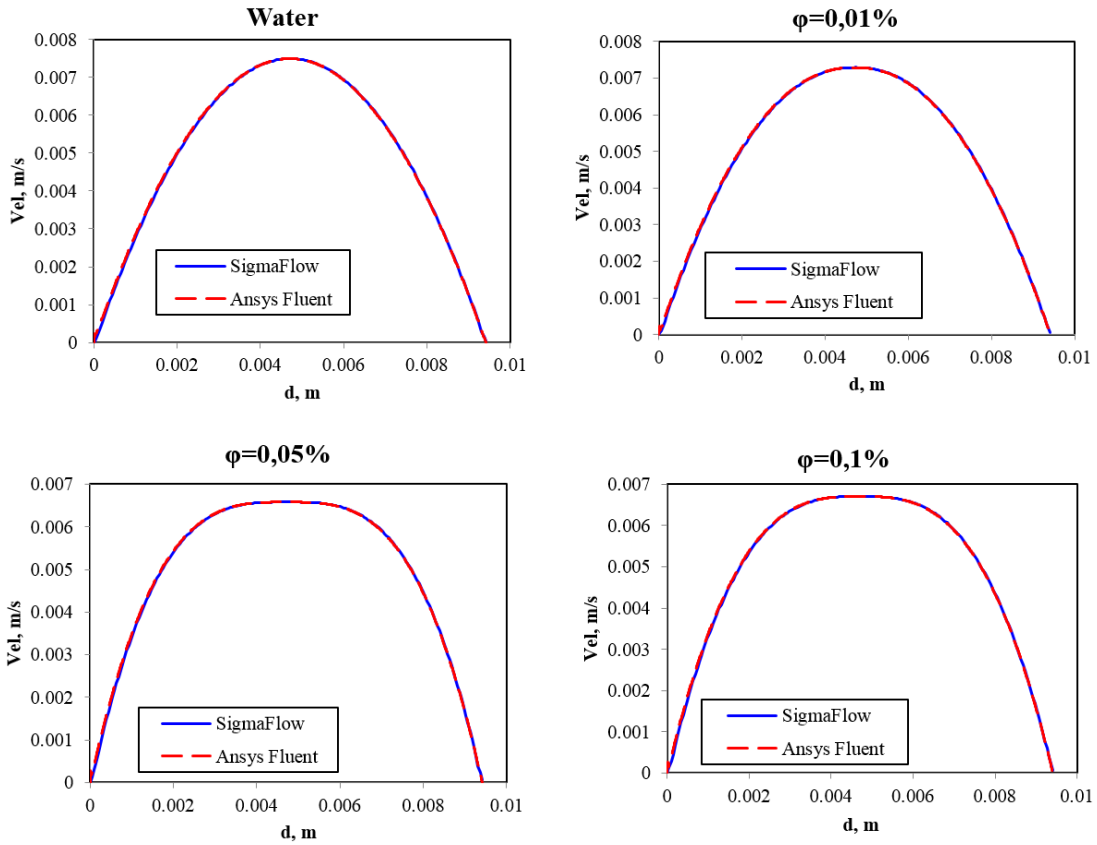

Fig. 1. Velocity profile in a flat channel for solutions with different concentrations of polyacrylamide

In addition to the velocity profiles in the channel, the magnitude of the pressure drop in the channel was compared for polyacrylamide solutions with different concentrations. Fig. 2 shows a graph of the pressure drop versus concentration for calculations performed on SigmaFlow and

Ansys Fluent. The discrepancy between the calculated differential pressure values obtained with SigmaFlow and Ansys Fluent does not exceed 0.5%.

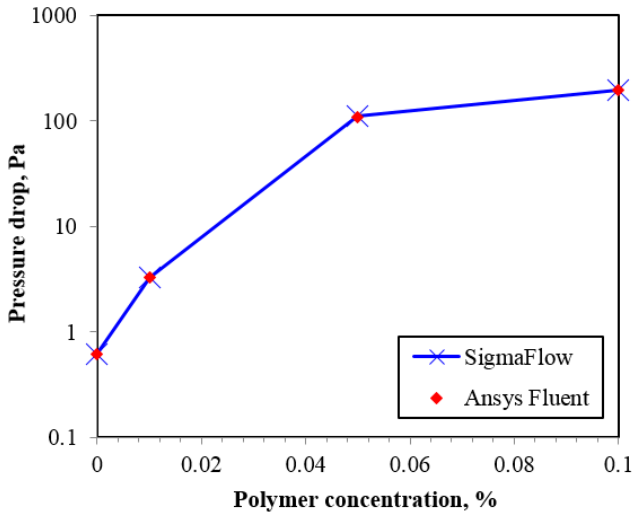

Fig. 2. Dependence of pressure drop on polymer concentration

2.2. A single-phase flow of polymer solution in a circular microchannell

Below, a single-phase isothermal flow of a polymer solution in a straight circular microchannel is considered. The channel diameter in the calculations is equal to 10 microns, and its length is 100 microns. The computational grid is built based on voxel geometry, and the total number of its calculation nodes is equal to 489,000. At the entrance to the computational domain, a constant velocity value of 0.005 m/s is set. Calculations are performed for polyacrylamide polymer solutions. The rheological properties of the polyacrylamide polymer used in the calculations are shown in Tab. 1. The results of the calculations performed using the developed numerical methodology are compared with those obtained on Ansys Fluent. The calculations are performed on a single grid, and for this purpose, the computational grid from SigmaFlow is imported into Ansys Fluent. As a result of calculations, the distributions of viscosity, pressure, and velocity fields in a straight circular channel have been obtained. As an example, Figs. 3–5 show comparisons of the viscosity, velocity, and pressure fields in the central section of the channel for a single-phase flow of a polyacrylamide solution with a mass concentration of 0.01% for SigmaFlow and AnsysFluent. The most indicative in this case is the effective viscosity distribution shown in Fig. 3. As can be seen, the viscosity in the flow core increases significantly due to a decrease in the shear rate. This leads to velocity profile flattening with decreasing index n. Apparently, the obtained distributions of viscosity, velocity, and pressure fields for different solvers are in good qualitative agreement with each other.

Fig. 6 shows a comparison of velocity profiles at the outlet from a straight circular channel for water and various concentrations of polymer solution obtained during calculations performed with SigmaFlow and Ansys Fluent. As can be seen from the presented graphs, there is a good agreement between the calculated velocity profiles obtained on the used software products for solutions with different concentrations of polyacrylamide.

In addition, the calculated dependences of the pressure drop in the channel for polyacrylamide solutions were compared with the analytical solution. For this purpose, it was expedient to

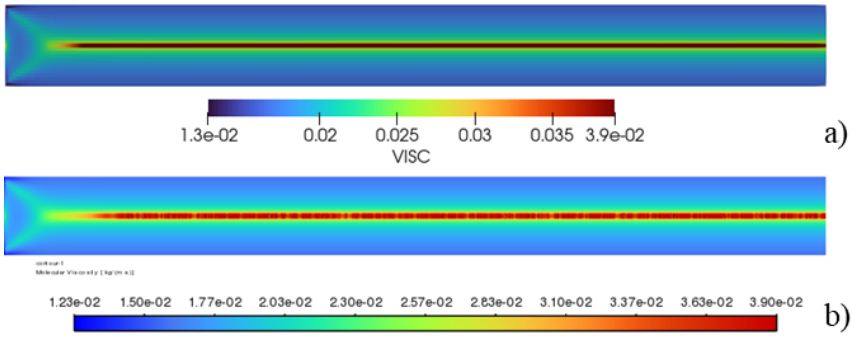

Fig. 3. Distribution of the dynamic viscosity coefficient for SigmaFlow (a) and AnsysFluent (b)

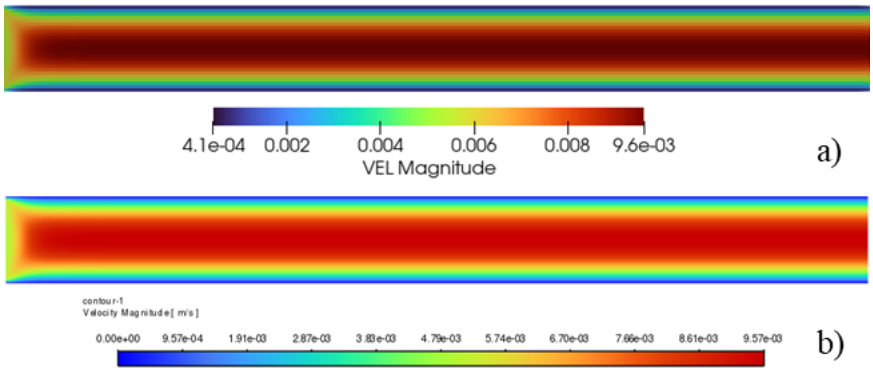

Fig. 4. Velocity field distribution for SigmaFlow (a) and AnsysFluent (b)

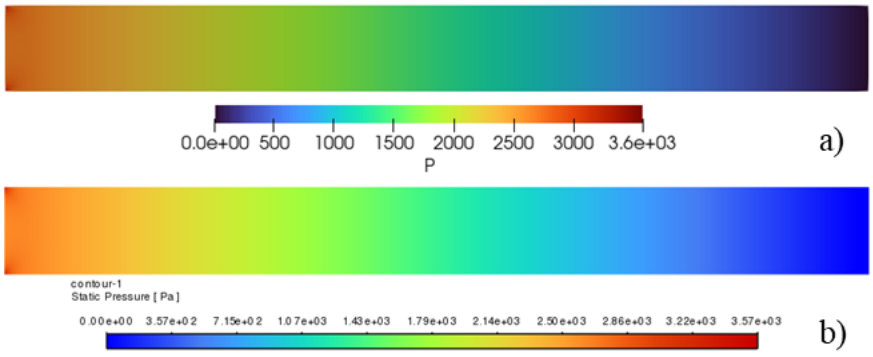

Fig. 5. Distribution of the pressure field for SigmaFlow (a) and AnsysFluent (b)

consider the established flow area, for which the analytical solution is accurate. For an established laminar flow of a power-law fluid in a straight circular channel, the exact solution for the pressure drop has the form [27]:

$$\Delta P = \frac{2kL}{r}\left(\frac{3n+1}{\pi r^3 n}Q\right)^n, \tag{21}$$

where k is the consistency index, n is the exponent, L is the channel length, r is the channel

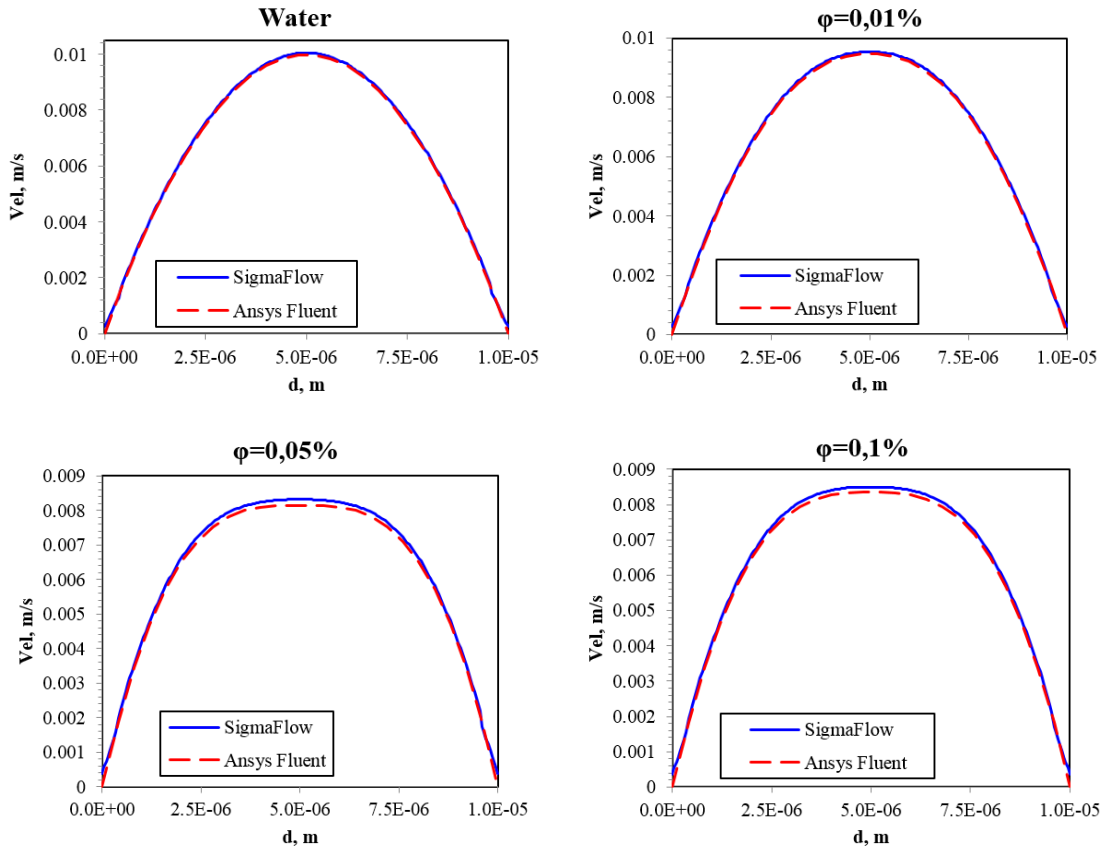

Fig. 6. Velocity profile in a straight circular channel for solutions with different concentrations of polyacrylamide

radius, and Q is the volumetric flow rate of the liquid. As can be seen from the graph shown in Fig. 7, the differential pressure values obtained using our methodology and Ansys Fluent are in good agreement with each other, and the maximum discrepancy between the results does not exceed 1%. The discrepancy between the calculated differential pressure values obtained with SigmaFlow and the analytical dependence does not exceed 5%.

2.3. A two-phase flow of polymer solution in a circular micro-channel

Further, to verify the calculation method, a two-phase flow in a circular microchannel was considered. The diameter of the channel in the calculations was equal to 10 microns, and its length was 100 microns. At the initial moment, the channel was filled with oil. At the entrance to the computational domain, a polymer solution with a concentration of 0.1% was supplied. The physical properties of the oil used in the calculations were: density of 727.42 kg/m^3 and viscosity of 0.048 Pa×s. The previously measured value of the interfacial tension coefficient in the calculations was set to 0.0253 N/m. In the calculation, two variants of the value of the contact angle on the wall of the circular channel were considered: 20 and 150 degrees. The first value of the contact angle corresponded to the flow of the polymer solution in the impregnation mode, i.e., the displacing liquid (polymer solution) moistened the surface better than the displaced liquid. The second value of the contact angle corresponded to the drainage mode, when the

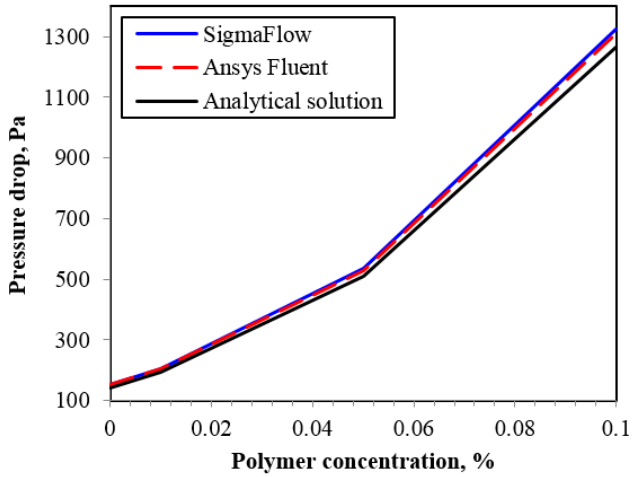

Fig. 7. Dependence of pressure drop on polyacrylamide concentration

displacing liquid wetted the channel walls worse. At the entrance to the computational domain, the constant velocity value of 0.005 m/s was set. In the calculations, patterns of the phase distribution during drainage and impregnation, as well as the distribution of pressure and velocity fields, were obtained. A qualitative comparison of the dynamics of the displacement fluid front motion was carried out. A quantitative comparison was also realized for the dependences of the volume of the displacing liquid and the pressure drop in the channel on time. Figs. 8–9 show the patterns of phase distribution in the drainage process at various points in time. As can

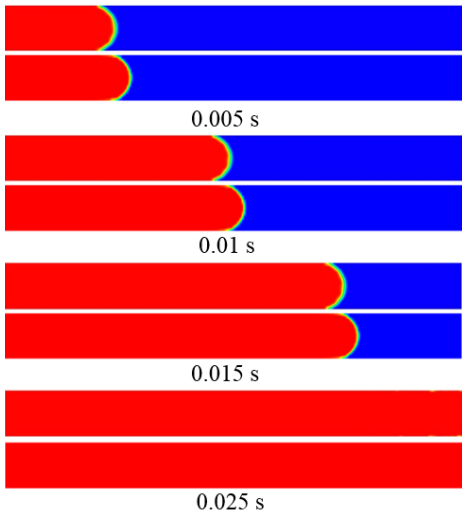

Fig. 8. Dynamics of the displacement fluid front motion in the mode of drainage with polymer solution

be seen from the comparison of the distributions, the dynamics of motion along the channel and the shape of the meniscus for both calculation methods are qualitatively similar in both drainage and impregnation modes. The quantitative verification results are shown in Fig. 10, presenting the behavior of the volume fraction of the wetting phase and the pressure drop in the

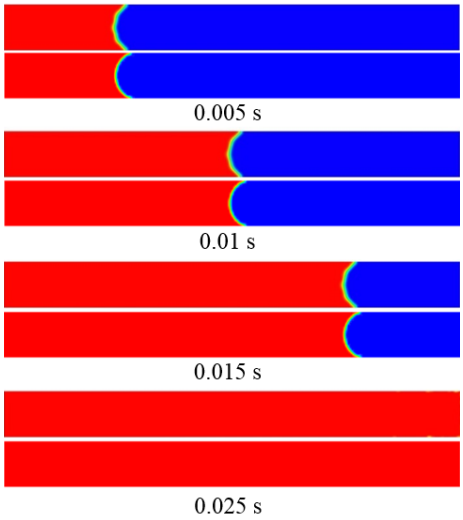

Fig. 9. Dynamics of the displacement fluid front motion in the mode of impregnation with polymer solution

channel over time. The volume fraction in the channel up to the moment of the displacement fluid breakthrough from the computational domain depends linearly on the injection time, which corresponds to the law of conservation of mass for incompressible liquids. The behavior of the total pressure is determined by the contribution of the capillary and hydrodynamic components. During impregnation, the capillary pressure is negative, while during drainage it is positive. The hydrodynamic component of pressure decreases as a more viscous liquid exits the channel and is replaced by water. After the displacing liquid leaves the computational domain, the pressure drop value corresponds to a single-phase flow. In general, as can be seen from the graphs in Fig. 10, both calculation programs generally agree well with each other. The observed slight differences in the behavior of the pressure drop at the moment, when the displacing liquid exits the computational domain, are due to the nuances of the implementation of boundary conditions.

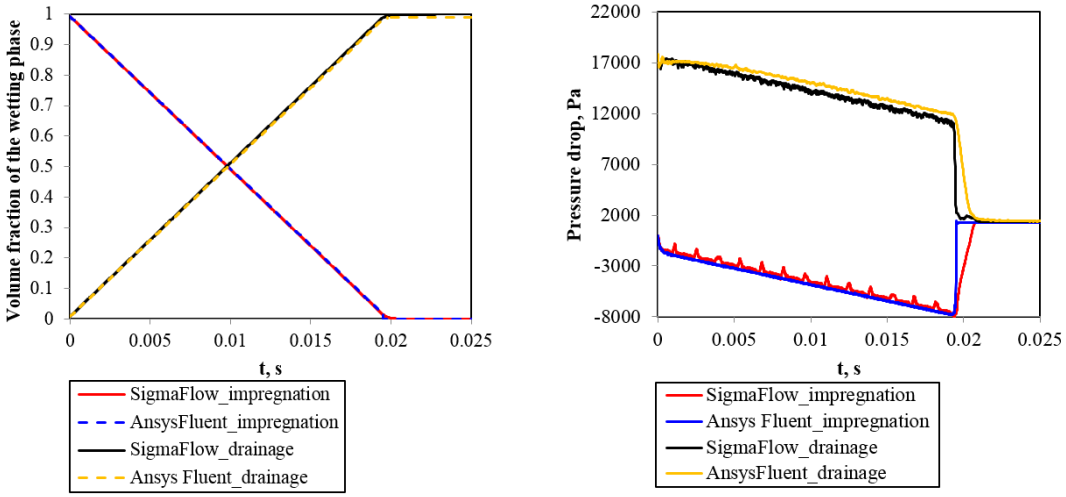

Fig. 10. Dependence of water volume and pressure drop on time during drainage and impregnation with polymer solution

Conclusion

A mathematical model and numerical technique have been developed to describe multiphase flows in three-dimensional digital models of porous media. It is based on the VOF method and takes into account the transfer of polymer concentration during flooding and its effect on the rheology of the displacing fluid. Within the framework of this model, the rheology of the flooding fluid was described by a nonlinear model of viscoplastic media (Herschel–Bulkley) based on the generalized viscosity approach. The rheological parameters of the model depended on the local polymer concentration, which in turn was determined by solving the convective-diffusion transfer equation. To regularize the effective viscosity and eliminate infinite values, an approach with exponential regularization of the shear rate at small values was used. The developed calculation methodology has been tested and verified. The problems of single-phase and multiphase immiscible flow of non-Newtonian fluids in a rectangular, flat and circular channel have been considered. The calculated data have been compared with analytical dependences and the results of calculations, obtained with the Ansys Fluent software product. Testing and verification have shown that the numerical solutions found with the developed numerical methodology are qualitatively and quantitatively in good agreement with known analytical solutions and with those obtained using the Ansys Fluent reference CFD solver.

This research was supported by the Russian Science Foundation grant no. 23-79-30022, https://rscf.ru/project/23-79-30022/.

References

[1] Cheng-yan LIN , Yu-qi WU, Li-hua REN, Yang WANG, Wei-chao YAN, Xiao-long SUN, Xian-guo ZHANG, Yi-min ZHANG, Review of digital core modeling methods, *Progress in Geophysics* **33**(2018), no. 2, 679–689 (in Chinese).

[2] G.Li, J.Zhao, Y.Liu, Z.Xiao, S.Cui, B.Wei, C.Zhang, Y.Mao, Y.Xia, L.Xu, J.Sun, Z.Hu, Research on multi-scale digital core construction of carbonate rock with fractures and caves characteristics: a case study of Dengying formation carbonate rocks in Sichuan Basin, *Front. Earth Sci.*, **13**(2025), 1528829. DOI: 10.3389/feart.2025.1528829

[3] J.Yun, S.Kim, J.Kim, Digital Twin Technology in the Gas Industry: A Comparative Simulation Study, *Sustainability*, **16**(2024), 5864. DOI: 10.3390/su16145864

[4] V.N.Bykova, E.Kim, M.R.Gadzhialiev, V.O.Musienko, A.O.Orudzhev, E.A.Turovskaya, Application of a digital twin in the oil and gas industry, *Actual Problems of Oil and Gas*, **1**(2020), no. 28, 8 (in Russian). DOI: 10.29222/ipng.2078-5712.2020-28.art8

[5] E.B.M.Meza, D.G.B.d.Souza, A.Copetti, A.P.B.Sobral, G.V.Silva, I.Tammela, R.Cardoso, Tools, Technologies and Frameworks for Digital Twins in the Oil and Gas Industry: An In-Depth Analysis, *Sensors*, **24**(2024), 6457. DOI: 10.3390/s24196457

[6] S.K.Dhar,V.Nandipati, A.Bhattacharya, Digital Core-New Tool for Petrophysical Evaluation and Enhanced Reservoir Characterization, SPE Oil and Gas India Conference and Exhibition, 2019. DOI: 10.2118/194635-MS

[7] S.A.Idrisova, M.A.Tugarova, E.V.Stremichev, B.V.Belozerov, Digital core. integration of carbonate rocks thin section studies with results of routine core tests, *PROneft'. Professional'no o nefti*, **2**(2018), 36–41 (in Russian). DOI: 10.24887/2587-7399-2018-2-36-41

[8] A.Q.Raeini, B.Bijeljic, M.J.Blunt, Numerical modelling of sub-pore scale events in two-phase flow through porous media, *Transp. Porous Media*, **101**(2014), no. 2, 191–213. DOI: 10.1007/s11242-013-0239-6

[9] O.Dorn, R.Villegas, History matching of petroleum reservoirs using a level set technique, *Inverse Problems*, **24**(2008), no. 3, 035015. DOI: 10.1088/0266-5611/24/3/035015

[10] S.Junjie, L.Cheng, R.Cao, Z.Jia, G.Liu, Phase-field simulation of imbibition for the matrix-fracture of tight oil reservoirs considering temperature change, *Water* **13**(2021), no. 7, 1004. DOI: 10.3390/w13071004

[11] H.Liu, Q.Kang, C.R.Leonardi, Multiphase lattice Boltzmann simulations for porous media applications, *Comput. Geosci.*, **20**(2016), no. 4, 777–805. DOI: 10.1007/s10596-015-9542-3

[12] A.M.Tartakovsky, P.Meakin, Pore scale modeling of immiscible and miscible fluid flows using smoothed particle hydrodynamics, *Adv. Water Resour*, **29**(2016), no. 10, 1464–1478. DOI: 10.1016/j.advwatres.2005.11.014

[13] D.Silin, T.Patzek, Pore space morphology analysis using maximal inscribed spheres, *Phys. A*, **371**(2006), no. 2, 336–360. DOI: 10.1016/j.physa.2006.04.048

[14] S.Cheng, M.Fu, F.A.Kulacki, Characterization of a porous transducer using a capillary bundle model: Permeability and streaming potential prediction, *Int. J. Heat Mass Transf.*, **118**(2018), 349–354. DOI: 10.1016/j.ijheatmasstransfer.2017.10.128

[15] A.Hosseinzadegan, A.Raoof, H.Mahdiyar, E.Nikooee, M.Ghaedi, J.Qajar, Review on pore-network modeling studies of gas-condensate flow: Pore structure, mechanisms, and implementations, *Geoenergy Science and Engineering*, **226**(2023), 211693.

[16] W.Song, F.Liu, Y.Li, Y.Yang, Pore scale modeling of fluid transport in complex reservoirs: Multi-scale digital rock construction, flow experiments and simulation methods, *Capillarity*, **11**(2024), no. 3, 81–88. DOI: 10.1002/2014WR015959

[17] A.A.Dekterev, A.A.Gavrilov, A.V.Minakov, State-of-the-art capability of using the SigmaFlow CFD code for solving thermophysical problems, *Modern Science: Researches, Ideas, Results, Technologies.*, **2**(2010), no. 4, 117–122 (in Russian).

[18] A.A.Dekterev, K.Yu.Litvintsev, A.A.Gavrilov, E.B.Kharlamov, S.A.Filimonov, Freely distributed SIGMA FW software complex for simulation of hydrodynamics and heat transfer, *J. Siberian Federal University. Engineering and Technology*, **10**(2017), no. 4, 534–542 (in Russian).

[19] A.A.Gavrilov, Computational algorithms and software complex for numerical simulation of non-Newtonian fluids flows in an annular channel, Dissertation Abstract, Cand. Sc. Physics and Mathematics, 05.13.18 – Mathematical modeling, numerical methods, and software complexes, 2014 (in Russian).

[20] C.W.Hirt, B.D.Nichols, Volume of fluid (VOF) method for the dynamics of free boundaries, *J Comput Phys.*, **39**(1981), no. 4, 201–225.

[21] A.A.Gavrilov, D.V.Guzei, A.A.Dekterev, A.V.Minakov, Verification of a numerical method for modeling two-phase flows of immiscible liquids with the transfer of modifying additives in three-demensional digital core models, *J. Sib. Fed. Univ. Math. Phys.*, **17**(2024), no. 6, 817–828. EDN: XYDYVJ

[22] A.A.Gavrilov, D.V.Guzei, A.I.Pryazhnikov, A.S.Yakimov, A.V.Minakov, Development and microfluidic testing of a new numerical algorithm and software for modeling immiscible fluid flows in digital core models, *J. Fuel*, **386**(2025), 134253. DOI: 10.1016/j.fuel.2024.134253

[23] J.U.Brackbill, D.B.Kothe, C.Zemach, A continuum method for modeling surface tension, *J. Comput Phys.*, **100**(1992), no. 2, 335–354.

[24] T.C.Papanastasiou, Flows of Materials with Yield, *Journal of Rheology*, **31**(1987), no. 5, 385–404.

[25] S.Popinet, Numerical models of surface tension, *Annu. Rev. Fluid Mech*, **50**(2018), 49–75. DOI: 10.1146/annurev-fluid-122316-045034

[26] Q.Raeini, M.J.Blunt, B.Bijeljic, Modelling two-phase flow in porous media at the pore scale using the volume-of-fluid method, *J. Comput. Phys.*, **231**(2012), 5653–5668. DOI: 10.1016/j.jcp.2012.04.011

[27] W.L.Wilkinson, Non-Newtonian fluids: Fluid Mechanics, Mixing and Heat Transfer, Oxford: Pergamon Press, 1960, 138.

Верификация численной методики моделирования двухфазных потоков несмешивающихся неньютоновских жидкостей в пористых средах

Дмитрий В. Гузей
Сибирский федеральный университет
Красноярск, Российская Федерация
Андрей А. Гаврилов
Александр А. Дектерев
Сибирский федеральный университет
Красноярск, Российская Федерация
Институт теплофизики СО РАН
Новосибирск, Российская Федерация
Андрей В. Минаков
Сибирский федеральный университет
Красноярск, Российская Федерация

Аннотация. В работе представлены результаты разработки и верификации расчетной методики для моделирования двухфазных несмешивающихся потоков в пористых средах с учетом переноса полимеров, меняющих реологию флюидов в процессе течения. Математическая модель основана на уравнениях Навье–Стокса и методе жидкости в ячейках VOF. Модель включает конвективно-диффузионное уравнение переноса концентрации с постоянным коэффициентом эффективной диффузии. В рамках данной модели реология вытесняющего флюида описывается нелинейной моделью вязкопластических сред (Гершеля–Балкли) на основе подхода обобщенной вязкости. Реологические параметры модели при этом зависят от локальной концентрации полимера. Для регуляризации эффективной вязкости и исключения бесконечных значений применяется подход с экспоненциальной регуляризацией величины скорости сдвига при малых значениях. Проведено тестирование и верификация разработанной расчетной методики. В результате тестирования и верификации было показано, что численные решения, полученные с помощью разработанной численной методики, качественно и количественно хорошо согласуются с известными аналитическими решениями и с численными решениями, получаемыми с помощью эталонного CFD решателя Ansys Fluent.

Ключевые слова: цифровые модели пористых сред; несмешивающееся вытеснение; неньютоновское течение, растворы полимеров; VOF метод; тестирование.

EDN: AHCYRE
УДК 537.31

Impedance Characteristics and Phase-dependent Conductivity of ZrO_{2-x} Nanopowders Produced by Vacuum-arc Synthesis

Igor V. Karpov*
Leonid Yu. Fedorov†
Siberian Federal University
Krasnoyarsk, Russian Federation
Federal Research Center Krasnoyarsk Scientific Center of the SB RAS
Krasnoyarsk, Russian Federation
Evgeniya A. Slyusareva¶
Siberian Federal University
Krasnoyarsk, Russian Federation
Alexander V. Pavlov
Alexey I. Lyamkin‡
Siberian Federal University
Krasnoyarsk, Russian Federation
Federal Research Center Krasnoyarsk Scientific Center of the SB RAS
Krasnoyarsk, Russian Federation
Almira M. Zhilkashinova§
D. Serikbayev East Kazakhstan Technical University
Ust-Kamenogorsk, The Republic of Kazakhstan

Received 10.06.2025, received in revised form 05.08.2025, accepted 27.09.2025

Abstract. The paper presents the results of studying the dielectric characteristics of unstabilized zirconium dioxide nanopowder (ZrO_{2-x}) obtained by vacuum-arc deposition at different pressures of argon-oxygen plasma. A comprehensive analysis of the phase composition, morphology, photoluminescent properties and impedance characteristics of three samples differing in the content of tetragonal, monoclinic and suboxide phases is carried out. It is found that the electrical response of the materials is determined by the interaction of the bulk conductivity of the tetragonal matrix, the barrier effects of grain boundaries (especially in the presence of m-ZrO_2) and the shunting effect of the conducting phase Zr_3O. The sample with the lowest content of the tetragonal phase exhibits minimal impedance, while the most heterophase composition is characterized by pronounced interphase polarization and high dielectric losses.

Keywords: zirconium oxide, vacuum arc, physical vapor deposition, phase stability.

Citation: I.V. Karpov, L.Yu. Fedorov, E.A. Slyusareva, A.V. Pavlov, A.I. Lyamkin, A.M. Zhilkashinova, Impedance Characteristics and Phase-dependent Conductivity of ZrO_{2-x} Nanopowders Produced by Vacuum-arc Synthesis, J. Sib. Fed. Univ. Math. Phys., 2026, 19(1), 35–49. EDN: AHCYRE.

*ikarpov@sfu-kras.ru https://orcid.org/0000-0001-6951-8025
† https://orcid.org/0000-0001-6951-8025 ¶ https://orcid.org/0000-0002-9124-3643
‡alyamkin@sfu-kras.ru https://orcid.org/0000-0001-8959-6856
§almira_1981@mail.ru https://orcid.org/0000-0002-1209-7335

The relevance of the study of phase-dependent conductivity of zirconium dioxide nanopowders ZrO_{2-x} ($1.5 \leqslant x \leqslant 2.0$) is due to a combination of fundamental and applied factors associated with the unique properties of this oxide and its polymorphism. [1–4] Zirconium dioxide exists in three main crystalline modifications – monoclinic, tetragonal and cubic, each of which demonstrates fundamentally different conductivity behavior. [5, 6] The monoclinic phase (m-ZrO_2) is characterized by extremely low electrical conductivity and high activation energy ($E_a = 1.5 - 1.8$ eV in an oxidizing environment), which makes it practically an insulator at temperatures below 1000 °C. In contrast, the tetragonal modification (t-ZrO_2), stabilized at small particle sizes or external stresses, has a significantly higher content of oxygen vacancies and demonstrates n-type conductivity with a lower transfer barrier ($E_a = 0.7 - 1.0$ eV) [7]. The cubic phase (c-ZrO_2), which is the most symmetrical, provides optimal channels for the migration of oxygen ions, and upon partial reduction is capable of exhibiting mixed ion-electron conductivity, reaching values comparable to doped YSZ ($\sigma \sim 10^{-1}$ S/cm at 1000 °C) [8]. A significant contribution to the increase in conductivity is also made by the formation of suboxide inclusions (e.g. Zr_3O), which are formed upon deep reduction and act as conducting bridges along grain boundaries, sharply increasing the electron component σ. Thus, it is the phase state and defect structure that determine the magnitude and nature of the conductivity of ZrO_{2-x}, and the transition from m- to t- and c-phases is accompanied by an increase in σ by several orders of magnitude. [9–12]

In ZrO_{2-x} nanostructures, a universal frequency response is often recorded: at very low frequencies $\sigma \approx \sigma_{dc} \approx$ const (flat region on the $\sigma(f)$ graph), turning into an increase in σ at higher f. In the Jonscher model, such a frequency dependence is described by the law:

$$\sigma(\omega) = \sigma_{dc} + A\omega^n. \tag{1}$$

Below a certain threshold ω_{min} ("critical frequency"), a plateau of constant current is observed, and at $\omega \gg \omega_{min}$ $\sigma(\omega)$ grows as ω^n (usually $n \approx 0.5$–1). For dispersion media, there is no sharp "development", and the σ_∞ limit is practically not visible at very high frequencies. For ZrO_{2-x} nanopowders, it is interesting to track the behavior of $\sigma(f)$ from 1 Hz to 10^8 Hz.

At low frequencies, grain boundary and interface effects (Maxwell–Wagner, polarization at the electrodes) often dominate, which results in a flattening or tilted section on the impedance hodograph. Then, at medium and high frequencies, the dispersion part behaves — $\sigma_{ac} \sim \omega^n$. Thus, experiments on such systems show that at small f, the conductivity can be lower and depend on the sample geometry, and at $f >$ kHz–MHz, an increase in $\sigma(\omega)$ is seen, which obeys the Jonscher law well. The transition from direct current to alternating current $\sigma_{dc} \to \sigma_{ac}$ is determined by the vacancy concentration and the charge transfer mechanism: the more vacancies, the higher ω_{min}.

Thus, the relevance of studying the phase-dependent conductivity of ZrO_{2-x} is determined by a number of factors:

1. Fundamental importance as a model system for studying defective electronics and transfer mechanisms in oxides;
2. The need to develop new materials for fuel cells, sensors, membranes and ReRAM devices;
3. The ability to control electrical properties through morphology, phase composition and synthesis conditions;
4. The prospect of targeted control of the ratio of ionic and electronic conductivity due to the concentration of oxygen vacancies and suboxide inclusions.

All this makes the studies of undoped ZrO_{2-x} ($1.5 \leqslant x \leqslant 2.0$) not only relevant, but also key for the development of modern materials science and practical applications in the field of energy and electronics.

1. Experimental part

The formation of zirconium dioxide nanoparticles (ZrO_{2-x}) in a vacuum chamber by gas-phase deposition or plasma synthesis methods goes through several key stages that determine the morphology, size and crystalline structure of the resulting particles [13–15]. In the first stage, evaporation of the starting material, for example, metallic zirconium, leads to the formation of a vapor phase that reacts with oxygen, initiating oxidation processes and the formation of nanoparticle nuclei. An important role is played by the environment containing argon and oxygen, since collisions of particles in the gas phase affect the rate of nucleation and further growth of nanoparticles. Under optimal conditions, stable crystalline phases are formed, among which the monoclinic and tetragonal modifications of ZrO_2 dominate, and their ratio depends on the degree of oxygen saturation and the cooling rate of the particles.

After the nucleation stage, the process of coagulation and growth of nanoparticles begins, during which individual nuclei collide, merge and stabilize. Depending on the precipitation kinetics and the concentration of the gas mixture, the particles can grow to a certain size or, conversely, remain within a few nanometers if the conditions are not conducive to agglomeration. Factors such as the density of zirconium vapor, the presence of oxygen and the ambient temperature determine the final properties of the nanoparticles, including their size range, degree of crystallinity and possible structural defects. With oxygen deficiency, oxygen-deficient nanoparticles containing vacancies can form, which leads to a change in their electrophysical characteristics. Thus, control over the synthesis parameters allows one to control the morphology and phase composition of zirconium dioxide nanoparticles.

A vacuum chamber with an arc evaporator mounted on the side wall and connected to an inverter power source providing an arc discharge current of 100 A was used to synthesize ZrO_{2-x} nanoparticles (Fig. 1). The experimental setup and the dependence of the powder properties on the spraying conditions are described in detail in [13–15]. The cathode with a diameter of 80 mm and a length of 100 mm was made of a zirconium alloy with a purity of 99.99% and mounted on a copper current lead with water cooling. The reaction chamber with a diameter of 0.6 m and a height of 0.6 m had double walls and stainless steel flanges.

The samples were obtained at vacuum chamber pressures of 90, 60 and 30 Pa (hereinafter referred to as samples N90, N60, N30) using argon as the plasma-forming gas. The oxygen content in the gas mixture was 20% for all pressures. Oxygen was supplied to the reactor in such a way as to form a uniform shell around the cathode. The reactor was pre-evacuated to a base pressure of 10^{-2} Pa. The reaction products were collected for 20 min on a hemispherical water-cooled stainless steel substrate located at a distance of 200 mm from the cathode. A typical powder yield under the described vacuum-arc synthesis conditions was estimated at approximately 150–180 mg/min, which in total amounted to ∼3.0–3.6 g per 20-min synthesis session.

Powder diffraction data for all samples (N90, N60, N30) were obtained at room temperature on a Bruker D8 Advance diffractometer with Cu-Kα radiation ($\lambda = 0.1540$ nm) and a linear detector for Rietveld analysis. The 2θ measurement step was 0.01°, and the counting time was 0.2 s per step. The PDF-4+ databases of the International Center for Diffraction Data (ICDD) were used to analyze the crystal structure of the experimental X-ray diffraction patterns.

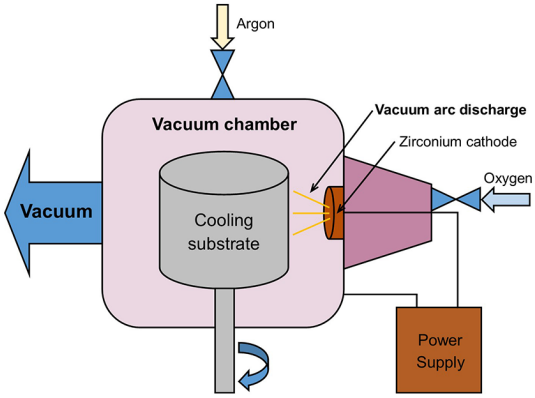

Fig. 1. Scheme of the synthesis process of experimental samples [13]

Transmission electron microscopy (TEM) of ZrO_2 nanoparticles was performed on a JEOL JEM-2100 high-resolution electron microscope with an accelerating voltage of 200 kV.

Photoluminescence spectra were obtained on a modular OmniFluo-900 spectrofluorimeter (Zolix Instruments, China), which allows measurements of emission and excitation spectra in a stationary mode. The device is equipped with:

- Excitation source — a high-pressure xenon lamp (150 W) with a spectral range of 200–1100 nm
- Excitation and emission monochromators.
- R13456 PMT detector (wavelength range of 185–980 nm)

Holders for solid samples were used, measurements were carried out at room temperature in the "front-face" measurement geometry. The results were automatically corrected for the spectral sensitivity of the recording system.

The excitation wavelength of 280 nm was chosen to study the photoluminescence of stabilized zirconium dioxide nanopowders, since it lies in the range corresponding to the absorption maximum of defect centers, primarily oxygen vacancies and F-centers, typical of such materials. At a photon energy of about 4.43 eV, electrons are effectively excited from the valence band or deep traps to levels located near the conduction band, which provides bright defect emission in the range of 420–550 nm. In contrast to the harder UV (244–266 nm), the use of 280 nm reduces the intensity of the scattered background and the risk of photodegradation of the sample, while maintaining high sensitivity of the method.

IR spectral studies were carried out on a Vertex 80V vacuum Fourier spectrometer (Bruker) in the wavelength range of 5000–370 cm^{-1} with a spectral resolution of 0.2 cm^{-1}. Sample preparation was performed as follows:

1. Thorough grinding of KBr crystals in an agate mortar with an agate pestle
2. Thorough grinding of 0.008–0.02 g of the measured sample in an agate mortar with an agate pestle

3. Mixing and additional grinding of the prepared KBr powder and sample in an agate mortar with an agate pestle. The range of proportions is 1/10–1/200 by weight depending on the optical density in the measured IR range

4. Final drying of the obtained powder for up to 30 min in a microwave oven at minimum heating mode (10%)

5. Pressing approximately 0.2 g of the mixture in a 13 mm mold, resulting in a transparent or translucent tablet with a diameter of 13 mm

To determine the electrophysical characteristics of the obtained samples, the impedance spectroscopy method was used using the E5061B vector network analyzer (Agilent Technology). The samples for the studies were prepared in the form of tablets with a diameter of 13 mm and a thickness of 1 mm by pressing under a pressure of 200 MPa. The relative density of the pressed samples without sintering was estimated by the hydrostatic weighing method taking into account the theoretical density of stoichiometric ZrO_2 (5.68 g/cm^3) and was $\sim$ 65–70%. High porosity contributes to a decrease in the effective permittivity and an increase in dielectric losses due to air gaps playing the role of low-dielectric inclusions. Before measurements, the samples were calcined at 200 °C to remove moisture.

The dielectric properties were specifically studied in the green state, since our main goal was to evaluate the effect of synthesis parameters and phase composition on the nanopowder itself, without additional structural changes caused by high-temperature sintering. To perform impedance measurements, a thin indium layer was rolled onto the end surfaces of the samples or graphite electrodes with a minimum (1–5 Ω) transition resistance were used. The measurement process was reduced to recording the impedance modulus $|Z|$ and the phase shift between current and voltage (φ) in the frequency range from 10^2 to 10^8 Hz. The obtained data allow us to calculate the real $Z'(f) = |Z| \cdot \cos\varphi$ and imaginary $Z''(f) = |Z| \cdot \sin\varphi$ components of the impedance.

2. Results and discussion

X-ray diffraction analysis. Almost all peaks, except for a small number of small peaks of unknown impurities, were indexed by the monoclinic and tetragonal phases of ZrO_2, as well as the suboxide phase of Zr_3O. Therefore, these structures were taken as a starting model for the Rietveld refinement, which was performed using TOPAS 4.2 software [16]. The atomic coordinates were fixed during the refinement, since the structures are known. The refinements were stable and gave low R-factors (Tab. 1, Fig. 2).

Rietveld refinement was used to accurately determine the crystallite size in all samples. Instrumental peak broadening was estimated using a silicon standard and subsequently taken into account in the crystallite size estimation process.

Fig. 3 shows a typical transmission electron microscopy image of ZrO_2 nanoparticles. According to the results, ZrO_2 nanopowder is highly agglomerated spherical particles.

Agglomeration of nanoparticles is caused by a combination of thermodynamic, structural and technological factors. The main reason is the high specific surface area of nanoparticles and the excess surface energy associated with it, due to which the system tends to minimize free energy through adhesion and coarsening of particles. An additional contribution is made by electrostatic interactions arising from the presence of charged defects, oxygen vacancies and suboxide fragments of Zr_3O on the surface, which form local centers of attraction and "gluing". The arc synthesis process itself also plays a significant role: in high-temperature plasma, particles

Table 1. Main parameters for sample processing and refinement

Sample	Phase	Content (%)	Space group	Cell parameters (Å)	R_{wp}, R_p, χ^2
N90	m-ZrO_2	45(1)	$P2_1/c$	$a = 5.137(4)$ $b = 5.214(4)$ $c = 5.312(4)$ $\beta = 99.174(9)$	6.23, 4.9, 1.37
	$t-ZrO_2$	52(1)	$P4_2/nmc$	$a = 3.583(3)$ $c = 5.178(4)$	
	Zr_3O	3(1)	$P6_322$	$a = 5.622(4)$ $c = 5.211(4)$	
N60	$m-ZrO_2$	10(1)	$P2_1/c$	$a = 5.125(3)$ $b = 5.223(3)$ $c = 5.314(3)$ $\beta = 98.88(1)$	6.47, 5.16, 1.34
	$t-ZrO_2$	75(1)	$P4_2/nmc$	$a = 3.623(3)$ $c = 5.185(4)$	
	Zr_3O	15(1)	$P6_322$	$a = 5.673(4)$ $c = 5.228(4)$	
N30	$t - ZrO_2$	90(1)	$P4_2/nmc$	$a = 3.535(3)$ $c = 5.173(4)$	6.12, 5.30, 1.11
	Zr_3O	9(1)	$P6_322$	$a = 5.647(5)$ $c = 5.535(4)$	

are generated in the gas phase and, upon rapid cooling, tend to condense into aggregates [17]. Surface defects and non-stoichiometry additionally enhance interparticle adhesion, and in the post-synthetic period, agglomeration is fixed due to the adsorption of moisture and gases from the air, which stabilizes the aggregates and makes them resistant to mechanical separation. Thus, the agglomeration of ZrO_2 in vacuum-arc synthesis is a natural consequence of the high surface energy of nanoparticles, the defectiveness of their structure and the features of formation in plasma.

The FTIR spectra of three zirconium dioxide nanopowder samples, shown in Fig. 4, demonstrate characteristic group bands corresponding to various structural modifications of ZrO_2 and possible impurity compounds.

Region 3500–3000 cm^{-1}.In the specified range of wave numbers, broad bands are observed, which can be associated with the stretching vibrations of O–H groups. This may indicate the presence of hydroxyl (OH^-) groups on the particle surface, which is typical of nanomaterials subject to moisture adsorption.

In the region of 1700–1300 cm^{-1} in the IR spectra of zirconium dioxide nanopowders, bands are observed that can be associated with the deformation vibrations of water molecules (δ(O–H)). These vibrations are typical of water in a physically adsorbed or chemically bound state on the surface of nanoparticles. Deformation vibrations of water occur when the H–O–H bond angle changes and are usually accompanied by more intense bands in the region of 3200–3500 cm^{-1},

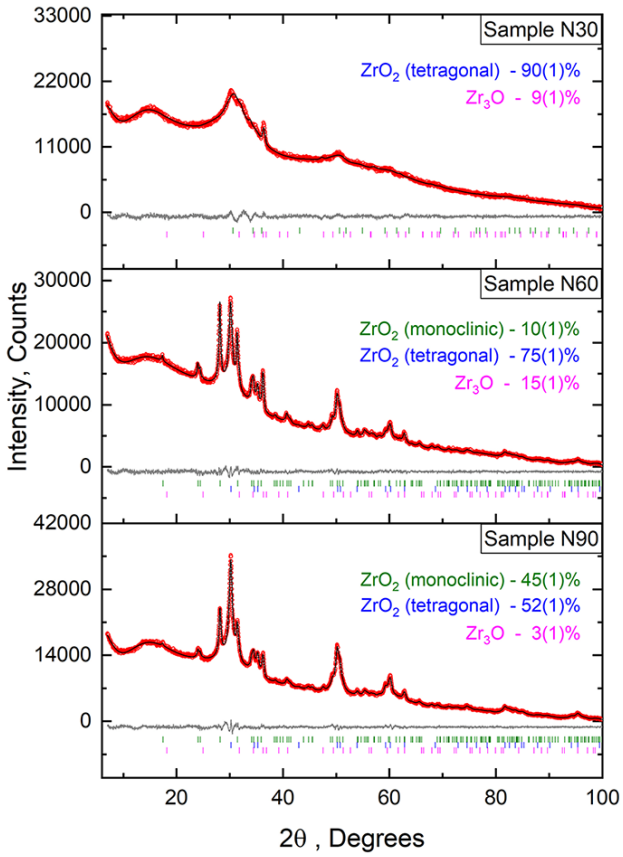

Fig. 2. X-ray diffraction patterns of the indicated samples of "black" zirconium dioxide ZrO_{2-x}

characteristic of the stretching vibrations of O–H groups. In the presented spectra, the intensity of the bands in the region of 1700–1600 cm^{-1} is most pronounced in samples N30 and N60, indicating a higher degree of hydration of their surface. This may be due to the presence of hydroxyl groups Zr–OH), which help retain water molecules, as well as the porous structure of the nanopowder, which ensures effective moisture adsorption. In sample N90, the intensity of this band is significantly lower, which may indicate a smaller number of surface-bound water molecules or a denser packing of nanoparticles, preventing adsorption. Thus, the analysis of this band allows us to estimate the level of hydration of the particle surface, their ability to absorb water and interaction with the environment.

The differences in the intensity of the bands in the region of 1700–1600 cm^{-1}, corresponding to the deformation vibrations of water (δ(O–H)), are due to the structural differences between the three samples. Samples with a higher proportion of the tetragonal phase (such as N30 and N60) exhibit a more porous morphology and a higher concentration of surface hydroxyl groups. Such a microstructure provides more adsorption sites and promotes the retention of physically adsorbed and bound water, which leads to more intense absorption bands. In contrast, sample N90 with a lower content of the tetragonal phase and a denser, less defective structure has fewer

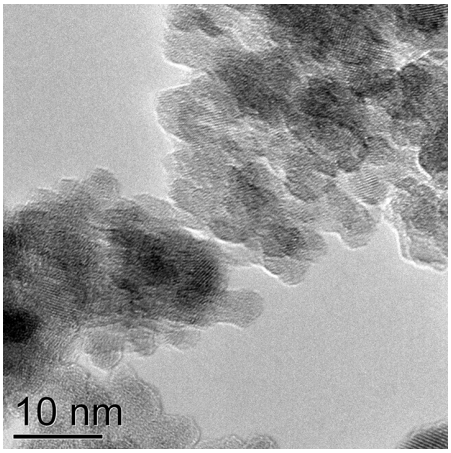

Fig. 3. TEM image of the indicated samples of "black" zirconium dioxide ZrO_{2-x}

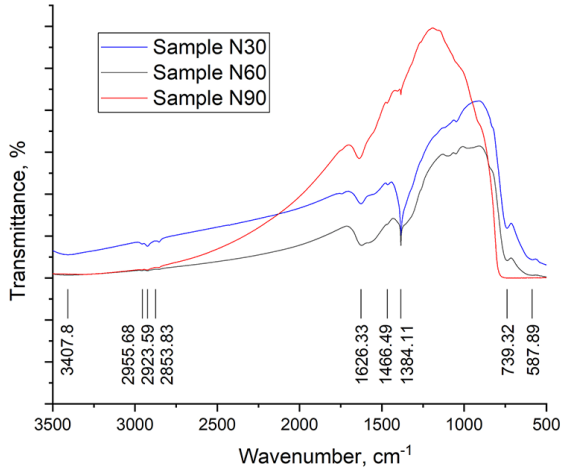

Fig. 4. Fourier transform infrared spectroscopy (FTIR) spectra of ZrO_{2-x} nanoparticle obtained by different gas mixture pressure

hydroxyl groups and fewer active sites for water adsorption, which leads to a decrease in the intensity of the bands in this region. In other words, changes in the phase composition and defect density directly affect the water absorption capacity of the nanopowders and are reflected in the observed IR spectra.

Region 800–500 cm^{-1}. The main bands correspond to vibrations of Zr–O bonds in different phases of zirconium dioxide. For all samples, peaks are observed in the region of 500–750 cm^{-1}, characteristic of the tetragonal and monoclinic phases of ZrO_2. Sample N30, containing 90% of the tetragonal modification, demonstrates the highest bands, which is confirmed by a strict understanding of the tetragonal structure. In sample N90, where the tetragonal phase is reduced to 52%, a weakening of the characteristic bands and possible appearance of new signals are observed, indicating a partial appearance of oxide in the monoclinic form. Sample N60 (75% of

the tetragonal phase and 15% Zr_3O) contains enhanced bands in the region of 600–650 cm^{-1}, which can be associated with the presence of oxygen-deficient Zr_3O compounds and phenomena associated with the presence of oxygen vacancies. The enhancement and small shifts of these bands, especially in the samples with higher Zr_3O content and predominant tetragonal phase, indicate distortions of the oxygen sublattice. Such spectral features should be due to vibrations of Zr–O bonds in the presence of oxygen vacancies and defect complexes formed under oxygen-deficient synthesis conditions. Thus, combining the phase analysis (confirming the presence of oxygen-deficient Zr_3O phases) with the observed changes in the FTIR bands, we concluded that the spectra reflect structural defects and oxygen vacancies in the material. Thus, the FTIR analysis, confirmed by the phase composition of the samples, reveals the presence of hydroxyl and carbonate groups on the surface of the nanoparticles and also indicates possible structural defects and oxygen formations, especially in the samples with high Zr_3O content.

The photoluminescence spectra of all three samples (N30, N60, N90) upon excitation at 280 nm demonstrate a similar structure: in the blue region (400–500 nm), a maximum is stably recorded in the region of 443–446 nm, and in the green region (500–600 nm), a wide maximum at about 515–520 nm. In the ultraviolet range (320–400 nm), comparatively weaker emission is observed, and in the red zone (>600 nm), a smooth decreasing "tail" is formed.

Sample N30 (Fig. 5) is characterized by a pronounced blue band with a maximum at about 445 nm, smoothly turning into the green region with a maximum at ∼520 nm; the relative contribution of the visible range within the spectrum itself prevails over the UV component, which indicates the dominance of bandless recombination paths through defect centers [18].

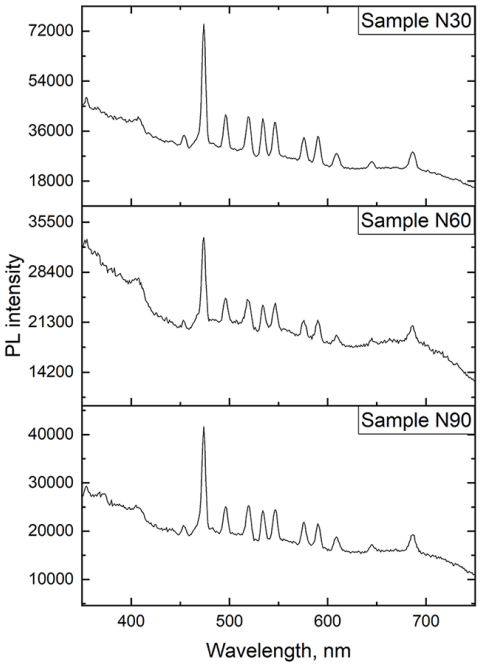

Fig. 5. Photoluminescence spectra of ZrO_{2-x} nanoparticles obtained at different pressures of the gas mixture.

The spectrum of sample N60 is generally identical in shape to samples N30/N90 (the same maxima at ∼445 nm and ∼515 nm), while within the spectrum itself the UV component appears somewhat more noticeable relative to the visible part, which gently hints at a larger share of near-band transitions with an unchanged set of luminescence centers.

The spectrum of sample N90 also reproduces the general picture with maxima at ∼443–446 nm (blue zone) and ∼515 nm (green zone) and a smooth red tail; relative to its own UV part, it is close to N30, but may demonstrate a slightly more pronounced short-wave contribution.

Taken together, this indicates that the main emitting centers of the samples are the same (coinciding positions of the maxima in the blue and green regions), and the differences are carefully expressed, quantitative in nature and concern mainly the internal shares of the UV and visible components within each spectrum.

Comparative analysis of the impedance spectra, phase angle and specific conductivity of three vacuum-arc synthesized ZrO_{2-x} nanopowders (Figs/ 6, 7) — sample N30 (t-ZrO_2 90%, Zr_2O 9%), sample N60 (t-ZrO_2 75%, m-ZrO_2 10%, Zr_3O 15%) and sample N90 (t-ZrO_2 52%, m-ZrO_2 45%, Zr_3O 3%) — shows that the electrical response is determined by the balance of the bulk conductivity of the tetragonal phase, the barrier properties of grain boundaries associated primarily with the monoclinic component, and the presence of suboxide (quasi-metallic) Zr_3O bridges.

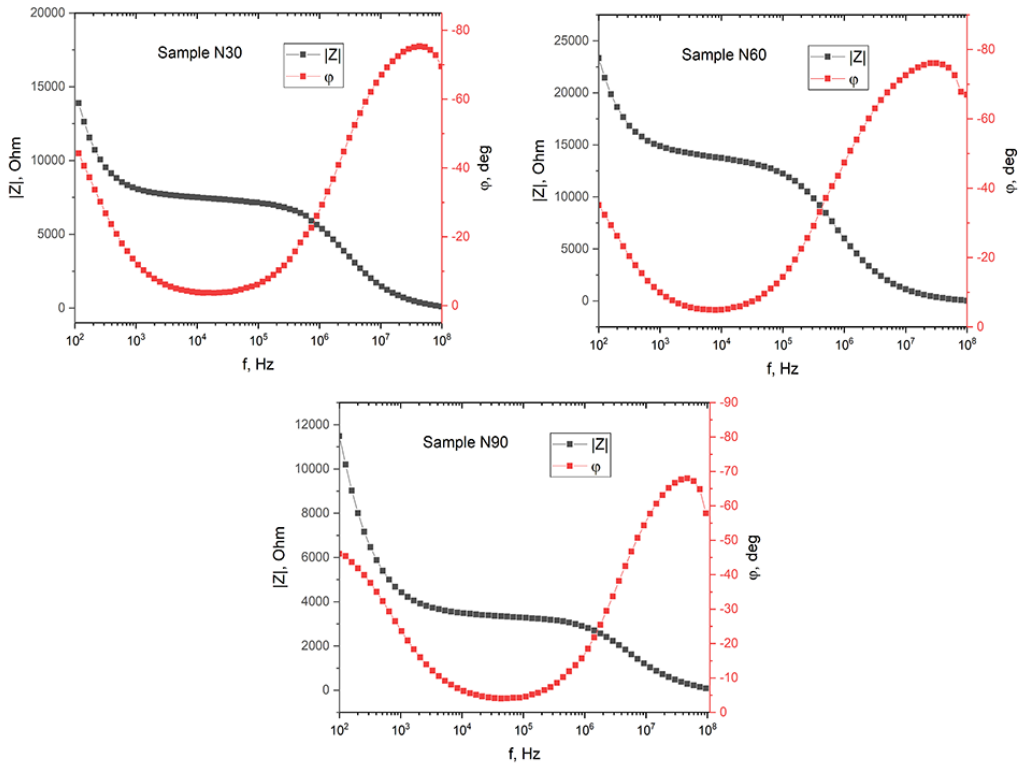

Fig. 6. Frequency dependence of the impedance modulus $|Z|(f)$ and phase (f) of ZrO_{2-x} nanoparticles

At low frequencies, the absolute impedance modulus |Z| is maximum for the most heterophase and "boundary-dominated" sample N60 (about $2.3{\cdot}10^4$ Ohm at 100 Hz), which reflects the high

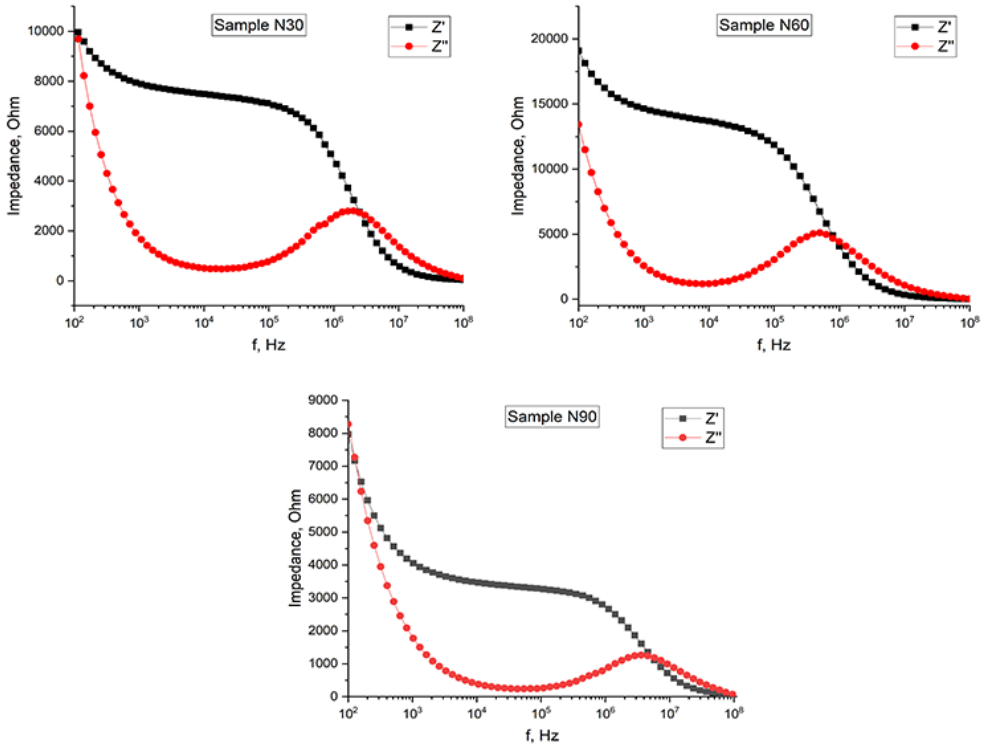

Fig. 7. Frequency dependence of the real (Z') and imaginary (Z") components of the impedance of ZrO_{2-x} nanoparticles

contribution of grain boundary resistance R_{gb} due to the significant proportion of m-ZrO2; followed by sample N30 ($1.4{\cdot}10^4$ Ohm at 100 Hz), which, despite the significant proportion of the conducting phase Zr_3O (9%), retains a noticeable barrier contribution and pronounced polarization at the interfaces; the minimum |Z| is demonstrated by sample N90 ($1.15{\cdot}10^4$ Ohm at 100 Hz), where the high content of t-ZrO_2 and moderate impurity of Zr_3O form relatively continuous transport paths. With increasing frequency, all three materials are characterized by a decrease in Z′ and Z″ (and, accordingly, |Z|), but the "speed" of the transition from the intergranular-limited regime to the bulk regime differs: sample N90 switches to resistive behavior the fastest (φ tends to 0° faster, noticeable "rectification" is already in the MHz range), sample N30 is slower (it retains a more pronounced capacitive character and a "long tail" of dispersion), sample N60 occupies an intermediate position.

The impedance phase confirms this picture: for sample N90 at low frequencies φ is about –46° (strong capacitive component due to Maxwell–Wagner interfacial polarization) [19–21], but with increasing f φ rapidly increases (decreases in absolute value), which indicates the dominance of Rbulk of the tetragonal matrix; for sample N60 φ starts less negative (about 35° at 100 Hz), which is consistent with more "resistive" grain boundaries, but retains noticeable dispersion effects wider in frequency, reflecting the heterogeneity of the contact areas of the t/m phases and the statistics of the barriers; for sample N30 φ is close to –40 . . . –45° at low f, similar to sample N90, but further evolution is less rapid due to competition: Zr_3O accelerates the

resistive response, while increased heterogeneity enhances the CPE behavior. The real part of the specific conductivity $\sigma'(\omega)$ for all samples increases monotonically with frequency and is well described by the Jonscher law $\sigma(\omega)=\sigma_{dc}+A^n$: at low f σ' is small and is determined primarily by tunneling/activation through R_{gb} (boundaries control the transport), at high f bulk transport in t-ZrO_2 begins to dominate with the participation of oxygen vacancies and local states of Zr^{3+}, and a steeper rise in σ' is observed for samples with Zr_3O due to shunting paths. In terms of conductivity ranking over the entire frequency range, sample N90 leads (the highest σ'), followed by sample N30 (which is associated with increased R_{gb}) and sample N60 closes (high σ' at high f due to 15% Zr_3O, but more noticeable interfacial polarization at low f). The imaginary part of $\sigma''(\omega)$ also increases with frequency and reflects dielectric losses: for sample N60 it is relatively higher over a wide range due to the distribution of relaxation times, for sample N90 it is more quickly "displaced" by bulk conductivity, and for sample N30 a balance is formed between interface losses and resistive shunting.

As a result, sample N90 is optimal for the transition to high-frequency bulk conductivity (Fig. 8) (minimum losses and the least intergranular confinement), sample N60 exhibits the most pronounced interfacial polarization and high barriers (the largest $|Z|$ and the smallest σ' at low f), and sample N30 combines accelerated high-frequency transport (due to 9% Zr_3O) with preserved dispersion and CPE behavior due to structural heterogeneity.

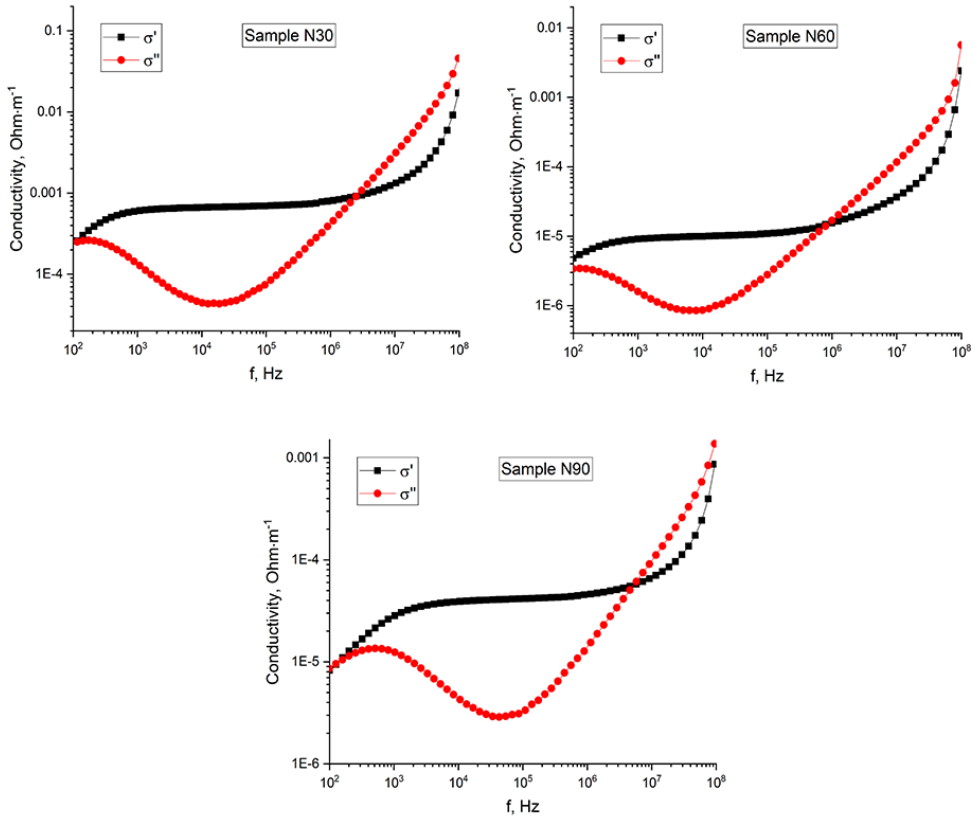

Fig. 8. Frequency dependence of the real (σ') and imaginary (σ'') components of the conductivity of ZrO_{2-x} nanoparticles

Thus, the study of the impedance characteristics of three zirconium dioxide nanopowders synthesized under vacuum-arc discharge conditions showed that the electrical response of the system is determined not only by the ratio of the phase components, but also by the synthesis parameters, in particular, the gas pressure in the vacuum chamber. At reduced pressure, a more reducing environment is formed, promoting the formation of Zr_3O suboxide, which plays the role of conducting shunts, reducing intergranular barriers and accelerating the transition to bulk conductivity; this explains the increased Zr_3O content and accelerated high-frequency response in sample N30. On the contrary, at higher gas pressure, intense oxidation of particles in the plasma and stabilization of the monoclinic modification occur, which leads to an increase in the proportion of m-ZrO_2 and an increase in the barrier properties of grain boundaries – characteristic of sample N60, where the impedance was maximum and the conductivity was minimum. Further increase in pressure (sample N90) ensures the predominance of the tetragonal phase with small inclusions of suboxide, which leads to the formation of an optimal combination of phases: a high proportion of t-ZrO_2 provides effective volume transport, and a moderate admixture of Zr_3O creates additional transport paths without excessive heterogeneity. As a result, it was sample N90 that demonstrated the lowest impedance over the entire frequency range, while sample N60 showed a pronounced CPE behavior, and N30 occupied an intermediate position, where low pressure enhanced the suboxide component and determined a combination of accelerated high-frequency response with preserved polarization dispersion.

The study was carried out with the help of the grant of the Russian Science Foundation no. 24-29-00374, https://rscf.ru/project/24-29-00374/.

References

[1] N.Kumari, S.Sareen, M.Verma, S.Sharma, A.Sharma, H.S.Sohal, S.K.Mehta, J.Park, V.Mutreja, Zirconia-based nanomaterials: recent developments in synthesis and applications, *Nanoscale Adv.*, **4**(2022), 4210–4236. DOI: 10.1039/D2NA00367H

[2] S.Liu, J.Wang, Y.Chen, Z.Song, B.Han, H.Wu, T.Zhang, M.Liu, Tetragonal Nanosized Zirconia: Hydrothermal Synthesis and Its Performance as a Promising Ceramic Reinforcement, *Inorganics*, **11**(2023), 217. DOI: 10.3390/inorganics11050217

[3] J.Zhang, H.Sun, L.Shu, L.Huang, et al., Fabrication of YSZ ceramic thin films with sol-gel method for mixed potential-type zirconia-based NO_2 sensor, *Ceramics International*, **50**(2024), 10698-10705.

[4] F.C.Antunes, J.P.J. De Oliveira, J.R.Verza, et al., Boosting ionic conductivity of Y_2O_3 co-doped ZrO_2 – CeO_2 electrolyte of SOFCs by successive thermal-treatments, *Ceramics International*, **51**(2025), 6815–6823. DOI: 10.1016/j.ceramint.2025.05.051

[5] D.R.Islamov, V.A.Gritsenko, T.V.Perevalov, V.Sh.Aliev, V.A.Nadolinny, A.Chin, Oxygen vacancies in zirconium oxide as the blue luminescence centres and traps responsible for charge transport: Part II-Films, *Materialia*, **15**(2021), 100980.
DOI: 10.1016/j.mtla.2020.100980

[6] Y.Mostafa, Y Bilge, Intrinsic point-defect equilibria in tetragonal ZrO_2: Density functional theory analysis with finite-temperature effects, *Phys. Rev. B*, **86**(2012), 144109.
DOI: 10.1103/PhysRevB.86.144109

[7] Y.Garanin, R.Shakirzyanov, D.Borgekov, A.Kozlovskiy, N.Volodina, D.Shlimas, M.Zdorovets, Study of morphology, phase composition, optical properties, and thermal stability of hydrothermal zirconium dioxide synthesized at low temperatures, *Sci. Rep.*, **14**(2024), 29398. DOI: 10.1038/s41598-024-80399-x

[8] E.Martin, U.C.Chung, M.Duttine, et al., Defect chemistry to trigger zirconia densification at low temperatures by Spark Plasma Sintering, *Open Ceramics*, **17**(2024), 100518.

[9] C.B.Martinez, J.L.V.Arce, A.K.C.Gallegos, H.Tiznado, Enhanced oxygen sensing in ZrO2 thin films via atomic layer deposition by post-deposition annealing, *Ceramics International*, **51**(2025), 9464–9471.

[10] D.Malgorzata, R.Piech, B.Paczosa-Bator, Electrochemical Impedance Spectroscopy Study of Ceria- and Zirconia-Based Solid Electrolytes for Application Purposes in Fuel Cells and Gas Sensors, *Materials*, **17**(2024), 5224. DOI: 10.3390/ma17215224

[11] G.Dutta, K.P.S.S.Hembram, G.Mohan Rao, U.V.Waghmare, Effects of O vacancies and C doping on dielectric properties of: A first-principles study, *Appl. Phys. Lett.*, **89**(2006), 202904.

[12] X.Junan, Z.Zhu, H.Tao, S.Zhou, Z.Liang, Z.Li, R.Yao, Y.Wang, H.Ning, J.Peng, Research Progress of High Dielectric Constant Zirconia-Based Materials for Gate Dielectric Application, *Coatings*, **10**(2020), 698. DOI: 10.3390/coatings10070698

[13] I.V.Karpov, L.Yu.Fedorov, A.K.Abkaryan, S.M.Zharkov, M.S.Molokeev, A.A.Ivanenko, I.V.Nemtsev, L.A.Irtyugo, Resistive switching properties of a nanostructured layer of mixed ZrO_2 phases obtained in low-pressure arc discharge plasma, *Vacuum*, **227**(2024), 113375. DOI: 10.2139/ssrn.4803212

[14] A.V. Uschakov, I.V. Karpov, A.A. Lepeshev, M.I. Petrov, Plasma-chemical synthesis of copper oxide nanoparticles in a low-pressure arc discharge, *Vacuum*, **133**(2016), 25–30. DOI:10.1016/j.vacuum.2016.08.007

[15] I.V.Karpov, A.V.Ushakov, A.A.Lepeshev, L.Yu.Fedorov, Plasma-chemical reactor based on a low-pressure pulsed arc discharge for synthesis of nanopowders, *Tech. Phys.*, **62**(2017), 168–173. DOI: 10.1134/S106378421701011X

[16] Bruker AXS TOPAS V4, General Profile and Structure Analysis Software for Powder Diffraction Data, User's Manual, Bruker AXS, Karlsruhe, Germany, 2008.

[17] G.A.Mesyats, N.M.Zubarev, The Rayleigh-Plateau instability and jet formation during the extrusion of liquid metal from craters in a vacuum arc cathode spot, *J. Appl. Phys.*, **117**(2015), 043302. DOI: 10.1063/1.4906559

[18] G.K.Sidhu, A.K.Kaushik, S.Rana, S.Bhansali, R.Kumar, Photoluminescence quenching of Zirconia nanoparticle by surface modification, *Applied Surface Science*, **334**(2015), 216–221. DOI: 10.1016/j.apsusc.2014.10.036

[19] D.Nuzhnyy, J.Petzelt, I.Rychetsky, G.Trefalt, Effective dielectric function of porous $Pb(Mg_1/3Nb_2/3)O_3$ ceramics, *Phys. Rev. B*, **89**(2014), 214307. DOI: 10.1103/PhysRevB.89.214307

[20] X.D.Liu, Z.L.Hou, B.X.Zhang, K.T.Zhan, P.He, K.L.Zhang, W.L.Song, A general model of dielectric constant for porous materials, *Appl. Phys. Lett.*, **108**(2016), 102902.

[21] Z.N Wing, J.W.Halloran, Dielectric loss in porous TiO_2, *Ceramics International*, **43**(2017), 4618–4621.

Импедансные характеристики и фазозависимая проводимость нанопорошков ZrO_{2-x}, полученных вакуумно-дуговым синтезом

Игорь В. Карпов
Леонид Ю. Федоров
Сибирский федеральный университет
Красноярск, Российская Федерация
Федеральный исследовательский центр КНЦ СО РАН
Красноярск, Российская Федерация
Евгения А Слюсарева
Сибирский федеральный университет
Красноярск, Российская Федерация
Александр В. Павлов
Алексей И. Лямкин
Сибирский федеральный университет
Красноярск, Российская Федерация
Федеральный исследовательский центр КНЦ СО РАН
Красноярск, Российская Федерация
Альмира М. Жилкашинова
Восточно-Казахстанский технический университет им. Д. Серикбаева
Усть-Каменогорск, Республика Казахстан

Аннотация. В работе представлены результаты исследования диэлектрических характеристик нестабилизированного нанопорошка диоксида циркония (ZrO_{2-x}), полученного методом вакуумно-дугового осаждения при различных давлениях аргоно-кислородной плазмы. Проведён комплексный анализ фазового состава, морфологии, фотолюминесцентных свойств и импедансных характеристик трёх образцов, различающихся по содержанию тетрагональной, моноклинной и субоксидной фаз. Установлено, что электрический отклик материалов определяется взаимодействием объёмной проводимости тетрагональной матрицы, барьерных эффектов межзеренных границ (особенно в присутствии m-ZrO_2) и шунтирующего влияния проводящей фазы Zr_3O. Образец с наименьшим содержанием тетрагональной фазы демонстрирует минимальный импеданс, тогда как наиболее гетерофазный состав характеризуется выраженной межфазной поляризацией и высокими диэлектрическими потерями.

Ключевые слова: оксид циркония, вакуумная дуга, физическое осаждение из паровой фазы, фазовая стабильность.

EDN: CGXTDZ
УДК 532.517

Numerical Study of Flow and Heat Transfer in a Single-Row Bundle of Horizontal Finned Tubes Under Conditions of Air Thermogravitational Convection

Marina A. Zasimova*
Alexey G. Abramov†
Aleksei A. Pozhilov‡
Anastasiya V. Filatova§
Peter the Great St. Petersburg Polytechnic University
St. Petersburg, Russian Federation
Galina S. Marshalova¶
Institute of Heat and Mass Transfer named
after A. V. Lykov of the NAS of Belarus
Belarusian State Technological University
Minsk, Republic of Belarus

Received 10.07.2025, received in revised form 26.08.2025, accepted 27.10.2025

Abstract. The results of numerical modeling of airflow and heat transfer in a horizontally oriented single-row bundle consisting of six finned heated tubes under thermogravitational conditions are presented. The study is performed for the bundles with a compact tube arrangement and varying fin pitch. The cases without and with the rectangular exhaust shafts of different heights installed above the bundle have been investigated. For the most compact bundle configuration in the absence of a shaft in the considered range of moderate values of the Grashof number (up to 5.5×10^5), a good agreement was obtained between the calculated integral Nusselt number at the tube surface and experimental data taken from the literature. The combination of the fin pitch (spatial arrangement on the tubes) and the shaft height determined in computations allowed to obtain the optimal bundle design with the highest intensity of heat removal.

Keywords: air-cooling, heat exchangers, tube bundles, finned tubes, fin pitch, exhaust shaft, thermogravitational convection, numerical simulation.

Citation: M.A. Zasimova, A.G. Abramov, A.A. Pozhilov, A.V. Filatova, G.S. Marshalova, Numerical Study of Flow and Heat Transfer in a Single-Row Bundle of Horizontal Finned Tubes Under Conditions of Air Thermogravitational Convection, J. Sib. Fed. Univ. Math. Phys., 2026, 19(1), 50–59. EDN: CGXTDZ.

Introduction

Air-cooled heat exchangers that operate in a passive mode, devoid of forcing mechanisms, under natural convection circumstances are extensively utilized in practice, ensuring process

*zasimova_ma@mail.ru https://orcid.org/0000-0002-4103-6574
†abramov@runnet.ru https://orcid.org/0000-0002-5186-957X
‡aapozhilov@mail.ru https://orcid.org/0009-0005-2458-7533
§filatova3.av@edu.spbstu.ru
¶galiana.sidorik@gmail.com https://orcid.org/0000-0003-4635-6144

dependability and cost-effectiveness [1]. The most commonly used heat exchangers consist of tube bundles with external fins.

The intensity of heat transfer from the tube surfaces is influenced to a large extent by thermal conditions and the geometric characteristics of the bundle, including its design as well as the shape and positioning of the fins. The efficiency of heat exchangers can be noticeably enhanced by placing an exhaust shaft above it, which leads to strengthening the flow adjacent to the tube surfaces. The challenge of choosing the best finning configuration and tube arrangement in bundles is always relevant due to the large range of technologies and operational conditions.

In recent decades, the long-dominant analytical approaches have been largely replaced by experimental and numerical studies on the problem of horizontally oriented finned tubes in the free convection mode using up-to-date methods and tools [1]. The related research has been mainly focused on single tubes with different geometric configurations and thermal conditions.

A number of experimental studies were aimed at investigations of the influence of the diameter of carrying tubes and fins, the number of fins, fin spacings and shapes, and the operating Rayleigh number on integral heat transfer rate (see, for example, [2, 3]). Based on the measurement results, generalized correlations have been proposed for calculating the mean Nusselt number depending on the geometric parameters and the Rayleigh number. Only a few experiments have studied features of local heat transfer in the inter-fin gaps with varying fin diameter, shape and spacing [4, 5].

A series of thorough experimental studies were devoted to tube bundles consisting of industrial finned tubes located in a free space (for example, [6–8] and links in them). The influence of the temperature difference between the tube base and ambient air, the longitudinal and transversal distances between tubes, the number of rows in the bundles, and the finning factor on the mean Nusselt number was analyzed.

The results of relatively recent experimental investigations for tube bundles with different numbers of rows and with an exhaust shaft are presented, in particular, in [9, 10]; the effects of the Rayleigh number, inter-tube and inter-fin spacing, the finning factor and shaft height on the mean Nusselt number and some local heat transfer characteristics were explored.

Numerical studies of free-convective heat transfer from a single horizontal finned tube have become relatively widespread since the 2010s. The calculations were based mainly on simplified spatial settings and stationary conditions; the values of the regime criteria and the geometric parameters of the tubes and fins were varied in order to discover optimal design with the best heat transfer properties [11–13].

The work [14] contains some key results of unsteady computations of laminar free convective flow and heat transfer in a single-row tube bundle, performed at a modern level on fairly detailed grids with varying transversal tube pitch and the temperature difference between the carrying tube and ambient air, performed under conditions close to the experiments [8]. In addition to comparison with the experiments on the mean Nusselt number, special attention has been paid to local features of the velocity and temperature fields and their influence on the integral characteristics.

The results of a numerical study of the influence of an exhaust shaft on the flow structure, local and integral heat exchange during unsteady thermogravitational airflow through a double-row bundle of finned tubes are given in [15]. Relevant experimental data on the values of the mean Nusselt number have been obtained in [10], showing that the installation of the shaft entails an increase in the intensity of heat removal up to three times.

Thus, numerical studies that systematically model the flow and heat transfer in tube bundles

with an emphasis on subtle local effects with a joint assessment of the influence on processes of such parameters as the inter-fin distance, thermal conditions, and the presence of an exhaust shaft of different heights above the bundle are very limited.

The present paper is focused on investigations of thermogravitational airflow near a horizontal single-row tube bundle consisting of six heated finned tubes at moderate values of the Grashof number (up to 5.5×10^5). Numerical modeling of the airflow and heat transfer is carried out for the cases with different geometrical configurations of the tube bundles (various fin pitches) and different heights of a rectangular exhaust shaft that was installed above the bundles. For the case without a shaft and with the most compact configuration of the bundles, the comparison with experimental data [8] on integral heat transfer rate in the considered range of the Grashof number values is performed.

1. Problem formulation and computational aspects

1.1. Geometrical model

The computational domain for the problem examined is presented in Fig. 1a,b. The single-row tube bundle consists of six horizontally oriented identical tubes. It is assumed that the bundle is unlimited in the axial direction, and the flow is periodic in the z-direction with the fin pitch. Additionally, the flow is considered symmetrical with respect to the middle plane of the inter-fin gap.

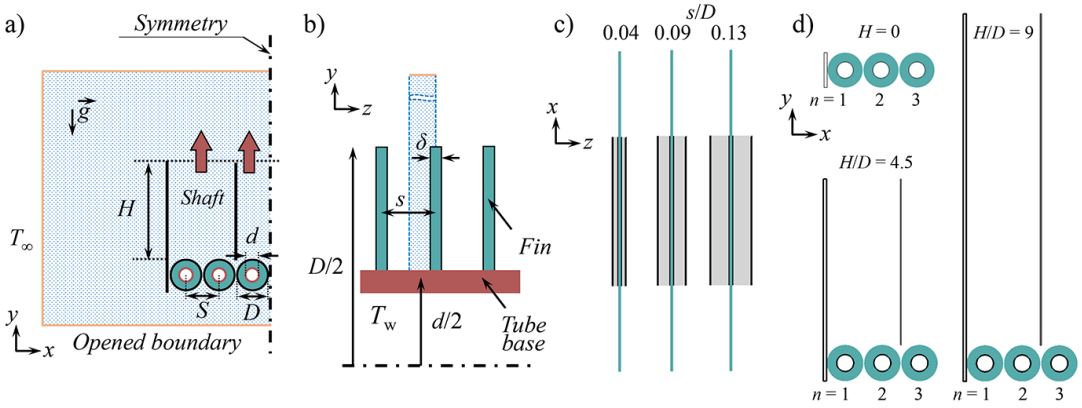

Fig. 1. The computational domain shown in two planes: a) z = Const and b) x = Const; the cases with different geometrical configurations of the tube bundle, variable parameter: c) the fin pitch (s/D) and d) the shaft height (H/D)

The following geometrical parameters of the tube bundle were set. The external diameter of the carrying tube was equal to d = 26.4 mm, the diameter of the solid aluminum fins was $D = 2.15d$, the transversal distance between tubes S corresponded to the dimensionless parameter $\sigma = S/D = 1.02$, and the fin thickness $\delta = 0.01D$. The fin pitch along the tube s was varied from $s_0 = 0.04D$ (the most compact configuration of the bundle) to $0.13D$ (Fig. 1c). Calculations with different tube bundle fashions were carried out both for the cases with a rectangular exhaust shaft installed above the bundle (the height H was equal to $4.5D$ and $9D$) and for the cases without

a shaft ($H = 0$). Schemes of the computational domain for the cases with different values of H are shown in Fig. 1d. The shaft contains a plane wall (barrier) located above the tubes with the numbers $n = 2$ and $n = 3$ (n is counted from the bundle side) to prevent the large-scale upward airflow.

The computational setup includes a side plate that is located near the bundle and prevents global airflow movement in the x-direction (Fig. 1d, case $H = 0$). The width and the height of the plate were about $D \times 0.09D$. The boundaries far from the tube bundle are located at least at a distance of $6D$ from the bundle and the shaft.

Note that the geometrical configuration with the most dense arrangement of the fins ($s = s_0$) without a shaft is close to that considered in the experimental research [8].

1.2. Boundary conditions

The following conditions were set for the problem at the boundaries of the computational domain. The boundaries far from the tube bundle were open; the ambient air temperature was imposed to $T_0 = 22.1°\mathrm{C}$ on them. The temperature of the tube base, T_w, was assumed to be constant and varied from 37 to 244°C. The corresponding values of the relative temperature difference (the buoyancy parameter) $\varepsilon_T = (T_w - T_0)/T_0$ varied from 0.05 to 0.7. The values of buoyancy velocity estimated as $V_b = (g\varepsilon_T d)^{0.5}$ were in the range $12 \ldots 44$ cm/s. The values of the Grashof number $Gr = (\rho V_b d/\mu)^2$ varied from $3.7{\times}10^4$ to $5.5{\times}10^5$, and the dynamic viscosity μ and density ρ of air were taken at the ambient temperature T_0. The values of the Rayleigh number $Ra = Gr{\cdot}Pr$ were in the range of $2.6{\times}10^4$ to $3.9{\times}10^5$, and the Prandtl number was $Pr = 0.7$. The given values indicate that the airflow near the tube bundle was laminar.

The side plate and the shaft with the barrier (Fig. 1d) were considered to be thermally insulated; at these boundaries the no-slip conditions were set.

1.3. Mathematical model and computational aspects

The numerical simulation is carried out on the basis of the Navier–Stokes system of governing equations, written for a perfect viscous gas with variable physical properties. The problem was solved in a conjugate formulation: heat transfer along the fins of the tubes was calculated together with the flow.

The unstructured grids consist of hexahedral elements that clustered to the wall surfaces were used. The size of the grids was varied from 140 ($H = 0$) to 300 ($H = 9D$) thousand cells. Automatic generation of computational grids for the cases with various geometrical parameters was organized using ANSYS Meshing. Computations have been performed using the CFD package ANSYS Fluent. The spatial discretization was done with the second-order upwind scheme for convective terms, and also the second-order pressure interpolation method was assigned.

The second-order implicit time integration scheme was applied. The time step was equal to 0.02 s, and it was chosen to provide the values of the Courant number less than 1. The duration of the processed sample, related to the statistically steady flow regime, was about 120 s, which for all the cases provided at least 540 characteristic times, estimated as $t_s = d/V_b$.

2. Results and discussion

2.1. Airflow structure inside the tube bundle: influence of the fin spacing

Typical airflow structure that forms near the tube bundle is shown in Fig. 2a using visualizations of the dimensionless velocity V/V_b and temperature $T^* = (T - T_0)/(T_w - T_0)$ fields in the middle section of the inter-fin space for the most compact geometrical configuration ($s = s_0$) and at $\varepsilon_T = 0.7$ ($Gr = 5.5{\times}10^5$). Note that for all the cases considered, the flow near the tube bundle is significantly unsteady. The thermal plume formed above the bundle periodically (approximately once every half of the time period, t_s) detached from the surface of the tubes. The fields and integral characteristics of heat transfer presented and discussed in the paper are averaged in time.

Under the action of buoyancy forces, the air below the bundle moves towards the heated tubes with area-averaged velocity values of about $V_{in} = 0.09V_b$ (the corresponding value of the Reynolds number $Re = \rho V_{in} d/\mu = 68$), passes through the inter-fin space of the tubes, where the values of velocity locally reach $0.4V_b$, and the inter-tube gap with the higher values of about $1.2V_b$. Above the tube bundle, the area of the increased velocity and temperature values take place, reflecting the presence of the thermal plume. In the inter-fin space, the temperature field is almost uniform.

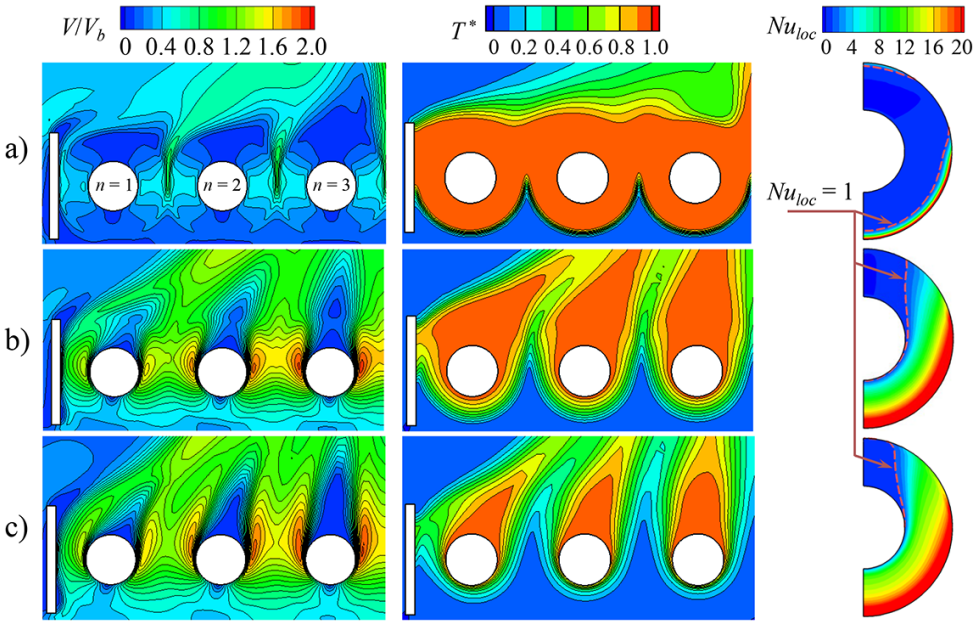

Fig. 2. Distributions of velocity magnitude (left column) and temperature (middle column) in the plane passing through the middle section of the inter-fin space and the local Nusselt number at the wall surface for $n = 3$ (right column) for the cases with different fin spacing s/D: a) 0.04, b) 0.09 and c) 0.13, for all the cases — $\varepsilon_T = 0.7$, $H = 0$

In the absence of a shaft, increasing the fin pitch by two times or more noticeably intensifies the airflow in the tube bundle and above it (Fig. 2). For the case with increased fin pitch,

the values of velocity in the bundle are comparable with buoyancy velocity. The Reynolds number for the case with $s/D = 0.09$ is equal to $Re = 240\,(V_{in} = 0.33V_b)$, and for the case with $s/D = 0.13 - Re = 305\,(V_{in} = 0.41V_b)$. The temperature field in the tube bundle has become spatially non-uniform.

2.2. Heat transfer parameters of the tubes: influence of the fin spacing

The distributions of a local Nusselt number $Nu_{loc} = q_{w,loc}\,d\,/\lambda\,(T_s - T_0)$ at the surface of the fins are presented in Fig. 2 (right column) for the cases with different fin spacing and at $\varepsilon_T = 0.7$. In this formula, $q_{w,loc}$ is the local heat flux, T_s is the local fin surface temperature, and the thermal conductivity coefficient was calculated based on the ambient temperature (the value of $\lambda = 0.0261$ W/(mK) was taken). In the absence of a shaft, very low efficiency of the fin surface takes place for the case with the most compact configuration (Fig. 2a): heat removal is realized mainly from the periphery of the fins (indicated by dashed lines), and the contribution of their inner part is relatively small. The low efficiency occurs due to uniform temperature distribution in the inter-fin space.

With an increase in the inter-fin pitch, the values of the local Nusselt number are also increased noticeably (Fig. 2). The integral (averaged over the tube bundle surfaces) values of the Nusselt number $<Nu>$ related to the value of s/s_0 for the cases with different fin pitch and values of the buoyancy parameter are shown in Fig. 3a. It has been established that by varying the fin pitch, it is possible to escalate the effective heat transfer from the tube bundle surface by more than two times compared to the configuration with the largest number of the fins. The optimal (among those considered) fin pitch with the maximum value of the effective Nusselt number depends on the buoyancy parameter, and it is observed for the cases with $s/D = 0.09$ at $0.2 \leqslant \varepsilon_T \leqslant 0.7$ and for the case with $s/D = 0.11$ at a fixed $\varepsilon_T = 0.05$.

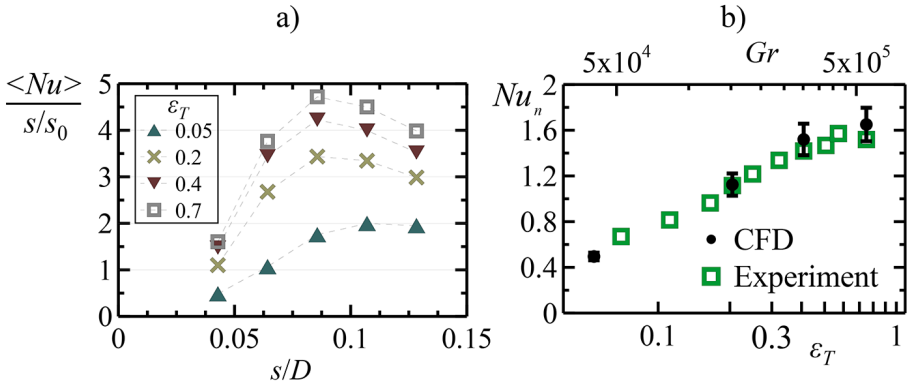

Fig. 3. a) The effective Nusselt number for the cases with different fin spacing at $H = 0$, b) comparison of computational and experimental [8] data on Nu_n values dependent on the Grashof number, the case with $s/D = 0.04$, $H = 0$

For the case without a shaft and with the most compact configuration of the tube bundle, the comparison with experimental data available from the literature [8] has been performed. Fig. 3b presents the experimental (for the tube with $n = 3$) and computational (indicated as "CFD") data of the Nusselt number $Nu_n = <q_{w,n}>\,d\,/\lambda\,(T_w - T_0)$, where $<q_{w,n}>$ is the mean heat flux

over the surface of tube n. CFD data plotted in the range of Nu_n values for the tubes with the numbers $n = 1$, 2 and 3.

The values of dimensionless heat transfer obtained in calculations, averaged over the surface of the middle tube of the bundle, are in good agreement with the experimental data in the examined range of the Grashof number. Computations show that for the side tube (with $n = 1$), the value of Nu_n is noticeably lower than for the central tube (with $n = 3$); maximum differences in Nu_n values are detected for the case with $\varepsilon_T = 0.7$ and reach 24%.

2.3. Effects of the shaft height

In the presence of the shaft, the airflow through the bundle is significantly more intense in the region above the bundle, as expected, and less concentrated near the symmetry boundary. The flow distribution for the case with $s = s_0$ is presented in Fig. 4a,b for $H/D = 4.5$ and 9, correspondingly. The volume flow rate under the bundle increases with the growth of the H/D ratio, and it corresponds to the values of the Reynolds number $Re = 260$, $V_{in} = 0.35\,V_b$ ($H/D = 4.5$), and $Re = 440$, $V_{in} = 0.6V_b$ ($H/D = 9$). The maximum values of the velocity in the tube bundle significantly exceed V_b.

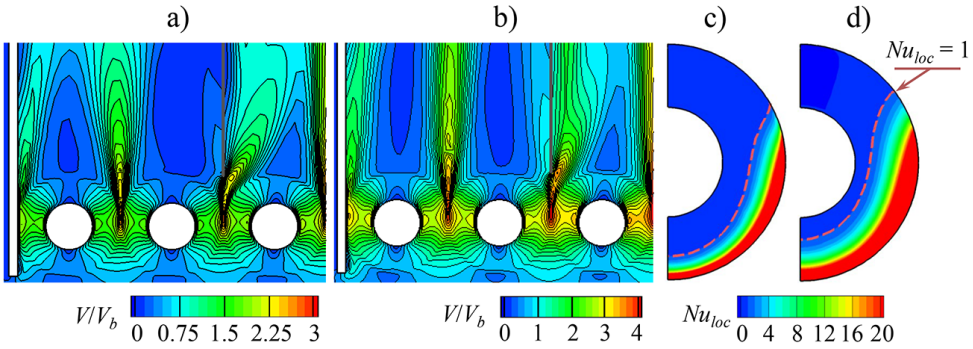

Fig. 4. a,b) Distributions of the velocity magnitude in the plane passing through the middle section and c,*d*) the local Nusselt number at the wall surface for $n = 3$ for the cases with different shaft height H/D: a,c) 4.5, b,d) 9, for all the cases – $s = s_0$, $\varepsilon_T = 0.7$

Figs. 4c,*d* show the distributions of the local Nusselt number (Nu_{loc}) over the surface of the fin (for the tube with $n = 3$), calculated for the cases with different H/D ratios. The area of the fin with $Nu_{loc} > 1$ (indicated by the dashed line) significantly increases with increasing the height of the shaft. The values of the mean effective Nusselt number for the cases with different heights of the shaft and by varying the buoyancy parameter are presented in Fig. 5.

The effective Nusselt number for the most compact bundle increases by about three times for the case with the shaft height of $H/D = 4.5$ and by six times for the case with $H/D = 9$. For the optimal fin pitch ($s/D = 0.09$), the shaft encourages the Nu number to increase by two times for the case with $H/D = 9$ and by one and a half for the case with $H/D = 4.5$. A further increase in fin pitch leads to a relatively small effect of the shaft: shaft installation whose height is 10 times greater than the diameter of the fins leads to an increase in the Nusselt number by only 1.5 times. Data on the effective Nusselt number for the cases with the shaft demonstrates that the most compact configuration with the densest arrangement of the fins becomes well suited for

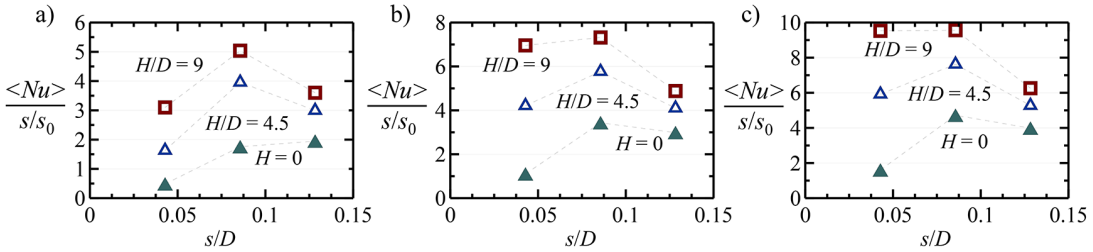

Fig. 5. The mean effective Nusselt number for the cases with different shaft height and fin spacing; the buoyancy parameter ε_T: a) 0.05, b) 0.2 and c) 0.7

the shaft with the height $H/D \geqslant 9$. Among the considered cases, the optimal value of the fin pitch is $s/D = 0.09$, since it provides the highest level of heat removal in a wide range of values of the buoyancy parameter ε_T and shaft height H.

Conclusion

Numerical modeling of the airflow and heat transfer in the single-row bundle of heated finned tubes under the action of free convective forces was carried out. The cases without and with the shaft installation above the tube bundle were considered.

The validation of the methods and tools used was performed for the case with the most compact tube bundle configuration: good agreement was obtained between the calculated average heat transfer from the surface of the tube and the experimental data available from the literature in the considered range of the buoyancy parameter (or the Grashof number).

In the absence of a shaft, the flow movement through the bundle with dense tube location is characterized by a relatively low level of velocity fields comparable with the values of buoyancy velocity. The compact tube bundle configuration provided a low level of the effective Nusselt number. The configuration with optimal fin pitch provides the highest values of airflow velocity and the effective Nusselt number.

In order to intensify significantly free convective airflow in the tube bundle, installation of the exhaust shaft could be used. The mean effective Nusselt number for the most compact bundle was greatly increased by increasing the shaft height. The customized combination of the fin pitch (spatial occupancy of the bundle) and the shaft height led to the optimal tube bundle configuration with the highest level of heat removal.

The study was supported by the Russian Science Foundation, grant no. 24-49-10003. Calculations were carried out using computational resources of Peter the Great St. Petersburg Polytechnic University Supercomputing Center (https://scc.spbstu.ru).

References

[1] G.F.Hewitt, Heat exchanger design handbook, 2008.

[2] N.Kayansayan, Thermal characteristics of fin-and-tube heat exchanger cooled by natural convection, *Experimental Thermal and Fluid Science*, **7**(1993), no. 3, 177–188. DOI: 10.1016/0894-1777(93)90001-Y

[3] S.Yildiz, H.Yuncu, An experimental investigation on performance of annular fins on a horizontal cylinder in free convection heat transfer, *Heat and Mass Transfer*, **40**(2004), 239–251. DOI: 10.1007/s00231-002-0404-x

[4] E.Hahne, D.Zhu, Natural convection heat transfer on finned tubes in air, *International Journal of Heat and Mass Transfer*, **37**(1994), 59–63. DOI: 10.1016/0017-9310(94)90009-4

[5] H.T.Chen, W.L.Hsu, Estimation of heat transfer coefficient on the fin of annular-finned tube heat exchangers in natural convection for various fin spacings, *International Journal of Heat and Mass Transfer*, **50**(2007), 1750–1761. DOI: 10.1016/j.ijheatmasstransfer. 2006.10.021

[6] A.V.Novozhilova, Z.G.Maryna, E.A.Lvov, A.Yu.Vereshchagin, Research of horizontal single-row bundles of ribbon finned tubes at free convection, *Journal of Physics: Conference Series*, **1565**(2020), Article ID 012046. DOI:10.1088/1742-6596/1565/1/012046

[7] E.S.Danil'chik, A.B.Sukhotskii, V.B.Kuntysh, Experimental studies of the efficiency of a single-row bundle of bimetallic finned tubes with different finning heights in free convective heat exchange with air, *Power engineering: research, equipment, technology*, **22**(2020), 128–141 (in Russian). DOI: 10.30724/1998-9903-2020-22-5-128-141

[8] G.S.Marshalova, A.B.Sukhotskii, V.B.Kuntysh, Free convection heat transfer on annular-finned tubes and bundles thereof, *Journal of Engineering Physics and Thermophysics*, **96**(2023), no. 4, 1089–1102. DOI: 10.1007/s10891-023-02774-1

[9] B.Unger, M.Beyer, J.Thiele, U.Hampel, Experimental study of the natural convection heat transfer performance for finned oval tubes at different tube tilt angles, *Experimental Thermal and Fluid Science*, **105**(2019), 100–108. DOI: 10.1016/j.expthermflusci.2019.03.016

[10] A.B.Sukhotskii, G.S.Sidorik, Specific of gravity flow of hot air in an air flue over a finned beam, *Thermal Processes in Engineering*, **10**(2018), no. 1–2, 62–70 (in Russian). DOI: 10.1007/s10556-021-00930-z

[11] S.C.Wong, W.Y.Lee, Numerical study on the natural convection from horizontal finned tubes with small and large fin temperature variations, *International Journal of Thermal Sciences*, **138**(2019), 116–123. DOI: 10.1016/j.ijthermalsci.2018.12.042

[12] J.R.Senapati, S.K.Dash, S.Roy, Numerical investigation of natural convection heat transfer over annular finned horizontal cylinder, *International Journal of Heat and Mass Transfer*, **96**(2016), 330–345. DOI: 10.1016/j.ijheatmasstransfer.2016.01.024

[13] A.Kumar, Y.B.Josh, A.K.Nayak, P.K.Vijayan, 3D CFD simulations of air cooled condenser-II: Natural draft around a single finned tube kept in a small chimney, *International Journal of Heat and Mass Transfer*, **92**(2016), 507–522. DOI: 10.1016/j.ijheatmasstransfer.2015.07.136

[14] A.G.Abramov, V.A.Baranov, M.A.Zasimova, A.V.Filatova, Applying machine learning techniques to air-cooled single-row finned tube bundles in free convection scenarios to forecast the amount of heat transfer, *Lobachevskii Journal of Mathematics*, **45**(2024), no. 10, 4858–4873. DOI: 10.1134/S1995080224605654

[15] A.G.Abramov, E.S.Danil'chik, M.A.Zasimova, et al., The influence of an exhaust shaft with dividing partitions on heat exchange during thermogravitational air flow through a two-row

bundle of finned tubes, *Journal of Engineering Physics and Thermophysics*, 2025 (accepted for publication).

Численное исследование течения и теплообмена при термогравитационной конвекции воздуха в однорядном пучке горизонтальных оребренных труб

Марина А. Засимова
Алексей Г. Абрамов
Алексей А. Пожилов
Анастасия В. Филатова
Санкт-Петербургский политехнический университет Петра Великого
Санкт-Петербург, Российская Федерация
Галина С. Маршалова
Институт тепло- и массообмена имени А. В. Лыкова НАН Беларуси
Белорусский государственный технологический университет
Минск, Республика Беларусь

Аннотация. Представлены результаты численного моделирования термогравитационного течения воздуха и теплообмена в горизонтальном однорядном пучке из шести оребренных нагретых труб. Расчеты выполнены для пучка с тесным расположением труб при варьировании шага оребрения. Рассмотрены постановки задач с установленной над пучком вытяжной шахтой прямоугольного сечения разной высоты и без шахты. Для наиболее сжатого пучка без шахты получено хорошее согласие рассчитанного интегрального числа Нуссельта на поверхности несущей трубы с доступными из литературы данными экспериментов в рассмотренном диапазоне умеренных значений числа Грасгофа (до 5.5×10^5). Сочетание шага ребер (пространственного расположения на трубах) и высоты шахты позволяет получить оптимальную конфигурацию пучка с наибольшей интенсивностью отвода тепла.

Ключевые слова: воздушное охлаждение, теплообменные аппараты, трубные пучки, оребренные трубы, межреберное расстояние, вытяжная шахта, термогравитационная конвекция, численное моделирование.

EDN: CLBQRT
УДК 544.032, 53.081.7

Reduction of Boron Oxide on Polycrystalline Al and Sm Substrates

Lev A. Akashev
Institute of Solid State Chemistry UB RAS
Ekaterinburg, Russian Federation
Yulia V. Korkh
M. N. Mikheev Institute of Metal Physics of the UB RAS
Ekaterinburg, Russian Federation
Nikolai A. Popov*
Institute of Solid State Chemistry UB RAS
Ekaterinburg, Russian Federation
Tatiana V. Kuznetsova
M. N. Mikheev Institute of Metal Physics of the UB RAS
Ekaterinburg, Russian Federation
Alla V. Konyukova
Vladimir G. Shevchenko
Institute of Solid State Chemistry UB RAS
Ekaterinburg, Russian Federation

Received 10.07.2025, received in revised form 24.08.2025, accepted 27.09.2025

Abstract. This paper investigates the reduction of boron oxide deposited by vacuum thermal evaporation on aluminum and samarium surfaces using optical methods of Raman spectroscopy (RS) and spectral ellipsometry. Raman peaks corresponding to vibrations of β-rhombohedral boron (β-B).were detected in the spectra of these samples. Spectral ellipsometry was used to determine the optical constants and thickness of the nanoscale boron film in the spectral range from 270 nm to 1000 nm.

Keywords: thin film ellipsometry, Cauchy formula, boron oxide reduction.

Citation: L.A. Akashev, Yu.V. Korkh, N.A. Popov, T.V. Kuznetsova, A.V. Konyukova, V.G. Shevchenko, Reduction of Boron Oxide on Polycrystalline Al and Sm Substrates, J. Sib. Fed. Univ. Math. Phys., 2026, 19(1), 60–64 EDN: CLBQRT.

To obtain the Raman spectra, a Confotec MR200 Raman microscope (SOL Instruments) with excitation wavelength of 532 nm was used. Measurements were performed by 40x objective with a focal length of 0.63 mm. Ellipsometric studies were carried out on a SPEL-7LED spectral automatic ellipsometer (Russia, Fryazino) in the spectral range from 270 nm to 1000 nm (1.24–2.4 eV, incidence angle φ=70°) [1, 2]. A boron oxide film B_2O_3 was deposited on a polished mirror surface of aluminum using the vacuum thermal evaporation method on a VUP-5M unit (Fig. 1).

Ellipsometric measurements of the surface showed that thickness of the obtained B_2O_3 layer on the aluminum substrate is 530–533 nm (Fig. 2). Fig. 2 shows the experimental and theoretical spectra of the ellipsometric angles Δ and Ψ. It turned out that experimental data are best described by spectra corresponding to a two-layer model containing an aluminum substrate and layers of aluminum and boron oxides. In this case, the optical data of the substrate (metal) were taken from [3], the parameters of the natural oxide film of Al_2O_3 were taken from the standard library of the SPEL program, and the dispersion of the optical parameters of the upper boron

*n168@mail.ru https://orcid.org/0000-0002-4976-1295

oxide layer was selected using the Cauchy formula [4]:

$$n_{film.2}(\lambda) = n_m + \mathrm{b}^2/(1/\lambda^2 - 1/\lambda_m^2) \quad (1)$$

$$k_{film.2}(\lambda) = k_m + \mathrm{c}^2/(1/\lambda^2 - 1/\lambda_m^2) \quad (2)$$

where, $n_m = 1.355$ and $k_m = 0.007$ are the refractive index and absorption coefficient at a wavelength of $\lambda_m = 550$ nm, the dd parameter, which introduces correction for the inhomogeneity of thickness of the sample upper film, was equal to 3. The thickness of the natural oxide film on the aluminum surface was 6–7 nm. The refractive index of the sputtered boron oxide turned out to be slightly lower (1.35) than that of a pure bulk B_2O_3 sample, whose refractive index at a wavelength of $\lambda = 500$ nm usually varies in the range of 1.4–1.46. This fact is explained by the hydration processes of the deposited film due to the absorption of water from the air after the sample is extracted from the deposition chamber.

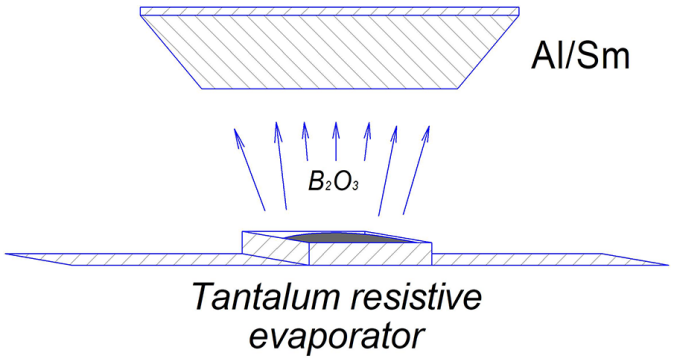

Fig. 1. Scheme of boron oxide deposition on polycrystalline aluminum and samarium using the VUP-5M installation (residual pressure in the chamber is $P = 2 \cdot 10^{-4}$ Pa)

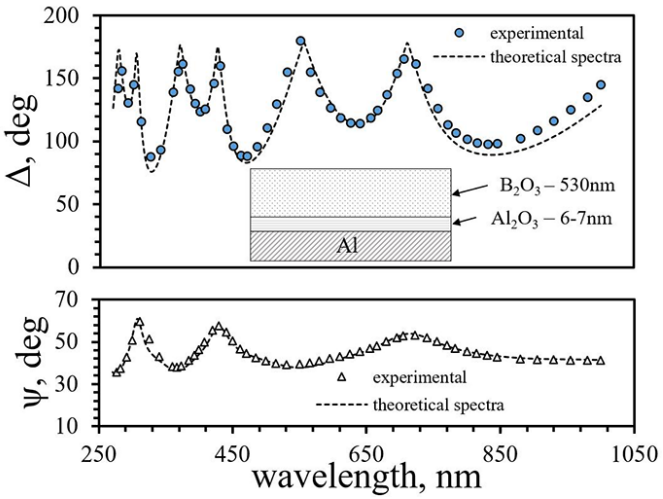

Fig. 2. Model and experimental curves of ellipsometric angles Δ and Ψ of the Al sample surface after deposition of boron oxide

After deposition, the sample was annealed in a vacuum furnace in an argon atmosphere (pressure P = 182 kPa) at a temperature of 630°C for one hour. At a temperature of 480°C, the

boron oxide melted, and upon further heating, a reduction reaction of boron oxide by aluminum occurred on the aluminum surface.

The spectral dependencies of the angles Δ and Ψ, measured on the surface of the sample with an aluminum substrate after annealing in argon, are presented in Fig. 3. As can be seen, the total film thickness has significantly decreased. The experimental dependencies are also described by a model curve for a two-layer structure. In this case, the optical parameters of the bottom layer correspond to an aluminum oxide film with a thickness of approximately 12–13 nm. The top layer corresponds to the optical data of a pure polycrystalline boron film of similar thickness (10–13 nm). The spectra of the optical constants of pure boron used for modeling this structure were obtained by us earlier on a bulk polycrystalline sample [5].

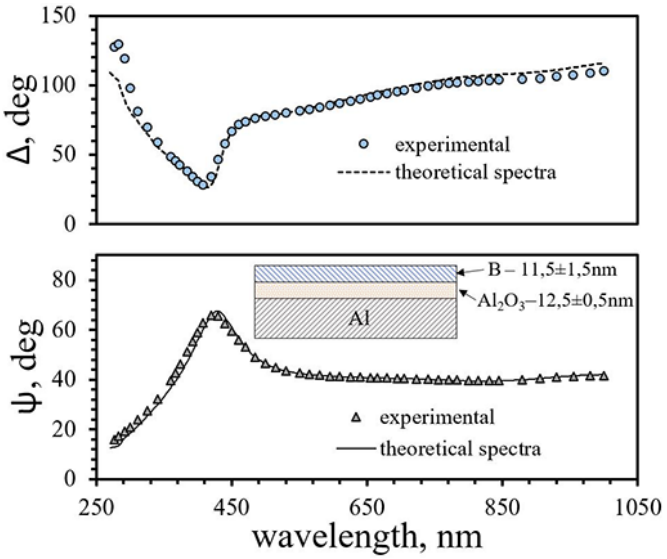

Fig. 3. Model and experimental curves of ellipsometric angles Δ and Ψ of the sample surface after annealing in argon at temperature of 630°C for 60 minutes

Fig. 4 shows the Raman spectra detected on the surface of the sample (the substrate is bulk aluminum). The spectra of this sample contain Raman peaks at frequencies of 186, 349, 532, 570, 995, 1098, and 1210 cm^{-1}, which, according to the literature [6], correspond to vibrations of β-rhombohedral boron (β-B), as well as carbon peaks at frequencies of 1350 and 1615 cm^{-1}, which are also detected in the spectrum of the aluminum substrate. Moreover, compared to the substrate, at some points on the coating surface the peak at 1350 cm^{-1} becomes sharply narrowed and highly intense, indicating a higher degree of carbon ordering.

In the spectra of the bulk aluminum substrate, recorded on the uncoated area of the film sample, numerous Raman scattering peaks were found at frequencies of 338, 405, 488, 565, 656, 747, 822, 909, 1010, 1095 cm^{-1}, which can be attributed to vibrations of Al-O bonds in AlO_4 tetrahedra and AlO_6 octahedra [7–9]. These peaks are also detected on the coating surface, which may indicate the presence of aluminum oxides on the coating surface (or suggest that the boron coating is too thin, causing the laser to also capture subsurface signals from the aluminum oxide of the substrate during focusing).

Thus, under annealing conditions in an inert atmosphere, a thin semi-transparent film of reduced boron is formed from the boron oxide film via aluminothermy.

The possibility of boron reduction from the oxide film was also demonstrated on a substrate made of samarium, a metal that is more chemically active than aluminum. As in the previous case, the polycrystalline samarium substrate had a polished, mirror-like surface. Deposition of the

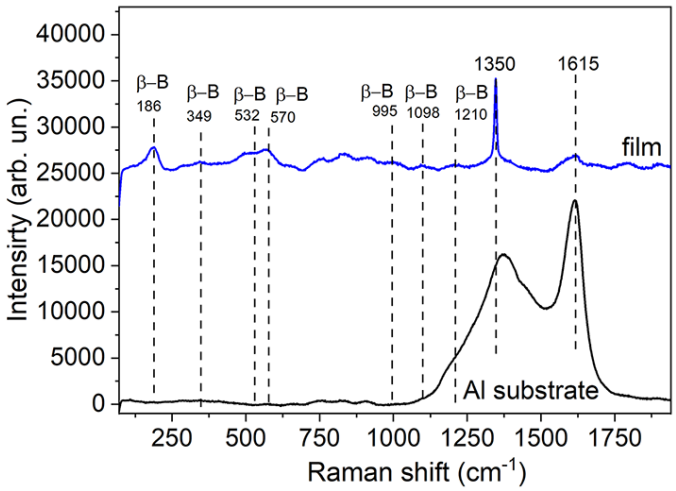

Fig. 4. Raman spectra detected on the surface of the sample (substrate - massive aluminum)

boron oxide (B_2O_3) film was carried out in the same installation (VUP-5M) using an analogous amount of boron oxide charge and the same distance from the substrate to the evaporator (Fig. 1).

According to Raman spectroscopy data (Fig. 5), the spectra of this sample, in addition to peaks from the samarium substrate, exhibits the following Raman peaks: a peak at 599 cm^{-1} corresponding to vibrations of icosahedral boron atoms near oxygen atoms (B(3)-O); a peak at 953 cm^{-1} corresponding to B_2O_3 vibrations; and peaks at 715, 1126, and 1250 cm^{-1}, which, according to literature data [6], correspond to vibrations of β-rhombohedral boron (β-B).

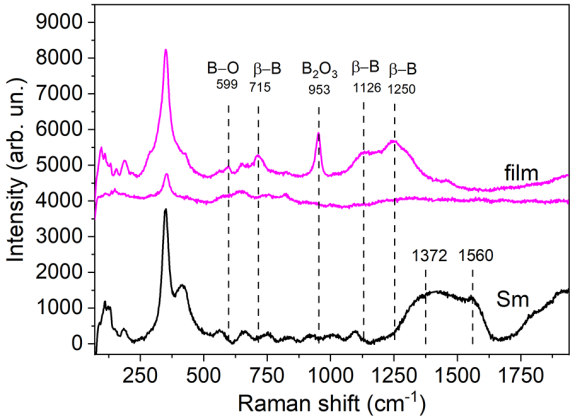

Fig. 5. Raman spectra detected on the sample surface (substrate – massive samarium)

Thus, the methodological conditions for obtaining nanoscale boron films from a vacuum-deposited boron oxide film using a substrate made of a chemically active metal are demonstrated.

The work was carried out in accordance with the state assignment of the Institute of Solid State Chemistry of the Russian Academy of Sciences (Ural Branch) (Registration no. 124020600007-8).

References

[1] A.V.Rzhanov, Osnovy ellipsometryy, Nauka, Moskow, 1979 (in Russian)

[2] R.M.A.Azzam, N.M.Bashsara, Ellipsometry and polarized light, North-Holland publishing comp., Amsterdam, 1977.

[3] A.D.Rakic, Algorithm for the determination of intrinsic optical constants of metal films: application to aluminum, *Appl. Opt.*, **34**(1995), no. 22 , 4755–4767. DOI: 10.1364/AO.34.004755

[4] H.G.Tompkins, E.A.Irene, Handbook of Ellipsometry, William Andrews Pub, NY, 2005.

[5] L.A.Akashev, N.A.Popov, Yu.V.Korkh, T.V.Kuznetsova, V.G.Shevchenko, L.Yu.Buldakova, Oxidation of the surface of polycrystalline boron, *Russian Journal of Physical Chemistry A*, **68**(2024), no. 6 , 181–187.

[6] H.Werheit, V.Filipov, U.Kuhlmann, et.al., Raman effect in icosahedral boron-rich solids, *Adv. Mater.*, **11**(2010), 023001. DOI: 10.1088/1468-6996/11/2/023001

[7] P.V.Thomas, V.Ramakrishnan, V.K.Vaidyan, Oxidation studies of aluminum thin films by Raman spectroscopy, *Thin Solid Films*, **170**(1989), no. 1, 35–40.

[8] M.Fukuhara, et al., Surface analyses of amorphous aluminum oxides with AlO6 clusters, *MRS Communications*, **10**(2020), 674–679. DOI: 10.1557/mrc.2020.82

[9] Y.Liu, B.Cheng, K.Wang, G.Ling, J.Cai, C.Song, G.Han, Study of Raman spectra for γ-Al2O3 models by using first-principles method, *Solid State Communications*, **178**(2014), 16–22. DOI: 10.1016/j.ssc.2013.09.030

Восстановление оксида бора на поликристаллических подложках алюминия и самария

Лев А. Акашев
Институт химии твердого тела УрО РАН
Екатеринбург, Российская Федерация

Юлия В. Корх
Институт физики металлов им. М.Н. Михеева УрО РАН
Екатеринбург, Российская Федерация

Николай А. Попов
Институт химии твердого тела УрО РАН
Екатеринбург, Российская Федерация

Татьяна В. Кузнецова
Институт физики металлов им. М.Н. Михеева УрО РАН
Екатеринбург, Российская Федерация

Алла В. Конюкова, Владимир Г. Шевченко
Институт химии твердого тела УрО РАН
Екатеринбург, Российская Федерация

Аннотация. В данной работе оптическими методами спектроскопии комбинационного рассеяния (КРС), спектральной эллипсометрии исследован процесс восстановления оксида бора, нанесенного вакуумным термическим испарением на поверхности алюминия и самария. По данным КРС на спектрах данных образцов обнаружены рамановские пики, соответствующие колебаниям β-ромбоэдрического бора (β-B). Методом спектральной эллипсометрии определены оптические постоянные и толщина наноразмерной пленки бора в диапазоне спектра от 270 до 1000 нм.

Ключевые слова: эллипсометрия тонких пленок, формула Коши, восстановление оксида бора.

EDN: HLTKIG
УДК 517.9

On the Dimensions of Components of Stable Rank 2 Vector Bundles with Odd Determinant on $\mathbb{P}^3$

Alexey A. Kytmanov*
Institute for Advanced Technologies and Industrial Programming
MIREA — Russian Technological University
Moscow, Russian Federation
Sergey A. Tikhomirov†
Ushinsky Yaroslavl State Pedagogical University
Yaroslavl, Russian Federation

Received 10.06.2025, received in revised form 05.08.2025, accepted 27.09.2025

Abstract. We prove that the irreducible components of the infinite series of stable rank 2 vector bundles on complex three-dimensional projectice space with odd determinant, constructed in 2019 by A. S. Tikhomirov, S. A. Tikhomirov, and D. A. Vasiliev, always have a dimension higher than the dimension predicted by the deformation theory.

Keywords: vector bundles, sheaves, moduli space, dimensions of components.

Citation: A.A. Kytmanov, S.A. Tikhomirov, On the Dimensions of Components of Stable Rank 2 Vector Bundles with Odd Determinant on $\mathbb{P}^3$, J. Sib. Fed. Univ. Math. Phys., 2026, 19(1), 65–71. EDN: HLTKIG.

Introduction

Over the past decade, the studies on the number-theoretic properties of sheaves, bundles, their invariants and components in moduli spaces have formed an independent field of interest. Below, we give an overview of the studies in this field. In [1], the authors study the number-theoretic properties of the irreducible Ein components of stable bundles with even determinant. In [2], the authors obtain the formulas for the dimensions of these components for the cases of even and odd determinants. In [3], these properties are studied for the bundles whose isomorphism classes form Ein components. In this study, the authors present the explicit formulas for the spectra of modified instanton bundles introduced by C. Almeida, M. Jardim, A. S. Tikhomirov, and S. A. Tikhomirov in 2021 in [4] and the formulas for the dimensions of the moduli spaces of these bundles. In [5], the authors give formulas for finding the exact number of the two types of irreducible Vedernikov components of stable bundles with an even determinant. Moreover, the authors find a criterion for the existence of these components for an arbitrary second Chern class $c_2 = n$. In [6], the author constructs an infinite series of irreducible components of the moduli space of stable rank 3 sheaves on $\mathbb{P}^3$ with an even determinant, proves the rationality of the components of this series, and gives the formulas for their dimensions for an arbitrary value of the first Chern class. In [7], the authors construct an infinite series of smooth irreducible components of the moduli space of symplectic vector bundles of arbitrary even rank $2r$, $(r \geqslant 1)$ and, as a special case, they obtain an infinite series of irreducible components of the moduli space

*kytmanov@mirea.ru https://orcid.org/0000-0003-3325-099X
†satikhomirov@mail.ru https://orcid.org/0000-0002-7409-8464

of rank 2 stable bundles on $\mathbb{P}^3$. We note that the formulas for the second Chern class of the bundles in this series are polynomial expressions in an increasing number of integer parameters.

Furthermore, in [8], the authors consider the moduli space of semistable reflexive rank 2 sheaves of on $\mathbb{P}^3$ and prove the uniqueness of irreducible components of the two infinite series constructed by M. Jardim, D. G. Markushevich, and A. S. Tikhomirov in 2017 for the case of an even determinant in [9] and by C. Almeida, M. Jardim, and A. S. Tikhomirov in 2022 for the case of an odd determinant in [10]. Finally, in [11] and [12], the authors construct four more infinite series of irreducible components of the moduli space of semistable reflexive rank 2 sheaves on $\mathbb{P}^3$. They study these series from the number-theoretical point of view, two of them for the case of an even determinant and another two for the case of an odd determinant. We note that the components of the series constructed in the four articles mentioned in this paragraph have the dimensions predicted by the deformation theory.

In [13], the authors construct two series of irreducible, rational components of the moduli space of stable reflexive rank 2 sheaves on $\mathbb{P}^3$, one series for the even and one for the odd determinant, and present formulas for the dimensions of these components. In [14], the authors presented a full classification stable rank 2 bundles on $\mathbb{P}^3$ with odd determinant, second Chern class $c_2 \leqslant 8$ and positive minimal monads based on their spectra, a key number-theoretic characteristics of bundles.

The dimensions of the components constituted by the equivalence (isomorphism) classes of various kinds of sheaves are of particular interest within the number-theoretic study framework. Sometimes researchers manage to establish explicit formulas for these dimensions, or show that these dimensions coincide with those predicted by the deformation theory. But this is not always the case. For example, in [15], L. Ein constructed two series of components of stable rank 2 bundles on $\mathbb{P}^3$, one for the case of an even determinant, and another for the case of an odd determinant. Yet, he did not present any formulas for computing the dimensions of these components, later called the "Ein components" (see [1] and later works of the authors). This problem remained open until 2019, when in [2] the authors presented the explicit formula for computing these dimensions together with the lists of the Ein components for certain ranges of values of the second Chern class containing the dimensions of the components.

At the present moment for the majority of the cases of the components of the infinite series constructed by various authors there is no clear understanding of how the dimensions of these components relate to the dimensions predicted by the deformation theory.

Recall that for the case of stable rank 2 bundles on $\mathbb{P}^3$ with an even determinant, the famous mathematical instanton components have the expected dimension (see [16, 17]). In contrast, for stable rank 2 bundles on $\mathbb{P}^3$ with an odd determinant, the question of how the dimensions of the components of the known infinite series relate to the expected dimensions has never been posed in the publications available, even when the authors managed to obtain specific formulas for these dimensions.

At the same time, it is traditionally believed that questions related to the "geography", i.e. the location and geometry of the components of sheaves of various kinds, play crucial role in the study of their moduli spaces [18], with the dimension being both a numerical and geometric characteristic of a component. Moreover, when exploring the geography of components, searching for new components, or studying the relationships between certain components, the fact that their dimensions coincide or not coincide can indicate the same relationship between the components themselves. In particular, it was precisely the coincidence of the dimensions of the Vedernikov components with the dimensions of a subfamily of Ein components of stable

rank 2 bundles on $\mathbb{P}^3$, first discovered via computational experiment, that led to the guess about the coincidence of these components themselves, which later received a rigorous proof in [5]. Similarly, studying dimensions with other characteristics, made it possible to discover and prove the fact that the Hartshorne families are an infinite series of components, which is a subset of the Ein components [3].

In [19], the authors constructed an infinite series of stable rank 2 bundles on $\mathbb{P}^3$ with odd determinant. The present study is focused on the question of how the dimensions of the components of these series are related to expected (i.e., predicted by the deformation theory) dimensions.

1. Results

By $\mathbb{Z}_+ = \{1, 2, 3, \ldots\}$ denote the set of positive integers. Let

$$n = 4m + 2\varepsilon + a(a+1), \text{ where } m \in \mathbb{Z}_+,\ \varepsilon \in \{0, 1\} \text{ and } a \geqslant 2(m+\varepsilon) + 3. \tag{1}$$

In [19, Theorem 2], the authors prove the existence an irreducible family of stable vector bundles $\mathscr{M}_n = \mathscr{M}_n(a, m, \varepsilon)$. Its dimension is given by

$$\dim \mathscr{M}_n(a, m, \varepsilon) = 4\binom{a+3}{3} + 2\binom{a+3}{2} - (2m+\varepsilon)(2a-19) - 17. \tag{2}$$

The expected dimension of $\mathscr{M}_n(a, m, \varepsilon)$ is

$$\dim^0 \mathscr{M}_n(a, m, \varepsilon) = 8n - 5. \tag{3}$$

The authors also pointed out that the closure of such a family in the Gieseker–Maruyama moduli scheme $\mathscr{B}(-1, n)$ of stable rank 2 bundles with odd determinant and second Chern class $c_2 = n \geqslant 1$ on $\mathbb{P}^3$ is a component, and the set Σ_1 of such components is an infinite series, different from all previously known.

Computational experiment conducted for 100 pairs of values of a and m for $\varepsilon = 0$ and for 100 pairs of values a and m for $\varepsilon = 1$ shows that the dimension of $\mathscr{M}_n(a, m, \varepsilon)$ given by (2) is always greater than its expected dimension given by (3). As an example, we present the computed dimensions of $\mathscr{M}_n(a, m, \varepsilon)$ for a few small values of a and m for $\varepsilon = 0$ and $\varepsilon = 1$ in Tab. 1.

Table 1. $\dim \mathscr{M}_n(a, m, \varepsilon)$ and $\dim^0 \mathscr{M}_n(a, m, \varepsilon)$ computed for small values of a and m

a	m	ε	$\dim \mathscr{M}_n$	$\dim^0 \mathscr{M}_n$	a	m	ε	$\dim \mathscr{M}_n$	$\dim^0 \mathscr{M}_n$
5	1	0	281	267	7	1	1	568	491
6	1	0	405	363	8	1	1	762	619
7	1	0	563	475	9	1	1	998	763
7	2	0	573	507	9	2	1	1000	795
8	1	0	759	603	10	1	1	1280	923
8	2	0	765	635	10	2	1	1278	955
9	1	0	997	747	11	1	1	1612	1099
9	2	0	999	779	11	2	1	1606	1131
9	3	0	1001	811	11	3	1	1600	1163
10	1	0	1281	907	12	1	1	1998	1291

Computational experiment conducted for 100 pairs of values of a and m for $\varepsilon = 0$ and for 100 pairs of values a and m for $\varepsilon = 1$ shows that the dimension of $\mathscr{M}_n(a, m, \varepsilon)$ given by (2) is always

greater than its expected dimension given by (3). As an example, we present the computed dimensions of $\mathscr{M}_n(a,m,\varepsilon)$ for a few small values of a and m for $\varepsilon=0$ and $\varepsilon=1$ in Tab. 1.

This observation has led us to the conjecture stated in the following theorem which we were able to prove.

Theorem 1.1. *For n, m, ε and a satisfying* (1)*, the inequality*

$$\dim \mathscr{M}_n(a,m,\varepsilon) > \dim^0 \mathscr{M}_n(a,m,\varepsilon)$$

holds, where the dimension $\dim \mathscr{M}_n(a,m,\varepsilon)$ *and the expected dimension* $\dim^0 \mathscr{M}_n(a,m,\varepsilon)$ *are given by* (2) *and* (3)*, respectively.*

Proof. Consider the difference

$$\dim \mathscr{M}_n(a,m,\varepsilon) - \dim^0 \mathscr{M}_n(a,m,\varepsilon) = \frac{2}{3}a^3 - 3a^2 + \frac{13}{3}a - 2\varepsilon a - 4ma + 3\varepsilon + 6m - 2.$$

It is easy to see that

$$\dim \mathscr{M}_n(a,m,\varepsilon) - \dim^0 \mathscr{M}_n(a,m,\varepsilon) = \frac{1}{3}(a^2 - 3a - 3\varepsilon - 6m + 2)(2a-3). \tag{4}$$

We also note that (1) implies that $a \geqslant 5$ which, in turn, yields $2a-3>0$. Consequently, the right-hand side of (4) is positive whenever

$$F(a,m,\varepsilon) = a^2 - 3a - 3\varepsilon - 6m + 2$$

is positive.

We now show that $F(a,m,\varepsilon) > 0$ for $\varepsilon = 0$ and for $\varepsilon = 1$.

Let $\varepsilon = 0$. Then $F(a,m,0) = a^2 - 3a - 6m + 2$. The roots of the equation $a^2 - 3a - 6m + 2 = 0$ are

$$a_{1,2} = \frac{3 \pm \sqrt{24m+1}}{2}.$$

Note that, for $\varepsilon = 0$, the last inequality in (1) is $a \geqslant 2m+3$. We show that this yields

$$a > \frac{3+\sqrt{24m+1}}{2}.$$

In other words, we need to show that

$$2m + 3 > \frac{3+\sqrt{24m+1}}{2},$$

or

$$4m + 3 > \sqrt{24m+1}. \tag{5}$$

Note that $4m+3>0$ and $24m+1>0$ since $m \geqslant 1$. Square both sides of (5) to get

$$16m^2 + 24m + 9 > 24m + 1, \quad \text{or} \quad 16m^2 + 8 > 0,$$

which is true for any real m.

Thus, if $a \geqslant 2m+3$ then a is greater than the larger root of the quadratic polynomial $F(a,m,0)$ with respect to a. Since the leading coefficient of $F(a,m,0)$ is positive, the graph of $F(a,m,0)$ for any fixed m is a parabola that opens upward. This means that $F(a,m,0) > 0$ for any fixed $m \geqslant 1$ and $a \geqslant 2m+3$ which completes the proof for the case $\varepsilon = 0$.

Now consider the case $\varepsilon = 1$ and use similar argument. We have $F(a, m, 1) = a^2 - 3a - 6m - 1$, and the equation $a^2 - 3a - 6m - 1 = 0$ has the roots

$$a_{1,2} = \frac{3 \pm \sqrt{24m + 13}}{2}.$$

Note that, for $\varepsilon = 1$, the last inequality in (1) is $a \geqslant 2m + 5$. We show that this yields

$$a > \frac{3 + \sqrt{24m + 13}}{2}.$$

In other words, we need to show that

$$2m + 5 > \frac{3 + \sqrt{24m + 13}}{2},$$

or

$$4m + 7 > \sqrt{24m + 13}. \tag{6}$$

Note that $4m + 7 > 0$ and $24m + 13 > 0$ since $m \geqslant 1$. Square both sides of (6) to get

$$16m^2 + 56m + 49 > 24m + 13, \quad \text{or} \quad 16(m + 1)^2 + 20 > 0,$$

which is true for any real m.

Thus, if $a \geqslant 2m + 5$ then a is greater than the larger root of the quadratic polynomial $F(a, m, 1)$ with respect to a. Since the leading coefficient of $F(a, m, 1)$ is positive, the graph of $F(a, m, 1)$ for any fixed m is a parabola that opens upward. This means that $F(a, m, 1) > 0$ for any fixed $m \geqslant 1$ and $a \geqslant 2m + 5$ which completes the proof for the case $\varepsilon = 1$. □

We conclude our note by extending the results obtained in [19], as the theorem below immediately follows from Theorem 2.1.

Theorem 1.2. *The components of the series Σ_1 of stable rank 2 vector bundles with odd determinant on $\mathbb{P}^3$ constructed in [19, Theorem 2] always have a dimension higher than the one predicted by the deformation theory.*

This work is supported by the Krasnoyarsk Mathematical Center and financed by the Ministry of Science and Higher Education of the Russian Federation (Agreement no. 075-02-2025-1790).

References

[1] A.A.Kytmanov, N.N.Osipov, S.A.Tikhomirov, Finding Ein components in the moduli spaces of stable rank 2 bundles on the projective 3-space, *Siberian Math. J.*, **57**(2016), no. 2, 322–329. DOI: 10.1134/S0037446616020142

[2] A.A.Kytmanov, A.S.Tikhomirov, S.A.Tikhomirov, Series of rational moduli components of stable rank two vector bundles on $\mathbb{P}^3$, *Sel. Math.-New Ser.*, **25**(2019), no. 2, article no. 29. DOI: 10.1007/s00029-019-0477-8

[3] A.A.Kytmanov, N.N.Osipov, S.A.Tikhomirov, T.V.Zykova, On numerical characteristics of some bundles and their isomorphism classes on $\mathbb{P}^3$, *Sib. Electron Math. Re.*, **19**(2022), no. 2, 415–425 (in Russian). DOI: 10.33048/semi.2022.19.036

[4] C.Almeida, M.Jardim, A.S.Tikhomirov, S.A.Tikhomirov, New moduli components of rank 2 bundles on projective space, *Sb. Math.*, **212**(2021), no. 11, 1503–1552. DOI: 10.1070/SM9490

[5] N.N.Osipov, S.A.Tikhomirov, On the number of Vedernikov-Ein irreducible components of the moduli space of stable rank 2 bundles on the projective space, *Siberian Math. J.*, **59**(2018), no. 1, 107–112. DOI: 10.1134/S0037446618010123

[6] D.A.Vassiliev, An infinite series of rational components of the moduli space of rank 3 sheaves on $\mathbb{P}^3$, *Siberian Math. J.*, **64**(2023), no. 3, 525–541. DOI: 10.1134/S0037446623030035

[7] A.S.Tikhomirov, D.A.Vassiliev, Construction of symplectic vector bundles on projective space $\mathbb{P}^3$, *J. Geom. Phys.*, **158**(2020), article no. 103949. DOI: 10.1016/j.geomphys.2020.103949

[8] A.A.Kytmanov, N.N.Osipov, S.A.Tikhomirov, On the number of irreducible components of the moduli space of semistable reflexive rank 2 sheaves on the projective space, *Siberian Math. J.*, **64**(2023), no. 1, 103–110. DOI: 10.1134/S0037446623010123

[9] M.Jardim, D.Markushevich, A.S.Tikhomirov, Two infinite series of moduli spaces of rank 2 sheaves on $\mathbb{P}^3$, *Ann. Mat. Pura Appl.*, **196**(2017), no. 4, 1573–1608. DOI: 10.1007/s10231-016-0630-3

[10] C.Almeida, M.Jardim, A.S.Tikhomirov, Irreducible components of the moduli space of rank 2 sheaves of odd determinant on projective space, *Adv. Math.*, **402**(2022), article no. 108363. DOI: 10.1016/j.aim.2022.108363

[11] A.A.Kytmanov, N.N.Osipov, S.A.Tikhomirov, Two series of components of the moduli space of semistable reflexive rank 2 sheaves on the projective space, *Siberian Math. J.*, **65**(2024), no. 1, 96–105. DOI: 10.1134/S0037446624010105

[12] A.A.Kytmanov, N.N.Osipov, S.A.Tikhomirov, Series of components of the moduli space of semistable reflexive rank 2 sheaves on $\mathbb{P}^3$, *Siberian Math. J.*, **66**(2025), no. 1, 53–63. DOI: 10.1134/S0037446625010070

[13] A.Cavalcante, M.Jardim, D.Santiago, Foliations by curves on threefolds, *Math. Nachr.* **296**(2023), no. 2, 552–573. DOI: 10.1002/mana.202100071

[14] A.L.Fontes, M.Jardim, Monads and moduli components for stable rank 2 bundles with odd determinant on the projective space, *Geom. Dedicata*, **217**(2023), article no. 21. DOI: 10.1007/s10711-022-00757-9

[15] L.Ein, Generalized null correlation bundles, *Nagoya Math. J.*, **111**(1988), 13–24. DOI: 10.1017/S0027763000000970

[16] A.S.Tikhomirov, Moduli of mathematical instanton vector bundles with odd c_2 on projective space, *Izv. Math.*, **76**(2012), no. 5, 991–1073. DOI: 10.1070/IM2012v076n05ABEH002613

[17] A.S.Tikhomirov, Moduli of mathematical instanton vector bundles with even c_2 on projective space, *Izv. Math.*, **77**(2013), no. 6, 1195–1223. DOI: 10.1070/IM2013v077n06ABEH002674

[18] D.A.Vassiliev, A.S.Tikhomirov, Moduli of rank 2 semistable sheaves on rational Fano threefolds of the main series, *Sb. Math.*, **215**(2024), no. 10, 1269–1320. DOI: 10.4213/sm10087e

[19] A.S.Tikhomirov, S.A.Tikhomirov, D.A.Vassiliev, Construction of stable rank 2 bundles on $\mathbb{P}^3$ via symplectic bundles, *Siberian Math. J.*, **60**(2019), no. 2, 343–358. DOI: 10.1134/S0037446619020150

О размерностях компонент стабильных расслоений ранга 2 с нечетным детерминантом на $\mathbb{P}^3$

Алексей А. Кытманов
Институт перспективных технологий и промышленного программирования
МИРЭА — Российский технологический университет
Москва, Российская Федерация
Сергей А. Тихомиров
Ярославский государственный педагогический университет им. К. Д. Ушинского
Ярославль, Российская Федерация

Аннотация. В работе доказывается утверждение о том, что неприводимые компоненты бесконечной серии стабильных расслоений ранга 2 с нечетным детерминантом на комплексном трехмерном проективном пространстве, построенной в 2019 году А. С. Тихомировым, С. А. Тихомировым и Д. А. Васильевым, всегда имеют размерность выше ожидаемой по теории деформаций.

Ключевые слова: векторные расслоения, пучки, пространство модулей, размерности компонент.

EDN: EZHYCC
УДК 517.9

Certain Incomplete R-Function Expansion Formulas Utilizing Fractional Calculus

Ravi Gupta*
Priti Purohit†
School of Science and Technology
Vardhman Mahaveer Open University
Kota, India

Received 14.12.2024, received in revised form 17.06.2025, accepted 27.09.2025

Abstract. This paper investigates incomplete R-function expansion formulae from a fractional calculus perspective. We reveal the underlying links between fractional calculus operators and incomplete R-functions through rigorous mathematical computation and analysis. Through the taking advantage of the Leibniz formula within fractional differentiation, our goal is towards acquire new expansion formulae that provide new perspectives on the characteristics and behavior of these functions. The findings of this investigation creates new directions regarding the study of fractional calculus image formulas with incomplete R-functions and new ways to advance scientific understanding. As a particular illustration to demonstrate our main findings, expansion formulas for additional special functions as well as incomplete functions are derived.

Keywords: incomplete gamma function, incomplete R-functions, Leibniz formula, fractional calculus.

Citation: R. Gupta, P. Purohit, Certain Incomplete R-Function Expansion Formulas Utilizing Fractional Calculus, J. Sib. Fed. Univ. Math. Phys., 2026, 19(1), 72–79.
EDN: EZHYCC.

1. Overview and initial investigations

It's been noted that in the fields of astrophysics and heat conduction, there are situations where the usual divisions of special functions aren't enough to solve the problem. To tackle this, researchers have turned to incomplete gamma functions and their extensions. Lately, there's been exploration into incomplete hypergeometric functions [25], incomplete Wright functions [18], incomplete H-functions [27], incomplete I-functions [10], incomplete Y-functions [12] and various other unconventional functions using incomplete gamma functions. The most recent work [2, 3, 20] and [21] contains more uses for incomplete special functions. Additionally, the authors in [8] have introduced a new set of incomplete special functions called incomplete R-functions and highlighted their unique properties. From a fractional calculus perspective, incomplete R-function expansion formulas are investigated in this study.

To begin with of this, we keep in mind the more common incomplete gamma functions $\gamma(\omega, x)$ as well $\Gamma(\omega, x)$, which are provided as:

$$\gamma(\omega, x) = \int_0^x t^{\omega-1} e^{-t} dt \quad (\Re(\omega) > 0, x \geqslant 0), \tag{1}$$

*rgupta@vmou.ac.in https://orcid.org/0000-0002-1749-8832
†pritipurohitmath@vmou.ac.in https://orcid.org/0009-0000-6823-3909

and

$$\Gamma(\omega, x) = \int_x^{\infty} t^{\omega-1} e^{-t} dt \ \ (x \geqslant 0; \Re(\omega) > 0 \text{ when } x = 0). \tag{2}$$

When we decide to $x = 0$ in (2), it becomes the well-known gamma function. Moreover, defintions (1) and (2) readily yeild to following decompostion formula:

$$\gamma(\omega, x) + \Gamma(\omega, x) = \Gamma(\omega) \ \ (\Re(\omega) > 0). \tag{3}$$

The incomplete R-functions corresponding to Rathie's R-function in relation to the incomplete gamma functions are characterized in the following manner, in accordance with Gupta and Purohit [8]:

$$\begin{aligned} {}^{\alpha,\,\beta}_{\varepsilon,\,\delta}\gamma^{m,\,n}_{p,\,q}(z) &= {}^{\alpha,\,\beta}_{\varepsilon,\,\delta}\gamma^{m,\,n}_{p,\,q}\left[z \,\middle|\, \begin{matrix} (\mathfrak{u}_1, \mathfrak{U}_1, x), (\mathfrak{u}_2, \mathfrak{U}_2), \cdots, (\mathfrak{u}_p, \mathfrak{U}_p) \\ (\mathfrak{v}_1, \mathfrak{V}_1), \cdots, (\mathfrak{v}_q, \mathfrak{V}_q) \end{matrix}\right] = \\ &= \frac{1}{2\pi i} \int_{\mathcal{L}} \frac{\mathsf{g}(s, x)}{(\alpha + \beta s)^{\varepsilon + \delta s}} \, z^{-s} \, ds, \end{aligned} \tag{4}$$

where

$$\mathsf{g}(s, x) = \frac{\gamma(1 - \mathfrak{u}_1 - \mathfrak{U}_1 s, x) \prod_{j=1}^{m} \Gamma(\mathfrak{v}_j + \mathfrak{V}_j s) \prod_{j=2}^{n} \Gamma(1 - \mathfrak{u}_j - \mathfrak{U}_j s)}{\prod_{j=m+1}^{q} \Gamma(1 - \mathfrak{v}_j - \mathfrak{V}_j s) \prod_{j=n+1}^{p} \Gamma(\mathfrak{u}_j + \mathfrak{U}_j s)}, \tag{5}$$

and

$$\begin{aligned} {}^{\alpha,\,\beta}_{\varepsilon,\,\delta}\Gamma^{m,\,n}_{p,\,q}(z) &= {}^{\alpha,\,\beta}_{\varepsilon,\,\delta}\Gamma^{m,\,n}_{p,\,q}\left[z \,\middle|\, \begin{matrix} (\mathfrak{u}_1, \mathfrak{U}_1, x), (\mathfrak{u}_2, \mathfrak{U}_2), \cdots, (\mathfrak{u}_p, \mathfrak{U}_p) \\ (\mathfrak{v}_1, \mathfrak{V}_1), \cdots, (\mathfrak{v}_q, \mathfrak{V}_q) \end{matrix}\right] = \\ &= \frac{1}{2\pi i} \int_{\mathcal{L}} \frac{\mathsf{G}(s, x)}{(\alpha + \beta s)^{\varepsilon + \delta s}} \, z^{-s} \, ds, \end{aligned} \tag{6}$$

where

$$\mathsf{G}(s, x) = \frac{\Gamma(1 - \mathfrak{u}_1 - \mathfrak{U}_1 s, x) \prod_{j=1}^{m} \Gamma(\mathfrak{v}_j + \mathfrak{V}_j s) \prod_{j=2}^{n} \Gamma(1 - \mathfrak{u}_j - \mathfrak{U}_j s)}{\prod_{j=m+1}^{q} \Gamma(1 - \mathfrak{v}_j - \mathfrak{V}_j s) \prod_{j=n+1}^{p} \Gamma(\mathfrak{u}_j + \mathfrak{U}_j s)}, \tag{7}$$

considering that p, q, m, n are integrers in a manner that $0 < m < q, 0 < n < p$, z cannot be equivalent to zero. Further, $\mathfrak{U}_j (j = 1, \cdots, p)$ and $\mathfrak{V}_j (j = 1, \cdots, q)$ are positive numbers and $\mathfrak{u}_j (j = 1, \cdots, p)$ and $\mathfrak{v}_j (j = 1, \cdots, q)$ are complex numbers. The constants $\alpha, \beta, \varepsilon$, and δ are selected in this case so as to make sure existence of the the right-side integral of (8). The incomplete R-functions exist for all $x \geqslant 0$ along with the exactly same specifications and assumptions as mentioned for R-function in [24].

The functions (4) and (6) readily yield the decomposition formula that follows:

$${}^{\alpha,\,\beta}_{\varepsilon,\,\delta}\gamma^{m,\,n}_{p,\,q}(z) + {}^{\alpha,\,\beta}_{\varepsilon,\,\delta}\Gamma^{m,\,n}_{p,\,q}(z) = {}^{\alpha,\,\beta}_{\varepsilon,\,\delta}R^{m,\,n}_{p,\,q}(z).$$

Additional characteristics of incomplete R-functions can be found in the authors' work in [7] and [19]. The characteristic that appears on the right side is known as the the widely recognized

R-function, which was initially developed by Rathie [24] to investigate further issues related to testing statistical hypotheses (see, [23]). Its definition is as follows:

$$\begin{aligned} {}^{\alpha,\,\beta}_{\varepsilon,\,\delta}R^{m,\,n}_{p,\,q}(z) = {}^{\alpha,\,\beta}_{\varepsilon,\,\delta}R^{m,\,n}_{p,\,q}\left[z\,\middle|\,\begin{matrix}(\mathfrak{u}_1,\mathfrak{U}_1),\cdots,(\mathfrak{u}_p,\mathfrak{U}_p)\\(\mathfrak{v}_1,\mathfrak{V}_1),\cdots,(\mathfrak{v}_q,\mathfrak{V}_q)\end{matrix}\right] = \\ = \frac{1}{2\pi i}\int_{\mathcal{L}}\frac{\mathsf{g}(s)}{(\alpha+\beta s)^{\varepsilon+\delta s}}\,z^{-s}\,ds, \end{aligned} \tag{8}$$

wherein

$$\mathsf{g}(s) = \frac{\prod\limits_{j=1}^{m}\Gamma(\mathfrak{v}_j+\mathfrak{V}_j s)\prod\limits_{j=1}^{n}\Gamma(1-\mathfrak{u}_j-\mathfrak{U}_j s)}{\prod\limits_{j=m+1}^{q}\Gamma(1-\mathfrak{v}_j-\mathfrak{V}_j s)\prod\limits_{j=n+1}^{p}\Gamma(\mathfrak{u}_j+\mathfrak{U}_j s)}. \tag{9}$$

It has become remarkable to observe that the incomplete R-functions lead to the family of incomplete H-functions, which are outlined under the subsequent order, for $\alpha = 1$ and $\beta = 0$ (or $\varepsilon = 0$ and $\delta = 0$) (see, also [27]):

$$\begin{aligned} {}^{1,\,0}_{\varepsilon,\,\delta}\gamma^{m,\,n}_{p,\,q}(z) = {}^{\alpha,\,\beta}_{0,\,0}\gamma^{m,\,n}_{p,\,q}(z) = \gamma^{m,\,n}_{p,\,q}\left[z\,\middle|\,\begin{matrix}(\mathfrak{u}_1,\mathfrak{U}_1,x),(\mathfrak{u}_2,\mathfrak{U}_2),\cdots,(\mathfrak{u}_p,\mathfrak{U}_p)\\(\mathfrak{v}_1,\mathfrak{V}_1),\cdots,(\mathfrak{v}_q,\mathfrak{V}_q)\end{matrix}\right] = \\ = \frac{1}{2\pi i}\int_{\mathcal{L}}\mathsf{g}(s,x)z^{-s}\,ds, \end{aligned} \tag{10}$$

and

$$\begin{aligned} {}^{1,\,0}_{\varepsilon,\,\delta}\Gamma^{m,\,n}_{p,\,q}(z) = {}^{\alpha,\,\beta}_{0,\,0}\Gamma^{m,\,n}_{p,\,q}(z) = \Gamma^{m,\,n}_{p,\,q}\left[z\,\middle|\,\begin{matrix}(\mathfrak{u}_1,\mathfrak{U}_1,x),(\mathfrak{u}_2,\mathfrak{U}_2),\cdots,(\mathfrak{u}_p,\mathfrak{U}_p)\\(\mathfrak{v}_1,\mathfrak{V}_1),\cdots,(\mathfrak{v}_q,\mathfrak{V}_q)\end{matrix}\right] = \\ = \frac{1}{2\pi i}\int_{\mathcal{L}}\mathsf{G}(s,x)\,z^{-s}\,ds, \end{aligned} \tag{11}$$

where $\mathsf{g}(s,x)$ and $\mathsf{G}(s,x)$ are already defined by (5) and (7) respectively. Fox's H-function and the aforementioned functions are closely related. Further details regarding the H-function, including recurrence relations, transformation formulas, integral transforms, fractional calculus, generating functions, and applications, are available in papers [4,6,11] and research monographs [5,13–15,26].

More importantly, the following is the definition of the conventional manner Leibniz formula for two differentiable functions, $\mathcal{F}$ and $\mathcal{G}$:

$$D^n[\mathcal{F}(t)\mathcal{G}(t)] = \sum_{k=0}^{n}\binom{n}{k}[D^k\mathcal{G}(t)][D^{n-k}\mathcal{F}(t)].$$

Considering the derivatives of the Riemann–Liouville type, this Leibniz rule can be expanded. This corresponds to the subsequent definition of the fractional extension of the Leibniz rule if $\mathcal{F}$ and $\mathcal{G}$ can be two functions of class C:

$$D^{\mu}[\mathcal{F}(t)\mathcal{G}(t)] = \sum_{k=0}^{\infty}\binom{\mu}{k}[D^k\mathcal{G}(t)][D^{\mu-k}\mathcal{F}(t)]\,;\quad \mu>0,\quad k\in\mathbb{N}. \tag{12}$$

Furthermore, the following is the description of the fractional derivative of order μ for $f(z)$ of Riemann–Liouville type (see [17]):

$$D^{\mu}_{z}f(z) = \frac{1}{\Gamma(-\mu)}\int_{0}^{z}(z-t)^{(-\mu-1)}f(t)dt\quad(\Re(\mu)<0). \tag{13}$$

In case $\Re(\mu) \geqslant 0$ and $m \in \mathbb{N}$ is the most small integer with $m-1 \leqslant \mathbb{R}(\mu) < m$, afterwards

$$D_z^{\mu} f(z) = \frac{d^m}{dz^m} D_z^{\mu-m} f(z) = \frac{d^m}{dz^m} \left[\frac{1}{\Gamma(-\mu+m)} \int_0^z (z-t)^{-\mu+m-1} f(t) dt \right]. \tag{14}$$

A framework for calculating the compositional representation of differential operators may be derived using the Leibniz rule, which is an extension of the product differentiation law. This method provides useful information on interesting expansions, generating functions, summation formulae, and transformations associated with different special functions of one or more variables. For further information, see [1, 9, 16, 17, 22]. In this work, our aim is to get novel expansion formulas that offer new understanding into the properties and behavior of these incmolpete R-functions by applying the Leibniz rule to fractional derivatives. We also construct expansion formulae for other special functions in addition to incomplete functions to demonstrate our key findings.

2. Main results

Here, we developed several new transformation formulas for the incomplete R-functions through the application of Leibniz rule for fractional derivatives.

Theorem 2.1. *Assume $\rho \geqslant 1$, $\omega > 0$, $m \in \mathbb{N}$ and $m-1 \leqslant \mathbb{R}(\mu) \leqslant m$, then the subsequent result sustains:*

$$\begin{aligned} &{}_{\varepsilon,\,\delta}^{\alpha,\,\beta}\Gamma_{p+1,\,q+1}^{m,\,n+1} \left[cz^{\omega} \,\middle|\, \begin{matrix} (1-\rho,\omega),(\mathfrak{u}_1,\mathfrak{U}_1,x),(\mathfrak{u}_2,\mathfrak{U}_2),\cdots,(\mathfrak{u}_p,\mathfrak{U}_p) \\ (\mathfrak{v}_1,\mathfrak{V}_1),\cdots,(\mathfrak{v}_q,\mathfrak{V}_q),(1-\rho+\mu,\omega) \end{matrix} \right] = \\ &= \sum_{k=0}^{\infty} \binom{\mu}{k} \frac{\Gamma(\rho)}{\Gamma(\rho-\mu+k)} {}_{\varepsilon,\,\delta}^{\alpha,\,\beta}\Gamma_{p+1,\,q+1}^{m,\,n+1} \left[cz^{\omega} \,\middle|\, \begin{matrix} (0,\omega),(\mathfrak{u}_1,\mathfrak{U}_1,x),(\mathfrak{u}_2,\mathfrak{U}_2),\cdots,(\mathfrak{u}_p,\mathfrak{U}_p) \\ (\mathfrak{v}_1,\mathfrak{V}_1),\cdots,(\mathfrak{v}_q,\mathfrak{V}_q),(k,\omega) \end{matrix} \right]. \end{aligned} \tag{15}$$

Proof. In order (15) is proven, let us make note that $\mathcal{F}(z) = z^{\rho-1}$ and

$$\mathcal{G}(z) = {}_{\varepsilon,\,\delta}^{\alpha,\,\beta}\Gamma_{p,\,q}^{m,\,n}(z) = {}_{\varepsilon,\,\delta}^{\alpha,\,\beta}\Gamma_{p,\,q}^{m,\,n} \left[cz^{\omega} \,\middle|\, \begin{matrix} (\mathfrak{u}_1,\mathfrak{U}_1,x),(\mathfrak{u}_2,\mathfrak{U}_2),\cdots,(\mathfrak{u}_p,\mathfrak{U}_p) \\ (\mathfrak{v}_1,\mathfrak{V}_1),\cdots,(\mathfrak{v}_q,\mathfrak{V}_q) \end{matrix} \right].$$

Now that we have altered the values of $\mathcal{F}(z)$ and $\mathcal{G}(z)$ in (12), we accomplish

$$D^{\mu} \left[z^{\rho-1}\, {}_{\varepsilon,\,\delta}^{\alpha,\,\beta}\Gamma_{p,\,q}^{m,\,n}(cz^{\omega}) \right] = \sum_{k=0}^{\infty} \binom{\mu}{k} \left[D^{k}\, {}_{\varepsilon,\,\delta}^{\alpha,\,\beta}\Gamma_{p,\,q}^{m,\,n}(cz^{\omega}) \right] \left[D^{\mu-k} z^{\rho-1} \right]. \tag{16}$$

Considering the known result of [8], i.e. the Riemann–Liouville fractional derivative of upper incomplete R-function, we possess

$$\begin{aligned} &D^{\mu} \left[z^{\rho-1}\, {}_{\varepsilon,\,\delta}^{\alpha,\,\beta}\Gamma_{p,\,q}^{m,\,n}(cz^{\omega}) \right] = \\ &= z^{\rho-\mu-1}\, {}_{\varepsilon,\,\delta}^{\alpha,\,\beta}\Gamma_{p+1,\,q+1}^{m,\,n+1} \left[cz^{\omega} \,\middle|\, \begin{matrix} (1-\rho,\omega),(\mathfrak{u}_1,\mathfrak{U}_1,x),(\mathfrak{u}_2,\mathfrak{U}_2),\cdots,(\mathfrak{u}_p,\mathfrak{U}_p) \\ (\mathfrak{v}_1,\mathfrak{V}_1),\cdots,(\mathfrak{v}_q,\mathfrak{V}_q),(1-\rho+\mu,\omega) \end{matrix} \right]. \end{aligned} \tag{17}$$

Likewise, using the definitions of (6) and (17), we get the right hand side of equation (16), as

follows:

$$\sum_{k=0}^{\infty}\binom{\mu}{k}\left[D^{k}\ {}^{\alpha,\,\beta}_{\varepsilon,\,\delta}\Gamma^{m,\,n}_{p,\,q}(cz^{\omega})\right]\left[D^{\mu-k}z^{\rho-1}\right]=$$

$$=z^{\rho-\mu-1}\sum_{k=0}^{\infty}\binom{\mu}{k}\frac{\Gamma(\rho)}{\Gamma(\rho-\mu+k)}\times$$

$$\times\ {}^{\alpha,\,\beta}_{\varepsilon,\,\delta}\Gamma^{m,\,n+1}_{p+1,\,q+1}\left[cz^{\omega}\ \middle|\ \begin{matrix}(0,\omega),(\mathfrak{u}_1,\mathfrak{U}_1,x),(\mathfrak{u}_2,\mathfrak{U}_2),\cdots,(\mathfrak{u}_p,\mathfrak{U}_p)\\(\mathfrak{v}_1,\mathfrak{V}_1),\cdots,(\mathfrak{v}_q,\mathfrak{V}_q),(k,\omega)\end{matrix}\right]. \tag{18}$$

Now, the necessary result, (15), is obtained by putting the equations (17) and (18) into (16). □

The definitions (4), (6), and (12) have immediate consequences below the theorem, which is the reason they are included below with no proof.

Theorem 2.2. *Let $\rho\geqslant 1$, $\omega>0$, $m\in\mathbb{N}$ and $m-1\leqslant\mathbb{R}(\mu)\leqslant m$, then the subsequent result sustains:*

$${}^{\alpha,\,\beta}_{\varepsilon,\,\delta}\Gamma^{m+1,\,n}_{p+1,\,q+1}\left[cz^{-\omega}\ \middle|\ \begin{matrix}(\mathfrak{u}_1,\mathfrak{U}_1,x),(\mathfrak{u}_2,\mathfrak{U}_2),\cdots,(\mathfrak{u}_p,\mathfrak{U}_p),(\rho-\mu,\omega)\\(\rho,\omega),(\mathfrak{v}_1,\mathfrak{V}_1),\cdots,(\mathfrak{v}_q,\mathfrak{V}_q),\end{matrix}\right]=$$

$$=\sum_{k=0}^{\infty}\binom{\mu}{k}\frac{\Gamma(\rho)}{\Gamma(\rho-\mu+k)}\ {}^{\alpha,\,\beta}_{\varepsilon,\,\delta}\Gamma^{m+1,\,n}_{p+1,\,q+1}\left[cz^{-\omega}\ \middle|\ \begin{matrix}(\mathfrak{u}_1,\mathfrak{U}_1,x),(\mathfrak{u}_2,\mathfrak{U}_2),\cdots,(\mathfrak{u}_p,\mathfrak{U}_p),(1-\mu,\omega)\\(1,\omega),(\mathfrak{v}_1,\mathfrak{V}_1),\cdots,(\mathfrak{v}_q,\mathfrak{V}_q)\end{matrix}\right]. \tag{19}$$

Theorem 2.3. *Let $\rho\geqslant 1$, $\omega>0$, $m\in\mathbb{N}$ and $m-1\leqslant\mathbb{R}(\mu)\leqslant m$, thereafter the subsequent outcome sustains:*

$${}^{\alpha,\,\beta}_{\varepsilon,\,\delta}\gamma^{m,\,n+1}_{p+1,\,q+1}\left[cz^{\omega}\ \middle|\ \begin{matrix}(1-\rho,\omega),(\mathfrak{u}_1,\mathfrak{U}_1,x),(\mathfrak{u}_2,\mathfrak{U}_2),\cdots,(\mathfrak{u}_p,\mathfrak{U}_p)\\(\mathfrak{v}_1,\mathfrak{V}_1),\cdots,(\mathfrak{v}_q,\mathfrak{V}_q),(1-\rho+\mu,\omega)\end{matrix}\right]=$$

$$=\sum_{k=0}^{\infty}\binom{\mu}{k}\frac{\Gamma(\rho)}{\Gamma(\rho-\mu+k)}\ {}^{\alpha,\,\beta}_{\varepsilon,\,\delta}\gamma^{m,\,n+1}_{p+1,\,q+1}\left[cz^{\omega}\ \middle|\ \begin{matrix}(0,\omega),(\mathfrak{u}_1,\mathfrak{U}_1,x),(\mathfrak{u}_2,\mathfrak{U}_2),\cdots,(\mathfrak{u}_p,\mathfrak{U}_p)\\(\mathfrak{v}_1,\mathfrak{V}_1),\cdots,(\mathfrak{v}_q,\mathfrak{V}_q),(k,\omega)\end{matrix}\right]. \tag{20}$$

Theorem 2.4. *Let $\rho\geqslant 1$, $\omega>0$, $m\in\mathbb{N}$ and $m-1\leqslant\mathbb{R}(\mu)\leqslant m$, then the subsequent result sustains:*

$${}^{\alpha,\,\beta}_{\varepsilon,\,\delta}\gamma^{m+1,\,n}_{p+1,\,q+1}\left[cz^{-\omega}\ \middle|\ \begin{matrix}(\mathfrak{u}_1,\mathfrak{U}_1,x),(\mathfrak{u}_2,\mathfrak{U}_2),\cdots,(\mathfrak{u}_p,\mathfrak{U}_p),(\rho-\mu,\omega)\\(\rho,\omega),(\mathfrak{v}_1,\mathfrak{V}_1),\cdots,(\mathfrak{v}_q,\mathfrak{V}_q),\end{matrix}\right]=$$

$$=\sum_{k=0}^{\infty}\binom{\mu}{k}\frac{\Gamma(\rho)}{\Gamma(\rho-\mu+k)}\ {}^{\alpha,\,\beta}_{\varepsilon,\,\delta}\gamma^{m+1,\,n}_{p+1,\,q+1}\left[cz^{-\omega}\ \middle|\ \begin{matrix}(\mathfrak{u}_1,\mathfrak{U}_1,x),(\mathfrak{u}_2,\mathfrak{U}_2),\cdots,(\mathfrak{u}_p,\mathfrak{U}_p),(1-\mu,\omega)\\(1,\omega),(\mathfrak{v}_1,\mathfrak{V}_1),\cdots,(\mathfrak{v}_q,\mathfrak{V}_q)\end{matrix}\right]. \tag{21}$$

3. Specific cases and final remarks

During this portion, we produce the expansion formulae for R-functions and additional incomplete functions as a specific example to illustrate our primary findings. In particular, throughout $x=0$ (as well as by applying the formula for decomposition), the results involving R-functions would roughly correspond with the specific examples of the implications provided in the preceding section, as follows:

Theorem 3.1. *Suppose $\rho \geqslant 1$, $\omega > 0$, $m \in \mathbb{N}$ and $m-1 \leqslant \mathbb{R}(\mu) \leqslant m$, then the subsequent consequence sustains:*

$$ {}^{\alpha,\,\beta}_{\varepsilon,\,\delta}R^{m,\,n+1}_{p+1,\,q+1}\left[cz^{\omega}\,\middle|\,\begin{matrix}(1-\rho,\omega),(\mathfrak{u}_1,\mathfrak{U}_1),(\mathfrak{u}_2,\mathfrak{U}_2),\cdots,(\mathfrak{u}_p,\mathfrak{U}_p)\\(\mathfrak{v}_1,\mathfrak{V}_1),\cdots,(\mathfrak{v}_q,\mathfrak{V}_q),(1-\rho+\mu,\omega)\end{matrix}\right] = $$

$$ =\sum_{k=0}^{\infty}\binom{\mu}{k}\frac{\Gamma(\rho)}{\Gamma(\rho-\mu+k)}\,{}^{\alpha,\,\beta}_{\varepsilon,\,\delta}R^{m,\,n+1}_{p+1,\,q+1}\left[cz^{\omega}\,\middle|\,\begin{matrix}(0,\omega),(\mathfrak{u}_1,\mathfrak{U}_1),(\mathfrak{u}_2,\mathfrak{U}_2),\cdots,(\mathfrak{u}_p,\mathfrak{U}_p)\\(\mathfrak{v}_1,\mathfrak{V}_1),\cdots,(\mathfrak{v}_q,\mathfrak{V}_q),(k,\omega)\end{matrix}\right]. \quad (22) $$

Theorem 3.2. *Let $\rho \geqslant 1$, $\omega > 0$, $m \in \mathbb{N}$ and $m-1 \leqslant \mathbb{R}(\mu) \leqslant m$, then the subsequent outcome sustains:*

$$ {}^{\alpha,\,\beta}_{\varepsilon,\,\delta}R^{m+1,\,n}_{p+1,\,q+1}\left[cz^{-\omega}\,\middle|\,\begin{matrix}(\mathfrak{u}_1,\mathcal{A}1),(\mathfrak{U}_2,\mathcal{A}2),\cdots,(\mathfrak{u}_p,\mathcal{A}p),(\rho-\mu,\omega)\\(\rho,\omega),(\mathfrak{v}_1,\mathfrak{V}_1),\cdots,(\mathfrak{v}_q,\mathfrak{V}_q),\end{matrix}\right] = $$

$$ =\sum_{k=0}^{\infty}\binom{\mu}{k}\frac{\Gamma(\rho)}{\Gamma(\rho-\mu+k)}\,{}^{\alpha,\,\beta}_{\varepsilon,\,\delta}R^{m+1,\,n}_{p+1,\,q+1}\left[cz^{-\omega}\,\middle|\,\begin{matrix}(\mathfrak{u}_1,\mathfrak{U}_1),(\mathfrak{u}_2,\mathfrak{U}_2),\cdots,(\mathfrak{u}_p,\mathfrak{U}_p),(1-\mu,\omega)\\(1,\omega),(\mathfrak{v}_1,\mathfrak{V}_1),\cdots,(\mathfrak{v}_q,\mathfrak{V}_q)\end{matrix}\right]. \quad (23) $$

Once more, the key results in the preceding section simply reduce to the well-known expansion formulae for incomplete H-functions, which are recently studied by [16], on setting $\alpha = 1$ and $\beta = 0$ (or $\varepsilon = 0$ and $\delta = 0$). Furthermore, the family of incomplete R-functions provides a range of special functions (including incomplete functions) such as Fox's H-functions, G-functions, Fox-Wright functions, hypergeometric functions, etc., by setting specific values to the parameters.

In this paper, we have established expansion formulas for the incomplete family of R-functions using the Leibniz formula involving Riemann-Liouville type fractional derivatives. We also derive special cases of our main results. It's worth noting that specific instances of our findings, such as when $x = 0$ or utilizing the decomposition formula, yield new expansion formulas involving classical Rathie's R-functions and other generalized hypergeometric functions. Thus, we finalize by suggesting that the results discussed herein appear to have a broad applicability and can lead to different expansion formulas regarding a specific category of special functions, that we do leave for anyone with an interest to explore further.

References

[1] A.K.Arora, C.L.Koul, Applications of fractional calculus, *Indian J. Pure Appl. Math.*, **18**(1987), 931–937.

[2] S.Bhatter, K.Jangid, S.Kumawat, S.D.Purohit, Determining glucose supply in blood using the incomplete I-function, *Partial Differential Equations in Applied Mathematics*, **10**(2024), 100729. DOI: 10.1016/j.padiff.2024.100729

[3] S.Bhatter, S.Kumawat, K.Jangid, S.D. Purohit, H.M. Baskonus, Fractional differential equations related to an integral operator involving the incomplete I-function as a kernel, *Math. Methods Appl. Sci.*, **46**(2023), no. 14, 15033–15047.

[4] B.L.J.Braaksma, Asymptotic expansions and analytic continuations for Barnes' integrals, *Compositio Mathematica*, **15**(1964), 239–341.

[5] Y.A.Brychkov, Handbook of Special Functions, Derivatives, Integrals, Series and Other Formulas, CRC Press, Taylor & Francis Group, Boca Raton, London, and New York, 2008.

[6] C.Fox, The G and H functions as symmetrical Fourier kernels, *Trans. Amer. Math. Soc.*, **98**(1961), 395–429.

[7] R.Gupta, P.Purohit, Unified integrals involving generalized hypergeometric R-function, *Adv. Math. Sci. Appl.*, **33**(2024), no. 2, 525-536.

[8] R.Gupta, P.Purohit, An incomplete category comprised of R-functions and their implications, *J. Nonlinear Convex Anal.*, **25**(2024), no. 9, 2249–2268.

[9] B.B.Jaimini, N.Shrivastava, H.M.Srivastava, The integral analogue of the Leibniz rule for fractional calculus and its applications involving functions of several variables, *Comput. Math. Appl.*, **41**(2001), no. 12, 149–155.

[10] K.Jangid, S.Bhatter, S.Meena, S.D.Purohit, Certain classes of the incomplete I-functions and their properties, *Discontin. Nonlinearity Complex.*, **12**(2023), no. 2, 437–454.
DOI: 10.5890/DNC.2023.06.014

[11] D.G.Kabe, Some applications of Meijer's G-functions to distribution problems in Statistics, *Biometrika*, **45**(1958), 578–580.

[12] Kritika and S.D.Purohit, An analysis of the Yang $\mathbb{Y}$-function class extension through its incomplete functions, *Int. J. Geom. Methods Mod. Phys.*, (2024).
DOI: 10.1142/S0219887824400218

[13] A.M.Mathai, R.K.Saxena, Generolized Hypergeometric Functions with Appli-cations in Statistics and Physical Sciences, Springer Verlag Lecture Notes Series in Mathematics, No. 348, New York, 1973.

[14] A.M.Mathai, R.K.Saxena, H.J.Haubold, The H-function with Applications in Statistics and Other Disciplines, Wiley, New York, 1978.

[15] A.M.Mathai, R.K.Saxena, H.J.Haubold, The H-Functions: Theory and Applications, Springer, New York, 2010.

[16] S.Meena, S.Bhatter, K.Jangid, S.D.Purohit, Certain expansion formulae of the incomplete H-functions assocaited with Leibniz rule, *TWMS J. App. and Eng. Math.*, **12**(2022), no. 2, 579–587.

[17] S.Min, Some algebra of Leibniz rule for fractional calculus, *Int. J. Innov. Sci. Math.*, **4**(2016), no. 6, 204–208.

[18] R.K.Parmar, R.K.Saxena, Incomplete extended Hurwitz-Lerch zeta functions and associated properties, *Commun. Korean Math. Soc.*, **32**(2017), 287–304.

[19] P. Purohit, R. Gupta, C. Sharma, Environmental pollution's effect on biological populations and incomplete R-function, 2024 IEEE 3rd World Conference on Applied Intelligence and Computing (AIC), Gwalior, India, 2024, 366–370.

[20] S.D.Purohit, K.Jangid, N.Jangra, M.E.Samei, S.Bhatter, A Study of the RLC, RC, and RL Electric Circuits Associated with Incomplete I-Functions. In: Singh, J., Anastassiou, G.A., Baleanu, D., Kumar, D. (eds) Advances in Mathematical Modelling, Applied Analysis and Computation. ICMMAAC 2024. Lecture Notes in Networks and Systems, vol. 1395. Springer, Cham.

[21] S.D.Purohit, A.M.Khan, D.L.Suthar, S.Dave, The impact on raise of environmental pollution and occurrence in biological populations pertaining to incomplete H-function, *Natl. Acad. Sci. Lett.*, **44**(2021), no. 3, 263–266.

[22] S.D.Purohit, D.L.Suthar, Ali A.Al-Jarrah, V.K.Vyas, K.S.Nisar, Certain expansion formulae involving incomplete I-functions, *TWMS J. App. & Eng. Math.*, **14**(2024), no. 1, 402–409.

[23] P.N.Rathie, G and H-functions and statistical distributions, *Metron*, **36**(1978), no. 3-4, 141–149.

[24] P.N.Rathie, Generalized hypergeometric functions and exact distributions of test statistics, *American Journal of Mathematical and Management Sciences*, **9**(1989), no. 1-2, 155–175.

[25] H.M.Srivastava, M.A.Chaudhry, R.P.Agarwal, The incomplete Pochhammer symbols and their applications to hypergeometric and related functions, *Int. Trans. Spec. Funct.*, **23**(2012), 659–683.

[26] H.M.Srivastava, K.C.Gupta, S.P.Goyal, The H-functions of one and two variables with applications, South Asian Publ., New Delhi and Madras, 1982.

[27] H.M.Srivastava, R.K.Saxena, R.K.Parmar, Some families of the incomplete H-functions and the incomplete $\bar{H}$-functions and associated integral transforms and operators of fractional calculus with applications, *Russ. J. Math. Phys.*, **25**(2018), 116–138.
DOI: 10.1134/S1061920818010119

Некоторые неполные формулы разложения R-функций, использующие дробное исчисление

Рави Гупта
Прити Пурохит
Школа наук и технологий
Открытый университет имени Вардхмана Махавира
Кота, Индия

Аннотация. В данной работе исследуются формулы разложения неполных R-функций с точки зрения дробного исчисления. Мы раскрываем глубинные связи между операторами дробного исчисления и неполными R-функциями посредством строгих математических вычислений и анализа. Используя формулу Лейбница в дробном дифференцировании, мы стремимся получить новые формулы разложения, которые открывают новые перспективы для изучения характеристик и поведения этих функций. Результаты данного исследования открывают новые направления в изучении формул изображения дробного исчисления с неполными R-функциями и новые пути развития научного понимания. В качестве конкретной иллюстрации, демонстрирующей наши основные результаты, выводятся формулы разложения для дополнительных специальных функций, а также для неполных функций.

Ключевые слова: неполная гамма-функция, неполные R-функции, формула Лейбница, дробное исчисление.

EDN: EMSCZU
УДК 517.9

Maximal Operators Associated with Singular Surfaces

Salim E. Usmanov*
Samarkand State University named after Sharof Rashidov
Samarkand, Uzbekistan
Kimyo International University in Tashkent
Tashkent, Uzbekistan
Ismail Ekincioglu†
Istanbul Medeniyet University
Istanbul, Turkey

Received 10.09.2024, received in revised form 27.11.2024, accepted 19.10.2025

Abstract. Maximal operators associated with a class of singular parametrized surfaces in $\mathbb{R}^3$ are analyzed in the paper. Boundedness of such operators in Lebesgue L^p space for $p > 2$ is shown. It is also proved that at least one of the principal curvatures does not vanish at each regular point of these surfaces.

Keywords: Maximal operator, averaging operator, fractional power series, singular surface, principal curvatures.

Citation: S.E. Usmanov, I. Ekincioglu, Maximal Operators Associated with Singular Surfaces, J. Sib. Fed. Univ. Math. Phys., 2026, 19(1), 80–87. EDN: EMSCZU.

1. Introduction and preliminaries

Let S be a hypersurface in $\mathbb{R}^{n+1}$ with a surface measure dS. Let us denote the "average" of f on $\mathbb{R}^{n+1}$ along the t-dilate of the hypersurface S as

$$\mathcal{A}_t f(y) := \int_S f(y - tx)\psi(x)dS(x),\ t > 0,$$

where ψ is a non-negative infinitely smooth function with compact support, i.e., $0 \leqslant \psi \in C_0^\infty(\mathbb{R}^{n+1})$ and $f \in C_0^\infty(\mathbb{R}^{n+1})$.

The associated maximal operator is defined by the following relation

$$\mathcal{M}f(y) := \sup_{t>0} \mid \mathcal{A}_t f(y) \mid . \tag{1}$$

The maximal operator (1) is said to be bounded on $L^p := L^p(\mathbb{R}^{n+1})$ if there exists $C > 0$ such that for any function $f \in C_0^\infty(\mathbb{R}^{n+1})$ the inequality

$$\|\mathcal{M}f\|_{L^p} \leqslant C \|f\|_{L^p}$$

holds true, where $\|\cdot\|_{L^p}$ is the natural norm of space L^p.

*usmanov-salim@mail.ru https://orcid.org/0000-0002-2065-8788
†ismail.ekincioglu@medeniyet.edu.tr https://orcid.org/0000-0002-5636-1214

The prototype of such kind of maximal operators is Stein's maximal function (in which S is the Euclidean unit sphere centred at the origin). It is known [1] that spherical maximal operator (1) is bounded on $L^p(\mathbb{R}^n)$ for $p > \dfrac{n}{n-1}, n \geqslant 3$ and it is not bounded on $L^p(\mathbb{R}^n)$ whenever $p \leqslant \dfrac{n}{n-1}$. The two dimensional case of Stein's result was considered by Bourgain [2].

Then Greenleaf proved that maximal operator (1) is bounded on $L^p(\mathbb{R}^{n+1})$ for $n \geqslant 2$ and $p > (n+1)/n$ when hypersurface has everywhere non-vanishing Gaussian curvature [3]. Moreover, Greenleaf showed that if hypersurface has at least $k (k \geqslant 2)$ non-vanishing principal curvatures then maximal operator is bounded on $L^p(\mathbb{R}^{n+1})$ $(n \geqslant 2)$ for all $p > (k+1)/k$. Later similar result for more difficult case $k = 1$ was obtained by Sogge [4].

Also, maximal operators (1) have been investigated [5–9]. Boundedness of maximal operators related to singular surfaces in three and multidimensional Euclidean spaces was studied [10–16].

2. Statement of the problem

Definition of the fractional power series is given in [17].

Definition 1. *Let $V \subseteq \mathbb{R}^n_+$ be an open connected set such that $0 \in \bar{V}$, f is called a fractional power series in set V if there is an open set $W \subseteq \mathbb{R}^n$ containing $\bar{V}$, a natural number N and a real analytic function g in $\Phi_N^{-1}(W)$ such that the identity $f = g \circ \Phi_{1/N}$ holds in set V, where $\Phi_N : \mathbb{R}^n \to \mathbb{R}^n$ is a map given by the formula $\Phi_N(x) = (x_1^N, x_2^N, \ldots, x_n^N)$.*

Let us consider a class of singular parametrized surfaces in $\mathbb{R}^3$ defined by

$$x_1(u_1,u_2) = r_1 + u_1^{a_1}u_2^{a_2}g_1(u_1,u_2),\ x_2(u_1,u_2) = r_2 + u_1^{b_1}u_2^{b_2}g_2(u_1,u_2),$$

$$x_3(u_1,u_2) = r_3 + u_1^{c_1}u_2^{c_2}g_3(u_1,u_2), \tag{2}$$

where r_1, r_2, r_3 are any real numbers, $a_1, a_2, b_1, b_2, c_1, c_2$ are non-negative rational numbers, $u_1 \geqslant 0, u_2 \geqslant 0$ and $\{g_k(u_1,u_2)\}_{k=1}^3$ are fractional power series.

For further statements the following designations are introduced

$$B_1 = \begin{vmatrix} a_1 & b_1 \\ a_2 & b_2 \end{vmatrix},\ B_2 = \begin{vmatrix} b_1 & c_1 \\ b_2 & c_2 \end{vmatrix},\ B_3 = \begin{vmatrix} a_1 & c_1 \\ a_2 & c_2 \end{vmatrix}.$$

L^p — boundedness of the maximal operator (1) was studied in a small neighborhood of the point $(r_1, r_2, r_3) \neq (0,0,0)$ [10–12, 15, 16], when $p > 2$ and at least two of the numbers B_1, B_2, B_3 are non-zero. $L^p\,(p > 2)$ — boundedness of the maximal operators related to singular hypersurfaces in the multidimensional Euclidean spaces was studied [13, 14].

In this paper, the case $r_1 = r_2 = r_3 = 0$ in (2) is investigated. More precisely, the problem of $L^p\,(p > 2)$ — boundedness of the maximal operator (1) along the parametrized surfaces of the form

$$x_1(u_1,u_2) = u_1^{a_1}u_2^{a_2}g_1(u_1,u_2),\ x_2(u_1,u_2) = u_1^{b_1}u_2^{b_2}g_2(u_1,u_2), x_3(u_1,u_2) = u_1^{c_1}u_2^{c_2}g_3(u_1,u_2) \tag{3}$$

is studied. These surfaces satisfy the following condition.

Remark 1. *If at least one of the numbers B_1, B_2, B_3 is non-zero then points of surface* (3) *lying in a sufficiently small neighbourhood of the origin in $\mathbb{R}^3_+$ outside the coordinate planes are regular (nonsingular). Points of surface* (3) *lying on the coordinate planes may be singular* (*see definition* 2 *in* [10]).

The averaging operator associated with surface (3) is defined as follows

$$\mathcal{A}_t^g f(y) = \int_{\mathbb{R}^2_+} f\Big(y_1 - tu_1^{a_1}u_2^{a_2}g_1(u_1,u_2), y_2 - tu_1^{b_1}u_2^{b_2}g_2(u_1,u_2), y_3 - tu_1^{c_1}u_2^{c_2}g_3(u_1,u_2)\Big)\times \\ \times \psi(u_1,u_2)du_1du_2.$$

Then corresponding maximal operator is defined by

$$\mathcal{M}^g f(y) := \sup_{t>0} |\mathcal{A}_t^g f(y)|,\ y \in \mathbb{R}^3.$$

For the case of smooth surfaces it corresponds to a surface integral.

3. Auxiliary assertions

Let us state some necessary facts known from geometry which are used to prove main result. As usual, the first and second fundamental forms of surfaces (3) have the following forms

$$G(u,du) = g_{11}(u_1,u_2)du_1^2 + 2g_{12}(u_1,u_2)du_1du_2 + g_{22}(u_1,u_2)du_2^2,$$
$$L(u,du) = l_{11}(u_1,u_2)du_1^2 + 2l_{12}(u_1,u_2)du_1du_2 + l_{22}(u_1,u_2)du_2^2,$$

respectively. Coefficients of the fundamental forms are calculated by the following formulas

$$g_{ij} = g_{ij}(u_1,u_2) = (\bar{r}_i\bar{r}_j),\ \ l_{ij} = l_{ij}(u_1,u_2) = (\bar{r}_{ij},\bar{m}), \tag{4}$$

where $\bar{r}_i = \dfrac{\partial \bar{r}}{\partial u_i}$, $\bar{r}_{ij} = \dfrac{\partial^2 \bar{r}}{\partial u_i u_j}$, $i,j = 1,2$, $\bar{m}$ is the unit normal vector at each regular point of surfaces (3).

Next let us use the change of variables

$$u_1 = u_1(z_1,z_2),\ \ u_2 = u_2(z_1,z_2) \tag{5}$$

in (3), where $u_1(z_1,z_2), u_2(z_1,z_2)$ are differentiable functions in a neighbourhood of zero in $\mathbb{R}^2$. Jacobi matrix of transformation (5) is denoted by J. Then the following lemma is valid.

Lemma 1. *If $detJ \neq 0$ then equalities $|\widetilde{L} - \lambda\widetilde{G}| = 0$ and $|L - \lambda G| = 0$ are equivalent equations, where $\widetilde{G}$ and $\widetilde{L}$ are matrices of the first and second fundamental forms of surfaces* (3) *after the change of variables* (5).

Proof. Indeed, applying the change of coordinates (5), matrices g_{ij} are transformed by the following rules

$$\widetilde{g}_{ij}(z_1,z_2) = \sum_{k,l} g_{kl}(u_1,u_2)\frac{\partial u_k}{\partial z_i}\frac{\partial u_l}{\partial z_j},\ \ k,l = 1,2$$

or in the matrix form $\widetilde{G} = J^T G J$, and, analogously, $\widetilde{L} = J^T L J$ (see [18], chapter 3, Sec. 16).

Obviously, principal curvatures of surfaces (3) are defined as solutions of the equation $|L - \lambda G| = 0$. It is easy to show that equality

$$|\widetilde{L} - \lambda\widetilde{G}| = (detJ)^2|L - \lambda G|$$

holds true for surfaces (3). Hence, this equation indicates that lemma is correct. □

The proof of main result of this paper is based on the following result due to Sogge [4].

Theorem 1. *Let S be a smooth hypersurface in $\mathbb{R}^n, n \geqslant 2$, with the property that at each $x \in S$ at least one principal curvature is non-zero. With $\mathcal{M}f$ as in* (1) *above then $\mathcal{M}f$ is bounded on $L^p(\mathbb{R}^n)$ for $p > 2$.*

4. Main result

The main result of the paper is the following theorem.

Theorem 2. *Let $\{g_k(u_1,u_2)\}_{k=1}^3$ be fractional power series which defined in a small neighbourhood of the origin of coordinate system of $\mathbb{R}^2$ and satisfy the following conditions: $g_k(0,0)\neq 0$. Suppose that at least one of the following conditions is satisfied:*

1. $B_1\neq 0$ and either $B_2B_3\neq 0$, or $B_2(B_2+B_1)\neq 0$, or $B_3(B_3-B_1)\neq 0$;

2. $B_3\neq 0$ and either $B_2B_1\neq 0$, or $B_2(B_2-B_3)\neq 0$, or $B_1(B_1-B_3)\neq 0$;

3. $B_2\neq 0$ and either $B_1B_3\neq 0$, or $B_3(B_3-B_2)\neq 0$, or $B_1(B_1+B_2)\neq 0$.

Then there exists a small neighbourhood U of the origin in $\mathbb{R}^3$, such that for any function $\psi\in C_0^\infty(U)$ maximal operator $\mathcal{M}^g f$ is bounded on $L^p(\mathbb{R}^3)$ for $p>2$.

Proof. Suppose that condition 1 is satisfied. Let us study the boundedness of maximal operator $\mathcal{M}^g f$ at nonsingular points of surface (3) (see Remark 1).

Using the change of variables

$$u_1=2^{-j_1}v_1,\ u_2=2^{-j_2}v_2$$

in (3), one can obtain

$$\begin{aligned}
\tilde{x}_1(v_1,v_2)&=2^{-(j_1a_1+j_2a_2)}v_1^{a_1}v_2^{a_2}g_1(2^{-j_1}v_1,2^{-j_2}v_2),\\
\tilde{x}_2(v_1,v_2)&=2^{-(j_1b_1+j_2b_2)}v_1^{b_1}v_2^{b_2}g_2(2^{-j_1}v_1,2^{-j_2}v_2),\\
\tilde{x}_3(v_1,v_2)&=2^{-(j_1c_1+j_2c_2)}v_1^{c_1}v_2^{c_2}g_3(2^{-j_1}v_1,2^{-j_2}v_2),
\end{aligned}\tag{6}$$

where $0,5\leqslant v_1\leqslant 2,\ 0,5\leqslant v_2\leqslant 2,\ j_1,j_2\geqslant j_0,\ j_0$ is a large number such that implies from the smallness of the support of ψ.

Next, let us introduce the change of variables

$$\begin{cases} w_1=v_1^{a_1}v_2^{a_2}g_1(2^{-j_1}v_1,2^{-j_2}v_2)\\ w_2=v_1^{b_1}v_2^{b_2}g_2(2^{-j_1}v_1,2^{-j_2}v_2),\end{cases}\tag{7}$$

and assume that $g_1(0,0)=g_2(0,0)=1$. If $g_1(0,0)<0,\ g_2(0,0)<0$, then one can obtain $-g_1(u_1,u_2),-g_2(u_1,u_2)$ instead of $g_1(u_1,u_2),g_2(u_1,u_2)$.

Now, calculating Jacobian of coordinate change (7), one can find

$$detJ_1=\begin{vmatrix}\dfrac{\partial w_1}{\partial v_1} & \dfrac{\partial w_2}{\partial v_1}\\ \dfrac{\partial w_1}{\partial v_2} & \dfrac{\partial w_2}{\partial v_2}\end{vmatrix}=v_1^{a_1+b_1-1}v_2^{a_2+b_2-1}\Big(B_1g_1(2^{-j_1}v_1,2^{-j_2}v_2)g_2(2^{-j_1}v_1,2^{-j_2}v_2)+h(v_1,v_2)\Big),$$

where

$$h(v_1,v_2)=v_1h_1(v_1,v_2)+v_2h_2(v_1,v_2)+v_1v_2h_3(v_1,v_2),$$

$$h_1(v_1,v_2)=b_2g_2(2^{-j_1}v_1,2^{-j_2}v_2)\frac{\partial g_1(2^{-j_1}v_1,2^{-j_2}v_2)}{\partial v_1}-a_2g_1(2^{-j_1}v_1,2^{-j_2}v_2)\frac{\partial g_2(2^{-j_1}v_1,2^{-j_2}v_2)}{\partial v_1},$$

$$h_2(v_1,v_2)=a_1g_1(2^{-j_1}v_1,2^{-j_2}v_2)\frac{\partial g_2(2^{-j_1}v_1,2^{-j_2}v_2)}{\partial v_2}-b_1g_2(2^{-j_1}v_1,2^{-j_2}v_2)\frac{\partial g_1(2^{-j_1}v_1,2^{-j_2}v_2)}{\partial v_2},$$

$$h_3(v_1,v_2)=\frac{\partial g_1(2^{-j_1}v_1,2^{-j_2}v_2)}{\partial v_1}\frac{\partial g_2(2^{-j_1}v_1,2^{-j_2}v_2)}{\partial v_2}-\frac{\partial g_1(2^{-j_1}v_1,2^{-j_2}v_2)}{\partial v_2}\frac{\partial g_2(2^{-j_1}v_1,2^{-j_2}v_2)}{\partial v_1}$$

— fractional power series. It is not difficult to see that $detJ_1 \neq 0$ at the point (v_1, v_2).

Let us consider the system

$$\begin{cases} w_1 = v_1^{a_1} v_2^{a_2} \\ w_2 = v_1^{b_1} v_2^{b_2}, \end{cases}$$

in the first quadrant $\mathbb{R}^2_+$ and obtain

$$\begin{cases} v_1 = w_1^{\frac{b_2}{B_1}} w_2^{\frac{-a_2}{B_1}} \\ v_2 = w_1^{\frac{-b_1}{B_1}} w_2^{\frac{a_1}{B_1}}. \end{cases} \tag{8}$$

In particular, relation (8) is in the set

$$\{(w_1, w_2) \in \mathbb{R}^2_+ : 2^{-(a_1+a_2)} \leqslant w_1 \leqslant 2^{a_1+a_2},\, 2^{-(b_1+b_2)} \leqslant w_2 \leqslant 2^{b_1+b_2}\}$$

.

Further, let us also introduce the change of variables

$$\begin{cases} v_1 = w_1^{\frac{b_2}{B_1}} w_2^{\frac{-a_2}{B_1}} \hat{g}_1 \\ v_2 = w_1^{\frac{-b_1}{B_1}} w_2^{\frac{a_1}{B_1}} \hat{g}_2 \end{cases} \tag{9}$$

where $\hat{g}_1, \hat{g}_2$ are new variables and suppose that $\hat{g}_1 \sim 1, \hat{g}_2 \sim 1$. As a result, system (7) implies

$$\begin{aligned} &(\hat{g}_1)^{a_1} (\hat{g}_2)^{a_2} g_1\Big(2^{-j_1} w_1^{\frac{b_2}{B_1}} w_2^{\frac{-a_2}{B_1}} \hat{g}_1,\, 2^{-j_2} w_1^{\frac{-b_1}{B_1}} w_2^{\frac{a_1}{B_1}} \hat{g}_2\Big) = 1 \\ &(\hat{g}_1)^{b_1} (\hat{g}_2)^{b_2} g_2\Big(2^{-j_1} w_1^{\frac{b_2}{B_1}} w_2^{\frac{-a_2}{B_1}} \hat{g}_1,\, 2^{-j_2} w_1^{\frac{-b_1}{B_1}} w_2^{\frac{a_1}{B_1}} \hat{g}_2\Big) = 1. \end{aligned} \tag{10}$$

Analogously, one can show that Jacobian of system (10) is non-zero in a small neighbourhood of the point $(0, 0, 1, 1)$. In view of the implicit function theorem this system has smooth solutions with respect to $\hat{g}_1, \hat{g}_2$ of the form

$$\tilde{g}_1(2^{-j_1}, 2^{-j_2}, w_1, w_2) = 1 + 2^{-j_1} \tilde{h}_1(2^{-j_1}, 2^{-j_2}, w_1, w_2) + 2^{-j_2} \tilde{h}_2(2^{-j_1}, 2^{-j_2}, w_1, w_2),$$

$$\tilde{g}_2(2^{-j_1}, 2^{-j_2}, w_1, w_2) = 1 + 2^{-j_1} \tilde{\rho}_1(2^{-j_1}, 2^{-j_2}, w_1, w_2) + 2^{-j_2} \tilde{\rho}_2(2^{-j_1}, 2^{-j_2}, w_1, w_2)$$

in a sufficiently small neighborhood of the point $(0, 0, 1, 1)$. Here $\tilde{h}_1, \tilde{h}_2, \tilde{\rho}_1, \tilde{\rho}_2$ are smooth functions. It is assumed that $\tilde{g}_1(0, 0, 1, 1) = 1, \tilde{g}_2(0, 0, 1, 1) = 1$.

Then taking into account (9), one can obtain

$$\begin{cases} v_1 = w_1^{\frac{b_2}{B_1}} w_2^{\frac{-a_2}{B_1}} \tilde{g}_1(2^{-j_1}, 2^{-j_2}, w_1, w_2) \\ v_2 = w_1^{\frac{-b_1}{B_1}} w_2^{\frac{a_1}{B_1}} \tilde{g}_2(2^{-j_1}, 2^{-j_2}, w_1, w_2). \end{cases} \tag{11}$$

By applying relations (7) and (11) to equations (6), one can find

$$\hat{x}_1(w_1, w_2) = 2^{-(j_1 a_1 + j_2 a_2)} w_1, \hat{x}_2(w_1, w_2) = 2^{-(j_1 b_1 + j_2 b_2)} w_2,$$

$$\hat{x}_3(w_1, w_2) = 2^{-(j_1 c_1 + j_2 c_2)} \alpha(w_1, w_2), \tag{12}$$

where $\alpha(w_1,w_2)=w_1^{\frac{-B_2}{B_1}}w_2^{\frac{B_3}{B_1}}g(w_1,w_2)$,

$$g(w_1,w_2)=\big(\tilde g_1(2^{-j_1},2^{-j_2},w_1,w_2)\big)^{c_1}\big(\tilde g_2(2^{-j_1},2^{-j_2},w_1,w_2)\big)^{c_2}\times$$
$$\times g_3\Big(2^{-j_1}w_1^{\frac{b_2}{B_1}}w_2^{\frac{-a_2}{B_1}}\tilde g_1(2^{-j_1},2^{-j_2},w_1,w_2),2^{-j_2}w_1^{\frac{-b_1}{B_1}}w_2^{\frac{a_1}{B_1}}\tilde g_2(2^{-j_1},2^{-j_2},w_1,w_2)\Big).$$

It is well-known that second fundamental form of the surface given by parametric equations (12) has the following form

$$L=L_{11}dw_1^2+2L_{12}dw_1dw_2+L_{22}dw_2^2.$$

Using (4), one can find

$$L_{11}=(\bar r_{11},\bar n),\ L_{12}=(\bar r_{12},\bar n),\ L_{22}=(\bar r_{22},\bar n), \tag{13}$$
$$\bar r_{11}=\frac{\partial^2\bar r}{\partial w_1^2},\ \bar r_{12}=\frac{\partial^2\bar r}{\partial w_1\partial w_2},\ \bar r_{22}=\frac{\partial^2\bar r}{\partial w_2^2},$$

$\bar n=\bar N\cdot|\bar N|^{-1}$ is unit normal vector. A normal vector $\bar N$ in any point of surface (12) defined by

$$barN=\begin{vmatrix} i & j & k\\ \dfrac{\partial\hat x_1}{\partial w_1} & \dfrac{\partial\hat x_2}{\partial w_1} & \dfrac{\partial\hat x_3}{\partial w_1}\\ \dfrac{\partial\hat x_1}{\partial w_2} & \dfrac{\partial\hat x_2}{\partial w_2} & \dfrac{\partial\hat x_3}{\partial w_2}\end{vmatrix}.$$

Now calculating coefficients L_{11},L_{22} and L_{12}, one can obtain

$$L_{11}=\frac{\partial^2\alpha}{\partial w_1^2}=Cw_1^{-\frac{B_2}{B_1}-2}w_2^{\frac{B_3}{B_1}}\bigg(B_2(B_2+B_1)g(w_1,w_2)-B_2B_1w_1\frac{\partial g(w_1,w_2)}{\partial w_1}+B_1^2w_1^2\frac{\partial^2g(w_1,w_2)}{\partial w_1^2}\bigg),$$

$$L_{22}=\frac{\partial^2\alpha}{\partial w_2^2}=Cw_1^{-\frac{B_2}{B_1}}w_2^{\frac{B_3}{B_1}-2}\bigg(B_3(B_3-B_1)g(w_1,w_2)+B_3B_1w_2\frac{\partial g(w_1,w_2)}{\partial w_2}+B_1^2w_2^2\frac{\partial^2g(w_1,w_2)}{\partial w_2^2}\bigg),$$

$$L_{12}=\frac{\partial^2\alpha}{\partial w_1\partial w_2}=-Cw_1^{-\frac{B_2}{B_1}-1}w_2^{\frac{B_3}{B_1}-1}\bigg(B_2B_3g(w_1,w_2)-B_3B_1w_1\frac{\partial g(w_1,w_2)}{\partial w_1}+$$
$$+B_2B_1w_2\frac{\partial g(w_1,w_2)}{\partial w_2}-B_1^2w_1w_2\frac{\partial^2g(w_1,w_2)}{\partial w_1w_2}\bigg),$$

where $C=2^{-(j_1c_1+j_2c_2)}\dfrac{|\bar N|^{-1}}{B_1^2}$.

It follows from condition 1 that at least one of numbers B_2B_3, $B_2(B_2+B_1)$ and $B_3(B_3-B_1)$ is not equal to zero. Therefore, at least one of coefficients L_{11},L_{12} and L_{22} is non-zero at each regular point of surfaces (12) in a small neighbourhood of the origin for sufficiently large j_0.

Consequently, singular surfaces (12) as well as singular surfaces given by (3) have at least one non vanishing principal curvature at each regular point of these surfaces.

Thus, making similar arguments under conditions 2 or 3, one can show that in a small neighbourhood of the origin of $\mathbb{R}^3_+$ at least one of the principal curvatures of singular surfaces (3) is non-zero. Therefore, in view of Theorem 1 maximal operator $\mathcal{M}^gf$ is bounded on $L^p(\mathbb{R}^3)$ for $p>2$. This completes the proof of Theorem 2.

Let us now consider some corollaries in connection with Theorem 2.

Corollary 1. *Let $\{g_k(u_1,u_2)\}_{k=1}^3$ be real analytic functions defined in a small neighbourhood of the origin of coordinate system of $\mathbb{R}^2$ and satisfy the following conditions: $g_k(0,0)\neq 0$. Then under assumptions of Theorem 2 its assertions are true.*

Corollary 2. *If conditions 1-3 of Theorem 2 are replaced with the relations*
1. $B_1\neq 0, A_1^{-1}\bar{c}\neq(1,0)^T$, $A_1^{-1}\bar{c}\neq(0,1)^T$, $A_1^{-1}\bar{c}\neq(0,0)^T$;
2. $B_2\neq 0, A_2^{-1}\bar{a}\neq(1,0)^T$, $A_2^{-1}\bar{a}\neq(0,1)^T$, $A_2^{-1}\bar{a}\neq(0,0)^T$;
3. $B_3\neq 0, A_3^{-1}\bar{b}\neq(1,0)^T$, $A_3^{-1}\bar{b}\neq(0,1)^T$, $A_3^{-1}\bar{b}\neq(0,0)^T$,
respectively, and other conditions are satisfied then assertions of Theorem 2 hold true. Here A_1, A_2, A_3 are matrices of B_1, B_2, B_3, respectively, and $\bar{a}=(a_1,a_2)^T$, $\bar{b}=(b_1,b_2)^T$, $\bar{c}=(c_1,c_2)^T$.

References

[1] E.M.Stein, Maximal functions. Spherical means, *Proc.Nat. Acad. Sci. U.S.A.* **73**(1976), no. 7, 2174–2175.

[2] J.Bourgain, Averages in the plane convex curves and maximal operators, *J.Anal. Math.*, **47**(1986), 69–85.

[3] A.Greenleaf, Principal curvature and harmonic analysis, *Indiana Univ. Math. J.*, **30**(1981), 519–537.

[4] C.D.Sogge, Maximal operators associated to hypersurfaces with one nonvanishing principal curvature, *Fourier analysis and partial differential equations, Stud. Adv. Math.*, (1995), 317–323.

[5] C.D.Sogge, E.M.Stein, Averages of functions over hypersurfaces in $\mathbb{R}^n$, *Inventiones mathematicae.*, **82**(1985), 543–556.

[6] I.A.Ikromov, M.Kempe, D.Müller, Damped oscillatory integrals and boundedness of maximal operators associated to mixed homogeneous hypersurfaces, *Duke Math. J.*, **126**(2005), 471–490. DOI: 10.1215/S0012-7094-04-12632-6

[7] I.A.Ikromov, M.Kempe, D.Müller, Estimates for maximal functions associated to hypersurfaces in $\mathbb{R}^3$ and related problems of harmonic analysis, *Acta. Math.*, **204**(2010), 151–271. DOI: 10.1007/s11511-010-0047-6

[8] S.Buschenhenke, S.Dendrinos, I.A.Ikromov, D. Müller, Estimates for maximal functions associated to hypersurfaces in $\mathbb{R}^3$ with height $h<2$: Part I, *Trans. Amer. Math. Soc.* **372**(2019), no. 2, 1363–1406.

[9] I.A.Ikromov, S.E.Usmanov, On boundedness of maximal operators associated with hypersurfaces, *J. Math. Sci.*, **264**(2022), 715–745.

[10] S.E.Usmanov, The Boundedness of Maximal Operators Associated with Singular Surfaces, *Russ. Math.*, **65**(2021), 73–83. DOI: 10.3103/S1066369X21060086

[11] S.E.Usmanov, On the Boundedness Problem of Maximal Operators, *Russ. Math.*, **66**(2022), 74–83. DOI: 10.3103/S1066369X22040077

[12] S.E.Usmanov, On Maximal Operators Associated with a Family of Singular Surfaces, *J. Sib. Fed. Univ. Math. Phys.*, **16**(2023), no. 2, 265–274. EDN: UBLKLU

[13] S.E.Usmanov, On the Boundedness of the Maximal Operators Associated with Singular Hypersurfaces. *Math. Notes.*, **114**(2023), no. 1-2, 108–116. DOI: 10.1134/S0001434623070118

[14] S.E.Usmanov, On Maximal Operators Associated with Singular Hypersurfaces, *Russ. Math.*, **68**(2024), 61–68. DOI: 10.3103/S1066369X24700051

[15] S.E.Usmanov, On the Boundedness of Maximal Operators Associated with Singular Surfaces, *J. Sib. Fed. Univ. Math. Phys.*, **17**(2024), no. 4, 455–463. EDN: AVGDOC

[16] S.E.Usmanov, On Estimates for Maximal Operators Associated with Singular Surfaces, *Lobachevskii J. Math.*, **45**(2024), no. 2, 875–882. DOI: 10.1134/S1995080224600146

[17] T.Collins, A.Greenleaf, M.Pramanik, A multi-dimensional resolution of singularities with applications to analysis, *Amer. J. of Math.*, **135**(2013), 1179–1252.

[18] B.A.Dubrovin, S.P.Novikov, A.T.Fomenko, Contemporary geometry, Published in "Nauka", Moscow, 1979 (in Russian).

Максимальные операторы, связанные с сингулярными поверхностями

Салим Э. Усманов
Самаркандский государственный университет им. Ш. Рашидова
Самарканд, Узбекистан
Международный университет Киме в Ташкенте
Ташкент, Узбекистан
Исмаил Экинджиоглу
Стамбульский университет Медениет
Стамбул, Турция

Аннотация. Статья анализирует максимальные операторы, ассоциированные с классом сингулярных параметризованных поверхностей в $\mathbb{R}^3$, показывая ограниченность таких операторов в пространстве Лебега L^p при $p > 2$. Также доказано, что хотя бы одна из главных кривизн не обращается в нуль в каждой регулярной точке этих поверхностей.

Ключевые слова: максимальный оператор, оператор усреднения, дробно-степенной ряд, сингулярная поверхность, главные кривизны.

EDN: IYRKHL
УДК 517.8

Efficient Inverse Barrier Method for Nonlinear Optimization

Aicha Kraria*
Bachir Merikhi†
Djamel Benterki‡
Laboratory of Fundamental and Numerical Mathematics
Department of Mathematics
Setif 1 University Ferhat Abbas
Setif, 19000, Algeria
Adnan Yassine§
Laboratory of Applied Mathematics of Le Havre
Le Havre University Normandy
76600, Le Havre, France

Received 28.03.2025, received in revised form 21.08.2025, accepted 27.09.2025

Abstract. In this paper, we use a new variant of inverse barrier method to solve a nonlinear optimization problem. The new inverse barrier function depends on the components of the penalty vector and preserves the properties of the original problem. The descent direction is calculated using Newton's method, while the step size is calculated using the tangent technique and the backtracking with interpolation technique in parallel with Wolfe's method.
Comparative numerical simulations are presented as a support for our approach.

Keywords: interior point method, nonlinear programming, inverse barrier method.

Citation: A. Kraria, B. Merikhi, D. Benterki, A. Yassine, Efficient Inverse Barrier Method for Nonlinear Optimization, J. Sib. Fed. Univ. Math. Phys., 2026, 19(1), 88–99.
EDN: IYRKHL.

Introduction

Nonlinear optimization problems play a fundamental role in many practical applications. They can be written in the following form:

$$m_p = \min_{\xi}[g(\xi) : B\xi = q, \xi \geqslant 0]. \tag{P}$$

These problems can be solved using several methods, including interior point methods, which are recognized for their theoretical and practical efficiency. In this paper, we propose a new variant of inverse barrier method for solving nonlinear programming problems. In this method, problem (P) is approximated by problem (P_r):

$$m_{p_r} = \min_{\xi}[g_r(\xi) : \xi \in \mathbb{R}^n], \tag{P_r}$$

*aicha.kraria@univ-setif.dz
†bmerikhi@univ-setif.dz
‡djbenterki@univ-setif.dz
§adnan.yassine@univ-lehavre.fr

where

$$g_r(\xi) = \begin{cases} g(\xi) + \sum_{i=1}^{n} \frac{r_i}{\xi_i^{r_i}}, & \text{if } B\xi = q,\ \xi > 0 \\ +\infty & \text{otherwise,} \end{cases}$$

and $r = (r_1, r_2, \ldots, r_n)^T$ is a strictly positive barrier vector in $\mathbb{R}^n$.
The choice of the step size plays a crucial role in the efficiency and stability of interior point algorithms. Unfortunately, its calculation is not trivial. For this reason, several strategies have been developed to determine it. One of the most commonly used approaches is the approach of approximate functions, which was proposed by Crouzeix and Merikhi [6] for solving semidefinite programming problems. Based on the results of [6], numerous studies have been conducted on this technique (see e.g., [1, 4, 5, 7, 12, 13]).

In our work, we focus on calculating the step size using two techniques, tangent technique and backtracking with interpolation technique. In contrast, the descent direction is calculated using the classical Newton method.

This paper is organized as follows. In Section 2, we present the principle of the proposed inverse barrier method and the convergence result. In Section 3, we solve the penalized problem using Newton's method for the descent direction and the two techniques mentioned above for the step size. Section 4 contains the algorithm corresponding to this method. In Section 5, we perform comparative numerical tests to show the efficiency of our approach. Finally, a general conclusion is given in Section 5.

1. Inverse barrier method for nonlinear programming

Let us reconsider the nonlinear programming problem:

$$m_p = \min_{\xi}[g(\xi) : B\xi = q, \xi \geqslant 0], \tag{P}$$

where $g : \mathbb{R}^n \longrightarrow \mathbb{R}$ is a convex and twice differentiable function, $B \in \mathbb{R}^{m\times n}$ is a full rank matrix and $q \in \mathbb{R}^m$. We note by:

$$\mathcal{F} = \{\xi \in \mathbb{R}^n : B\xi = q,\ \xi \geqslant 0\},$$
$$\mathcal{F}^0 = \{\xi \in \mathbb{R}^n : B\xi = q,\ \xi > 0\},$$

the sets of feasible and strictly feasible solutions of (P).
In what follows, we assume that:

1. The set $\mathcal{F}^0$ is non-empty.
2. The set of optimal solutions of (P) is non-empty and bounded.

Since (P) is a convex problem, then solving this problem is equivalent to solve the following system given by Karush-Kuhn-Tucker (KKT) conditions [14]

$$\begin{cases} B\xi = q, & \xi \geqslant 0, \\ B^T y + \nabla g(\xi) = s, & s \geqslant 0, \\ \xi^T s = 0, \end{cases} \tag{1}$$

where y is a Lagrange multiplier.
Let (P_r) be the penalized problem associated to (P)

$$(P_r)\begin{cases} \min g_r(\xi), \\ \xi \in \mathbb{R}^n, \end{cases}$$

1.1. Theoretical study of the penalized problem (P_r)

1.1.1. Existence

Definition 1. *The function g_r is called inf-compact if its recession cone*
$C(g_r) = \Big\{d \in \mathbb{R}^n : (g_r)_\infty(d) \leqslant 0\Big\}$, *reduced to the origin, where $(g_r)_\infty$ is the asymptotic function of g_r, defined by:*

$$(g_r)_\infty(d) = \lim_{\alpha\to+\infty} \frac{g_r(\xi^* + \alpha d) - g_r(\xi^*)}{\alpha}.$$

Lemma 1. *Problem (P_r) has at least one optimal solution.*

Proof. To show that problem (P_r) admits a solution, it suffices to demonstrate that g_r is inf-compact. We have

$$\begin{aligned}(g_r)_\infty(d) &= \lim_{\alpha\to+\infty} \frac{g_r(\xi^* + \alpha d) - g_r(\xi^*)}{\alpha} = \\ &= \lim_{\alpha\to+\infty} \frac{g(\xi^* + \alpha d) - g(\xi^*)}{\alpha} + \lim_{\alpha\to+\infty} \frac{\sum\limits_{i=1}^{n} \frac{r_i}{(\xi_i^* + \alpha d_i)^{r_i}} - \sum\limits_{i=1}^{n} \frac{r_i}{(\xi_i^*)^{r_i}}}{\alpha} = \\ &= \lim_{\alpha\to+\infty} \frac{g(\xi^* + \alpha d) - g(\xi^*)}{\alpha},\end{aligned}$$

with $\xi^* + \alpha d \in \mathcal{F}$, so:

$$C(g_r) = \Big\{d \in \mathbb{R}^n : Bd = 0, d \geqslant 0, \lim_{\alpha\to+\infty} \frac{g(\xi^* + \alpha d) - g(\xi^*)}{\alpha} \leqslant 0\Big\}. \tag{2}$$

Since the set of optimal solutions of problem (P) is convex, we deduce from assumption 2 that its recession cone reduces to zero [11], i.e.,

$$\Big\{d \in \mathbb{R}^n : Bd = 0, d \geqslant 0, g(\xi^* + \alpha d) \leqslant g(\xi^*), \forall \alpha > 0\Big\} = \{0\},$$

this implies that

$$\Big\{d \in \mathbb{R}^n : Bd = 0, d \geqslant 0, \lim_{\alpha\to+\infty} \frac{g(\xi^* + \alpha d) - g(\xi^*)}{\alpha} \leqslant 0\Big\} = \{0\}. \tag{3}$$

from (2) and (3), we deduce that $C(g_r) = \{0\}$, hence, (P_r) has at least one solution. □

1.1.2. Uniqueness

Lemma 2. *Problem (P_r) has a unique optimal solution.*

Proof. Let $H(\xi) = \sum\limits_{i=1}^{n} \frac{r_i}{\xi_i^{r_i}}$, then

$$\nabla^2 H(\xi) = diag\Big(\frac{r^2(r+e)}{\xi^{r+2e}}\Big),$$

with

$$r^2 = (r_1^2, r_2^2, \ldots, r_n^2)^T, \quad e = (1, 1, \ldots, 1)^T, \quad \xi^{r+2e} = \left(\xi_1^{r_1+2}, \xi_2^{r_2+2}, \ldots, \xi_n^{r_n+2}\right)^T.$$

The matrix $\nabla^2 H$ is positive definite (because $r > 0, \xi > 0$), this implies that the function H is strictly convex, and since g is a convex function, then $g_r = g + H$ is strictly convex, which means that the problem (P_r) has a unique solution. □

1.1.3. Convergence

In the following lemma, we show the convergence of problem (P_r).

Lemma 3. *Let $\xi(r) = \xi_r$ be the optimal solution of problem (P_r), then $\xi^* = \lim_{\|r\| \to 0} \xi_r$ is an optimal solution of problem (P), where $\|.\|$ represents the Euclidean norm.*

Proof. To solve problem (P_r), it is sufficient to solve the following system

$$\begin{cases} \nabla g(\xi) - \dfrac{r^2}{\xi^{r+e}} + B^T y = 0, \\ B\xi = q. \end{cases} \tag{4}$$

Let $\xi \in \mathcal{F}$. Since the function g is convex and $\xi(r) = \xi_r \in \mathcal{F}$, then

$$g(\xi) \geqslant g(\xi(r)) + \langle \nabla g(\xi(r)), \xi - \xi(r) \rangle$$

using (4), we obtain

$$\begin{aligned} g(\xi) &\geqslant g(\xi(r)) + \left\langle \frac{r^2}{\xi_r^{r+e}} - B^T y, \xi - \xi(r) \right\rangle = \\ &= g(\xi(r)) + \left\langle \frac{r^2}{\xi_r^{r+e}}, \xi - \xi(r) \right\rangle - \left\langle B^T y, \xi - \xi(r) \right\rangle = \\ &= g(\xi(r)) + \left\langle \frac{r^2}{\xi_r^{r+e}}, \xi - \xi(r) \right\rangle - \left\langle y, B\xi - B\xi(r) \right\rangle \end{aligned}$$

since $\xi(r) \in \mathcal{F}$, then $B\xi - B\xi(r) = 0$, therefore

$$g(\xi) \geqslant g(\xi(r)) + \left\langle \frac{r^2}{\xi_r^{r+e}}, \xi - \xi(r) \right\rangle,$$

hence

$$\min_{\xi \in \mathcal{F}} g(\xi) \geqslant g(\xi(r)) + \left\langle \frac{r^2}{\xi_r^{r+e}}, \xi - \xi(r) \right\rangle,$$

i.e.,

$$g(\xi(r)) \leqslant \min_{\xi \in \mathcal{F}} g(\xi) - \left\langle \frac{r^2}{\xi_r^{r+e}}, \xi - \xi(r) \right\rangle. \tag{5}$$

Furthermore, we have

$$\min_{\xi \in \mathcal{F}} g(\xi) \leqslant g(\xi), \ \forall \xi \in \mathcal{F},$$

then

$$\min_{\xi\in\mathcal{F}} g(\xi) \leqslant g(\xi(r)). \tag{6}$$

From (5) and (6), we deduce that

$$\min_{\xi\in\mathcal{F}} g(\xi) \leqslant g(\xi(r)) \leqslant \min_{\xi\in\mathcal{F}} g(\xi) - \Big\langle \frac{r^2}{\xi^{r+e}}, \xi - \xi(r)\Big\rangle.$$

If $\|r\| \to 0$, then

$$\lim_{\|r\|\to 0} g(\xi(r)) = \min_{\xi\in\mathcal{F}} g(\xi) = g(\xi^*).$$

□

2. Newton descent direction and the line search

2.1. Descent direction

Computing the descent direction requires solving the following problem:

$$\begin{cases} \min\limits_{d} \frac{1}{2} d^T \nabla^2 g_r(\xi) d + \nabla^T g_r(\xi) d, \\ Bd = 0. \end{cases}$$

For solving this problem, we apply the optimality condition. Thus, we obtain

$$\begin{cases} \Big(\nabla^2 g(\xi) + diag\Big(\frac{r^2(r+e)}{\xi^{r+2e}}\Big)\Big) d + B^T v = \frac{r^2}{\xi^{r+e}} - \nabla g(\xi), \\ Bd = 0. \end{cases} \tag{7}$$

To show that the algorithm is well-defined, we must ensure the strict feasibility of the iterates. To achieve this, we integrate a step size α at each iteration, such that the new iteration will be defined by: $\xi^{k+1} = \xi^k + \alpha^k d^k$.

2.2. Line search

To calculate the step size that ensures the condition $\xi + \alpha d > 0$, we minimize the function $\theta : \mathbb{R}_{++} \to \mathbb{R}$, such that $\theta(\alpha) = g_r(\xi + \alpha d)$, that is a convex function, so its minimum is the solution to the following equation $\theta'(\alpha) = 0$. Unfortunately, solving this equation is very difficult, especially when the problem size is large. To avoid this difficulty we use two techniques to solve it.

2.2.1. Tangent technique

This technique involves the following steps:

1. We search for an interval $[\bar{a}, \bar{b}]$ which the step size α belongs to this interval, i.e., $\theta'(\bar{a})\theta'(\bar{b}) < 0$, with $\bar{a}, \bar{b} \in I = [0, \alpha_{max}[$ and

$$\alpha_{max} = \min_{i\in I}\Big\{\frac{-\xi_i}{d_i}\Big\}, \tag{8}$$

with $I = \{i : d_i < 0\}$.

2. Determine the tangents (T_1) and (T_2) at points $\bar{a}$ and $\bar{b}$, respectively, then determine the point of intersection $\bar{\alpha}$ of these tangents,

$$\bar{\alpha} = \frac{\theta(\bar{b}) - \theta(\bar{a}) - \theta'(\bar{b})\bar{b} + \theta'(\bar{a})\bar{a}}{\theta'(\bar{a}) - \theta'(\bar{b})}. \tag{9}$$

3. Finally, we verify if $|\theta'(\bar{\alpha})| \leqslant \epsilon$ and in this case we take $\alpha = \bar{\alpha}$. Otherwise, we have two cases:

   (a) If $\theta'(\bar{a})\theta'(\bar{\alpha}) < 0$, we replace $\bar{b}$ with $\bar{\alpha}$, then return to 2.

   (b) If $\theta'(\bar{\alpha})\theta'(\bar{b}) < 0$, we replace $\bar{a}$ with $\bar{\alpha}$, then return to 2.

The algorithm below details the steps involved in this technique.

Algorithm 1: Tangent technique

Input
Accuracy parameters $\epsilon > 0$;
Calculate α_{max} from (8);
$\bar{a} = 0$; $\bar{b} = \beta\alpha_{max}$, such that $0 < \beta < 1$ (β is close to 1 and verifies $\theta'(\beta\alpha_{\max}) > 0$);
$\alpha = \frac{\bar{b}}{2}$;
begin
While $|\theta'(\alpha)| > \epsilon$ **do**
If $\theta'(\bar{a})\theta'(\alpha) < 0$
$\bar{b} := \alpha$;
else if $\theta'(\alpha)\theta'(\bar{b}) < 0$
$\bar{a} := \alpha$;
end
Calculate α from (9);
end
If $\alpha > 1$
$\alpha := 1$;
end
end.

2.2.2. Backtracking with interpolation technique

The main idea behind this technique is to first determine an initial value ($j = 0$) for the step size

$$\alpha^{(j)} = \begin{cases} 1 & \text{if } \alpha_{max} > 1 \\ \eta\alpha_{max} & \text{if } \alpha_{max} \leqslant 1, \ (0 < \eta < 1). \end{cases} \tag{10}$$

Then, we verify whether the chosen value satisfies Armijo condition:

$$\theta(\alpha) \leqslant \theta(0) + w\alpha\theta'(0), \tag{11}$$

with $w \in [0, \frac{1}{2}]$, if not, we determine a new step $\alpha^{(j+1)} \in [\tau_{\min}\alpha^{(j)}, \tau_{\max}\alpha^{(j)}]$, where
$0 < \tau_{\min} < 1$, $\tau_{\min} < \tau_{\max} < 1$, by minimizing the function θ using a quadratic polynomial as an interpolation of θ to approximate its minimum. To model this polynomial, we use the most current information about θ:

$$\begin{cases} \theta(0) = g_r(\xi) \\ \theta'(0) = d^T \nabla g_r(\xi) \\ \theta(\alpha^{(j)}) = g_r(\xi + \alpha^{(j)} d) \end{cases}$$

therefore, the quadratic polynomial will be defined by: $Q(\alpha) = a\alpha^2 + b\alpha + c$, where

$$\begin{cases} a = \dfrac{g_r(\xi + \alpha^{(j)} d) - g_r(\xi) - \alpha^{(j)} d^T \nabla g_r(\xi)}{(\alpha^{(j)})^2}, \\ b = d^T \nabla g_r(\xi), \\ c = g_r(\xi). \end{cases} \tag{12}$$

Since Q is convex, its minimum is obtained by solving the equation $Q'(\alpha^*) = 0$, hence: $\alpha^* = -\frac{b}{2a}$. According to Armijo condition, we have $a > 0$, which gives: $\alpha^* > 0$.

We summarize this technique in the following algorithm:

Algorithm 2: Backtracking with interpolation technique

Input
Initial step α^0 (10); $w \in [0, \frac{1}{2}]$; $\tau_{\min} = 0.1$; $\tau_{\max} = 0.5$;
begin
$j := 0$;
While $\theta(\alpha^{(j)}) > \theta(0) + w\alpha^{(j)}\theta'(0)$ **do**
$s_1 := \tau_{\min}\alpha^{(j)}$; $s_2 := \tau_{\max}\alpha^{(j)}$;
Calculate a, b and c from (12);
$\alpha^{(j+1)} := -\frac{b}{2a}$;
If $\alpha^{(j+1)} < s_1$
$\alpha^{(j+1)} := s_1$;
else if $\alpha^{(j+1)} > s_2$
$\alpha^{(j+1)} := s_2$;
end
$j := j + 1$;
end
end.

3. Interior point algorithm for problem (P)

In this section, we present the algorithm corresponding to this method for problem (P).

Algorithm 3: Interior point algorithm for problem (P)

Input
A strictly feasible point ξ^0; A barrier vector r^0; Accuracy parameter $\epsilon > 0$;
An update parameter $\lambda \in]0, 1[$;
begin
1. $\xi := \xi^0$; $r := r^0$;
2. Calculate d from system (7);
While $\|d\| > \epsilon$ **do**
Calculate α using different techniques:
(Tangent technique, Backtracking with interpolation technique and Wolfe's method)
$\xi := \xi + \alpha d$;
Calculate d from system (7);
end
If $\|r\| > \epsilon$
$r = \lambda r$; then return to 2;
else
We obtained a good approximation of the optimal solution of (P);
end
end.

4. Numerical tests

In order to evaluate the efficiency of our approach, we conduct some numerical tests for several examples, comparing both techniques introduced in this paper with Wolfe's line search method. The algorithm was implemented in MATLAB, where we have taken $\epsilon = 10^{-3}$ and $\lambda = 0.1$. In the table of results, we denote by: N.I. (the number of iterations), T (the computation time in seconds), Method 1 (the approach that uses tangent technique), Method 2 (the approach that uses backtracking with interpolation technique), Method 3 (the approach that uses Wolfe's line search method).

Example 1 ([9]). $\min\left\{\frac{1}{2}\xi^T Q\xi + c^T\xi \ : \ B\xi = q,\ \xi \geqslant 0\right\}$, *where*

$$B = \begin{pmatrix}1 & 1 & 2 & 1\end{pmatrix},\ q = \begin{pmatrix}3\end{pmatrix},\ Q = \begin{pmatrix}4 & 2 & 2 & 0\\ 2 & 4 & 0 & 0\\ 2 & 0 & 2 & 0\\ 0 & 0 & 0 & 0\end{pmatrix},\ c = \begin{pmatrix}-8\\ -6\\ -4\\ 0\end{pmatrix}.$$

The obtained optimal solution is: $\xi^* = \begin{pmatrix}1.3336 & 0.7777 & 0.4444 & 0.0000\end{pmatrix}^T$.

Example 2 ([3]). $\min\left\{\frac{1}{2}\xi^T Q\xi + c^T\xi \ : \ B\xi = q,\ \xi \geqslant 0\right\}$, *where*

$$B = \begin{pmatrix}-1 & 1 & 0\\ 1 & 1 & 1\end{pmatrix},\ q = \begin{pmatrix}1\\ 2\end{pmatrix},\ Q = \begin{pmatrix}2 & 0 & 0\\ 0 & 2 & 0\\ 0 & 0 & 0\end{pmatrix},\ \ c = \begin{pmatrix}-2\\ -4\\ 0\end{pmatrix}.$$

The obtained optimal solution is: $\xi^* = \begin{pmatrix}0.5 & 1.499 & 0.0\end{pmatrix}^T$.

Example 3 ([5]). $\min\left\{\frac{1}{2}\xi^T Q\xi + c^T\xi \ : \ B\xi = q,\ \xi \geqslant 0\right\}$, *where*

$$B = \begin{pmatrix} 1 & 2 & 1 & 0 \\ 3 & 1 & 0 & 1 \end{pmatrix},\ q = \begin{pmatrix} 4 \\ 7 \end{pmatrix},\ Q = \begin{pmatrix} 2 & 0 & 0 & 0 \\ 0 & 2 & 0 & 0 \\ 0 & 0 & 0 & 0 \\ 0 & 0 & 0 & 0 \end{pmatrix},\quad c = \begin{pmatrix} -3 \\ -5 \\ 0 \\ 0 \end{pmatrix}.$$

The obtained optimal solution is: $\xi^* = \begin{pmatrix} 1 & 1.5 & 0 & 2.5 \end{pmatrix}^T$.

Example 4 ([3]).

$$\min\left\{\frac{1}{2}\xi^T Q\xi + c^T\xi \ : \ B\xi = q,\ \xi \geqslant 0\right\},$$

where

$$B = \begin{pmatrix} 1 & 1.2 & 1 & 1.8 & 0 \\ 3 & -1 & 1.5 & -2 & 1 \\ -1 & 2 & -3 & 4 & 2 \end{pmatrix},\quad Q = \begin{pmatrix} 20 & 1.2 & 0.5 & 0.5 & -1 \\ 1.2 & 32 & 1 & 1 & 1 \\ 0.5 & 1 & 14 & 1 & 1 \\ 0.5 & 1 & 1 & 15 & 1 \\ -1 & 1 & 1 & 1 & 16 \end{pmatrix},$$

$$q = \begin{pmatrix} 9.31 & 5.45 & 6.60 \end{pmatrix}^T,\quad c = \begin{pmatrix} 1 & -1.5 & 2 & 1.5 & 3 \end{pmatrix}^T.$$

The obtained optimal solution is:

$$\xi^* = \begin{pmatrix} 2.632 & 0.7018 & 1.3995 & 2.4643 & 1.0847 \end{pmatrix}^T.$$

The results obtained for these examples are summarized in the following Tab. 1.

Table 1. Numerical results obtained for fixed size examples

Examples	Size(m,n)	Method 1		Method 2		Method 3	
		N.I.	T	N.I	T	N.I	T
Example 1	(1,4)	13	0.0587	15	0.0301	21	0.0356
Example 2	(2,3)	7	0.0379	11	0.0237	14	0.0235
Example 3	(2,4)	14	0.0491	17	0.0252	28	0.0448
Example 4	(3,5)	7	0.0256	8	0.0129	13	0.0394

Example 5 ([2]).

$$\min\left\{\frac{1}{2}\xi^T Q\xi + c^T\xi \ : \ B\xi = q,\ \xi \geqslant 0\right\},$$

$$B(i,j) = \begin{cases} 1 & \text{if } (j = i \text{ or } j = i+m) \\ 0 & \text{otherwise,} \end{cases},\quad Q(i,j) = \begin{cases} 1 & \text{if } i = j \\ 0 & \text{otherwise,} \end{cases}$$

$$c(i) = \begin{cases} -1 & \text{if } i = 1:m \\ 0 & \text{if } i = m+1:n, \end{cases}$$
$$q(i) = 2 \quad \text{for } i = 1:m,$$

where $n = 2m$. *The obtained optimal solution is:*

$$\xi^*(i) = \begin{cases} 1.5 & \text{if } i = 1:m \\ 0.5 & \text{if } i = m+1:n. \end{cases}$$

Table 2. Numerical results obtained for example 5

Size(m,n)	Method 1		Method 2		Method 3	
	N.I.	T	N.I	T	N.I	T
(10,20)	6	0.0259	6	0.00926	9	0.0303
(100,200)	8	0.0593	7	0.03829	13	0.0599
(1000,2000)	7	2.6407	7	2.4064	14	4.7609
(1500,3000)	10	10.4664	10	10.0604	15	14.6968
(2000,4000)	10	20.9651	10	20.1461	15	29.3138

Example 6 ([8, 10]).

$$\begin{cases} \min\left[f(\xi) = \sum_{i=1}^{n} \xi_i \ln\left(\frac{\xi_i}{a_i}\right)\right] \\ \xi_i + \xi_{i+m} = q_i, \qquad\qquad i = 1:m,\ n = 2m \\ \xi \geqslant 0, \end{cases}$$

where $a_i \in \mathbb{R}_+^*$ *and* $q_i \in \mathbb{R}$.
We test this example for different values of m, a_i *and* q_i. *The results are summarized in the following tables.*

Table 3. Case 1: $a_i = 1$ and $q_i = 1$

Size(m,n)	Method 1		Method 2		Method 3	
	N.I.	T	N.I	T	N.I	T
(10,20)	8	0.0247	8	0.0112	11	0.019927
(100,200)	10	0.0958	9	0.03904	14	0.065
(150,300)	10	0.0978	10	0.0678	15	0.0815
(1000,2000)	10	3.5179	10	3.7226	14	4.500
(1500,3000)	11	11.6343	11	11.3652	15	13.3785
(2000,4000)	11	21.3618	11	20.7197	15	27.9176

Table 4. Case 2: $a_i = 1$ and $q_i = 6$

Size(m,n)	Method 1		Method 2		Method 3	
	N.I.	T	N.I	T	N.I	T
(10,20)	8	0.0211	8	0.0104	13	0.01967
(100,200)	9	0.0570	9	0.0415	18	0.0791
(150,300)	9	0.0813	9	0.0697	18	0.1252
(1000,2000)	10	4.2298	10	4.2054	19	7.8108
(1500,3000)	11	13.1987	11	12.7618	20	23.3412
(2000,4000)	11	28.0187	11	27.447	20	48.9402

Comments

Numerical tests we have carried out show that the tangent and backtracking with interpolation techniques perform unevenly in terms of number of iterations. In some examples, tangent technique takes fewer iterations, while in others, backtracking with interpolation takes fewer. However, in most cases, both methods converge with approximately iterations. While, Wolfe's

Table 5. Case 3: $a_i = 2$ and $q_i = 4$

Size(m, n)	Method 1		Method 2		Method 3	
	N.I.	T	N.I	T	N.I	T
(10,20)	9	0.0311	9	0.0180	17	0.0206
(100,200)	10	0.0654	10	0.0429	22	0.1018
(150,300)	10	0.1197	10	0.0642	22	0.1374
(1000,2000)	10	4.0826	10	3.7252	25	9.7089
(1500,3000)	11	12.3451	11	11.325	26	27.8858
(2000,4000)	11	24.2373	11	23.2449	26	58.7148

method always require more iterations than the other two techniques. In terms of computation time, backtracking with interpolation technique is consistently the fastest among the three methods.
Therefore, we conclude that both techniques introduced in this paper are more efficient than Wolfe's method.

Conclusion

In this work, we have succeeded in enriching the field of nonlinear optimization, by introducing a new solving method based on inverse barrier functions. In this regard, a theoretical and numerical study was conducted.
The numerical simulations performed show that the technique of backtracking with interpolation effectively reduces the computational cost of the proposed algorithm relative to the classical line search.

The authors are very grateful and would like to thank the Editor-in-Chief and the anonymous referees for their comments and suggestions which helped to improve the presentation of this paper.

References

[1] B.Alzalg, A logarithmic barrier interior-point method based on majorant functions for second-order cone programming, *Optim. Lett.*, **14**(2020), 729–746. DOI:10.1007/s11590-019-01404-1

[2] N.Boudjellal, Méthodes de points intérieurs pour la programmation quadratique convexe: théorie, Algorithmes et Applications, *Ferhat Abbas University Setif 1, Algeria*, (2020).

[3] N.Boudjellal, H.Roumili, D.Benterki, Complexity analysis of interior point methods for convex quadratic programming based on a parameterized kernel function, *Bol. Soc. Paran. Mat.*, **40**(2022), 1–16. DOI: 10.5269/bspm.47772

[4] S.Chaghoub, D.Benterki, A Logarithmic Barrier Method Based On a New Majorant Function for Convex Quadratic Programming, *IAENG Int. J. Appl. Math.*, **51**(2021), no. 3.

[5] L.B.Cherif, B.Merikhi, A penalty method for nonlinear programming, *RAIRO Oper. Res.,* **53**(2019), no. 1, 29–38. DOI: 10.1051/ro/2018061

[6] J.P.Crouzeix, B.Merikhi, A logarithm barrier method for semi-definite programming, *RAIRO Oper. Res.*, **42**(2008), no. 2, 123–139. DOI: 10.1051/ro:2008005

[7] B.Fellahi, B.Merikhi, A Logarithmic Barrier Approach Via Majorant Function for Nonlinear Programming, *Journal of Siberian Federal University. Math. and Phys.*, **16**(2023), no. 4, 528–539. EDN: TEUNYB

[8] M.Goutali, Complexité et implémentation numérique d'une méthode de points intérieurs pour la programmation convexe, Ferhat Abbas University Setif 1, Algeria, 2018.

[9] W.Hock, K.Schittkowski, Test Examples for Nonlinear Programming Codes, *Springer Berlin, Heidelberg*, 1981.

[10] Z.Kebbiche, D.Benterki, A weighted path-following method for linearly constrained convex programming, *Rev. Roumaine Math. Pures Appl.*, **57**(2012), no. 3, 245–256.

[11] A.Keraghel, Analyse convexe: Théorie fondamentale et exercices, Editions Dar el'Houda, Ain Mlila, Algeria, 2001.

[12] A.Leulmi, B.Merikhi, D.Benterki, Study of a logarithmic barrier approach for linear semidefinite programming, *Journal of Siberian Federal University. Math. and Phys.*, **11**(2018), no. 3, 300–312. DOI: 10.17516/1997-1397-2018-11-3-300-312

[13] L.Menniche, D.Benterki, A logarithmic barrier approach for linear programming, *J. Comput. Appl. Math.*, **312**(2017), 267–275. DOI: 10.1016/j.cam.2016.05.025

[14] J.Nocedal, S.J.Wright, Numerical optimization, Springer Series in Operations Research and Financial Engineering, 2006.

Эффективный метод обратного барьера для нелинейной оптимизации

Айча Крария
Бачир Мерихи
Джамель Бентерки
Кафедра математики
Университет имени Ферхата Аббаса в Сетифе 1
Сетиф, 19000, Алжир
Аднан Яссин
Лаборатория прикладной математики Гавра
Университет Гавра в Нормандии
76600, Гавр, Франция

Аннотация. В данной работе мы используем новый вариант метода обратного барьера для решения нелинейной задачи оптимизации. Новая функция обратного барьера зависит от компонентов вектора штрафа и сохраняет свойства исходной задачи. Направление спуска вычисляется методом Ньютона, а размер шага — методом касательных и методом обратного отслеживания с интерполяцией параллельно с методом Вульфа.
В поддержку нашего подхода представлены сравнительные численные модели.

Ключевые слова: метод внутренних точек, нелинейное программирование, метод обратных барьеров.

EDN: MQBJTT
УДК 517.5

Subclasses of Bi-univalent Functions Defined by the Normalized Le Roy-type Mittag-Leffler Function

Shrouq Khaldoon Al-Titi*
Basem Aref Frasin†
Faculty of Science, Department of Mathematics
Al al-Bayt University, Mafraq, Jordan

Received 10.08.2025, received in revised form 27.09.2025, accepted 15.11.2025

Abstract. Let $\mathbb{F}_{\varkappa,\mu}^{(\gamma)}(\xi) = \xi + \sum_{n=1}^{\infty} \left[\frac{\Gamma(\mu)}{\Gamma(\varkappa n+\mu)}\right]^{\gamma} \xi^{n+1}$ be the normalized Le Roy-type Mittag-Leffler function. The purpose of the present paper is to introduce two new subclasses $\mathbb{H}_{\Sigma}^{\gamma}(\varkappa,\mu,\lambda,\tau)$ and $\mathbb{H}_{\Sigma}^{\gamma}(\varkappa,\mu,\lambda,\delta)$ of the function class Σ of bi-univalent functions defined by the function $\mathbb{F}_{\varkappa,\mu}^{(\gamma)}(\xi)$. Furthermore, we find estimates on the coefficients $|a_2|$ and $|a_3|$ for functions in these new subclasses. Also, we solve the Fekete–Szegö functional problem for functions in the classes $\mathbb{H}_{\Sigma}^{\gamma}(\varkappa,\mu,\lambda,\tau)$ and $\mathbb{H}_{\Sigma}^{\gamma}(\varkappa,\mu,\lambda,\delta)$. Several examples of the main results are also considered.

Keywords: analytic and univalent functions, bi-univalent functions, Le Roy-type Mittag-Leffler function, coefficients bounds.

Citation: S.K. Al-Titi, B.A. Frasin, Subclasses of Bi-univalent Functions Defined by the Normalized Le Roy-type Mittag-Leffler Function, J. Sib. Fed. Univ. Math. Phys., 2026, 19(1), 100–110. EDN: MQBJTT.

1. Introduction and definitions

Let $\mathcal{A}$ denote the class of functions of the form :

$$f(\xi) = \xi + \sum_{n=2}^{\infty} a_n \xi^n \tag{1.1}$$

which are analytic in the open unit disc $\mathcal{U} = \{\xi : |\xi| < 1\}$. Further, by $\mathcal{S}$ we shall denote the class of all functions in $\mathcal{A}$ which are univalent in $\mathcal{U}$.

It is well-known that, if $f(\xi)$ is analytic and univalent from a domain $\mathbb{D}_1$ onto a domain $\mathbb{D}_2$, then the inverse function $g(\xi)$ defined by $g(f(\xi)) = \xi \quad (\xi \in \mathbb{D}_1)$, is an analytic and univalent mapping from $\mathbb{D}_2$ to $\mathbb{D}_1$. Moreover, by the familiar Koebe one-quarter theorem every function $f \in \mathcal{S}$ has an inverse map f^{-1} that satisfies the following conditions

$$f^{-1}(f(\xi)) = \xi \quad \text{and } f\left(f^{-1}(w)\right) = w \quad \left(\xi \in \mathcal{U}, |w| < r_0(f); r_0(f) \geqslant \frac{1}{4}\right),$$

where

$$f^{-1}(w) = w - a_2 w^2 + (2a_2^2 - a_3)w^3 - (5a_2^3 - 5a_2 a_3 + a_4)w^4 + \cdots . \tag{1.2}$$

A function $f \in \mathcal{A}$ is said to be bi-univalent in $\mathcal{U}$ if both f and f^{-1} are univalent in $\mathcal{U}$.

*shrouqtiti@gmail.com https://orcid.org/0000-0001-8608-8063
†bafrasin@yahoo.com

Let Σ denote the class of bi-univalent functions in $\mathcal{U}$. Examples of functions in the class Σ are $\frac{\xi}{1-\xi}$, $\log\frac{1}{1-\xi}$, $\log\sqrt{\frac{1+\xi}{1-\xi}}$. However, the familiar Koebe function is not a member of Σ. Other common examples of functions in $\mathcal{U}$ such as $\frac{2\xi-\xi^2}{2}$ and $\frac{\xi}{1-\xi^2}$ are also not members of Σ.

Lewin [16] investigated the bi-univalent function class Σ and showed that $|a_2|<1.51$. Subsequently, Brannan and Clunie [6] conjectured that $|a_2|<\sqrt{2}$. Netanyahu [19], on the other hand, showed that $\max_{f\in\Sigma}|a_2|=4/3$.

The coefficient estimate problem for each of the Taylor–Maclaurin coefficients $|a_n|\,(n\geqslant 3;\ n\in\mathbb{N})$ is presumably still an open problem. Brannan and Taha [8] (see also [23]) introduced certain subclasses of the bi-univalent function class Σ similar to the familiar subclasses $\mathcal{S}^*(\tau)$ and $\mathcal{K}(\tau)$ of starlike and convex functions of order $\tau(0\leqslant\tau<1)$, respectively.

Following Brannan and Taha [8] (see also [23]), a function $f\in\mathcal{A}$ is in the class $\mathcal{S}^*_\Sigma[\tau]$ of strongly bi-starlike functions of order $\tau(0<\tau\leqslant 1)$ if each of the following conditions are satisfied: $f\in\Sigma$ and $\left|\arg\left(\frac{\xi f'(\xi)}{f(\xi)}\right)\right|<\frac{\tau\pi}{2}$ $(0<\tau\leqslant 1,\ \xi\in\mathcal{U})$ and $\left|\arg\left(\frac{\xi g'(w)}{g(w)}\right)\right|<\frac{\tau\pi}{2}$ $(0<\tau\leqslant 1,$ $w\in\mathcal{U})$, where g is the extension of $f^{-1}$to $\mathcal{U}$. The classes $\mathcal{S}^*_\Sigma(\tau)$ and $\mathcal{K}_\Sigma(\tau)$ of bi-starlike functions of order τ and bi-convex functions of order τ, corresponding to the function classes of starlike functions of order τ and the function classes of convex functions of order τ. For each of the function classes $\mathcal{S}^*_\Sigma(\tau)$ and $\mathcal{K}_\Sigma(\tau)$, they found non-sharp estimates on the first two Taylor–Maclaurin coefficients $|a_2|$ and $|a_3|$ (for details, see [8, 23]).

Geometric Function Theory is an important branch of complex analysis. It deals with the geometric properties of analytic functions. Special functions are very important in the study of geometric function theory, applied mathematics, physics, statistics and many other subjects. One of these functions is the Mittag–Leffler function [18], widely used in the solution of fractional-order integral equations or fractional-order differential equations.

The family of the two-parameter Mittag–Leffler functions $E_{\varkappa,\mu}(\xi)=\sum_{n=0}^{\infty}\frac{\xi^n}{\Gamma(\varkappa n+\mu)}$, $\varkappa,\mu,\xi\in\mathbb{C},\ \Re(\varkappa)>0,$ is named after the great Swedish mathematician Gösta Magnus Mittag–Leffler (1846–1927), who defined the function in one parameter [18], given by $E_\varkappa(\xi)=\sum_{n=0}^{\infty}\frac{\xi^n}{\Gamma(\varkappa n+1)},\ \varkappa,\xi\in\mathbb{C},\ \Re(\varkappa)>0.$

The Mittag–Leffler function and its generalizations has many applications in physics, biology, chemistry, engineering, and other applied sciences, making it better known among scientists.

Very recently, the study of the Mittag–Leffler function has become an interesting topic in Geometric Function Theory. Geometric properties, including starlikeness, convexity and close-to-convexity, of the Mittag–Leffler function $E_{\varkappa,\mu}(\xi)$ were investigated by Bansal and Prajapat in [7] and by Srivastava and Bansal (see [22]). In fact, the generalized Mittag–Leffler function $E_{\varkappa,\mu}(\xi)$ and its extensions and generalizations continue to be used in many different contexts in geometric function theory (see [4, 5, 9, 11, 12]).

Recently, Gerhold [13] and Garra and Polito [14] independently introduced the Le Roy-type Mittag–Leffler function, defined as $F^{(\gamma)}_{\varkappa,\mu}(\xi)=\sum_{n=0}^{\infty}\frac{\xi^n}{[\Gamma(\varkappa n+\mu)]^\gamma},\quad \varkappa,\mu,\gamma>0,\ \xi\in\mathbb{C}$. In particular, when $\varkappa=\mu=1$, $F^{(\gamma)}_{\varkappa,\mu}(\xi)$ leads to the following Le Roy-type function [17] defined as $R_\gamma(\xi)=\sum_{n=0}^{\infty}\frac{1}{(n!)^\gamma}\,\xi^n,\ \gamma>0,\ \xi\in\mathbb{C}$. It can be easily noted that $F^{(\gamma)}_{\varkappa,\mu}(\xi)$ is a generalization of the familiar Mittag–Leffler function $E_{\varkappa,\mu}(\xi)$.

It is clear that the Le Roy-type Mittag–Leffler function $F^{(\gamma)}_{\varkappa,\mu}(\xi)$ does not belong to the family $\mathcal{A}$. Thus, it is natural to consider the following normalization of $F^{(\gamma)}_{\varkappa,\mu}(\xi)$:

$$\begin{aligned}\mathbb{F}_{\varkappa,\mu}^{(\gamma)}(\xi) &= \xi\left[\Gamma(\mu)\right]^{\gamma} F_{\varkappa,\mu}^{(\gamma)}(\xi) = \\ &= \xi + \sum_{n=1}^{\infty}\left[\frac{\Gamma(\mu)}{\Gamma(\varkappa n+\mu)}\right]^{\gamma}\xi^{n+1}, \quad \varkappa,\mu,\gamma>0,\ \xi\in\mathbb{C}. \end{aligned} \tag{1.3}$$

In this paper, we shall restrict our attention to the case of positive real valued $\varkappa, \mu, \gamma$ and $\xi \in \mathcal{U}$.

Observe that the function $\mathbb{F}_{\varkappa,\mu}^{(\gamma)}$ contains many well-known functions as its special case, for example,

$$\begin{cases} \mathbb{F}_{0,1}^{(1)}(\xi) = \xi/(1-\xi), \\ \mathbb{F}_{1,1}^{(1)}(\xi) = \xi e^{\xi}, \\ \mathbb{F}_{1,2}^{(1)}(\xi) = e^{\xi}-1, \\ \mathbb{F}_{1,3}^{(1)}(\xi) = 2(e^{\xi}-\xi-1)/\xi, \\ \mathbb{F}_{1,4}^{(1)}(\xi) = (6(e^{\xi}-\xi-1)-3\xi^2)/\xi^2, \\ \mathbb{F}_{2,1}^{(1)}(\xi) = \xi\cosh(\sqrt{\xi}), \\ \mathbb{F}_{2,2}^{(1)}(\xi) = \sqrt{\xi}\sinh(\sqrt{\xi}), \\ \mathbb{F}_{2,3}^{(1)}(\xi) = 2\left[\cosh(\sqrt{\xi})-1\right], \\ \mathbb{F}_{2,4}^{(1)}(\xi) = 6\left[\sinh(\sqrt{\xi})-\sqrt{\xi}\right]/\sqrt{\xi}. \end{cases}$$

Geometric properties, including starlikeness, convexity and close-to-convexity, for the normalized geometric properties of the Le Roy-type Mittag–Leffler function $\mathbb{F}_{\varkappa,\mu}^{(\gamma)}$ were recently investigated by Mehrez and Das in [19]. From the normalization of the Le Roy-type Mittag–Leffler function $\mathbb{F}_{\varkappa,\mu}^{(\gamma)}(\xi)$ given by (1.3), let the function $\mathbb{V}_{\varkappa,\mu}^{(\gamma)}f(\xi)$ defined as follows:

$$\mathbb{V}_{\varkappa,\mu}^{(\gamma)}f(\xi) = \mathbb{F}_{\varkappa,\mu}^{(\gamma)}(\xi) * f(\xi) = \xi + \sum_{n=2}^{\infty}\left[\frac{\Gamma(\mu)}{\Gamma(\varkappa(n-1)+\mu)}\right]^{\gamma} a_n\xi^n, \qquad (\xi\in\mathcal{U}). \tag{1.4}$$

This paper is divided into three sections with this introduction being the first. In Section 2, we define the class of analytic and bi-univalent functions $\mathbb{H}_{\Sigma}^{\gamma}(\varkappa,\mu,\lambda,\tau)$ using the normalization of the Le Roy-type Mittag–Leffler function, and we also find estimates on the coefficients $|a_2|$ and $|a_3|$ for functions in these new subclasses of the function class Σ employing the techniques used earlier by Srivastava et al. [21] (see also, [1–3, 10, 15, 24, 26]). Section 3 is devoted to solving problems concerning the coefficients of functions in the class $\mathbb{H}_{\Sigma}^{\gamma}(\varkappa,\mu,\lambda,\delta)$. Section 4 is the main part of the paper, we find the sharp bounds of functional of Fekete–Szegö type.

In order to derive our main results, we have to recall here the following lemma [20].

Lemma 1.1. *If $h \in \mathcal{P}$ then $|c_k| \leqslant 2$ for each k, where $\mathcal{P}$ is the family of all functions h analytic in $\mathcal{U}$ for which $\Re(h(\xi)) > 0, h(\xi) = 1 + c_1\xi + c_2\xi^2 + c_3\xi^3 + \ldots$ for $z \in \mathcal{U}$.*

2. Coefficient bounds for the function class $\mathbb{H}_{\Sigma}^{\gamma}(\varkappa,\mu,\lambda,\tau)$

This section introduces our new subclass of bi-univalent functions, denoted as $\mathbb{H}_{\Sigma}^{\gamma}(\varkappa,\mu,\lambda,\tau)$.

Definition 2.1. *A function $f(\xi)$ given by (1.1) is said to be in the class $\mathbb{H}_{\Sigma}^{\gamma}(\varkappa,\mu,\lambda,\tau)$ if the following conditions are satisfied:*

$$f\in\Sigma \text{ and } \left|\arg\left(\left(\mathbb{V}_{\varkappa,\mu}^{(\gamma)}f(\xi)\right)' + \lambda\xi\left(\mathbb{V}_{\varkappa,\mu}^{(\gamma)}f(\xi)\right)''\right)\right| < \frac{\tau\pi}{2} \quad (\xi\in\mathcal{U}) \tag{2.1}$$

and

$$\left| \arg\left(\left(\mathbb{V}^{(\gamma)}_{\varkappa,\mu} g(w) \right)' + \lambda\xi \left(\mathbb{V}^{(\gamma)}_{\varkappa,\mu} g(w) \right)'' \right) \right| < \frac{\tau\pi}{2} \quad (w \in \mathcal{U}), \tag{2.2}$$

where $\gamma, \varkappa, \mu > 0,\ \lambda \geqslant 0,\ 0 < \tau \leqslant 1$ *and the function* $g = f^{-1}(w)$ *given by (1.2).*

In particular, a function $f(\xi)$ given by (1.1) is said to be in the class $\mathbb{H}^{\gamma}_{\Sigma}(\varkappa, \mu, \tau)$ if the following conditions are satisfied:

$$f \in \Sigma \text{ and } \quad \left| \arg\left(\mathbb{V}^{(\gamma)}_{\varkappa,\mu} f(\xi) \right)' \right| < \frac{\tau\pi}{2} \quad (\xi \in \mathcal{U}) \tag{2.3}$$

and

$$\left| \arg\left(\mathbb{V}^{(\gamma)}_{\varkappa,\mu} g(w) \right)' \right| < \frac{\tau\pi}{2} \quad (w \in \mathcal{U}), \tag{2.4}$$

where $\gamma, \varkappa, \mu > 0,\ 0 < \tau \leqslant 1$ and the function $g = f^{-1}(w)$ given by (1.2).

We begin by finding the estimates on the coefficients $|a_2|$ and $|a_3|$ for functions in the class $\mathbb{H}^{\gamma}_{\Sigma}(\varkappa, \mu, \lambda, \tau)$.

Theorem 2.2. *Let* f *be in the class* $\mathbb{H}^{\gamma}_{\Sigma}(\varkappa, \mu, \lambda, \tau)$ *where* $\gamma, \varkappa, \mu > 0,\ \lambda \geqslant 0,\ 0 < \tau \leqslant 1$. *Then*

$$|a_2| \leqslant \frac{2\tau}{\sqrt{\left| 6\tau \left(\frac{\Gamma(\mu)}{\Gamma(2\varkappa+\mu)} \right)^{\gamma} (1+2\lambda) - 4(\tau-1)(1+\lambda)^2 \left(\frac{\Gamma(\mu)}{\Gamma(\varkappa+\mu)} \right)^{2\gamma} \right|}} \tag{2.5}$$

and

$$|a_3| \leqslant \frac{\tau^2}{\left(\frac{\Gamma(\mu)}{\Gamma(\varkappa+\mu)} \right)^{2\gamma} (1+\lambda)^2} + \frac{2\tau}{3\left(\frac{\Gamma(\mu)}{\Gamma(2\varkappa+\mu)} \right)^{\gamma} (1+2\lambda)}. \tag{2.6}$$

Proof. It follows from (2.1) and (2.2) that

$$\left(\mathbb{V}^{(\gamma)}_{\varkappa,\mu} f(\xi) \right)' + \lambda\xi \left(\mathbb{V}^{(\gamma)}_{\varkappa,\mu} f(\xi) \right)'' = [p(\xi)]^{\varkappa} \tag{2.7}$$

and

$$\left(\mathbb{V}^{(\gamma)}_{\varkappa,\mu} g(w) \right)' + \lambda\xi \left(\mathbb{V}^{(\gamma)}_{\varkappa,\mu} g(w) \right)'' = [q(w)]^{\tau} \tag{2.8}$$

where $p(\xi)$ and $q(w)$ in $\mathcal{P}$ and have the forms

$$p(\xi) = 1 + p_1\xi + p_2\xi^2 + p_3\xi^3 + \cdots \tag{2.9}$$

and

$$q(w) = 1 + q_1 w + q_2 w^2 + q_3 w^3 + \cdots . \tag{2.10}$$

Now, equating the coefficients in (2.7) and (2.8), we get

$$2\left(\frac{\Gamma(\mu)}{\Gamma(\varkappa+\mu)} \right)^{\gamma} (1+\lambda) a_2 = \tau p_1, \tag{2.11}$$

$$3\left(\frac{\Gamma(\mu)}{\Gamma(2\varkappa+\mu)} \right)^{\gamma} (1+2\lambda) a_3 = \tau p_2 + \frac{\tau(\tau-1)}{2} p_1^2, \tag{2.12}$$

$$-2\left(\frac{\Gamma(\mu)}{\Gamma(\varkappa+\mu)} \right)^{\gamma} (1+\lambda) a_2 = \tau q_1 \tag{2.13}$$

and

$$3\left(\frac{\Gamma(\mu)}{\Gamma(2\varkappa+\mu)}\right)^{\gamma}(1+2\lambda)(2a_2^2-a_3)=\tau q_2+\frac{\tau(\tau-1)}{2}q_1^2. \tag{2.14}$$

From (2.11) and (2.13), we get

$$p_1=-q_1 \tag{2.15}$$

and

$$8\left(\frac{\Gamma(\mu)}{\Gamma(\varkappa+\mu)}\right)^{2\gamma}(1+\lambda)^2a_2^2=\tau^2(p_1^2+q_1^2). \tag{2.16}$$

Now from (2.12), (2.14) and (2.16), we obtain

$$\begin{aligned}6\left(\frac{\Gamma(\mu)}{\Gamma(2\varkappa+\mu)}\right)^{\gamma}(1+2\lambda)a_2^2 &= \tau(p_2+q_2)+\frac{\tau(\tau-1)}{2}(p_1^2+q_1^2)= \\ &= \tau(p_2+q_2)+\frac{4(\tau-1)(1+\lambda)^2}{\tau}\left(\frac{\Gamma(\mu)}{\Gamma(\varkappa+\mu)}\right)^{2\gamma}a_2^2.\end{aligned}$$

Therefore, we have

$$a_2^2=\frac{\tau^2(p_2+q_2)}{6\tau\left(\frac{\Gamma(\mu)}{\Gamma(2\varkappa+\mu)}\right)^{\gamma}(1+2\lambda)-4(\tau-1)(1+\lambda)^2\left(\frac{\Gamma(\mu)}{\Gamma(\varkappa+\mu)}\right)^{2\gamma}}. \tag{2.17}$$

Applying Lemma 1.1 for the coefficients p_2 and q_2, we immediately have

$$|a_2|\leqslant\frac{2\tau}{\sqrt{\left|6\tau\left(\frac{\Gamma(\mu)}{\Gamma(2\varkappa+\mu)}\right)^{\gamma}(1+2\lambda)-4(\tau-1)(1+\lambda)^2\left(\frac{\Gamma(\mu)}{\Gamma(\varkappa+\mu)}\right)^{2\gamma}\right|}}.$$

This gives the bound on $|a_2|$ as asserted in (2.6).

Next, in order to find the bound on $|a_3|$, by subtracting (2.15) from (2.13), we get

$$\begin{aligned}&6\left(\frac{\Gamma(\mu)}{\Gamma(2\varkappa+\mu)}\right)^{\gamma}(1+2\lambda)a_3-6\left(\frac{\Gamma(\mu)}{\Gamma(2\varkappa+\mu)}\right)^{\gamma}(1+2\lambda)a_2^2= \\ &= \tau p_2+\frac{\tau(\tau-1)}{2}p_1^2-\left(\tau q_2+\frac{\tau(\tau-1)}{2}q_1^2\right).\end{aligned} \tag{2.18}$$

Upon substituting the value of a_2^2 from (2.17) and observing that $p_1^2=q_1^2$, it follows that

$$a_3=\frac{\tau^2p_1^2}{4\left(\frac{\Gamma(\mu)}{\Gamma(\varkappa+\mu)}\right)^{2\gamma}(1+\mu)^2}+\frac{\tau(p_2-q_2)}{6\left(\frac{\Gamma(\mu)}{\Gamma(2\varkappa+\mu)}\right)^{\gamma}(1+2\lambda)}.$$

Applying Lemma 1.1 once again for the coefficients p_1, p_2, q_1 and q_2, we readily get

$$|a_3|=\frac{\tau^2}{\left(\frac{\Gamma(\mu)}{\Gamma(\varkappa+\mu)}\right)^{2\gamma}(1+\lambda)^2}+\frac{2\tau}{3\left(\frac{\Gamma(\mu)}{\Gamma(2\varkappa+\mu)}\right)^{\gamma}(1+2\lambda)}.$$

This completes the proof of Theorem 2.2. □

Corollary 2.3. *Let* $\mathbb{F}_{\varkappa,1}^{(\gamma)}$ *be in the class* $\mathbb{H}_{\Sigma}^{\gamma}(\varkappa,\mu,\tau)$ *where* $\gamma,\varkappa>0,\ 0<\tau\leqslant 1$. *Then*

$$|a_2| \leqslant \frac{2\tau}{\sqrt{\left|6\tau\left(\frac{\Gamma(\mu)}{\Gamma(2\varkappa+\mu)}\right)^{\gamma} - 4(\tau-1)\left(\frac{\Gamma(\mu)}{\Gamma(\varkappa+\mu)}\right)^{2\gamma}\right|}} \tag{2.19}$$

and

$$|a_3| \leqslant \frac{\tau^2}{\left(\frac{\Gamma(\mu)}{\Gamma(\varkappa+\mu)}\right)^{2\gamma}} + \frac{2\tau}{3\left(\frac{\Gamma(\mu)}{\Gamma(2\varkappa+\mu)}\right)^{\gamma}}. \tag{2.20}$$

3. Coefficient bounds for the function class $\mathbb{H}_{\Sigma}^{\gamma}(\varkappa, \mu, \lambda, \delta)$

Definition 3.1. *A function $f(\xi)$ is said to be in the class $\mathbb{H}_{\Sigma}^{\gamma}(\varkappa, \mu, \lambda, \delta)$ if the following conditions are satisfied:*

$$f \in \Sigma \text{ and } \Re\left(\left(\mathbb{V}_{\varkappa,\mu}^{(\gamma)} f(\xi)\right)' + \lambda\xi\left(\mathbb{V}_{\varkappa,\mu}^{(\gamma)} f(\xi)\right)''\right) > \delta \qquad (\xi \in \mathcal{U}) \tag{3.1}$$

and

$$\Re\left(\left(\mathbb{V}_{\varkappa,\mu}^{(\gamma)} g(w)\right)' + \lambda\xi\left(\mathbb{V}_{\varkappa,\mu}^{(\gamma)} g(w)\right)''\right) > \delta \qquad (w \in \mathcal{U}), \tag{3.2}$$

where $\gamma, \varkappa, \mu > 0,\ \lambda \geqslant 0,\ 0 \leqslant \delta < 1$ and the function g is given by (1.2).

In particular, a function $f(\xi)$ is said to be in the class $\mathbb{H}_{\Sigma}^{\gamma}(\varkappa, \mu, \delta)$ if the following conditions are satisfied:

$$f \in \Sigma \text{ and } \Re\left(\mathbb{V}_{\varkappa,\mu}^{(\gamma)} f(\xi)\right)' > \delta \qquad (\xi \in \mathcal{U}) \tag{3.3}$$

and

$$\Re\left(\mathbb{V}_{\varkappa,\mu}^{(\gamma)} g(w)\right)' > \delta \qquad (w \in \mathcal{U}), \tag{3.4}$$

where $\gamma, \varkappa, \mu > 0,\ 0 \leqslant \delta < 1$ and the function g is given by (1.2).

Theorem 3.2. *Let f be in the class $\mathbb{H}_{\Sigma}^{\gamma}(\varkappa, \mu, \lambda, \delta)$ where $\gamma, \varkappa, \mu > 0, \lambda \geqslant 0$ and $0 \leqslant \delta < 1$. Then*

$$|a_2| \leqslant \sqrt{\frac{2(1-\delta)}{3\left(\frac{\Gamma(\mu)}{\Gamma(2\varkappa+\mu)}\right)^{\gamma}(1+2\lambda)}}. \tag{3.5}$$

and

$$|a_3| \leqslant \frac{(1-\delta)^2}{\left(\frac{\Gamma(\mu)}{\Gamma(\varkappa+\mu)}\right)^{2\gamma}(1+\lambda)^2} + \frac{2(1-\delta)}{3\left(\frac{\Gamma(\mu)}{\Gamma(2\varkappa+\mu)}\right)^{\gamma}(1+2\lambda)}. \tag{3.6}$$

Proof. It follows from (3.1) and (3.2) that there exist $p(\xi)$ and $q(w)$ in $\mathcal{P}$ such that

$$\left(\mathbb{V}_{\varkappa,\mu}^{(\gamma)} f(\xi)\right)' + \lambda\xi\left(\mathbb{V}_{\varkappa,\mu}^{(\gamma)} f(\xi)\right)'' = \delta + (1-\delta)p(\xi) \tag{3.7}$$

and

$$\left(\mathbb{V}_{\varkappa,\mu}^{(\gamma)} g(w)\right)' + \lambda\xi\left(\mathbb{V}_{\varkappa,\mu}^{(\gamma)} g(w)\right)'' = \delta + (1-\delta)q(w) \tag{3.8}$$

where $p(\xi)$ and $q(w)$ in $\mathcal{P}$ and have the forms (2.10) and (2.11),respectively. Equating coefficients in (3.7) and (3.8) yields

$$2\left(\frac{\Gamma(\mu)}{\Gamma(\varkappa+\mu)}\right)^{\gamma}(1+\lambda)a_2 = (1-\delta)p_1, \tag{3.9}$$

$$3\left(\frac{\Gamma(\mu)}{\Gamma(2\varkappa+\mu)}\right)^{\gamma}(1+2\lambda)a_3=(1-\delta)p_2, \tag{3.10}$$

$$-2\left(\frac{\Gamma(\mu)}{\Gamma(\varkappa+\mu)}\right)^{\gamma}(1+\lambda)a_2=(1-\delta)q_1 \tag{3.11}$$

and

$$3\left(\frac{\Gamma(\mu)}{\Gamma(2\varkappa+\mu)}\right)^{\gamma}(1+2\lambda)(2a_2^2-a_3)=(1-\delta)q_2. \tag{3.12}$$

From (3.9) and (3.11), we get

$$p_1=-q_1 \tag{3.13}$$

and

$$8\left(\frac{\Gamma(\mu)}{\Gamma(\varkappa+\mu)}\right)^{2\gamma}(1+\lambda)^2a_2^2=(1-\delta)^2(p_1^2+q_1^2). \tag{3.14}$$

Now from (3.10)and (3.12) , we find that

$$6\left(\frac{\Gamma(\mu)}{\Gamma(2\varkappa+\mu)}\right)^{\gamma}(1+2\lambda)a_2^2=(1-\delta)(p_2+q_2)$$

Thus,we have

$$\left|a_2^2\right| \leqslant \frac{(1-\delta)(|p_2|+|q_2|)}{6\left(\frac{\Gamma(\mu)}{\Gamma(2\varkappa+\mu)}\right)^{\gamma}(1+2\lambda)}=\frac{2(1-\delta)}{3\left(\frac{\Gamma(\mu)}{\Gamma(2\varkappa+\mu)}\right)^{\gamma}(1+2\lambda)}$$

which is the bound on $\left|a_2^2\right|$ as given in (3.5).

Next, in order to find the bound on $|a_3|$, by subtracting (3.12) from (3.10), we get

$$6\left(\frac{\Gamma(\mu)}{\Gamma(2\varkappa+\mu)}\right)^{\gamma}(1+2\lambda)a_3-6\left(\frac{\Gamma(\mu)}{\Gamma(2\varkappa+\mu)}\right)^{\gamma}(1+2\lambda)a_2^2=(1-\delta)(p_2-q_2)$$

or, equivalently,

$$a_3=a_2^2+\frac{(1-\delta)(p_2-q_2)}{6\left(\frac{\Gamma(\mu)}{\Gamma(2\varkappa+\mu)}\right)^{\gamma}(1+2\lambda)}.$$

Upon substituting the value of a_2^2 from (3.14), we obtain

$$a_3=\frac{(1-\delta)^2(p_1^2+q_1^2)}{8(1+\lambda)^2}+\frac{(1-\delta)(p_2-q_2)}{6\left(\frac{\Gamma(\mu)}{\Gamma(2\varkappa+\mu)}\right)^{\gamma}(1+2\lambda)}.$$

Applying Lemma 1.1 for the coefficients p_1, p_2, q_1 and q_2, we readily get

$$|a_3|\leqslant\frac{(1-\delta)^2}{\left(\frac{\Gamma(\mu)}{\Gamma(\varkappa+\mu)}\right)^{2\gamma}(1+\lambda)^2}+\frac{2(1-\delta)}{3\left(\frac{\Gamma(\mu)}{\Gamma(2\varkappa+\mu)}\right)^{\gamma}(1+2\lambda)}$$

which is the bound on $|a_3|$ as asserted in (3.6). □

Corollary 3.3. *Let $f(\xi)$ be in the class $\mathbb{H}_{\Sigma}^{\gamma}(\varkappa,\mu,\delta)$ where $\gamma,\varkappa>0$ and $0\leqslant\delta<1$. Then*

$$|a_2|\leqslant\sqrt{\frac{2(1-\delta)}{3\left(\frac{\Gamma(\mu)}{\Gamma(2\varkappa+\mu)}\right)^{\gamma}}}. \tag{3.15}$$

and

$$|a_3|\leqslant\frac{(1-\delta)^2}{\left(\frac{\Gamma(\mu)}{\Gamma(\varkappa+\mu)}\right)^{2\gamma}}+\frac{2(1-\delta)}{3\left(\frac{\Gamma(\mu)}{\Gamma(2\varkappa+\mu)}\right)^{\gamma}}. \tag{3.16}$$

4. Fekete-Szegö inequality

In this section, we will find the sharp bounds of Fekete-Szegö functional $|a_3 - \eta a_2^2|$, $\eta \in \mathbb{R}$, for $f \in \mathbb{H}_{\Sigma}^{\gamma}(\varkappa, \mu, \lambda, \tau)$.

Theorem 4.1. *Let $f(z)$ given by (1.1) be in the class $\mathbb{H}_{\Sigma}^{\gamma}(\varkappa, \mu, \lambda, \tau)$, $\gamma, \varkappa, \mu > 0$, $\lambda \geqslant 0$ and $0 < \tau \leqslant 1$. Then for some $\eta \in \mathbb{R}$,*

$$\left|a_3 - \eta a_2^2\right| \leqslant \begin{cases} \dfrac{4\tau}{6\left(\frac{\Gamma(\mu)}{\Gamma(2\varkappa+\mu)}\right)^{\gamma}(1+2\lambda)}, & \text{for} \quad 0 \leqslant |\varphi(\eta)| \leqslant \dfrac{1}{6\left(\frac{\Gamma(\mu)}{\Gamma(2\varkappa+\mu)}\right)^{\gamma}(1+2\lambda)}, \\ 4\tau\,|\varphi(\eta)|, & \text{for } |\varphi(\eta)| \geqslant \dfrac{1}{6\left(\frac{\Gamma(\mu)}{\Gamma(2\varkappa+\mu)}\right)^{\gamma}(1+2\lambda)}, \end{cases}$$

where

$$\varphi(\eta) = (1-\eta)\,\frac{\tau}{6\tau\left(\frac{\Gamma(\mu)}{\Gamma(2\varkappa+\mu)}\right)^{\gamma}(1+2\lambda) - 4(\tau-1)(1+\lambda)^2\left(\frac{\Gamma(\mu)}{\Gamma(\varkappa+\mu)}\right)^{2\gamma}}.$$

Proof. Let $f \in \mathbb{H}_{\Sigma}^{\gamma}(\varkappa, \mu, \lambda, \tau)$. In view of (2.15), it follows from (2.18) that

$$a_3 = a_2^2 + \frac{\tau\,(p_2 - q_2)}{6\left(\frac{\Gamma(\mu)}{\Gamma(2\varkappa+\mu)}\right)^{\gamma}(1+2\lambda)}. \tag{4.1}$$

By using (4.1) and (2.17) for some $\eta \in \mathbb{R}$, we get

$$\begin{aligned} a_3 - \eta a_2^2 &= (1-\eta)\left(\frac{\tau^2(p_2+q_2)}{6\tau\left(\frac{\Gamma(\mu)}{\Gamma(2\varkappa+\mu)}\right)^{\gamma}(1+2\lambda) - 4(\tau-1)(1+\lambda)^2\left(\frac{\Gamma(\mu)}{\Gamma(\varkappa+\mu)}\right)^{2\gamma}}\right) + \\ &\quad + \frac{\tau\,(p_2-q_2)}{6\left(\frac{\Gamma(\mu)}{\Gamma(2\varkappa+\mu)}\right)^{\gamma}(1+2\lambda)} = \\ &= \tau\left[\left(\varphi(\eta) + \frac{1}{6\left(\frac{\Gamma(\mu)}{\Gamma(2\varkappa+\mu)}\right)^{\gamma}(1+2\lambda)}\right)p_2 + \left(\varphi(\eta) - \frac{1}{6\left(\frac{\Gamma(\mu)}{\Gamma(2\varkappa+\mu)}\right)^{\gamma}(1+2\lambda)}\right)q_2\right], \end{aligned}$$

where

$$\varphi(\eta) = (1-\eta)\,\frac{\tau}{6\tau\left(\frac{\Gamma(\mu)}{\Gamma(2\varkappa+\mu)}\right)^{\gamma}(1+2\lambda) - 4(\tau-1)(1+\lambda)^2\left(\frac{\Gamma(\mu)}{\Gamma(\varkappa+\mu)}\right)^{2\gamma}}.$$

Therefore, we have

$$\left|a_3 - \eta a_2^2\right| \leqslant \begin{cases} \dfrac{4\tau}{6\left(\frac{\Gamma(\mu)}{\Gamma(2\varkappa+\mu)}\right)^{\gamma}(1+2\lambda)}, & \text{for } 0 \leqslant |\varphi(\eta)| \leqslant \dfrac{1}{6\left(\frac{\Gamma(\mu)}{\Gamma(2\varkappa+\mu)}\right)^{\gamma}(1+2\lambda)}, \\ 4\tau\,|\varphi(\eta)|, & \text{for } |\varphi(\eta)| \geqslant \dfrac{1}{6\left(\frac{\Gamma(\mu)}{\Gamma(2\varkappa+\mu)}\right)^{\gamma}(1+2\lambda)}. \end{cases}$$

The proof is completed. □

The proof of Theorem 4.2 (below) is similar to that of Theorem 4.1 and can be omitted.

Theorem 4.2. *Let $f(z)$ given by (1.1) be in the class $\mathbb{H}_{\Sigma}^{\gamma}(\varkappa,\mu,\lambda,\delta)$ where $\gamma,\varkappa,\mu>0$, $\lambda\geqslant 0$ and $0\leqslant\delta<1$. Then for some $\eta\in\mathbb{R}$,*

$$\left|a_3-\eta a_2^2\right|\leqslant\begin{cases}\dfrac{4(1-\delta)}{6\left(\frac{\Gamma(\mu)}{\Gamma(2\varkappa+\mu)}\right)^{\gamma}(1+2\lambda)}, & \text{for } 0\leqslant|\psi(\eta)|\leqslant\dfrac{1}{6\left(\frac{\Gamma(\mu)}{\Gamma(2\varkappa+\mu)}\right)^{\gamma}(1+2\lambda)},\\ 4(1-\delta)\left|\psi(\eta)\right|, & \text{for } |\psi(\eta)|\geqslant\dfrac{1}{6\left(\frac{\Gamma(\mu)}{\Gamma(2\varkappa+\mu)}\right)^{\gamma}(1+2\lambda)},\end{cases}$$

where

$$\psi(\eta)=\frac{(1-\eta)}{6\left(\frac{\Gamma(\mu)}{\Gamma(2\varkappa+\mu)}\right)^{\gamma}(1+2\lambda)}.$$

From Theorems 4.1 and 4.2, we get the following corollaries.

Corollary 4.3. *Let $f(z)$ given by (1.1) be in the class $\mathbb{H}_{\Sigma}^{\gamma}(\varkappa,\mu,\tau)$, $\gamma,\varkappa,\mu>0$ and $0<\tau\leqslant 1$. Then for some $\eta\in\mathbb{R}$,*

$$\left|a_3-\eta a_2^2\right|\leqslant\begin{cases}\dfrac{4\tau}{6\left(\frac{\Gamma(\mu)}{\Gamma(2\varkappa+\mu)}\right)^{\gamma}}, & \text{for } 0\leqslant|\varphi(\eta)|\leqslant\dfrac{1}{6\left(\frac{\Gamma(\mu)}{\Gamma(2\varkappa+\mu)}\right)^{\gamma}},\\ 4\tau\left|\varphi(\eta)\right|, & \text{for } |\varphi(\eta)|\geqslant\dfrac{1}{6\left(\frac{\Gamma(\mu)}{\Gamma(2\varkappa+\mu)}\right)^{\gamma}},\end{cases}$$

where

$$\varphi(\eta)=(1-\eta)\frac{\tau}{6\tau\left(\frac{\Gamma(\mu)}{\Gamma(2\varkappa+\mu)}\right)^{\gamma}-4(\tau-1)\left(\frac{\Gamma(\mu)}{\Gamma(\varkappa+\mu)}\right)^{2\gamma}}.$$

Corollary 4.4. *Let $f(z)$ given by (1.1) be in the class $\mathbb{H}_{\Sigma}^{\gamma}(\varkappa,\mu,\delta)$ where $\gamma,\varkappa,\mu>0$ and $0\leqslant\delta<1$. Then for some $\eta\in\mathbb{R}$,*

$$\left|a_3-\eta a_2^2\right|\leqslant\begin{cases}\dfrac{4(1-\delta)}{6\left(\frac{\Gamma(\mu)}{\Gamma(2\varkappa+\mu)}\right)^{\gamma}}, & \text{for } 0\leqslant|1-\eta|\leqslant 1,\\ \dfrac{4(1-\delta)}{6\left(\frac{\Gamma(\mu)}{\Gamma(2\varkappa+\mu)}\right)^{\gamma}}\left|1-\eta\right|, & \text{for } |1-\eta|\geqslant 1.\end{cases}$$

Conclusions

In this study, we introduce two new subclasses $\mathbb{H}_{\Sigma}^{\gamma}(\varkappa,\mu,\lambda,\tau)$ and $\mathbb{H}_{\Sigma}^{\gamma}(\varkappa,\mu,\lambda,\delta)$ of the function class Σ of bi-univalent functions connected to the Le Roy-type Mittag–Leffler function $\mathbb{V}_{\varkappa,\mu}^{(\gamma)}f(\xi)$ given in (1.4). We have derived estimates for the Taylor–Maclaurin coefficients $|a_2|$ and $|a_3|$ for the function in the subclasses $\mathbb{H}_{\Sigma}^{\gamma}(\varkappa,\mu,\lambda,\tau)$ and $\mathbb{H}_{\Sigma}^{\gamma}(\varkappa,\mu,\lambda,\delta)$. Furthermore, the Fekete-Szegö problem for these subclasses is solved. Making use of the normalized Le Roy-type Mittag–Leffler function $\mathbb{V}_{\varkappa,\mu}^{(\gamma)}f(\xi)$ could inspire researchers to derive the estimates of the Taylor-Maclaurin coefficients $|a_2|$ and $|a_3|$ and Fekete–Szegö functional problems for functions belonging to new subclasses of bi-univalent functions.

References

[1] A.Amourah, M.Illafe, A Comprehensive subclass of analytic and Bi-univalent functions associated with subordination, *Palestine J. Math.*, **9**(2020), 187–193.

[2] A.Amourah, B.A.Frasin, T.M.Seoudy, An Application of Miller-Ross-Type Poisson Distribution on Certain Subclasses of Bi-Univalent Functions Subordinate to Gegenbauer Polynomials, *Mathematics*, **10**(2022), 2462. DOI: 10.3390/math10142462

[3] A.Amourah, T.Al-Hawary, B.A.Frasin, Application of Chebyshev polynomials to certain class of bi-Bazilevič functions of order $\alpha + i\beta$, *Afr. Mat.*, **32**(2021), 1059–1066. DOI: 10.1007/s13370-021-00881-x

[4] A.A.Attiya, Some applications of Mittag-Leffler function in the unit disk, *Filomat*, **30**(2016), 2075–2081.

[5] M.Ahmad, B.Frasin ,G.Murugusundaramoorthy, A.Al-khazaleh, An application of Mittag–Leffler-type Poisson distribution on certain subclasses of analytic functions associated with conic domains, *Heliyon*, **7**(2021), e08109. DOI: 10.1016/j.heliyon.2021.e08109

[6] D.A.Brannan, J.G.Clunie (Eds.), Aspects of Contemporary Complex Analysis (Proceedings of the NATO Advanced Study Institute held at the University of Durham, Durham; July 1-20, 1979), Academic Press, New York and London, 1980.

[7] D.Bansal, J.K.Prajapat, Certain geometric properties of the Mittag-Leffler functions, *Complex Var. Elliptic Equ.*, **61**(2016), 338–350. DOI: 10.1080/17476933.2015.1079628

[8] D.A.Brannan, T.S.Taha, On some classes of bi-univalent functions, in: S.M. Mazhar,A. Hamoui, N.S. Faour (Eds.), Mathematical Analysis and Its Applications, Kuwait; Feb ruary 18-21, 1985, in: KFAS Proceedings Series, vol. 3, Pergamon Press (Elsevier Science Limited), Oxford, 1988, pp. 53-60; see also *Studia Univ. Babes-Bolyai Math.*, **31**(1986), no. 2, 70–77.

[9] B.A.Frasin, T.Al-Hawary, F.Yousef, Some properties of a linear operator involving generalized Mittag-Leffler function, *Stud.Univ. Babes-Bolyai Math*, **65**(2020), no. 1, 67–75. DOI: 10.24193/subbmath.2020.1.06

[10] B.A.Frasin, M.K.Aouf, New subclasses of bi-univalent functions, *Appl. Math. Letters*, **24**(2011), no. 9, 1569–1573. DOI: 10.1016/j.aml.2011.03.048

[11] B.A.Frasin, L.I.Cotîrlă, Partial Sums of the Normalized Le Roy-Type Mittag-Leffler Function, *Axioms,* **12**2023, 441. DOI: 10.3390/axioms12050441

[12] M.Garg, P.Manohar, S.L.Kalla, A Mittag-Leffler-type function of two variables, *Integral Transform, Spec. Funct.*, **24**(2013), 934–944. DOI: 10.1080/10652469.2013.789872

[13] S.Gerhold, Asymptotics for a variant of the Mittag–Leffler function, *Integral Transform. Spec. Funct.*, **23**(2012), 397–40. DOI: 10.1080/10652469.2011.596151

[14] R.Garra, F. Polito, On some operators involving Hadamard derivatives, *Integral Transform. Spec. Funct.*, **24**(2013), 773–782. DOI: 10.1080/10652469.2012.756875

[15] T.Al-Hawary, A.Amourah, B.A.Frasin, Fekete–Szego inequality for bi-univalent functions by means of Horadam polynomials, *Bol. Soc. Mat. Mex.*, **27**(2021), 79. DOI: 10.1007/s40590-021-00385-5

[16] M.Lewin, On a coefficient problem for bi-univalent functions, *Proc. Amer. Math. Soc.*, **18**(1967), 63–68.

[17] K.Mehrez, S.Das, On some geometric properties of the Le Roy-type Mittag-Leffler function, *Hacet. J. Math. Stat.*, **51**(2022), 1085–1103.

[18] G.M.Mittag-Leffler, Sur la nouvelle fonction $E(x)$, *Comptes Rendus Acad. Sci.*, **137**(1903), 554–558.

[19] E.Netanyahu, The minimal distance of the image boundary from the origin and the second coefficient of a univalent function in $|\xi| < 1$, *Arch. Rational Mech. Anal.*, **32**(1969), 100–112.

[20] C.Pommerenke, Univalent functions, Vandenhoeck and Rupercht, Gottingen, 1975.

[21] H.M.Srivastava, A.K.Mishra, P.Gochhayat, Certain subclasses of analytic and bi univalent functions, *Appl. Math. Lett.*, **23**(2010), 1188–1192.

[22] H.M.Srivastava, D.Bansal, Close-to-convexity of a certain family of q-Mittag-Leffer functions, *J. Nonlinear Var. Anal.*, **1**(2017), 61–69.

[23] T.S.Taha, Topics in Univalent Function Theory, Ph.D. Thesis, University of London, 1981.

[24] F.Yousef, T.Al-Hawary, G. Murugusundaramoorthy, Fekete-Szego functional problems for some subclasses of bi-univalent functions defined by Frasin differential operator, *Afr. Mat.*, **30**(2019), 495–503.

[25] F.Yousef, S.Alroud, M.Illafe, A comprehensive subclass of bi-univalent functions associated with Chebyshev polynomials of the second kind, Bol. Soc. Mat. Mex., 2019, 1–11.

[26] Q.Xu, Y.Gui, and H. M.Srivastava, Coefficient estimates for a certain subclass of analytic and bi-univalent functions, *Appl. Math. Lett.*, **25**(2012), 990–994.

Подклассы двузначных функций, определяемых нормализованной функцией Миттаг-Леффлера типа Ле Руа

Шрук Халдун Аль-Тити
Базем Ареф Фразин
Факультет естественных наук
Университет Аль-аль-Байт, Мафрак, Иордания

Аннотация. Пусть $\mathbb{F}^{(\gamma)}_{\varkappa,\mu}(\xi) = \xi + \sum_{n=1}^{\infty} \left[\frac{\Gamma(\mu)}{\Gamma(\varkappa n+\mu)}\right]^{\gamma} \xi^{n+1}$ — нормированная функция Миттаг–Леффлера типа Ле Руа. Целью настоящей статьи является введение двух новых подклассов $\mathbb{H}^{\gamma}_{\Sigma}(\varkappa,\mu,\lambda,\tau)$ и $\mathbb{H}^{\gamma}_{\Sigma}(\varkappa,\mu,\lambda,\delta)$ функционального класса Σ биоднолистных функций, определенных функцией $\mathbb{F}^{(\gamma)}_{\varkappa,\mu}(\xi)$. Кроме того, мы находим оценки коэффициентов $|a_2|$ и $|a_3|$ для функций из этих новых подклассов. Также решается функциональная задача Фекете-Сега для функций классов $\mathbb{H}^{\gamma}_{\Sigma}(\varkappa,\mu,\lambda,\tau)$ и $\mathbb{H}^{\gamma}_{\Sigma}(\varkappa,\mu,\lambda,\delta)$. Также рассматриваются несколько примеров основных результатов.

Ключевые слова: аналитические и однолистные функции, двуоднолистные функции, функция Миттаг-Леффлера типа Ле Руа, оценки коэффициентов.

EDN: KUFSJS
УДК 517.9

Fixed Point Results for Paired Meir-Keeler Contraction with Application

Rachna Rathee*
Mohammad Asim†
Department of Mathematics
Faculty of Applied and Basic Sciences
SGT University
Gurugram (Haryana) – 122505 India

Received 10.07.2025, received in revised form 05.09.2025, accepted 27.09.2025

Abstract. In this paper, we introduce a paired Meir–Keeler contraction mapping and utilize it to prove some fixed point results in the framework of metric spaces. We also construct examples to emphasize the usefulness and relevance of our results. Furthermore, we use an integral equation in order to validate our newly proved results.

Keywords: fixed point, paired Meir–Keeler contraction, integral equation.

Citation: R. Rathee, M. Asim, Fixed Point Results for Paired Meir-Keeler Contraction with Application, J. Sib. Fed. Univ. Math. Phys., 2026, 19(1), 111–121. EDN: KUFSJS.

1. Introduction

Fixed point theory has made remarkable contributions to various topics. Some of them are analysis, topology and applied mathematics. It underpins many important theorems and helps in solving equations, differential equations, integral equations, addressing optimization problems and system dynamics. Fixed point theory was initiated by L. E. J. Brouwer. Later in 1922, S. Banach [20] introduced a remarkable results, whose pioneering contribution laid the groundwork for its growth, which is known as Banach contraction principle. This principle also plays a fundamental role in the theory of metric spaces. It requires a self-mapping by using some condition on a complete metric space in order to get fixed point. One of its primary applications lies in demonstrating the existence and uniqueness of solutions to equation, particularly within the framework of differential equations, integral and functional equation. The results of Banach contraction principle is used for solving equations in the analysis of iterative schemes. Furthermore, it serves as a key tool in proving the well-posedness of many problems in nonlinear analysis, control theory and economics.

Its impact encouraged mathematicians to extend its scope to a broader class of spaces and function. One key area of development focused on analyzing contraction in more generalized metric spaces that exhibit additional structural properties. For instance, b-metric space [11, 22], extended b-metric space [26], rectangular metric space [1], rectangular b-metric space [19], extended rectangular b-metric space [14], partial metric space [23], partial b-metric space [25], C^*-algebra valued metric space [28], C^*-algebra valued partial metric space [21], C^*-algebra valued b-metric space [29], C^*-algebra valued partial b-metric space [17] and there are many others, one can see([3, 12, 13, 16]).

*rachnarathee81@gmail.com
†mailtoasim27@gmail.com

The Meir–keeler contraction, a generalization of Banach contraction principle was introduce by A. Meir and E. Keeler [2]. In this contraction, we need a self-mapping in a metric space following some properties in order to find a unique fixed point. Numerous studies have been conducted on this topic. Some of them are mentioned as below. In 2009, C. M. Chen and T. H. Chang [4] introduced the concept of "weaker Meir–Keeler function" and "strong Meir-Keeler function". In 2018, U. A. K. Aksoy et. al., [27] give fixed point results using Meir–Keeler type contraction. There are also many generalization on the topic of Meir–Keeler contraction for that one can see([5–8, 10, 24]).

In this work, we introduce paired Meir–Keeler contraction. After that we have proved fixed point results by using paired Meir–Keeler contraction. The paper includes paired Meir–Keeler as a central tool to investigate the solvability of a certain class of integral equations, thereby highlighting its effectiveness in handling nonlinear structures within the framework of metric fixed point theory.

2. Preliminaries

Now, we recall some of the basic definition that will be useful to understand our result in a better way.

At first, we begin with a fundamental and essential definition which was given by M. R. Frechet in 1906. The definition of standard metric space which is as follows:

Definition 2.1 ([15]). *Let $U \neq \emptyset$. Then, a mapping $d_\theta : U \times U \to \mathbb{R}^+$ is referred to be a metric space if upcoming conditions hold, $(\forall u, v, w \in U)$:*

(1) $d_\theta(u, v) = 0$ *iff* $u = v$,

(2) $d_\theta(u, v) = d_\theta(v, u)$,

(3) $d_\theta(u, v) \leqslant d_\theta(u, w) + d_\theta(w, v)$.

Then, we assure that the pair (U, d_θ) is metric space.

Definition 2.2 ([18]). *Let T be a self mapping such that $T : U \to U$ and (U, d_θ) be a metric space. A point $u \in U$ is said to be a periodic point with period n if $T^n u = u$. The prime period of u is the smallest positive integer n with the value $T^n u = u$.*

Definition 2.3 ([9]). *Let (U, d_θ) be a metric space having cardinality greater than or equal to three. A mapping $T : U \to U$ is called paired contraction if $\exists\ L \in [0, 1)$ such that $(\forall u, v, w \in U)$*

$$d_\theta(Tu, Tv) + d_\theta(Tv, Tw) \leqslant L[d_\theta(u, v) + d_\theta(v, w)].$$

Remark 2.1. *If we put $u = w$ or $v = w$ in the above definition, then we are able to get contraction mapping.*

The example of paired contraction is as follows.

Example 2.1 ([9]). *Let $U = \{1, 2, 3\}$ and $d_\theta : U \times U \to [0, \infty)$ be defined as $\forall u, v \in U$*

$$d_\theta(u, v) = \begin{cases} 0, & \text{if } u = v \\ \dfrac{1}{4}, & \text{if } u, v \in \{1, 2\},\ u \neq v \\ \dfrac{1}{3}, & \text{if } u, v \in \{2, 3\},\ u \neq v \\ \dfrac{1}{2}, & \text{if otherwise.} \end{cases}$$

A mapping $T : U \to U$ be defined as

$$T(u) = \begin{cases} 2, & \text{if } u = 2, \\ 1, & \text{if otherwise}, \end{cases}$$

Now, $T(1) = 1$, $T(2) = 2$ and $T(T(3)) = 1 \neq 3$, then it is obvious that T does not have periodic points of prime period two. Moreover, let $L = \dfrac{9}{10}$

(1) $d_\theta(T(1), T(2)) + d_\theta(T(2), T(3)) \leqslant L[d_\theta(1, 2) + d_\theta(2, 3)] = \dfrac{1}{2} < \dfrac{33}{40}$.

(2) $d_\theta(T(1), T(3)) + d_\theta(T(3), T(2)) \leqslant L[d_\theta(1, 3) + d_\theta(3, 2)] = \dfrac{1}{4} < \dfrac{3}{4}$.

(3) $d_\theta(T(3), T(1)) + d_\theta(T(1), T(2)) \leqslant L[d_\theta(3, 1) + d_\theta(1, 2)] = \dfrac{1}{4} < \dfrac{27}{40}$.

(4) $d_\theta(T(3), T(2)) + d_\theta(T(2), T(1)) \leqslant L[d_\theta(3, 2) + d_\theta(2, 1)] = \dfrac{1}{2} < \dfrac{21}{40}$.

(5) $d_\theta(T(2), T(1)) + d_\theta(T(1), T(3)) \leqslant L[d_\theta(2, 1) + d_\theta(1, 3)] = \dfrac{1}{4} < \dfrac{27}{40}$.

(6) $d_\theta(T(2), T(3)) + d_\theta(T(3), T(1)) \leqslant L[d_\theta(2, 3) + d_\theta(3, 1)] = \dfrac{1}{4} < \dfrac{3}{4}$,

implies T is paired contraction.

Now, we present the following theorem given by D. Chand and Y. Rohen [9].

Theorem 2.1 ([9]). *Let $T : U \to U$ be the paired contraction and (U, d_θ) be a complete metric space having cardinality greater than or equal to three. Then T have a fixed point iff it does not have periodic points of prime period two and the maximum number of fixed point is two.*

Now, we recall the definition of Meir–Keeler contraction as given under:

Definition 2.4 ([2]). *Let (U, d_θ) be a complete metric space and $T : U \to U$ be a mapping. If for every $\epsilon > 0$ $\exists$ $\delta > 0$ such that*

$$\epsilon \leqslant d_\theta(u, v) < \epsilon + \delta \implies d_\theta(Tu, Tv) < \epsilon.$$

Then a mapping T is said to be a Meir–Keeler contraction.

3. Main Results

First of all, we give the definition of paired Meir–Keeler contraction which is the generalization of paired contraction.

Definition 3.1. *Suppose (U, d_θ) be a metric space having cardinality greater than or equal to three. A mapping $T : U \to U$ is said to be a paired Meir–Keeler contraction if for every $\epsilon > 0$ $\exists$ $\delta > 0$ such that*

$$\epsilon \leqslant d_\theta(u, v) + d_\theta(v, w) < \epsilon + \delta \implies d_\theta(Tu, Tv) + d_\theta(Tv, Tw) < \epsilon.$$

Now, we construct the example of paired Meir–Keeler contraction.

Example 3.1. *Let* $U = \{1, 2, 3, 4\}$ *and* $d_\theta : U \times U \to [0, \infty)$ *be defined as* $\forall u, v \in U$

$$d_\theta(u,v) = \begin{cases} 0, & \text{if } u = v \\ d_\theta(u,v) = d_\theta(v,u) & \forall\ u, v \in U \\ 1, & \text{if } u = 1, v \in U \setminus 1 \\ \dfrac{1}{10}, & \text{if } u = 2, v \in \{3,4\} \\ \dfrac{1}{3}, & \text{if otherwise.} \end{cases}$$

A mapping $T : U \to U$ *be defined as*

$$T(u) = \begin{cases} 4, & \text{if } u = 1, \\ 2, & \text{if otherwise,} \end{cases}$$

Let $\epsilon = \dfrac{1}{2}$ *and* $\delta = 5$. *Now,* $T(T(2)) = 2$ *and* $T(T(1)) = T(T(3)) = T(T(4)) = 2$. *Then, it is obvious that* T *does not have periodic points of prime period two. Moreover, taking* $u = 3$ *and* $v = 4$,

$$\epsilon \leqslant d_\theta(u,v) < \epsilon + \delta \implies d_\theta(Tu, Tv) < \epsilon$$

$$\frac{1}{2} \nleqslant d_\theta(3,4) < 5 + \frac{1}{2} \implies d_\theta(T(3), T(4)) < \frac{1}{2}$$

$$\frac{1}{2} \nleqslant d_\theta(3,4) < 5 + \frac{1}{2} \implies d_\theta(2,2) < \frac{1}{2}$$

$$\frac{1}{2} \nleqslant \frac{1}{3} < 5 + \frac{1}{2} \implies 0 < \frac{1}{2}$$

T is not Meir–Keeler contraction but

(1) $\epsilon \leqslant d_\theta(1,2) + d_\theta(2,3) < \epsilon + \delta \implies d_\theta(T(1), T(2)) + d_\theta(T(2), T(3))$
$\dfrac{1}{2} \leqslant \dfrac{11}{10} < \dfrac{11}{2} \implies \dfrac{1}{10} < \dfrac{1}{2}.$

(2) $\epsilon \leqslant d_\theta(1,2) + d_\theta(2,4) < \epsilon + \delta \implies d_\theta(T(1), T(2)) + d_\theta(T(2), T(4))$
$\dfrac{1}{2} \leqslant \dfrac{11}{10} < \dfrac{11}{2} \implies \dfrac{1}{10} < \dfrac{1}{2}.$

(3) $\epsilon \leqslant d_\theta(1,3) + d_\theta(3,4) < \epsilon + \delta \implies d_\theta(T(1), T(3)) + d_\theta(T(3), T(4))$
$\dfrac{1}{2} \leqslant \dfrac{4}{3} < \dfrac{11}{2} \implies \dfrac{1}{10} < \dfrac{1}{2}.$

(4) $\epsilon \leqslant d_\theta(2,3) + d_\theta(3,1) < \epsilon + \delta \implies d_\theta(T(2), T(3)) + d_\theta(T(3), T(1))$
$\dfrac{1}{2} \leqslant \dfrac{11}{10} < \dfrac{11}{2} \implies \dfrac{1}{10} < \dfrac{1}{2}.$

(5) $\epsilon \leqslant d_\theta(2,1) + d_\theta(1,4) < \epsilon + \delta \implies d_\theta(T(2), T(1)) + d_\theta(T(1), T(4))$
$\dfrac{1}{2} \leqslant \dfrac{11}{10} < \dfrac{11}{2} \implies \dfrac{1}{5} < \dfrac{1}{2}.$

(6) $\epsilon \leqslant d_\theta(2,3) + d_\theta(3,4) < \epsilon + \delta \implies d_\theta(T(2), T(3)) + d_\theta(T(3), T(4))$
$\dfrac{1}{2} \leqslant \dfrac{13}{10} < \dfrac{11}{2} \implies 0 < \dfrac{1}{2}.$

(7) $\epsilon \leqslant d_\theta(3,4) + d_\theta(4,2) < \epsilon + \delta \implies d_\theta(T(3), T(4)) + d_\theta(T(4), T(2))$
$\dfrac{1}{2} \leqslant \dfrac{13}{10} < \dfrac{11}{2} \implies 0 < \dfrac{1}{2}.$

(8) $\epsilon \leqslant d_\theta(3,4) + d_\theta(4,1) < \epsilon + \delta \implies d_\theta(T(3),T(4)) + d_\theta(T(4),T(1))$
$\frac{1}{2} \leqslant \frac{4}{3} < \frac{11}{2} \implies \frac{1}{10} < \frac{1}{2}.$

(9) $\epsilon \leqslant d_\theta(3,1) + d_\theta(1,2) < \epsilon + \delta \implies d_\theta(T(3),T(1)) + d_\theta(T(1),T(2))$
$\frac{1}{2} \leqslant 2 < \frac{11}{2} \implies \frac{1}{5} < \frac{1}{2}.$

(10) $\epsilon \leqslant d_\theta(4,3) + d_\theta(3,1) < \epsilon + \delta \implies d_\theta(T(4),T(3)) + d_\theta(T(3),T(1))$
$\frac{1}{2} \leqslant \frac{4}{3} < \frac{11}{2} \implies \frac{1}{10} < \frac{1}{2}.$

(11) $\epsilon \leqslant d_\theta(4,3) + d_\theta(3,2) < \epsilon + \delta \implies d_\theta(T(4),T(3)) + d_\theta(T(3),T(2))$
$\frac{1}{2} \leqslant \frac{13}{30} < \frac{11}{2} \implies 0 < \frac{1}{2}.$

(12) $\epsilon \leqslant d_\theta(4,1) + d_\theta(1,2) < \epsilon + \delta \implies d_\theta(T(4),T(1)) + d_\theta(T(1),T(2))$
$\frac{1}{2} \leqslant 2 < \frac{11}{2} \implies \frac{1}{5} < \frac{1}{2}.$

Then it is obvious that T is paired Meir–Keeler contraction.

We now present the main result of our work.

Theorem 3.1. *Suppose (U, d_θ) be a complete metric space having cardinality greater than or equal to three. A continuous function $T : U \to U$ is a paired Meir–Keeler contraction. Then the mapping T has a fixed point iff it does not have periodic points of prime period two. Moreover, the maximum number of fixed points is two.*

Proof. Suppose T be a prime period two mapping in which there are no periodic points. Our aim is to show that T admits fixed point. Let $Tu_0 = u_1,\ Tu_1 = u_2$ and so on such that

$$Tu_n = u_{n+1} \quad \forall n \in \mathbb{N}_0.$$

Now, if no element of u_n is a fixed point of the mapping T for every $n \in \mathbb{N}_0$ then it follows that all terms of the sequence u_n are distinct. As u_n is not fixed point, implies $u_{n+1} = Tu_n \neq u_n$. In addition, it follows that $u_{n+2} = T(Tu_n) \neq u_n$ as prime period two does not have any periodic points. As a results all u_n, u_{n+1} and u_{n+2}, all are distinct from one another. By using the definition of paired Meir-Keeler contraction, for every $\epsilon > 0\ \exists\ \delta > 0$ such that

$$\epsilon \leqslant d_\theta(u_{n-1}, u_n) + d_\theta(u_n, u_{n+1}) < \epsilon + \delta.$$

Now,

$$\begin{aligned} d_\theta(u_n, u_{n+1}) + d_\theta(u_{n+1}, u_{n+2}) &= d_\theta(Tu_{n-1}, Tu_n) + d_\theta(Tu_n, Tu_{n+1}) \leqslant \\ &\leqslant d_\theta(u_{n-1}, u_n) + d_\theta(u_n, u_{n+1}) - \delta \leqslant \\ &\leqslant d_\theta(u_{n-2}, u_{n-1}) + d_\theta(u_{n-1}, u_n) - 2\delta \leqslant \\ &\vdots \\ &\leqslant d_\theta(u_0, u_1) + d_\theta(u_1, u_2) - n\delta. \end{aligned}$$

Let $\psi_n = d_\theta(u_n, u_{n+1}) + d_\theta(u_{n+1}, u_{n+2}) - \delta$ for every $n \in \mathbb{N}_0$, then we have

$$\psi_n \leqslant \psi_{n-1} - \delta \leqslant \psi_{n-2} - 2\delta \leqslant \ldots \leqslant \psi_0 - n\delta \tag{1}$$

Let there exists a minimal natural number $j \geqslant 3$ for which $u_j = u_i$ holding $0 \leqslant i \leqslant j-2$. It implies that $u_{j+1} = u_{i+1}$ and $u_{j+2} = u_{i+2}$. Hence,

$$\psi_i = d_\theta(u_i, u_{i+1}) + d_\theta(u_{i+1}, u_{i+2}) = d_\theta(u_j, u_{j+1}) + d_\theta(u_{j+1}, u_{j+2}) = \psi_j$$

which is a contradiction to equation 1. Hence, there cannot exists such i and j. Now, suppose $\exists\ \epsilon_0 > 0$ and a subsequence ψ_{n_k} such that $\psi_{n_k} \geqslant \epsilon_0\ \forall k$. Then $\exists\ \delta > 0$ such that

$$\epsilon_0 \leqslant d_\theta(u, v) + d_\theta(v, w) < \epsilon_0 + \delta \implies d_\theta(Tu, Tv) + d_\theta(Tv, Tw) < \epsilon_0.$$

But by definition, we have

$$d_\theta(u_{n_k}, u_{n_k+1}) + d_\theta(u_{n_k+1}, u_{n_k+2}) = \psi_{n_k} \in [\epsilon_0, \epsilon_0 + \delta),$$

so,

$$d_\theta(u_{n_k+1}, u_{n_k+2}) + d_\theta(u_{n_k+2}, u_{n_k+3}) = d_\theta(Tu_{n_k}, Tu_{n_k+1}) + d_\theta(Tu_{n_k+1}, Tu_{n_k+2}) < \epsilon_0$$

which is a contradiction and implies $\psi_n \to 0$. Now, we claim that the sequence $\{u_n\}$ is cauchy. For any $m, n \in \mathbb{N}_0$ with $m \geqslant n$ and using triangular inequality.

$$\begin{aligned} d_\theta(u_n, u_m) &\leqslant d_\theta(u_n, u_{n+1}) + d_\theta(u_{n+1}, u_{n+2}) + \cdots + d_\theta(u_{m-1}, u_m) \leqslant \\ &\leqslant \psi_n + \psi_{n+1} + \cdots + \psi_{m-1} = \\ &= \sum_{r=n}^{m-1} \psi_r = \\ &= (m-n)\frac{\epsilon}{2} < \\ &< \epsilon \end{aligned}$$

implies $\{u_n\}$ is a cauchy sequence. As (U, d_θ) is a complete metric space let the sequence $\{u_n\}$ has a limit point u^*. Now, we will prove that u^* is the fixed point of T. By the continuity of T, we have

$$u^* = \lim_{n\to\infty} u_{n+1} = \lim_{n\to\infty} Tu_n = Tu^*$$

which implies that u^* is a fixed point of T.

Now, suppose three pairwise distinct fixed points, u^*, v^* and w^*. Then $Tu^* = u^*$, $Tv^* = v^*$ and $Tw^* = w^*$.

Now,

$$\begin{aligned} d_\theta(u^*, v^*) + d_\theta(v^*, w^*) &= d_\theta(Tu^*, Tv^*) + d_\theta(Tv^*, Tw^*) \leqslant \\ &\leqslant d_\theta(u^*, v^*) + d_\theta(v^*, w^*) - \delta \end{aligned}$$

which is a contradiction. Hence, T has two fixed points. □

Now, we prove the theorem for uniqueness as given under:

Theorem 3.2. *Let the fixed point u^* is a limit point of Picard iteration sequence $u_n = Tu_{n-1}$ having a starting point $u_0 \in U$. Then the mapping T of Theorem 3.1 has a unique fixed point.*

Proof. Suppose there exists another fixed point u^{**} for T such that $u^* \neq u^{**}$ where $u_n \neq u^{**}\ \forall n \in \mathbb{N}$ from the Theorem 3.1. It follows that all three elements u^*, u^{**} and u_n are pairwise distinct for any $n \in \mathbb{N}$. By using triangular inequality, we get

$$\begin{aligned} d_\theta(u^*, u^{**}) &\leqslant d_\theta(u^*, Tu_n) + d_\theta(Tu_n, u^{**}) = \\ &= d_\theta(u^*, u_{n+1}) + d_\theta(u_{n+1}, u^{**}) \\ &\to 0 \ \ as \ \ n \to \infty \end{aligned}$$

Hence, $d_\theta(u^*, u^{**}) = 0 \implies u^* = u^{**}$. Hence, T has a unique fixed point. □

Let us now illustrate the concept with an example.

Example 3.2. *In Example 3.1, we take $u = 1$, $v = 2$ and $w = 4$. Then from paired Meir–Keeler contraction, we have*

$$\epsilon \leqslant d_\theta(1,2) + d_\theta(2,4) < \epsilon + \delta \implies d_\theta(T1,T2) + d_\theta(T2,T4) < \epsilon.$$
$$\epsilon \leqslant d_\theta(1,2) + d_\theta(2,4) < \epsilon + \delta \implies d_\theta(4,2) + d_\theta(2,2) < \epsilon.$$
$$\frac{1}{2} \leqslant \frac{11}{10} < \frac{11}{2} \implies \frac{1}{10} < \frac{1}{2}.$$

Hence, 2 is a unique fixed point of T.

We now provide an additional example to demonstrate the conclusion of the Theorem 3.2.

Example 3.3. *Let (U, d_θ) be usual metric space, where $U = \{u_n\} \subset \mathbb{R}$ for $n \in \mathbb{N}_0$ defined as follows:*

$$u_n = \begin{cases} \dfrac{5}{2k}, & \text{if } n = 3r, \\ \dfrac{4}{2k}, & \text{if } n = 3r+1, \\ \dfrac{3}{2k}, & \text{if } n = 3r+2, \end{cases}$$

where $r \in \mathbb{N}_0$ and $k < 0$. Now, one can easily see that (U, d_θ) is a complete metric space. Suppose a mapping $T : U \to U$ defined by $Tu_n = u_{n+1}$ $\forall n \in \mathbb{N}_0$. Now, we take $u_{3n}, u_{3n+1}, u_{3n+2}$ in U. Then

$$d_\theta(Tu_{3n}, Tu_{3n+1}) = d_\theta(u_{3n+1}, u_{3n+2}) = d_\theta\left(\frac{4}{2k}, \frac{3}{2k}\right) = \frac{1}{2k}$$

$$d_\theta(u_{3n}, u_{3n+1}) = \frac{1}{2k}$$

implies that it is not Meir–Keeler contraction $\forall$ $k = 0, 1, 2, 3 \ldots$. Now,

$$d_\theta(Tu_{3n}, Tu_{3n+1}) + d_\theta(Tu_{3n+1}, Tu_{3n+2}) = d_\theta(u_{3n+1}, u_{3n+2}) + d_\theta(u_{3n+2}, u_{3n+3})$$
$$= d_\theta\left(\frac{4}{2k}, \frac{3}{2k}\right) + d_\theta\left(\frac{3}{2k}, \frac{5}{2k}\right) = \frac{1}{2k} + \frac{2}{2k} = \frac{3}{2k}$$
$$d_\theta(u_{3n}, u_{3n+1}) + d_\theta(u_{3n+1}, u_{3n+2}) = \frac{1}{2k} + \frac{1}{2k} = \frac{2}{2k} > \frac{3}{2k}$$

Hence, T is paired Meir–Keeler contraction which satisfied all the condition of Theorem 3.2. Hence, 0 is the unique fixed point of T (as shown in the Fig. 1).

The following corollary is a result due to D. Chand and Y. Rohen [9].

Corollary 3.1. *Suppose (U, d_θ) be a complete metric space having cardinality greater than or equal to three. A continuous function $T : U \to U$ is a paired contraction. Then the mapping T has a fixed point iff it does not have periodic points of prime period two. Moreover, the maximum number of fixed points is two.*

Proof. If we replace Meir–Keeler contraction with standard contraction mapping in the Theorem 3.1, then we get results. □

The following corollary is the result of A. Meir and E. Keeler [2].

Corollary 3.2. *Suppose (U, d_θ) be a metric space having cardinality greater than or equal to three. A mapping $T : U \to U$ is said to be a paired Meir–Keeler contraction if for every $\epsilon > 0$ $\exists$ $\delta > 0$ such that*

$$\epsilon \leqslant d_\theta(u,v) + d_\theta(v,w) < \epsilon + \delta \implies d_\theta(Tu,Tv) + d_\theta(Tv,Tw) < \epsilon.$$

Proof. Put $u = w$ or $v = w$ in the Theorem 3.1. The intended results is established. □

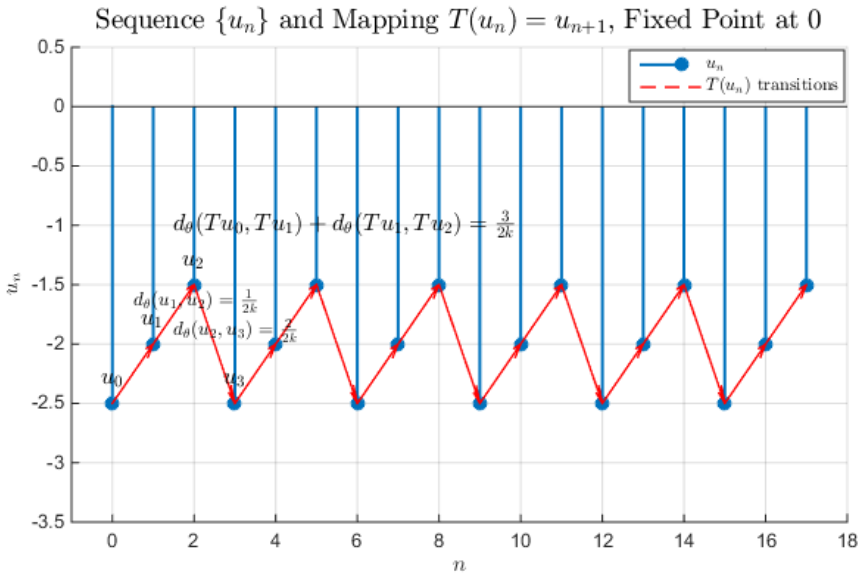

Fig. 1.

4. Application

As an application of the Theorem 3.1, we establish the existence and uniqueness of solution to the following type of integral equation.

$$u(\phi) = \int_\alpha^\beta \Gamma(\phi, \xi, u(\xi))d\xi + h(\phi), \ \forall \phi, \xi \in [\alpha, \beta]. \tag{2}$$

Let $U = C([\alpha, \beta]], \mathbb{R})$ and $\Gamma, h \in C([\alpha, \beta], \mathbb{R})$. Assume $d_\theta : U \times U \to \mathbb{R}^+$ such that

$$d_\theta(u, v) = \sup_{\phi \in [\alpha, \beta]} |(u(\phi) - v(\phi))|, \ \forall u, v \in U.$$

Thus, the pair (U, d_θ) is a complete metric space.

Theorem 4.1. *Suppose*

$$|\Gamma(\phi, \xi, u(\xi)) - \Gamma(\phi, \xi, v(\xi))| \leqslant \frac{\alpha}{(\beta - \alpha)(\epsilon + \delta)^2} |u(\phi) - v(\phi)|, \ \forall \phi, \xi \in [\alpha, \beta].$$

This implies that integral equation 2 has a solution which is unique.

Proof. Assume $T : U \to U$ by

$$Tu(\phi) = \int_\alpha^\beta \Gamma(\phi, \xi, u(\xi))d\xi + h(\phi), \ \forall \phi, \xi \in [\alpha, \beta].$$

As it is obvious that, u is the fixed point iff it is a solution of the integral equation 2. Now, for any $\epsilon > 0 \ \exists \ \delta > 0 \ \forall \ u, v, w \in U$, such that $\epsilon = \sqrt{\alpha}$

$$\epsilon \leqslant d_\theta(u, v) + d_\theta(v, w) < \epsilon + \delta.$$

Then

$$\begin{aligned}
d_\theta(Tu,Tv)+d_\theta(Tv,Tw) &= |T(u(\phi))-T(v(\phi))|+|T(v(\phi))-T(w(\phi))| = \\
&= \left|\int_\alpha^\beta \Gamma(\phi,\xi,u(\xi))-\Gamma(\phi,\xi,v(\xi))d\xi\right| + \\
&+ \left|\int_\alpha^\beta \Gamma(\phi,\xi,v(\xi))-\Gamma(\phi,\xi,w(\xi))+d\xi\right| \leqslant \\
&\leqslant \left(\int_\alpha^\beta \frac{\alpha}{(\beta-\alpha)(\epsilon+\delta)^2}|u(\phi)-v(\phi)|d\xi\right)+ \\
&+ \left(\int_\alpha^\beta \frac{\alpha}{(\beta-\alpha)(\epsilon+\delta)^2}|v(\phi)-w(\phi)|d\xi\right) \leqslant \\
&\leqslant \frac{(\alpha)}{(\beta-\alpha)(\epsilon+\delta)^2}\sup_{\phi\in[\alpha,\beta]}|u(\phi)-v(\phi)|\left(\int_\alpha^\beta d\xi\right)+ \\
&+ \frac{(\alpha)}{(\beta-\alpha)(\epsilon+\delta)^2}\sup_{\phi\in[\alpha,\beta]}|v(\phi)-w(\phi)|\left(\int_\alpha^\beta d\xi\right) \leqslant \\
&\leqslant \frac{(\alpha)}{(\epsilon+\delta)^2}d_\theta(u,v)+\frac{(\alpha)}{(\epsilon+\delta)^2}d_\theta(v,w) = \\
&= \frac{(\alpha)}{(\epsilon+\delta)^2}[d_\theta(u,v)+d_\theta(v,w)] \leqslant \\
&\leqslant \frac{(\alpha)}{(\epsilon+\delta)^2}(\epsilon+\delta) \leqslant \\
&\leqslant \frac{(\alpha)}{(\epsilon+\delta)} \leqslant \\
&\leqslant \epsilon.
\end{aligned}$$

Hence, the condition of Theorem 3.1 is satisfied. So, we are able to say that T has a solution which is unique. □

Conclusion

The paper provided the concept of paired Meir–Keeler contraction and also gave fixed point results by using paired Meir–Keeler contraction. This idea helps further generalizes the theory of fixed point. We had also provided some example to validate the usefulness of theoretical results. At end, we applies our results to find the solution of the system of integral equation.

References

[1] A.Branciari, A fixed point theorem of Banach-Caccioppoli type on a class of generalized metric spaces, *Publ. Math.,* **57**(2000), 31–37.

[2] A.Meir, E Keeler, A theorem on contraction mapping, *Journal of Mathematical Analysis and application,* **28**(1969), 326–329.

[3] B.Moeini, M.Asadi, H.Aydi, H.Alsamir, M.S.Noorani, C^*-algebra valued M-metric spaces and some related fixed point results, *Ital. J. Pure Appl. Math.,* **41**(2019), 708–723.

[4] C.M.Chen, T.H.Chang, Fixed Point Theorems for a weaker Meir-Keeler Type ψ-Set Contraction in Metric Spaces, *Fixed Point Theory Appl.,* **2009**(2009), 129124.

[5] C M.Chen, E.Karapinar, Fixed point results for the alpha-Meir-Keeler contraction on partial Hausdroff metric spaces, *J. Inequal. Appl.,* **2013**(2013), 410. DOI:10.1186/1029-242X-2013-410

[6] C.M.Chen, E.Karapinar, I.J.Lin, Periodic points of weaker MEir-Keeler contractive mappings on generalized quasi-metric spaces, *Abstract Appl. Anal.,* **2014**(2014), 490450. DOI: 10.1155/2014/490450

[7] C.M.Chen, E.Karapinar, G.T.Chen, On Meir-Keeler-Khan set contractions, *J. Nonlinear Sci. Appl.,* **9**(2016), 5271–5280. DOI: 10.22436/jnsa.009.08.13

[8] C.M.Chen, E.K.D.O'regan, On $(\alpha - \phi)$-Meir-Keeler Contraction mapping on partial Hausdorff Metric Spaces, *Univ. Politeh. Buchar. Sci. Bull. Ser. A Appl. Math. Phys.,* **80**(2018), 101–110.

[9] D.Chand, Y.Rohen, Paired contractive mappings and fixed point results, *AIMS Mathematics,* **9**(2023), no. 1, 1959–1968. DOI: 10.3934/math.2024097

[10] H.Aydi, E.Karapinar, D.Zhang, A note on generalized admissible-Meir-Keeler-contraction in the context of generalized metric spaces, *Results MAth.,* **71**(2017), 73–92.

[11] I.A.Bakhtin, The contraction mappings in b-metric spaces, *Funct. Anal.,* (1989), no. 1, 5–11.

[12] M.Asadi, E.Karapinar, P.Salimi, New extension of p-metric spaces with some fixed-point results on M-metric spaces, *J. Inequal. Appl.,* **18**(2014). DOI: 10.1186/1029-242X-2014-18

[13] M Asim, A.R.Khan, M.Imdad, Rectangular M_b-metric spaces and fixed point results, *Ital. Journal of mathematics analysis,* **10**(2019), no. 1, 10–18.

[14] M.Asim, M.Imdad, S.Radenovic, Fixed Point Results In Extended Rectangular b-Metric Spaces With An Application, *J. Math. Anal. Appl.,* **81**(2019), no. 2, 43–50.

[15] M.R.Frechet, Sur quelques points du calcul fonctionnel, *Rendic. Circ. Mat. Palermo.,* **22**(1906), 1–74.

[16] N.Mlaiki, A.Zarrad, N.Souayah, A.Mukheimer, T.Abedeljawed, Fixed Point Theorems in M_b-metric spaces, *J. Math. Anal.,* **7**(2016), 1–9.

[17] N.Mlaiki, M.Asim, M.Imdad, C^*-algebra valued partial b-metric spaces and fixed point results with an application, *Mathematics,* **8**(2020), 1381. DOI: 10.3390/math8081381,

[18] R.Devaney, An introduction to chaotic dynamical systems, 2 Eds., CRC Press. DOI: 10.4324/9780429502309

[19] R.George, S.Radeovic, K.P.Reshma, S.Shukla, Rectangular b-metric spaces and contraction principles, *J. Nonlinear Sci. Appl.,* **8**(2015), 1005–1013.

[20] S.Banach, Sur les operations dans les ensembles abstraits et leur application aux equations integrals, *Fund. Math.,* **3**(1922), 133–181.

[21] S.Chandok, D.Kumar, C.Park, C^*-algebra valued partial metric spaces and fixed point theorems, *Proc. Indian Acad. Sci. (Math Sci.),* **129**(2019), no. 37, 1–8.

[22] S.Czerwik, Contraction mappings in b-metric spaces, *Acta Mathematica et Informatica Universitatis Ostraviensis,* **1**(1993), no. 1, 5–11.

[23] S.G.Matthews, Partial metric topology, *Annals of the New York Academy of Science,* **728**(1994), 183–197.

[24] S.Gulyaz, I.Erhan, E.Karapinar, Generalized α-Meir-Keeler-contraction in the context of generalized metric spaces, *Filomat,* **31**(2017), 5445–5456. DOI: 10.2298/FIL1717445G

[25] S.Shukla, Partial b-metric Spaces and Fixed Point Theorems, *Mediterr. J. Math,* **11**(2014), no. 2, 703–711. DOI: 10.1007/s00009-013-0327-4

[26] T.Kamran, M.Samreen, Q.U.Ain, A generalization of b-metric space and some fixed point theorems, *Mathematics,* **5**(2017), Paper No. 19. DOI:10.3390/math5020019

[27] U.E.K.Aksoy, I.M.Erhan, V.Rakocevic, Meir-Keeler Type Contraction on Modular Metric Spaces, *Filomat,* **32**(2018), 3697–3707. DOI: 10.2298/FIL1810697A

[28] Z.H.Ma, L.N.Jiang, H.K.Sun, C^*-algebra valued metric spaces and related fixed point theorems, *Fixed Point Theory Appl.,* **206**(2014), 1–11.

[29] Z.H.Ma, L.N.Jiang, C^*-algebra valued b-metric spaces and related fixed point theorems, *Fixed Point Theory Appl.,* **222**(2015), 1–12. DOI: 10.1186/s13663-015-0471-6

Результаты с фиксированной точкой для парного сокращения Мейра-Килера с приложением

Рахна Рати
Мохаммад Асим
Факультет прикладных и фундаментальных наук
Университет SGT
Гуруграм (Харьяна) – 122505, Индия

Аннотация. В этой статье мы вводим парное отображение сжатия Мейра–Килера и используем его для доказательства некоторых результатов о неподвижных точках в рамках метрических пространств. Мы также приводим примеры, подчеркивающие полезность и актуальность наших результатов. Кроме того, мы используем интегральное уравнение для проверки наших новых результатов.

Ключевые слова: неподвижная точка, парное сокращение Мейра–Килера, интегральное уравнение.

EDN: MWDAOG
УДК 519.174.7; 535.3

Edge States on Hexagonal Array of Resonators with Complex Coupling Constants

Dmitry P. Fedchenko*
Kirensky Institute of Physics
Federal Research Center KSC SB RAS
Krasnoyarsk, Russian Federation
Siberian Federal University
Krasnoyarsk, Russian Federation
Daria V. Goryacheva†
Siberian Federal University
Krasnoyarsk, Russian Federation
Ivan V. Timofeev‡
Kirensky Institute of Physics
Federal Research Center KSC SB RAS
Krasnoyarsk, Russian Federation
Siberian Federal University
Krasnoyarsk, Russian Federation

Received 10.06.2025, received in revised form 05.10.2025, accepted 20.11.2025

Abstract. A waveguide system consisting of a hexagonal array of resonators with the sixth-order symmetry is studied. Using deformations in the system obtained by permuting vertices on the coordination spheres and changing the constants of coupling between the resonators, the edge states have been obtained, the origin of which is explained by elementary means. The edge solutions are preserved for an array with the complex coupling constants.

Keywords: photonic edge states, graphene crystal lattice, tight binding approximation, complex coupling constants.

Citation: D.P. Fedchenko, D.V. Goryacheva, I.V. Timofeev, Edge States on Hexagonal Array of Resonators with Complex Coupling Constants, J. Sib. Fed. Univ. Math. Phys., 2026, 19(1), 122–128. EDN: MWDAOG.

Introduction

The one-dimensional Su–Schrieffer–Heeger (SSH) lattice model originated from physics of condensed matter [1] has found application in describing edge states in acoustics and photonics. Edge and defect modes of phononic and photonic crystals, Tamm states [2], and stable waveguide modes of photonic topological insulators [3,4] can be described through the bulk-edge correspondence for topologically nontrivial dispersion surfaces. Such a description opens up the possibility of creating new materials and devices with the unique properties, which provide immunity to defects and disorder. In the SSH model and its generalizations to two-dimensional lattices [5], Maxwell's equations are used to describe the propagation of electromagnetic waves in photonic crystals and on metasurfaces. Generalization of the crystal concept to photonic and phononic structures allows one to cover a variety of periodic structures with a characteristic lattice parameter on the scales from nanometers to millimeters.

*fdp@iph.krasn.ru https://orcid.org/0000-0003-2684-6226
†dgoryacheva@sfu-kras.ru
‡tiv@iph.krasn.ru https://orcid.org/0000-0002-6558-5607

At a certain parity of the number of resonators in a chain with periodically changing strong and weak couplings, topologically protected Tamm states arise at its edges. Among the important problems of topological photonics, one can highlight the use of electronic topological insulators as optical materials [3] and application of photonic topological insulators [6], in particular, to obtain topologically stable optical Tamm states [2] and topological states on arrays of vertical-cavity surface-emitting microlasers [7] and in photonic topological insulators assembled on an array of ring [8] or prism resonators [9, 10].

The discovery of graphene has stimulated considerable interest in its unique properties. Along with graphene, other materials with a hexagonal structure have been intensively studied. The connectivity matrix corresponding to a hexagonal lattice is symmetric with a real spectrum. A specific arrangement of strong and weak couplings between structural elements allows for the creation of an edge vibrational eigenmode, which is preserved when introducing the complex coupling constants. By preserving the Hermitian property of the connectivity matrix, a system with a real spectrum is obtained. Of particular interest are specific implementations of systems with the complex coupling constants (see, for example, [11]).

Another observation concerning the hexagonal structure is that it decomposes into numerous concentric coordination spheres (circles). Groups of permutations of the sphere elements generate structure symmetries that are similar in properties to moir? patterns in the frequency domain (see, for example, [12]). These symmetries are inherent in the vibrational modes that arise in the hexagonal structure.

1. Projection onto a plane

In this work, the eigenmodes of a resonator array forming a hexagonal lattice are examined. To obtain a model with alternating strong and weak couplings, we project points of the positive octant of a three-dimensional integer lattice with side length 1 onto the plane orthogonal to the diagonal vector $\mathrm{e}_d = (1,\ 1,\ 1)$, as shown in Figs. 1a–1c, and consider two tetrahedra in each cell of the lattice (Fig. 1b). The tetrahedron height is $h_t = \sqrt{4/3}$. The distance ρ_t between the bases of the tetrahedra of one cell is calculated as $\rho_t = 2h_t - d$, where $d = \sqrt{3}$ is the cube diagonal.

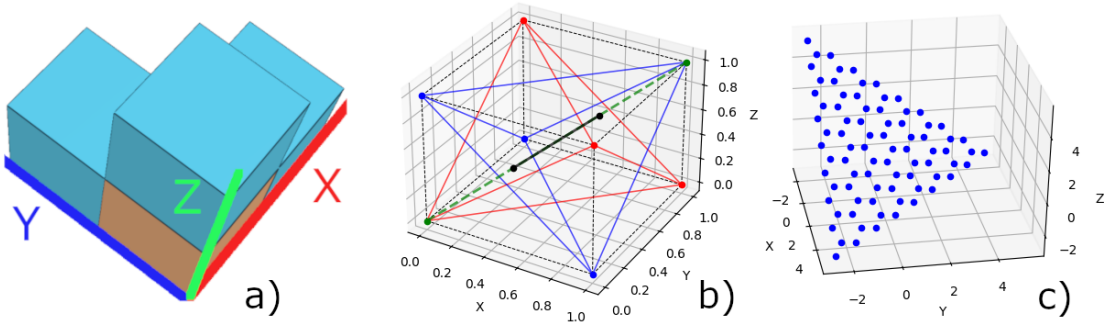

Fig. 1. (a) Three-dimensional Young diagram$(1,\ 1,\ 1)^2$. The exponent 2 denotes the number of layers in the Young diagram. (b) Tetrahedra inside the cube are colored in red and blue. The black line shows the distance $\rho_t = \sqrt{1/3}$ between the bases of the tetrahedra, which is half the tetrahedron height $h_t = \sqrt{4/3}$ (c) Projection of the spatial Young diagram onto the plane orthogonal to the vector e_d

To obtain a two-dimensional hexagonal (graphene) lattice, it is sufficient to leave only the points for which the ratio of the projection lengths to ρ_t is expressed as an integer (see Fig. 1c)

in the plane $p_1 : x + y + z = 0$. To implement the design, we consider the orthonormal basis

$$u_k = \left[\frac{\omega^0}{\sqrt{3}}, \frac{\omega^k}{\sqrt{3}}, \frac{\omega^{2k}}{\sqrt{3}}\right]^T, \quad k = 0, 1, 2,$$

which consists of the eigenvectors of the circulant matrix $C_3 = [a_0, a_1, a_2]$, $a_j \in \mathbb{C}$. Here, $\omega = e^{2\pi i/3}$ is the primitive third root of unity. In the basis of the eigenvectors of the circulant matrix C_3, the projector onto the plane p_1 will have the form $P^{'} = \mathrm{diag}(0, 1, 1)$ and, in the standard orthonormal basis, it is $P = BP^{'}B^{-1}$, where $B = [u_0, u_1, u_2]$ is the matrix of transformation to a new basis, the columns of which are vectors u_j. The circulant matrices form an important class and find application in many areas of mathematics, in particular, in the graph theory [13]. Affecting the integer vectors $v = (v_x, v_y, v_z) = (i, j, k)$, $i, j, k \in \mathbb{Z}_{\geqslant 0}$, by the P matrix, we will obtain projections of these points onto the plane p_1. The internal coordinates in the plane p_1 are specified by the formulas $((B^{-1}Pv)_x, (B^{-1}Pv)_y)$. Let us assume that the projection point preserves the color of the tetrahedron's base. We consider two classes of couplings. Coupling w is called weak if adjacent nodes of the hexagonal lattice have the same color. Coupling v is called strong if adjacent nodes are colored differently. The two nearest lattice nodes are called neighbors. In this case, $v \geqslant w$ are the real numbers called the coupling constants. To obtain a trivial lattice with only the v-type couplings, we need to project the top layer of the three-dimensional Young diagram (see Fig. 1 a). Indeed, every two cubes are adjacent along the edge one vertex of which belongs to the blue tetrahedron and the other, to the red one. In the projection onto the plane p_1, we obtain a hexagonal lattice in which every two neighbors have different colors (Fig. 2a). We denote the ordinal number of the resonator in the array by $N \in [0, 42)$. Let us exclude some points from the consideration so that the graph $G = (V, E)$ had the hexagon shape and symmetryC_3, where V is the set of the graph vertices and E is the set of the graph edges.

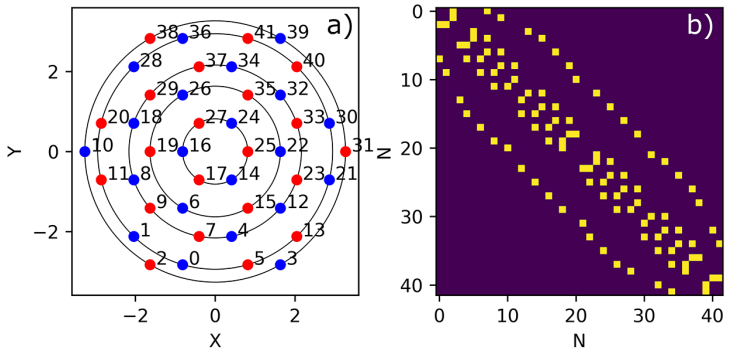

Fig. 2. (a) Hexagonal lattice consisting of 42 resonators. The vertex color corresponds to the tetrahedron color (see Fig. 1b). Two types of couplings (weak w and strong v) are introduced and it is assumed that there is a strong coupling between resonators of different colors and a weak coupling between resonators of the same color. Each vertex is assigned serial number N of a resonator. (b) Connectivity matrix of the graph corresponding to the resonator array. Nonzero elements of the matrix are highlighted in a special color

For the structure shown in Fig. 2a, the graph vertices are located on concentric circles with the respective radii

$$r,\ 2r,\ \mathrm{dr}(1),\ \mathrm{da}(3),\ 4r \tag{1}$$

starting from the small circle. In Eq. (1), r is the radius of the circle circumscribed around one hexagon of the hexagonal lattice and $\mathrm{dr}\,(k)$ and $\mathrm{da}(k)(k \in \mathbb{Z}_{\geqslant 0})$ are the functions for calculating

the trapezoid diagonal length:

$$\mathrm{dr}(k), \mathrm{da}(k) = \sqrt{AB + C^2 + B(D^2 - C^2)/(B - A)},$$

where the parameters A, B, C, D are

$$A = ka,\ B = r\sqrt{3}/2 + A,\ C = r/2,\ D = r$$

for dr and

$$A = kr,\ B = r/2 + A,\ C = a/2,\ D = r$$

for da. Here, $a = \sqrt{2}$ is the two-dimensional square diagonal, which is simultaneously the tetrahedron side (Fig. 1b).

2. Edge states of the structure

Let us write the connectivity matrix $A(G)$ of the graph G (Fig. 2b). The units are highlighted in bright colors. Recall that two adjacent vertices are connected by an edge. The edge's weight, or the coupling strength, is determined by the coloring of the adjacent vertices. Figure 1a shows the graph in which all the coupling constants have the same v value.

The graph serves as an effective mathematical model for describing waveguide systems in physics of solid state, photonics, and acoustics. The presence of an edge between vertices indicates wave propagation in a specified direction. To obtain the Hamiltonian of the system in tight binding approximation $H_\mathrm{k} = A(G)\mathrm{e}^{i\mathrm{kr}}$, we multiply the connectivity matrix $A(G)$ by the phase factore$^{i\mathrm{kr}}$, where k is the quasimomentum and r is the lattice translation vector. To find the Bloch wave function, we solve the eigenvalue problem for the equation

$$H_\mathbf{k}\psi = E_\mathbf{k}\psi.$$

In physics, a topological insulator is the state of a waveguide system that is conductive at the boundary and prevents wave propagation in the bulk. In our search for the edge states, we consider a simplified problem, which ignores the phase shift. To do this, we find the eigenvectors of the connectivity matrix $A(G)$, the elements of which yield the resonator radiation amplitudes for the corresponding mode. A boundary or edge is defined as a set of lattice nodes that have fewer than three neighbors. Figure 3a shows the spectrum of a structure in which the strong and weak couplings coincide in amplitude: $w = v = 0.5$. When introducing a contrast (difference) between the strong and weak coupling constants, a gap arises in the energy spectrum (Fig. 3c). The eigenvector matrices for the structures without and with contrast are presented in Figs. 3b and 3d, respectively. Here, eigenvalue 35 is highlighted. The corresponding mode is localized at the boundary (see Fig. 4a).

The hexagonal lattice structure introduced by us allows for rotational symmetries. Let us consider rotations of the concentric circles that permutate elements of a specified orbit. By rotating the ring following the inner one by an angle of $\pi/3$, we perform a cyclic permutation of the vertices lying on a circle of radius $2r$. This yields a mode localized at the boundary of the structure. Indeed, the investigated symmetry closes the channels for propagation of a surface wave into the structure.

Conclusion

In this study, a waveguide system based on a hexagonal array of resonators, which is decomposed into concentric coordination spheres, was examined. By introducing the strong and weak couplings between the resonators and permuting the vertices, the eigenmodes of the system with

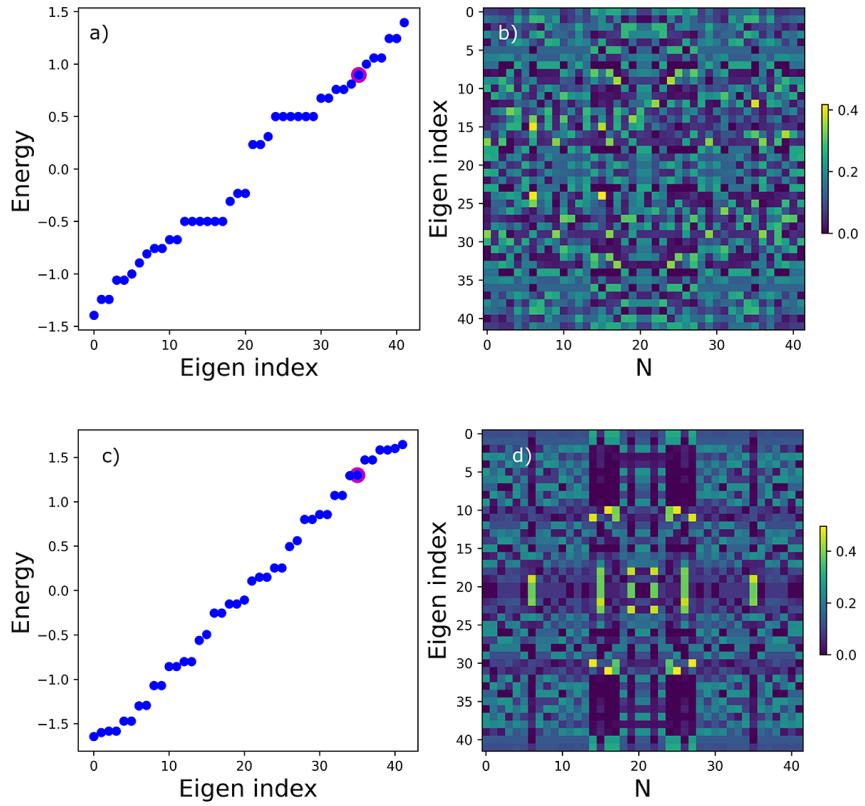

Fig. 3. (a) Real spectrum of a symmetric operator. Dots show the eigenvalues of the connectivity matrix sorted in ascending order. The point with an eigenindex of 35 is marked separately in the spectrum. (b) Each row of the matrix corresponds to a wave function, which is an eigenvector of the resonator radiation amplitudes. (c) Spectrum with a contrast between the strong and weak couplings: $w = 0.2$ and $v = 0.8$. (d) Matrix of eigenvectors

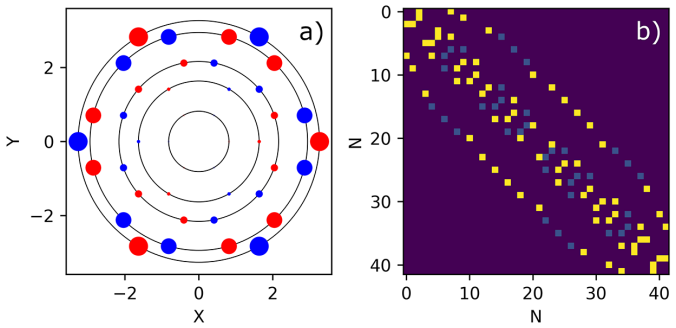

Fig. 4. (a) Hexagonal resonator lattice in which the coloring of the nodes located on the second coordination sphere from the center is changed. This transformation corresponds to a rotation of this circle by $\pi/3$ in any direction. Defects appear in the structure and the eigenstates are localized on them. The radius of the circle representing the resonator is related to the radiation amplitude. The mode with an Eigen index of 35 is shown. (b) Connectivity matrix of the graph corresponding to an array of resonators with the coupling constants of two types: $w = 0.2$ and $v = 0.8$

different properties can be obtained. With a certain rotation of the coordination spheres and an increase in the contrast between the strong and weak couplings, the edge solutions located in the energy spectrum gap were obtained. The edge solutions are preserved for a structure with the complex coupling constants.

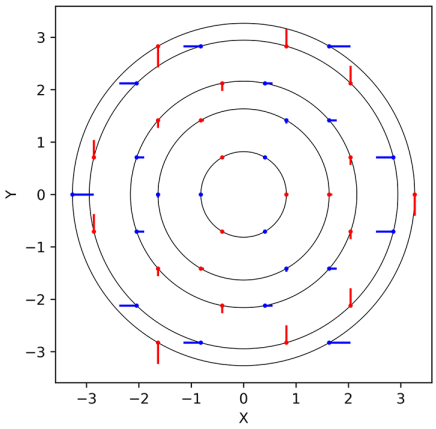

Fig. 5. Hexagonal resonator array with a radiation vector field depicted on it. The vector length at each point indicates the oscillation amplitude. The arrow direction corresponds to the oscillation phase

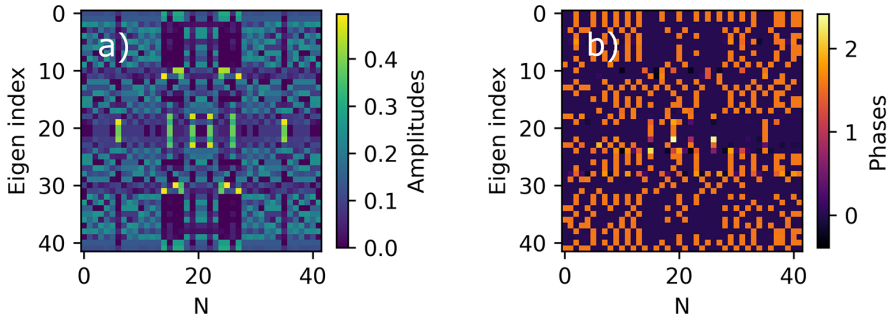

Fig. 6. Eigenmodes of the structure with the complex coupling constants: (a) oscillation amplitude and (b) oscillation phase (rad)

This study was supported by the Russian Science Foundation, project no. 24-12-00236.

References

[1] W.P.Su, J.R.Schrieffer, A.J.Heeger, Solitons in polyacetylene, *Physical review letters*, **42**(1979), no. 25, 1698.

[2] P.St-Jean, et al., Lasing in topological edge states of a one-dimensional lattice, *Nature Photonics*, **11**(2017), no. 10, 651–656.

[3] A.S.Sergeev, Topological insulators and geometry of vector bundles, SciPost Physics Lecture Notes, 2023.

[4] I.Maresin, A.Sergeev, E.Teplyakov, On mathematical aspects of the theory of topological insulators, *Acta Mathematica Sinica, English Series*, **40**(2024), no. 1, 81–106.
DOI: 10.1007/s10114-023-1677-x

[5] J.Wu, et al., Higher-order topological polariton corner state lasing, *Science Advances*, **9**(2023), no. 21, eadg4322. DOI: 10.1126/sciadv.adg4322

[6] Z.He, et al., Reconfigurable topological states in arrays of bianisotropic particles, ACS Photonics, vol. 9, 2022, issue 7, 2322–2326. DOI: 10.1021/acsphotonics.2c00309

[7] A.Dikopoltsev, et al., Topological insulator vertical-cavity laser array, *Science*, **373**(2021), no. 6562, 1514–1517. DOI: 10.1126/science.abj2232

[8] F.Gao, et al., Probing topological protection using a designer surface plasmon structure, *Nature communications*, **7**(2016), no. 1, 11619. DOI: 10.1038/ncomms11619

[9] D.P.Fedchenko, P N.Kim, I.V.Timofee, Photonic topological insulator based on frustrated total internal reflection in array of coupled prism resonators, *Symmetry*, **14**(2022), no. 12, 2673. DOI: 10.3390/sym14122673

[10] P.N.Kim, et al., Tiling photonic topological insulator for laser applications, *Applied Sciences*, **13**(2023), no. 6, 4004. DOI: 10.3390/app13064004

[11] D.N.Vavulin, A.A.Sukhorukov, Robust generation of orbital-angular-momentum–entangled biphotons in twisted nonlinear-waveguide arrays, *Physical Review A*, **96**(2017), no. 1, 013812. DOI: 10.1103/PhysRevA.96.013812

[12] D.Yu, et al., Moiré lattice in one-dimensional synthetic frequency dimension, *Physical Review Letters*, **130**(2023), no. 14, 143801. DOI: 10.1103/PhysRevLett.130.143801

[13] Y.S.Kwon, A.D.Mednykh, I.A.Mednykh, On the structure of Laplacian characteristic polynomial of circulant graphs, *Doklady Mathematics*, Moscow: Pleiades Publishing, **109**(2024), no. 1, 25–29. DOI: 10.1134/S1064562424701771

Граничные состояния на гексагональной решетке резонаторов с комплексными константами связи

Дмитрий П. Федченко
Институт физики им. Л. В. Киренского ФИЦ КНЦ СО РАН
Красноярск, Российская Федерация
Сибирский федеральный университет
Красноярск, Российская Федерация
Дарья В. Горячева
Сибирский федеральный университет
Красноярск, Российская Федерация
Иван В. Тимофеев
Институт физики им. Л. В. Киренского ФИЦ КНЦ СО РАН
Красноярск, Российская Федерация
Сибирский федеральный университет
Красноярск, Российская Федерация

Аннотация. В статье рассматривается волноводная система, представляющая собой гексагональный массив резонаторов с симметрией шестого порядка. За счет деформаций в системе, получаемых перестановками вершин на координационных сферах и изменением значений констант связи между резонаторами, были получены краевые состояния, происхождение которых объясняется элементарными средствами. Краевые решения сохраняются для массива с комплексными константами связи.

Ключевые слова: фотонные краевые состояния, кристаллическая решетка графена, приближение жесткой связи, комплексные константы связи.

Journal of Siberian Federal University. Mathematics & Physics 2026, 19(1), 129–138

EDN: UHQSLL
УДК 532.5; 519.62

Mass Transfer Analysis in Microchannels with Single and Dual Scale Pin Fin Array Configurations

Olga A. Solnyshkina*
Nazgul B. Bikkinina†
Karina A. Galieva‡
Aiguzel Z.Bulatova§
Iskandar Sh.Garifullin¶
Ufa University of Science and Technology
Ufa, Russian Federation

Received 10.06.2025, received in revised form 05.08.2025, accepted 27.09.2025

Abstract. An important aspect in designing efficient micro heat sink devices is selecting the optimal geometry of the internal microstructure of microchannels to minimize hydrodynamic resistance and enhance transverse flows. This work investigates the influence of altering the internal configuration of microchannels with an array of cylindrical pins on the hydrodynamic features of viscous incompressible fluid flow. The numerical approach used to solve the Stokes equations in three dimensions for asymmetric domains is based on the boundary element method accelerated by the fast multipole method on heterogeneous computing architectures. Validation of the developed software modules was carried out by comparing them with experimental data obtained from microfluidic chips. A series of calculations was performed, and new data were obtained on the effect of changing the pin packaging parameters within a microchannel element on the intensification of transverse flows and the variation in throughput capacity.

Keywords: microchannel, microfluidics, Boundary element method, direct numerical simulation, pin fin array, micro heat sink.

Citation: O.A. Solnyshkina, N.B. Bikkinina, K.A. Galieva, A.Z. Bulatova, I.Sh. Garifullin, Mass Transfer Analysis in Microchannels with Single and Dual Scale Pin Fin Array Configurations, J. Sib. Fed. Univ. Math. Phys., 2026, 19(1), 129–138. EDN: UHQSLL.

1. Motivation

Recent advances in miniaturization, increasingly complex designs, and cutting-edge developments in electronic devices have led to premature failures due to uneven thermal energy distribution and localized overheating. Traditional cooling methods often prove inadequate, as they fail to provide sufficient heat transfer intensity or cause excessive cooling in certain device regions. A promising solution lies in microchannel heat exchangers, which are widely used in power electronics, aerospace, energy systems, microelectronics, and other fields. Their key advantages include high efficiency, compactness, a large surface-area-to-volume ratio for coolant contact, and design flexibility. The microchannel structure is critical, as it must simultaneously maximize heat transfer surface area while maintaining acceptable hydrodynamic losses for coolant flow.

In recent years, the electronics industry has been actively advancing three-dimensional integrated circuit (3D-IC) technologies, where multiple substrates with electronic components are

*olgasolnyshkina@gmail.com https://orcid.org/0000-0001-8767-1453
†nazgulbay@mail.ru https://orcid.org/0000-0002-3944-1976
‡espscnart@gmail.com https://orcid.org/0009-0005-3880-0040
§bulatova29@yandex.ru https://orcid.org/0000-0003-1741-7024
¶is@bgutmo.ru https://orcid.org/0000-0002-2695-9944

stacked in parallel with gaps of 50–100 μm [1]. Such configurations significantly complicate thermal management tasks, driving the development of efficient microscale liquid cooling systems. The design of these systems requires a thorough understanding of flow hydrodynamics and heat transfer processes in microchannels. A critical aspect of microheat sink design is the optimization of the internal microchannel geometry. In practice, arrays of micropins with various shapes—including cylindrical, triangular, rectangular, and hexagonal cross-sections are widely employed [2–4]. However, studies indicate that the highest heat transfer performance is achieved with circular and square pin geometries due to their optimal balance of hydraulic resistance and thermal transfer intensity [5]. The dimensions of these elements vary depending on the device purpose, with their height ranging from 50% to 100% of the microchannel height. The void fraction α may also vary between 40% and 80%, with the most efficient heat exchange observed in heat sinks featuring a void fraction of approximately 70%. In [6], the effect of increasing the packing density of ellipsoidal pins in a microchannel on heat transfer was investigated. The results demonstrated that a denser pin arrangement enhances thermal performance by generating vortex structures and secondary flows, thereby increasing the effective heat transfer area.

A review of the literature revealed that, despite the significant number of studies focused on the design of microfluidic heat sinks, most research is limited to structures with uniformly distributed pins or fins. The effectiveness of multi-scale configurations (e.g., hierarchical or fractal geometries) remains virtually unexplored. Furthermore, existing studies primarily examine microchannels with hydraulic diameters exceeding 100 μm, while the hydrodynamics of flows in microchannels featuring non-uniform micropin arrays with heights below 100 μm has not been sufficiently investigated. Thus, a systematic study of heat transfer and hydrodynamics in microfluidic systems with subcritical-scale non-uniform pin structures holds not only fundamental importance for advancing microfluidic hydrodynamics but also substantial practical value for the development of next-generation high-efficiency microheat sinks.

The objective of this study is to perform numerical analysis of the influence of secondary-scale ordering of circular cross-section pins on both hydrodynamic resistance in a microchannel section and intensification of transverse flows. For this class of problems, we employ for the first time a numerical approach based on the Boundary Element Method (BEM) for three-dimensional problems, accelerated through both a highly efficient scalable algorithm (Fast Multipole Method (FMM)) and utilization of heterogeneous computing architectures (multi-core CPUs and graphics processing units GPUs). This approach enables detailed investigation of hydrodynamic flow features in microfluidic elements with non-trivial spatial pin arrangements while performing computationally intensive simulations on a personal workstation.

2. Problem statement and numerical approach

The schematic formulation of the industrial problem, computational domain, and experimental setup assembled for validation of computational modules are presented in Fig. 1. The functional element of the microfluidic device considered in this work is modeled as a rectangular cross-section plane microchannel with cylindrical pins arranged transverse to the flow. The simulation examines periodic flow of a viscous incompressible fluid (with dynamic viscosity and density μ and ρ) under a constant pressure drop ΔP.

Flows at low Reynolds numbers are typical in microfluidics. In such regimes, viscous forces dominate over inertial forces caused by fluid particle acceleration/deceleration, allowing complete neglect of inertial terms in calculations. Consequently, the flow is governed by the Stokes equations

$$-\nabla p + \mu \nabla^2 \mathbf{u} = \mathbf{0}, \quad \nabla \cdot \mathbf{u} = 0, \tag{1}$$

where $\mathbf{u}$ is the fluid velocity and p is the pressure. When specifying boundary conditions, the surface of the considered channel S is represented as a union of the impermeable side surface of

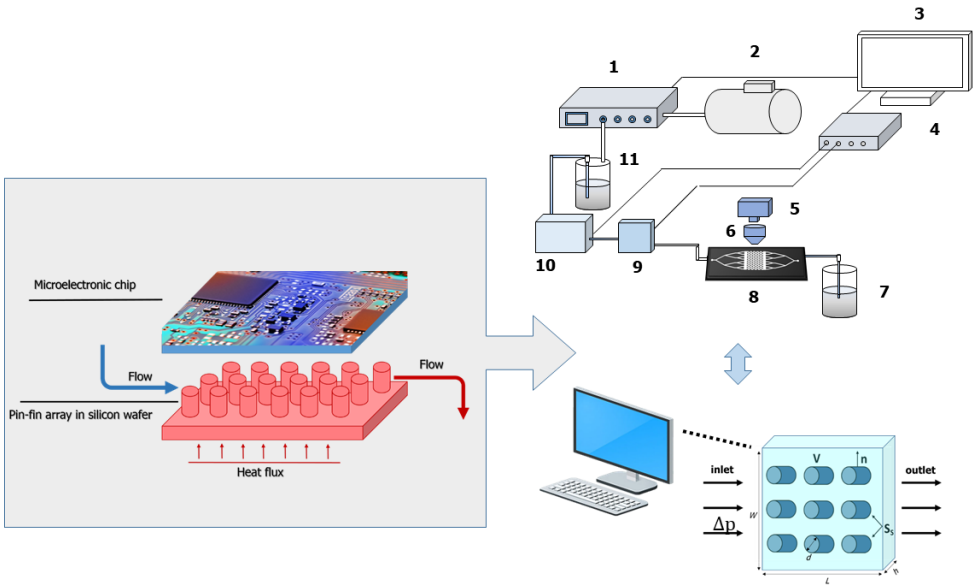

Fig. 1. Schematic representation of problem statement and experimental setup diagram (1 — pressure sensor, 2 — air compressor, 3 — personal computer, 4 — sensor readout module, 5 — high-speed video camera, 6 — optical microscope, 7, 11 — fluid tanks, 8 — microfluidic chip, 9 — pressure sensor, 10 — flow rate sensor)

the microchannel S_{side} (which includes the pin surfaces), the inlet section S_{in}, and the outlet section S_{out}: $S = S_{in} \cup S_{out} \cup S_{side}$. The side surface of the microchannel and the flow are assumed to be periodic with period L along the x-axis. The no-slip condition is imposed on S_{side}, supplemented by periodicity conditions on S_{in} and S_{out}

$$\mathbf{u}|_{x=0} = \mathbf{u}|_{x=L} = \mathbf{u}_s, \quad \mathbf{f}|_{x=L} = -\mathbf{f}|_{x=0} + \mathbf{f}_p = \mathbf{f}_s, \quad \mathbf{f}_p = \mathbf{i}_x \Delta P, \tag{2}$$

where ΔP is the prescribed pressure drop over a segment of length L, $\mathbf{u}s$ and $\mathbf{f}s$ are unknown functions at the inlet and outlet sections, and $\mathbf{f}$ is the traction.

To solve the formulated problem, we employ a numerical approach based on the Bboundary Element Method for three-dimensional problems. This method reduces the solution of the original partial differential equations in the entire simulated volume to solving boundary integral equations that connect the values of target functions only on the domain boundary. The channel surface is discretized using a triangular mesh. The collocation method applied at the centers of triangular elements transforms the boundary integral equations for computational points into a system of linear algebraic equations (SLAE) with a dense nonsymmetric matrix.

For accurate flow simulations in channels with complex geometries, their surfaces must be discretized using sufficiently refined meshes containing tens of thousands of triangular elements. In such cases, the inevitable memory limitations of computational systems can be addressed through a combined approach of algorithmic and hardware acceleration. The direct SLAE solution method was replaced with the Generalized Minimal Residual Method(GMRES), where the matrix-vector multiplication module is implemented using the Fast Multipole Method. Originally developed in the late 1980s for N-body problems, FMM reduces the computational complexity of matrix-vector products from quadratic to linear. This highly parallelizable algorithm enables additional acceleration through heterogeneous computing architectures and clusters [7]. The current implementation combines OpenMP parallelization on CPUs with CUDA-enabled GPU

acceleration. This approach enables three-dimensional simulations in asymmetric domains with complex configurations within reasonable time on a single workstation. The methodology was developed by the authors for Stokes equations and successfully applied to simulation of large number of emulsion droplets in unbounded shear flows [8], dynamics of compressible bubbles in unbounded domains [9], motion of deformable droplets in asymmetric microchannels [10], and analysis of viscous incompressible flow features in complex 3D microchannels [11]. Detailed implementation aspects, features, and validation tests for the computational modules are described in the authors previous work [11].

3. Results and discussion

The described computational modules were thoroughly verified by comparison with known analytical solutions for viscous flow in channels of various geometries [11]. Performance testing results of the computational modules are presented in [10]. Mesh convergence was investigated by comparing the calculated volumetric flow rate Q in a plane rectangular microchannel for several mesh configurations. Six meshes were considered with the number of triangular elements N_Δ ranging from 3000 to 90000, where each subsequent mesh was twice as refined as the previous one. Fig. 2 shows the plot of relative error ϵ_{Mesh} between computed Q values for different discretizations, where $\epsilon_{Mesh} = |Q_{i+1} - Q_i|/Q_i$ with Q_i and Q_{i+1} being the flow rates for the current and finer meshes respectively. The plot demonstrates good mesh convergence of the implemented modules.

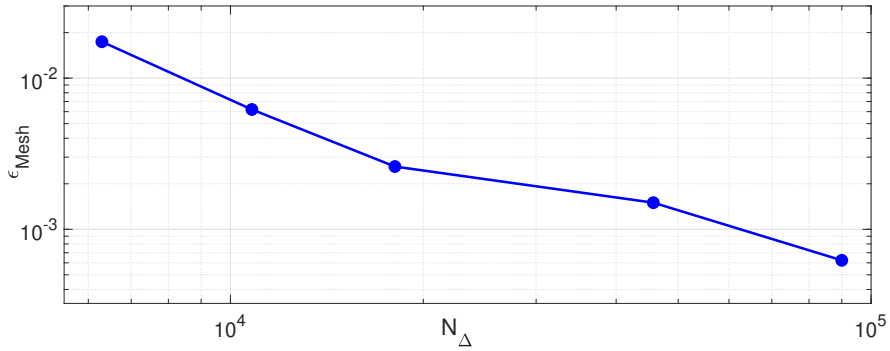

Fig. 2. Mesh convergence testing results for BEM computational modules

The optimization of microtextured heat sinks for industrial applications requires combined experimental and numerical approaches (Fig. 1) with data cross-validation. To validate the obtained results, a series of laboratory experiments were conducted using microfluidic chips. An experimental setup for microfluidic research was assembled and calibrated (Fig. 1), where fluid flows in the chip were generated using a VSO-BT pressure controller (Parker Hannifin). The volumetric flow rate was measured using a flow sensor (Elveflow, France). The microfluidic chip was mounted on the stage of an Olympus IX-71 optical microscope (Olympus, Japan) coupled with a Photron FASTCAM SA5 high-speed camera (MKOI LLC, Russia). Hydrodynamic experiments were performed on microfluidic chips made of cross-linked polydimethylsiloxane (PDMS) polymer fabricated by soft lithography (ELASTOSIL RT 601 A/B). Detailed experimental methodology is described in previous publications [12,13]. For flow visualization, $1\mu m$ polymer tracer particles were added to the fluid, and the velocity field was determined by analyzing particle dynamics using the PIVlab software package.

This work investigates rectangular microchannels with cylindrical pins featuring hierarchical structures achieved through controlled grouping with independent adjustment of intra-group

(Δ_{el}) and inter-group (Δ_{gr}) spacing. Previous studies by the authors examined dual-scale pin arrangements in 9-pin clusters ([12,13]), revealing significant flow stagnation within such clusters even with minor reductions in Δ_{el} spacing. This inevitably leads to substantially degraded heat removal efficiency from the substrate in these regions, causing dry spots and localized overheating. Consequently, the current study focuses on 4-pin cluster configurations.

To conduct a series of laboratory experiments, microchannels with a height of $h = 30\ \mu m$ were fabricated. The working region width was $W = 1\ mm$, with pin diameter $d = 110\ \mu m$ and pin height matching the total microchannel height. Two packing configurations were examined: a single-scale uniform distribution (SP) and a dual-scale distribution (DP). The packing parameters were varied as follows: $\Delta_{el} = \Delta_{gr} = 40\ \mu m$ (Fig. 3a), $\Delta_{el} = \Delta_{gr} = 50\ \mu m$ (Fig. 3b), $\Delta_{el} = 30\ \mu m$, $\Delta_{gr} = 50\ \mu m$ (Fig. 3c), and $\Delta_{el} = 40\ \mu m$, $\Delta_{gr} = 50\ \mu m$ (Fig. 3d). Consequently, the void fraction α of the simulated microchannel section calculated as the ratio of liquid volume in the pin configuration to the total liquid volume in a pin-free microchannel of identical dimensions varied from 59.4% to 70.1%.

For the investigated structures, velocity field visualization was performed using flow tracer techniques, and hydrodynamic flow patterns were analyzed at a constant pressure drop of $\Delta P = 1\ kPa$. The study demonstrated that introducing a secondary scale in the microchannel internal structure packing significantly alters both the fluid velocity redistribution and the overall chip throughput (Fig. 3a–d). Velocity fields were computed for analogous structures using the developed BEM-based code (Fig. 3e–h). Fig. 3 presents a comparative analysis of the obtained flow patterns, revealing good qualitative agreement between experimental and numerical results.

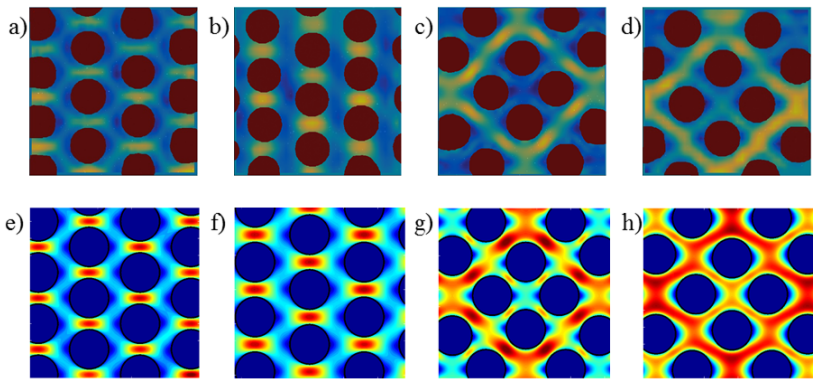

Fig. 3. Comparison of the velocity magnitude fields obtained experimentally (a)–(d) and numerically (e)–(h) for structures with single ((a) and (e): $\alpha = 59.4\%$, (b) and (f): $\alpha = 70.1\%$) and dual ((c) and (g): $\alpha = 57.0\%$, (d) and (h): $\alpha = 62.1\%$) pin distribution scales at a constant pressure drop $\Delta P = 1$ kPa

For numerical analysis of pin spatial distribution parameters, a series of computational experiments was conducted. The study examined microchannel sections with $h = 50\ \mu m$ and $h = 100\ \mu m$, where the working region length and width were $L = W = 1000\ \mu m$, and pin diameter $d = 50\ \mu m$. Uniform void fraction (SP) configurations were considered with $\Delta = \Delta_{el} = \Delta_{gr} = 20\ \mu m$, $25\ \mu m$, $30\ \mu m$, and $35\ \mu m$, resulting in void fractions ranging from 51% to 72%. Among the most important geometric characteristics are the height-to-pitch ratio $A_r = h/\Delta$ and pitch-to-diameter ratio $A_d = \Delta/d$, where Δ is the distance between pin surfaces. Optimal A_r values range from 2.4 to 3.1 for microchannels with hydraulic diameters on the order of hundreds of microns [14, 15]. The literature reports a wide range of A_d values from 0.22 to 2.78, and d/h ratios from 0.15 to 1.5 [16]. In the considered configurations, A_r varied from 1.43 to 5, A_d from 0.4 to 0.7, and d/h from 0.5 to 1.

Figs. 4 and 5 present velocity fields in the $z = h/2$ midplane and profiles of longitudinal (U_x) and transverse (U_y) velocity components in the $x = L/2$ plane as functions of $\Delta_{el} = \Delta_{gr}$ variations for uniform packing. When Δ increases from 25 μm to 35 μm (corresponding to a decrease in A_r from 2.5 to 1.43), the maximum flow velocity increases by approximately 60%, while the flow pattern in the channel undergoes significant changes. The results demonstrate that a 12% increase in channel void fraction leads to an average 50% increase in maximum flow velocity (Fig. 5).

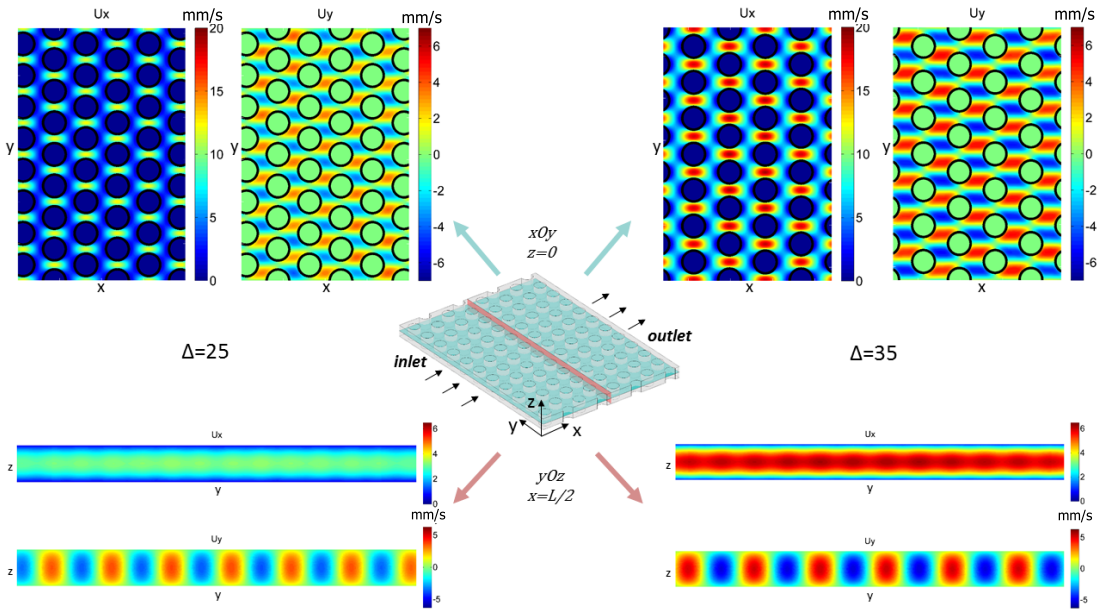

Fig. 4. The velocity fields of longitudinal (U_x) and transverse (U_y) components in xOy and yOz planes within microchannels featuring uniform pin distributions with $\Delta_{el} = \Delta_{gr} = 25$ μm and $\Delta_{el} = \Delta_{gr} = 35$ μm spacing

Numerical simulation of fluid flow was additionally performed in microchannels with dual-scale pin arrangements (DP) using 4-pin clusters. The geometric parameters of microchannels and pins remained identical to previous SP cases. The spacing between pins (Δ_{el}) and between pin clusters (Δ_{gr}) was varied, with four combinations examined: $\Delta_{el} = 20$ μm, $\Delta_{gr} = 25$ μm; $\Delta_{el} = 25$ μm, $\Delta_{gr} = 30$ μm; $\Delta_{el} = 20$ μm, $\Delta_{gr} = 35$ μm; and $\Delta_{el} = 25$ μm, $\Delta_{gr} = 35$ μm. The resulting void fractions ranged from 65.11% to 69.25%. Flow patterns were computed for all configurations in the $z = h/2$ midplane for both longitudinal (Fig. 6) and transverse (Fig. 7) velocity components.

Furthermore, comparative analysis of flow patterns between uniform (SP) and dual-scale (DP) void fraction configurations revealed distinct changes in transverse flow intensity at equivalent void fractions. For structures with SP ($\Delta = \Delta_{el} = \Delta_{gr} = 30$ μm) and DP ($\Delta_{el} = 25$ μm, $\Delta_{gr} = 35$ μm) arrangements exhibiting equal void fraction ($\alpha \approx 69\%$), the introduction of dual-scale packing increased transverse velocity intensity by 54%. Similarly, configurations with SP ($\Delta = \Delta_{el} = \Delta_{gr} = 25$ μm) and DP ($\Delta_{el} = 20$ μm, $\Delta_{gr} = 30$ μm) at identical void fraction ($\alpha \approx 65\%$) demonstrated a 102% enhancement in transverse flow intensity through dual-scale implementation.

In addition, a study was conducted on the change in throughput capacity of the microchannel section with varying packing arrangements for different channel heights $h = 50$ μm and $h =$

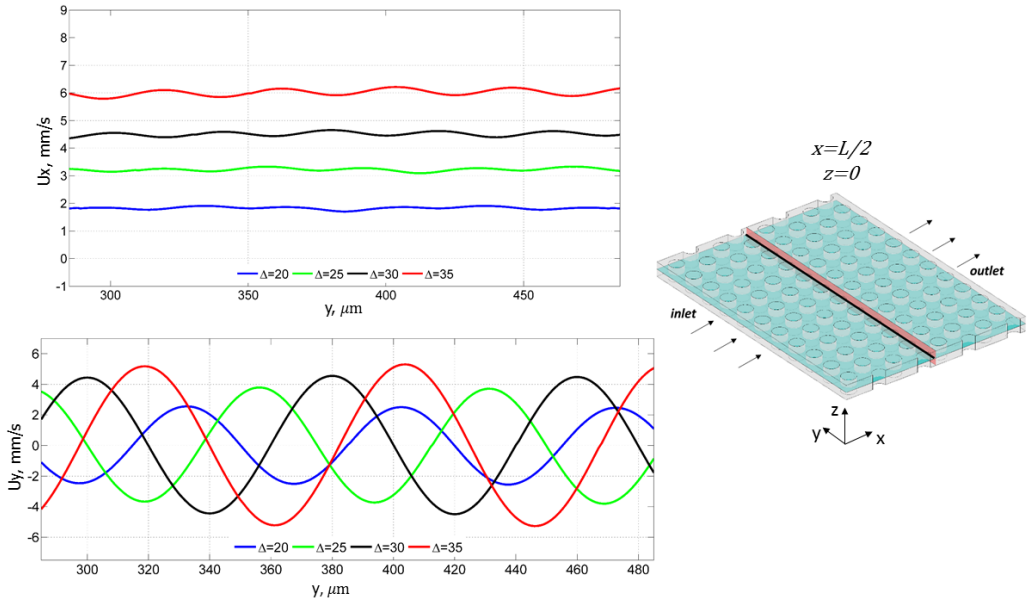

Fig. 5. Profiles of longitudinal (U_x) and transverse (U_y) velocity components in different cross-sections of a microchannel with uniform pin distribution (SP) at various $\Delta_{el} = \Delta_{gr}$ spacing values

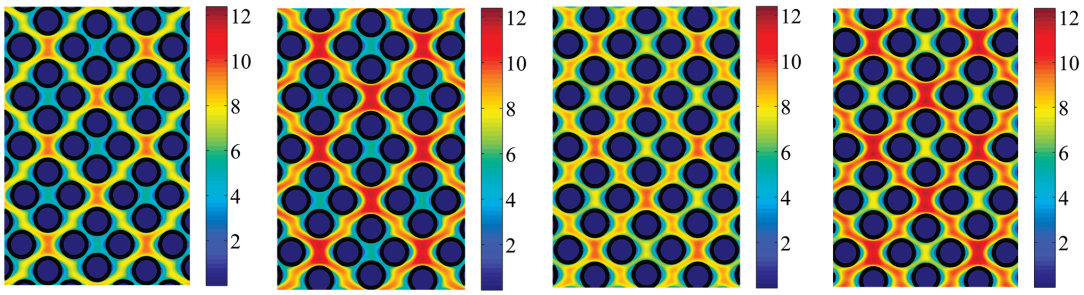

Fig. 6. Velocity fields of the longitudinal component (U_x) in the $z = h/2$ midplane of the microchannel with dual-scale pin arrangements at varying Δ_{el} and Δ_{gr} spacing values

100 μm (Fig. 8). The graphs in Fig. 8 show that at equal void fraction values, the throughput capacity of channels with uniform pin array distribution is higher than in cases with dual-scale distribution. Moreover, for channels with $h = 100$ μm, which correspond to smaller d/h values and consequently larger A_r, the difference in flow rates is more significant at lower α values (reaching 9%), while for microchannels with height $h = 50$ μm, the flow rate for dual void fraction models is 5% lower than for SP models.

In all considered cases, it is observed that as A_r values decrease, the hydraulic resistance of the channels reduces. It is also shown that the volumetric flow rate Q differs for DP cases with equal α: for $\Delta_{el} = 20$ μm, $\Delta_{gr} = 35$ μm it is higher than for $\Delta_{el} = 25$ μm, $\Delta_{gr} = 30$ μm by 3.5% at $h = 50$ μm and by 12.7% at $h = 100$ μm. Thus, the microchannel height significantly affects the throughput capacity with identical internal structure.

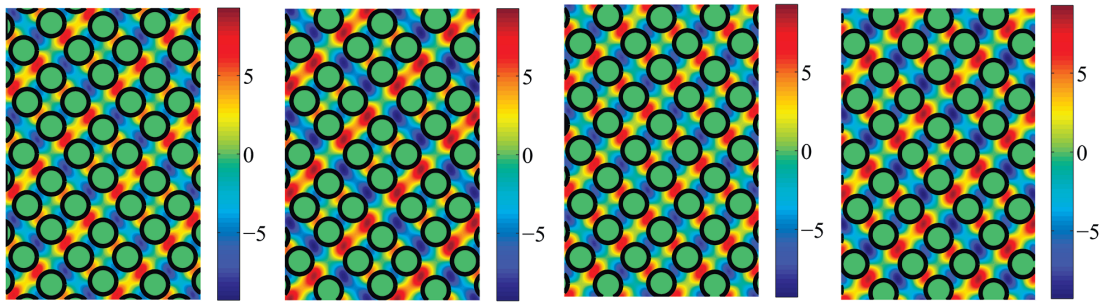

Fig. 7. Velocity fields of the transverse component (U_y) in the $z = h/2$ midplane of the microchannel with dual-scale pin arrangements at varying Δ_{el} and Δ_{gr} spacing values

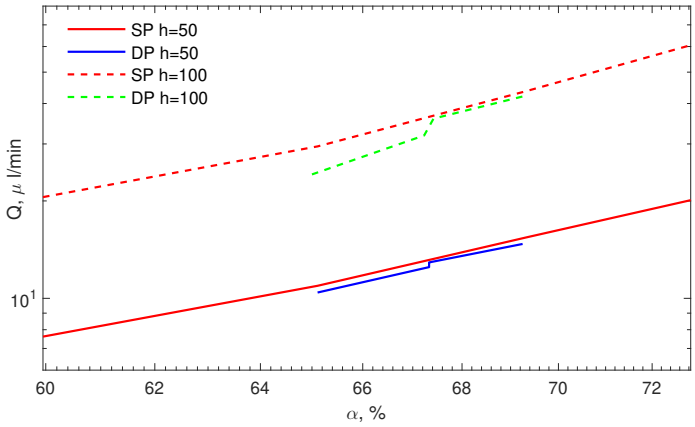

Fig. 8. Dependence of volumetric flow rate Q on void fraction α for various pin arrangement configurations with increasing microchannel height

Conclusions

The conducted study demonstrates significant influence of microchannel internal geometry, particularly cylindrical pin array configurations, on hydrodynamic characteristics of viscous incompressible fluid flow. Numerical simulation based on accelerated Boundary Element Method incorporating Fast Multipole Method and heterogeneous computing architectures enabled detailed investigation of flow features in complex three-dimensional microchannels. Verification and validation against experimental data confirmed high accuracy of the developed approach and its applicability for solving physically meaningful practical problems.

Calculations were performed and new numerical data were obtained on hydrodynamics in microchannels with single- and dual-scale pin packing configurations, where pins constitute 100% of the channel height. Velocity fields were constructed in various cross-sections and velocity profiles were analyzed for different pin packing characteristics. The key result of this work is the identification of significant influence of dual-scale pin packing on flow velocity redistribution and transverse flow intensity. It was established that introducing a second packing scale while maintaining overall void fraction leads to 54–102 % increase in transverse flow intensity, which may enhance heat transfer. However, this is accompanied by a moderate 5–9 % reduction in throughput capacity compared to uniformly distributed arrays.

The study also revealed that microchannel height is a critical parameter significantly affecting hydraulic resistance: for 100 μm high channels, the difference in throughput between single- and dual-scale configurations reaches 12.7%. A new criterion characterizing flows in plane microchannels with multiple pin distribution scales was identified - the ratio of distances between individual pins within packing groups (Δ_{el}) to distances between pin groups (Δ_{gr}). It was shown that for microstructures with dual-scale packing at equal void fraction, the throughput increases with decreasing Δ_{el}/Δ_{gr} ratios.

The obtained results are of significant importance for designing next-generation microheat sinks, enabling optimization of their geometry to achieve a balance between hydraulic resistance and heat removal efficiency. The developed computational approach opens prospects for simulation of more complex flows, including multiphase flows, in microfluidic systems. Further research may focus on investigating the combined influence of pin geometry and their thermal conductivity properties on heat transfer processes.

The research was supported by the Russian Science Foundation grant no. 24-19-00697 https://rscf.ru/project/24-19-00697/.

References

[1] R.Van Erp, R.Soleimanzadeh, L.Nela, G.Kampitsis, E.Matioli, Co-designing electronics with microfluidics for more sustainable cooling, *Nature*, **585**(2020), 211–216. DOI: 10.1038/s41586-020-2666-1

[2] T.Yang, X.Zhang, Z.Chang, R.Xu, J.Ma, L.Xu, L.Xi, A Review on Application of Pin-Fins in Enhancing Heat Transfer, *Energies*, **17**(2024), no. 17, 4305. DOI: 10.3390/en17174305

[3] H.Chen, Q.Gao, Y.Zhang, X.Yang, J.Wei, P.Di Marco, Experimental study of the flow boiling heat transfer characteristics of teardrop-like micro-pin-finned chip surface in semi-open microchannel, *Int. J. of Heat and Mass Transfer*, **238**(2025), 1264442.

[4] X.Rao, C.Jin, H.Zhang, J.Song, C.Xiao, A hybrid microchannel heat sink with ultra-low pressure drop for hotspot thermal management, *Int. J. of Heat and Mass Transfer*, **211**(2023), 124201. DOI: 10.1016/j.ijheatmasstransfer.2023.124201

[5] P.Bhandari, D.Padalia, L.Ranakoti, R.Khargotra, K.Andras, T.Singh, Thermo-hydraulic investigation of open micro prism pin fin heat sink having varying prism sides, *Alexandria Engineering Journal*, **69**(2023), 457–468. DOI: 10.1016/j.aej.2023.02.016

[6] M.Bahiraei, N.Mazaheri, M.R. Daneshyar, Employing elliptical pin-fins and nanofluid within a heat sink for cooling of electronic chips regarding energy efficiency perspective, *Applied thermal engineering*, **183**(2021), 116159. DOI: 10.1016/j.applthermaleng.2020.116159

[7] N.A.Gumerov, R.Duraiswami, Fast multipole methods on graphics processors, *J. Comput. Phys.*, **227**(2008), N 18, 8290–8313.

[8] O.A.Abramova, Y.A.Pityuk, N.A.Gumerov, I.S.Akhatov, High-Performance BEM Simulation of 3D Emulsion Flow, Communications in Computer and Information Science, Vol. 753, 2017, 317–330. DOI: 10.1007/978-3-319-67035-_23

[9] Y.A.Itkulova, O.A.Abramova, N.A.Gumerov, Boundary element simulations of compressible bubble dynamics in Stokes flows, Proceedings of the ASME 2013 International Mechanical Engineering Congress and Exposition, Vol. 7B: Fluids Engineering Systems and Technologies, 2013, V07BT08A010.

[10] O.A.Abramova, Y.A.Itkulova, N.A.Gumerov, FMM/GPU accelerated BEM simulation of emulsion flow in microchannels, Proceedings of the ASME 2013 International Mechanical Engineering Congress and Exposition, Vol. 7B: Fluids Engineering Systems and Technologies, 2013, IMECE2013-63193, V07BT08A009.

[11] O.A.Solnyshkina, A.Z.Bulatova, N.B.Bikkinina, Three-dimensional simulation and analysis of the fluid flow in contraction–expansion array microchannels, *European Journal of Mechanics - B/Fluids*, **113**(2025), 204270. DOI: 10.1016/j.euromechflu.2025.204270

[12] O.A.Solnyshkina, E.S.Batyrshin, Yu.A.Pityuk, Investigation of hydrodynamic flows in micromodels of double porosity media, *Fluid Dynamics*, **56**(2021), no.4, 451–459. DOI: 10.1134/S001546282104011X

[13] K.A.Galieva, I.Sh.Garifullin, E.S.Batyrshin, O.A.Solnyshkina, Experimental analysis of fluid dynamics in microchannels featuring two-scale fin pin arrays, *EPJ Web Conf.*, **321**(2025), 01006. DOI: 10.1051/epjconf/202532101006

[14] J.Lee, I.Mudawar, Low-temperature two-phase microchannel cooling for high-heat-flux thermal management of defense electronics, *IEEE transactions on components and packaging technologies*, **32**(2009), no. 2, 453–465.

[15] S.S.Bertsch, E.A.Groll, S.V.Garimella, Refrigerant flow boiling heat transfer in parallel microchannels as a function of local vapor quality, *Int. J. of Heat and Mass Transfer*, **51**(2008), no. 19-20 47–4787.

[16] P.Asrar, X.Zhang, C.E.Green, M.Bakir, Y.K. Joshi, Flow boiling of R245fa in a microgap with staggered circular cylindrical pin fins, *Int. J. of Heat and Mass Transfer*, **121**(2018), 329–342.

Исследование массопереноса в микроканалах с одним и двумя масштабами упаковки массива пинов

Ольга А. Солнышкина
Назгуль Б. Биккинина
Карина А. Галиева
Айгузель З.Ḃулатова
Искандар Ш. Гарифуллин
Уфимский государственный университет науки и технологий
Уфа, Российская Федерация

Аннотация. Важным аспектом в конструировании эффективных микротеплообменных устройств является подбор оптимальной геометрии внутренней структуры микроканалов с целью минимизации гидродинамического сопротивления и интенсификации поперечных потоков. Данная работа посвящена исследованию влияния изменения внутренней конфигурации микроканалов с массивом цилиндрических пинов на гидродинамические особенности течения вязкой несжимаемой жидкости. Используемый численный подход для решения уравнений Стокса в трехмерном случае для несимметричных областей основывается на методе граничных элементов, ускоренном быстрым методом мультиполей на гетерогенных вычислительных архитектурах. Валидация разработанных программных модулей проведена путем сопоставления с данными лабораторных экспериментов на микрофлюидных чипах. Проведена серия расчетов и получены новые данные по влиянию изменения параметров упаковки пинов внутри элемента микроканала на интенсификацию поперечных потоков и изменение пропускной способности.

Ключевые слова: микроканалы, микрофлюидика, метод граничных элементов, прямое численное моделирование, массив пинов, микротеплообменник.

Письмо в редакцию

Сергей В. Чеботарев
Алтайский государственный педагогический университет
Барнаул, Российская Федерация

Продолжая работать по темам, близким к материалам изложенным в моих публикациях в Вашем журнале, я обнаружил ошибки. Ниже я обозначил фрагменты с ошибками и мои предложения по исправлению.

А именно: в статье

S.V. Chebotarev, About limit distribution of sums of random variables, Journal of Siberian Federal University. Mathematics & Physics, 2016, 9(1), 17–29

На странице 19 на 12-й строке сверху напечатано:
$\boldsymbol{m}_k(\eta),\ k = 0, 1, \ldots, m.$
Должно быть напечатано:
$\boldsymbol{m}_k(\eta),\ k = 0, 1, \ldots, l.$

На странице 20 с первой строки сверху и до раздела **Rademacher random variables** напечатано:
then we obtain

$$\begin{aligned} v_m(\pi_{(n)}) &= \sum_{k=0}^{n} \mathbf{P}_{\pi_{(n)}}(k) \cdot \frac{B_n(m,k)}{\sqrt{n^m}}\Big|_{x_n=\frac{2k-n}{\sqrt{n}}}^{\text{exchange}} = \\ &= \sum_{x_n=-\sqrt{n}}^{\sqrt{n}} \left(\frac{h_m(x_n)}{\sqrt{m!}} + \mathcal{O}\Big(\frac{1}{\sqrt{n}}\Big) \right) \cdot \mathbf{P}_{\pi_{(n)}}(x_n) = \\ &= \frac{1}{\sqrt{m!}} \left(\sum_{x_n=-\sqrt{n}}^{\sqrt{n}} h_m(x_n)\mu_\eta(x_n)\triangle \right. \end{aligned}$$

Thus

$$\left. x_n + \mathcal{O}_1\Big(\frac{1}{\sqrt{n}}\Big) \right) \to \frac{1}{\sqrt{m!}} L_m(\eta).$$

It proves relation (4).
To prove (5) we use the relation

$$v_m(\pi_{(n)}) = \theta^m v_m(\xi_{(n)}) = \frac{v_m(\xi_{(n)})}{\sqrt{n^m}} \to \frac{1}{\sqrt{m!}} L_m(\eta). \tag{8}$$

It is true for any fixed m. Taking into account that $\lim\limits_{n\to\infty} \frac{n^m}{C_n^m m!} = 1$, for a big value n we have $v_m(\xi_{(n)}) = C_n^m \dot{v}_m(\xi_{(n)})$ and

$$v_m(\xi_{(n)}) \sim \frac{n^m}{m!} \dot{v}_m(\xi_{(n)})$$

The proof of (6) is the same, and (7) follows the previous relations. □

Let us assume that the average mixed moments of the sequence ξ exist. Then their limits are

$$\sqrt{n^m}\dot{v}_m(\xi_{(n)}) \sim \sqrt{n^m}\frac{m!}{n^m} \cdot v_m(\xi_{(n)}) = m!\frac{v_m(\xi_{(n)})}{\sqrt{n^m}} \to \sqrt{m!}L_m(\eta).$$

There is a relation between limited values of the average mixed moments of this sequence and values of moments of the limited random variable η, assuming that it exists and is absolutely continuous.

Theorem 2. *The first r moments $\ddot{v}_k(\xi) = \lim\limits_{n\to\infty} \ddot{v}_k(\xi_{(n)}), \quad k = 1, 2, \dots,$ of a random variable η are limited then and only then, when the first r of the average mixed moments $\boldsymbol{m}_k(\eta),\ k = 1, 2, \dots, r$ of the sequence ξ are limited and $\ddot{v}_m(\xi) = h_m(\boldsymbol{m}_\eta)$.*

Proof. The statement follows from the following relation:

$$\ddot{v}_m(\xi) = \int\limits_{-\infty}^{\infty} h_m(x)\mu_\eta(x)\,dx = \int\limits_{-\infty}^{\infty} \sum_{l=0}^{m} a_l x^l \mu_\eta(x)\,dx = \sum_{l=0}^{m} a_l \int\limits_{-\infty}^{\infty} x^l \mu_\eta(x)\,dx = h_m(\boldsymbol{m}_\eta).$$

□

Должно быть напечатано:
then we obtain

$$\begin{aligned} v_m(\pi_{(n)}) &= \sum_{k=0}^{n} \mathbf{P}_{\pi_{(n)}}(k) \cdot \frac{B_n(m,k)}{\sqrt{n^m}}\Big|_{x_n=\frac{2k-n}{\sqrt{n}}}^{\text{exchange}} = \\ &= \sum_{x_n=-\sqrt{n}}^{\sqrt{n}} \left(\frac{h_m(x_n)}{\sqrt{m!}} + \mathcal{O}\Big(\frac{1}{\sqrt{n}}\Big)\right) \cdot \mathbf{P}_{\pi_{(n)}}(x_n) = \\ &= \frac{1}{\sqrt{m!}} \left(\sum_{x_n=-\sqrt{n}}^{\sqrt{n}} h_m(x_n)\mu_\eta(x_n) \triangle x_n + \mathcal{O}_1\Big(\frac{1}{\sqrt{n}}\Big)\right) \to \frac{1}{\sqrt{m!}} L_m(\eta). \end{aligned}$$

Thus

$$v_m(\pi_{(n)}) = \theta^m v_m(\xi_{(n)}) = \frac{v_m(\xi_{(n)})}{\sqrt{n^m}} \to \frac{1}{\sqrt{m!}} L_m(\eta).$$

It proves relation (4).
To prove (5) we use the relation

$$\lim_{n\to\infty} \frac{n^m}{C_n^m m!} = 1 \tag{8}$$

that is true for any fixed m. Taking into account that $v_m(\xi_{(n)}) = C_n^m \dot{v}_m(\xi_{(n)})$, for a big value n we have $v_m(\xi_{(n)}) \sim \frac{n^m}{m!}\dot{v}_m(\xi_{(n)})$ and

$$\sqrt{n^m}\dot{v}_m(\xi_{(n)}) \sim \sqrt{n^m}\frac{m!}{n^m} \cdot v_m(\xi_{(n)}) = m! \frac{v_m(\xi_{(n)})}{\sqrt{n^m}} \to \sqrt{m!} L_m(\eta).$$

The proof of (6) is the same, and (7) follows the previous relations. □

Let us denote the averaged mixed moments limit values of the sequence ξ, when it exist, as

$$\ddot{v}_k(\xi) = \lim_{n\to\infty} \ddot{v}_k(\xi_{(n)}), \quad k = 1, 2, \dots.$$

There is a relation between this limited values of the average mixed moments and values of moments of the limited random variable η, assuming that it exists and is absolutely continuous.

Теорема 2. *The first r moments $\boldsymbol{m}_k(\eta),\ k = 1, 2, \dots, r$ of a random variable η are limited then and only then, when the first r of the average mixed moments $\ddot{v}_k(\xi),\ k = 1, 2, \dots, r$ of the sequence ξ are limited and $\ddot{v}_m(\xi) = h_m(\boldsymbol{m}_\eta)$.*

Proof. The statement follows from the following relation:

$$\ddot{v}_m(\xi) = \int\limits_{-\infty}^{\infty} h_m(x)\mu_\eta(x)\,dx = \int\limits_{-\infty}^{\infty} \sum_{l=0}^{m} a_l x^l \mu_\eta(x)\,dx = \sum_{l=0}^{m} a_l \int\limits_{-\infty}^{\infty} x^l \mu_\eta(x)\,dx = h_m(\boldsymbol{m}_\eta).$$

□

На странице 27 в 20-й строке сверху напечатано:

$$\ddot{v}_m(\hat{\xi}_{(n)}) = \frac{v_m(\hat{\xi}_{(n)})}{\sqrt{C_n^m}} = \frac{v_{I_m}(\hat{\xi}_{(n)})}{\sqrt{C_n^m}},$$

Должно быть напечатано:

$$\ddot{v}_m(\hat{\xi}_{(n)}) = \frac{v_m(\hat{\xi}_{(n)})}{\sqrt{C_n^m}} = \frac{v_{I_m}(\hat{\xi}_{(n)})C_n^m}{\sqrt{C_n^m}} = v_{I_m}(\hat{\xi}_{(n)})\sqrt{C_n^m},$$

На странице 27 в 24-й строке сверху напечатано:

$$\theta^m s^m \mathbf{E}\hat{\gamma}_{1,0}\hat{\gamma}_{2,0}\dots\hat{\gamma}_{m,0} = \theta^m s^m v_{I_m}(\hat{\gamma}_{(ns)}) = \theta^m s^m v_m(\hat{\gamma}_{(ns)}) = \theta^m s^m v_m(\gamma_{(ns)}).$$

Должно быть напечатано:

$$\theta^m s^m \mathbf{E}\hat{\gamma}_{1,0}\hat{\gamma}_{2,0}\dots\hat{\gamma}_{m,0} = \theta^m s^m v_{I_m}(\hat{\gamma}_{(ns)}) = \theta^m s^m \dot{v}_m(\hat{\gamma}_{(ns)}) = \theta^m s^m \dot{v}_m(\gamma_{(ns)}).$$

На странице 27 в 26-й строке сверху напечатано:

$$\ddot{v}_m(\hat{\xi}_{(n)}) = \frac{\theta^m s^m v_m(\gamma_{(ns)})}{\sqrt{C_n^m}} = \theta^m s^m \ddot{v}_m(\gamma_{(ns)})\sqrt{\frac{C_{ns}^m}{C_n^m}}.$$

Должно быть напечатано:

$$\ddot{v}_m(\hat{\xi}_{(n)}) = \theta^m s^m \dot{v}_m(\gamma_{(ns)})\sqrt{C_n^m} = \theta^m s^m \ddot{v}_m(\gamma_{(ns)})\sqrt{\frac{C_n^m}{C_{ns}^m}}.$$

На странице 27 в 28-й строке сверху напечатано:

$$\ddot{v}_m(\hat{\xi}) = \theta^m s^{\frac{3m}{2}} \ddot{v}_m(\gamma) \tag{16}$$

Должно быть напечатано:

$$\ddot{v}_m(\hat{\xi}) = \theta^m s^{\frac{m}{2}} \ddot{v}_m(\gamma) \tag{16}$$

На странице 28 во 2-й строке сверху напечатано:

$$\ddot{v}_m(\gamma) = \theta^{-m} s^{-\frac{3m}{2}} \ddot{v}_m(\hat{\xi}).$$

Должно быть напечатано:

$$\ddot{v}_m(\gamma) = \theta^{-m} s^{-\frac{m}{2}} \ddot{v}_m(\hat{\xi}).$$

На странице 28 во 4-й строке сверху напечатано:

$$\mu_\eta(x) = \frac{1}{\sqrt{2\pi\theta^2 s}} e^{-\frac{x^2}{2\theta^2 s}} \sum_{m=0}^{\infty} \frac{\ddot{v}_m(\hat{\xi})}{\theta^m s^{\frac{3m}{2}}} \cdot h_m\Big(\frac{x}{\theta\sqrt{s}}\Big).$$

Должно быть напечатано:

$$\mu_\eta(x) = \frac{1}{\sqrt{2\pi\theta^2 s}} e^{-\frac{x^2}{2\theta^2 s}} \sum_{m=0}^{\infty} \frac{\ddot{v}_m(\hat{\xi})}{\theta^m s^{\frac{m}{2}}} \cdot h_m\Big(\frac{x}{\theta\sqrt{s}}\Big).$$

На странице 28 с 10-й строки сверху и до раздела **References** напечатано:

Let us consider two special cases: the expression for the density of sum of sequence $\xi \in \Xi_2$, when $\theta = \frac{1}{\sqrt{s}}$ and $\theta = \frac{1}{s\sqrt{s}}$. In the first case the change scale of x is conserved but the values of mixed moments are changed. In the second case the values of the moments are conserved but the change scale of x is changed.

Corollary 4.2. *Let us assume that sequence $\xi \in \Xi_2$ is given and $\theta = \frac{1}{\sqrt{s}}$. Then the random variable η*

$$\frac{1}{\sqrt{n}} \sum_{t=1}^{n} \xi_t \underset{n\to\infty}{\Rightarrow} \eta$$

for any $x \in \mathbf{R}$ has the density distribution function

$$\mu_\eta(x) = \frac{1}{\sqrt{2\pi}} e^{-\frac{x^2}{2}} \sum_{m=0}^{\infty} \frac{\ddot{v}_m(\hat{\xi})}{s^m} \cdot h_m(x).$$

Corollary 4.3. *Let us assume that sequence $\xi \in \Xi_2$ is given and $\theta = \frac{1}{s\sqrt{s}}$. Then the random variable η*

$$\frac{1}{\sqrt{n}} \sum_{t=1}^{n} \xi_t \underset{n\to\infty}{\Rightarrow} \eta$$

for any $x \in \mathbf{R}$ has the density distribution function

$$\mu_\eta(x) = \frac{s}{\sqrt{2\pi}} e^{-\frac{(sx)^2}{2}} \sum_{m=0}^{\infty} \ddot{v}_m(\hat{\xi}) \cdot h_m(sx).$$

Должно быть напечатано:

Let us consider one special case: the expression for the density of sum of sequence $\xi \in \Xi_2$, when $\theta = \frac{1}{\sqrt{s}}$. In this case the simplest expression for density distribution function is obtained.

Corollary 4.2. *Let us assume that sequence $\xi \in \Xi_2$ is given and $\theta = \frac{1}{\sqrt{s}}$. Then the random variable η*

$$\frac{1}{\sqrt{n}} \sum_{t=1}^{n} \xi_t \underset{n\to\infty}{\Rightarrow} \eta$$

for any $x \in \mathbf{R}$ has the density distribution function

$$\mu_\eta(x) = \frac{1}{\sqrt{2\pi}} e^{-\frac{x^2}{2}} \sum_{m=0}^{\infty} \ddot{v}_m(\hat{\xi}) \cdot h_m(x).$$

В добавление к предыдущей корректуре моей статьи S.V. Chebotarev, About limit distribution of sums of random variables, Journal of Siberian Federal University. Mathematics & Physics, 2016, 9(1), 17–29 высылаю Вам еще ряд некорректностей, которые я обнаружил:

На странице 26 в строках с 11-й по 16-ю сверху напечатано:

$$\frac{1}{\sqrt{k}} \sum_{\tau=1}^{k} \gamma_\tau = \frac{1}{\sqrt{k}} \Big(\sum_{\tau=1}^{n''s} \gamma_\tau - \sum_{\tau=k+1}^{n''s} \gamma_\tau \Big) = \frac{n''s}{\sqrt{k}} \frac{1}{\sqrt{k}} \Big(\sum_{\tau=1}^{n''s} \gamma_\tau - \sum_{\tau=k+1}^{n''s} \gamma_\tau \Big)$$

and

$$\frac{1}{\sqrt{k}}\sum_{\tau=1}^{k}\gamma_\tau=\frac{1}{\sqrt{k}}\Big(\sum_{\tau=1}^{n's}\gamma_\tau+\sum_{\tau=k+1}^{n's}\gamma_\tau\Big)=\frac{n's}{\sqrt{k}}\frac{1}{\sqrt{n's}}\Big(\sum_{\tau=1}^{n's}\gamma_\tau+\sum_{\tau=k+1}^{n's}\gamma_\tau\Big),$$

we obtain that

$$\mathbf{P}\Big(\frac{1}{\sqrt{n''s}}\Big(\sum_{\tau=1}^{n''s}\gamma_\tau-\sum_{\tau=k+1}^{n''s}\gamma_\tau\Big)<x\Big)\leqslant\mathbf{P}\Big(\frac{1}{\sqrt{k}}\sum_{\tau=1}^{k}\gamma_\tau<x\Big)\leqslant$$
$$\leqslant\mathbf{P}\Big(\frac{1}{\sqrt{n's}}\Big(\sum_{\tau=1}^{n's}\gamma_\tau+\sum_{\tau=k+1}^{n's}\gamma_\tau\Big)<x\Big).$$

Должно быть напечатано:

$$\frac{1}{\sqrt{n''s}}\Big(\sum_{\tau=1}^{n''s}\gamma_\tau-\sum_{\tau=k+1}^{n''s}\gamma_\tau\Big)\leqslant\sqrt{\frac{n''s}{k}}\frac{1}{\sqrt{n''s}}\Big(\sum_{\tau=1}^{n''s}\gamma_\tau-\sum_{\tau=k+1}^{n''s}\gamma_\tau\Big)=\frac{1}{\sqrt{k}}\Big(\sum_{\tau=1}^{n''s}\gamma_\tau-\sum_{\tau=k+1}^{n''s}\gamma_\tau\Big)=\frac{1}{\sqrt{k}}\sum_{\tau=1}^{k}\gamma_\tau$$

and

$$\frac{1}{\sqrt{k}}\sum_{\tau=1}^{k}\gamma_\tau=\frac{1}{\sqrt{k}}\Big(\sum_{\tau=1}^{n's}\gamma_\tau+\sum_{\tau=k+1}^{n's}\gamma_\tau\Big)=\sqrt{\frac{n's}{k}}\frac{1}{\sqrt{n's}}\Big(\sum_{\tau=1}^{n's}\gamma_\tau+\sum_{\tau=k+1}^{n's}\gamma_\tau\Big)\leqslant\frac{1}{\sqrt{n's}}\Big(\sum_{\tau=1}^{n's}\gamma_\tau+\sum_{\tau=k+1}^{n's}\gamma_\tau\Big),$$

we obtain that

$$\mathbf{P}\Big(\frac{1}{\sqrt{n''s}}\Big(\sum_{\tau=1}^{n''s}\gamma_\tau-\sum_{\tau=k+1}^{n''s}\gamma_\tau\Big)<x\Big)\geqslant\mathbf{P}\Big(\frac{1}{\sqrt{k}}\sum_{\tau=1}^{k}\gamma_\tau<x\Big)\geqslant$$
$$\geqslant\mathbf{P}\Big(\frac{1}{\sqrt{n's}}\Big(\sum_{\tau=1}^{n's}\gamma_\tau+\sum_{\tau=k+1}^{n's}\gamma_\tau\Big)<x\Big).$$

На странице 26 в строках с 17-й по 21-ю сверху напечатано:
for $x\geqslant 0$.

It follows that

$$\mathbf{P}\Big(\frac{1}{\sqrt{n''s}}\sum_{\tau=1}^{n''s}\gamma_\tau<x+\frac{1}{\sqrt{n''}}\Big)\leqslant\mathbf{P}\Big(\frac{1}{\sqrt{k}}\sum_{\tau=1}^{k}\gamma_\tau<x\Big)\leqslant\mathbf{P}\Big(\frac{1}{\sqrt{n's}}\sum_{\tau=1}^{n's}\gamma_\tau<x-\frac{1}{\sqrt{n'}}\Big).$$

and for $x<0$ we have

$$\mathbf{P}\Big(\frac{1}{\sqrt{n''s}}\sum_{\tau=1}^{n''s}\gamma_\tau<x+\frac{1}{\sqrt{n''}}\Big)\geqslant\mathbf{P}\Big(\frac{1}{\sqrt{k}}\sum_{\tau=1}^{k}\gamma_\tau<x\Big)\geqslant\mathbf{P}\Big(\frac{1}{\sqrt{n's}}\sum_{\tau=1}^{n's}\gamma_\tau<x-\frac{1}{\sqrt{n'}}\Big).$$

Должно быть напечатано:

It follows that

$$\mathbf{P}\Big(\frac{1}{\sqrt{n''s}}\sum_{\tau=1}^{n''s}\gamma_\tau<x+\sqrt{\frac{s}{n''}}\Big)\geqslant\mathbf{P}\Big(\frac{1}{\sqrt{k}}\sum_{\tau=1}^{k}\gamma_\tau<x\Big)\geqslant\mathbf{P}\Big(\frac{1}{\sqrt{n's}}\sum_{\tau=1}^{n's}\gamma_\tau<x-\sqrt{\frac{s}{n'}}\Big).$$

В статье 2017 года

S.V. Chebotarev, On the limit distribution of sums of real random variables, Journal of Siberian Federal University. Mathematics & Physics 2017, 10(3), 310–313

в связи с изменением формулы (16) из статьи 2016 года рассмотренной выше, замечены следующие ошибки:

На странице 313 во 2-й строке сверху напечатано:

$$\ddot{v}_m(\hat{\xi}) = \lim_{n\to\infty}\lim_{s\to\infty} s^m \cdot \ddot{v}_m(\hat{\gamma}_{(n),s}) = 0,\ \forall m \geqslant 2,$$

Должно быть напечатано:

$$\ddot{v}_m(\hat{\xi}) = \lim_{n\to\infty}\lim_{s\to\infty} s^{\frac{m}{2}} \cdot \ddot{v}_m(\hat{\gamma}_{(n),s}) = 0,\ \forall m \geqslant 2,$$

На странице 313 в 6-й строке сверху напечатано:

$$\ddot{v}_m(\hat{\xi}) = \lim_{n\to\infty}\lim_{s\to\infty} s^m \cdot \ddot{v}_m(\hat{\gamma}_{(n),s}) < \infty,\ \forall m \geqslant 2,$$

Должно быть напечатано:

$$\ddot{v}_m(\hat{\xi}) = \lim_{n\to\infty}\lim_{s\to\infty} s^{\frac{m}{2}} \cdot \ddot{v}_m(\hat{\gamma}_{(n),s}) < \infty,\ \forall m \geqslant 2,$$

На странице 313 в 9-й строке сверху напечатано:

$$\ddot{v}_m(\hat{\xi}) = \lim_{n\to\infty}\lim_{s\to\infty} s^m \cdot \ddot{v}_m(\hat{\gamma}_{(n),s}) = \infty,\ \forall m \geqslant 2,$$

Должно быть напечатано:

$$\ddot{v}_m(\hat{\xi}) = \lim_{n\to\infty}\lim_{s\to\infty} s^{\frac{m}{2}} \cdot \ddot{v}_m(\hat{\gamma}_{(n),s}) = \infty,\ \forall m \geqslant 2.$$